UNIVERSITY OF SOUTHAMPTON

FACULTY OF NATURAL AND ENVIRONMENTAL SCIENCES
Ocean and Earth Science
2015/2016

GEOLOGICAL STORAGE OF CARBON DIOXIDE IN OCEANIC CRUST

by

Chiara Marieni

Thesis for the degree of Doctor of Philosophy

June 2016

UNIVERSITY OF SOUTHAMPTON

ABSTRACT

FACULTY OF NATURAL AND ENVIRONMENTAL SCIENCES

Ocean and Earth Science

GEOLOGICAL STORAGE OF CARBON DIOXIDE IN OCEANIC CRUST

Chiara Marieni

The rise of atmospheric carbon dioxide (CO_2), due to decades of burning of fossil fuels, is a key driver of anthropogenic climate change. Carbon Capture and Storage (CCS) is one of the most promising mitigation strategies for long-term sequestration of CO_2.

Unlike most conventional CCS investigations targeting deep saline aquifers, this thesis focuses on the potential of the uppermost oceanic crust, inspired by the strong evidence that basaltic seafloor has acted, in the past, as a major sink for CO_2.

The study of temperature, pressure, and density of CO_2 and seawater at the sediment-basement interface for the whole seafloor highlights the influence of water depth, sediment thickness, and oceanic crustal age on the relative gravitational stability of CO_2. Consequently, 8% of the entire oceanic crust is recognised as suitable for gravitational and physical trapping of CO_2 injected into the basement. Five potential targets are proposed, and even the smallest of these provides sufficient carbon dioxide sequestration capacity for the next centuries.

Batch experiments on the mineral dissolution of submarine mafic rocks and ophiolitic gabbro, in CO_2-rich solutions, contribute to improve the fundamental understanding of geochemical reactions at mid-ocean ridge flank temperatures (40 ˚C). Concentrations of silicon and calcium in solution, and particle size are identified as the key factors to quantify the rock reactivity. Ca dissolution rates suggest calcite, plagioclase and amphibole are the principal sources of calcium at pH ~5.

The attempted estimation of costs related to the transport and storage of 20 Mt/yr of CO_2 in deep-sea basalts, as a function of distance from the shore, injection rate, and water depth, shows the economic feasibility of potential offshore CCS projects. Overall, the expenditures are dominated by the number of ships and wells required to deliver large volumes of CO_2 to reservoirs located far from the coast, rather than by the water depth. These financial considerations could potentially improve if the CCS strategies conquered a significant place in the global market.

Table of Contents

ABSTRACT

Table of Contents i

List of tables v

List of figures ix

DECLARATION OF AUTHORSHIP xiii

Acknowledgements xv

List of accompanying material xvii

Abbreviations xix

Chapter 1: Introduction 1

1.1 Anthropogenic CO_2 emissions into the atmosphere 1
1.2 Mitigation strategies 4
1.3 Geological storage of CO_2 5
1.4 Unconventional reservoirs 7
1.5 Deep-sea basalts 10
1.6 Chapter summaries 11

Chapter 2: Thermodynamic properties of CO_2 at oceanic crust conditions 13

2.1. Introduction 13
2.1.1. Oceanic crust 14
2.1.2. Heat flow in oceanic crust 16
2.1.3. Oceanic floor carbon uptake 21
2.2. CO_2 and seawater 22
2.3. Thermodynamic properties of oceanic crust 24
2.3.1. Heat flow estimation for the oceanic lithosphere 24
2.3.2. Temperature at the sediment-basement interface of the oceanic lithosphere 26
2.3.3. Pressure at the sediment-basement interface of the oceanic lithosphere 27
2.3.4. CO_2 density at the sediment-basement interface of the oceanic lithosphere 28

2.4. Thermodynamic properties of two case studies in oceanic crust 31
2.4.1. Juan de Fuca Plate 31
2.4.2. Eastern equatorial Pacific Ocean 34
2.4.3. Summary of two case studies 38
2.4.4. Validation process of temperature and pressure estimations .. 39
2.5. Conclusions 41
Chapter 3: Oceanic crust as a reservoir for CCS 43
3.1. Introduction 43
3.2. CO_2 trapping mechanisms in offshore basalts 44
3.3. Gravitational trapping 46
3.4. Physical trapping 47
3.5. Offshore basalt targets 50
3.5.1. JdF and eePO as unsuitable CCS targets 56
3.5.2. Target a: Indian Ocean 58
3.5.2.1. Comparison between estimated and measured values 60
3.5.2.2. Implications of target a in offshore CCS 63
3.6. Conclusions 66
Chapter 4: Low temperature batch dissolution experiments in a CO_2-seawater-rock system 67
4.1. Introduction 67
4.2. Material and methods 71
4.2.1. Starting material 71
4.2.2. Sample preparation 76
4.2.3. Experimental setup 81
4.3. Results 85
4.3.1. Fluid chemistry 85
4.3.2. Fine particle removal 91
4.3.3. Rock dissolution 94
4.4. Discussion 95
4.4.1. Characterisation of physical properties 95
4.4.2. Rock dissolution characterisation 96

4.4.2.1. Rock dissolution rates....97
4.4.2.2. Reactive mass....98
4.4.2.3. Rock mass transfer....100
4.4.2.4. Calcium source....101
4.4.3. Comparison with previous rock dissolution experiments....105
4.5. Conclusions....112
Chapter 5: Costs linked with offshore CO_2 sequestration projects in oceanic crust....115
5.1. Introduction....115
5.2. Costs for CO_2 transport offshore....116
5.3. Costs for CO_2 storage offshore....121
5.4. Summary of costs for CO_2 transport and storage offshore....123
5.5. Costs for CO_2 sequestration in deep-sea basalts....124
5.6. Conclusions....129
Chapter 6: Discussion and conclusions....131
6.1. Results summary....131
6.2. CO_2 trapping mechanism implications....132
6.3. Carbon sequestration on mid-ocean ridge flanks....134
6.4. Batch CO_2 dissolution experiment implications....135
6.5. CO_2 cost implications for CCS offshore....136
6.6. Social implications....138
6.7. Limitations....140
6.8. Future work....142
6.9. Conclusions....144
Appendix….. 145
A-Chapter 1....145
A-Chapter 2....151
A-Chapter 3....159
A-Chapter 4, Methods....166
A-Chapter 4, Analyses....176
A-Chapter 4, Samples....197
Bibliography....203

List of tables

Table 2.1: *Summary of the key parameters used in PSM, GDH1 model, and HSCM to calculate heat flow and oceanic depth.* 18

Table 2.2: *Summary of the equations used by GDH1 and HSCM to calculate heat flow and bathymetry.* 25

Table 2.3: *Summary of the properties of the sites on JdFP drilled during the ODP Leg168*.. 34

Table 2.4: *Summary of the properties of the eePO Sites 504, 896 and 1256 drilled during several expeditions*.. 37

Table 3.1: *Oceanic sediment types and relative porosity and permeability*.... 48

Table 3.2: *Properties of the five potential reservoirs*.................................... 53

Table 3.3: *Surface area estimations as a function of type of trapping and sediment thickness*... 54

Table 3.4: *Summary of drilling results and estimations from the global databases used in this study for the representative sites of each scientific cruise*.. 61

Table 4.1: *Summary of the experiments on mafic and ultramafic rocks carried out in the last two decades to investigate the rock dissolution potential*..... 70

Table 4.2: *Summary of previous experimental results on rock dissolution potential, described as maximum silicon release rates, normalised to surface area*.. 70

Table 4.3: *Chemical composition of the starting solution for the experimental work* 73

Table 4.4: *Mineralogical composition of the MOR basalts (JdF mix 1, 2, 3, and CD80WP132) and ophiolitic gabbro (G1)*... 74

Table 4.5: *Summary of rock chemical compositions for 63-125 µm and <63 µm size fractions, expressed in percent (data from XRF analyses)* 76

Table 4.6: *Surface areas measured with BET and geometrically calculated for each of the five samples*.. 78

Table 4.7: *Summary of the initial conditions for the CO_2-seawater-oceanic rock dissolution experiments* 83

Table 4.8: *Summary of evaporation effect* 86

Table 4.9: *Summary of the R-squared coefficients for the regression curves applied to silicon and calcium concentrations in aqueous solution, for all the experimental run.* 89

Table 4.10: *Particle diameters and correspondent geometric surface areas for each sample, before and after the dissolution experiments* 93

Table 4.11: *Rock dissolution extent in % using Si and Ca concentrations for all the samples used during the experiment. All the rock is considered to be "reactive".* 95

Table 4.12: *Summary of rock dissolution rates, normalised to the geometric surface area, for all the experimental runs* 98

Table 4.13: *Summary of top-surface reactive mass for all the experimental runs, with Si and Ca rock dissolution extent* 100

Table 4.14: *Averages of mineral molar compositions, and relative stoichiometric Ca/Si ratios* 101

Table 4.15: *Summary of mineral dissolution rates and relative experimental conditions at which they have been measured* 104

Table 4.16: *Composition comparison between basalts and gabbro used in this study with the rocks used by Wolff-Boenisch et al. [2011] ,Critelli et al. [2014] and Gudbrandsson et al. [2011]* 105

Table 4.17: *Summary of experimental conditions of current study and previous works* 106

Table 4.18: *Summary of rock mineralogy for metabasalt [Critelli et al., 2014], and crystalline basalt [Gudbrandsson et al., 2014] used during dissolution experiments* 109

Table 5.1: *Details of the facilities and timings for which the cost estimations are based.* 119

Table 5.2: *Cost estimates for CO_2 offshore transport via ships, from two point-sources (2 * 10 Mt CO_2/yr) along the coastline to a storage site located 500, 1000, or 1500 km from shore.* 120

Table 5.3: *Cost estimates for four offshore scenarios, each able to store 20 Mt CO_2 per year, taking into account injection rate, number of wells, pipeline distance and template.* 121

Table 5.4: *Summary of cost estimations for transporting and storing 20 Mt of CO_2 per year, in a 25-years long offshore project* 123

Table 5.5: *Comparison of total cost estimations for transporting and storing 500Mt of CO_2 in 25 years in deep-sea basalts located at water depth of ~2500 and ~5000 m, for two distance scenarios (500 and 1500 km, respectively).* 128

List of figures

Figure 1.1: *Global carbon budget shown as average values between 2004 and 2015* 2

Figure 1.2: *Trends of carbon dioxide concentration into the atmosphere, in the last 200 years, and over the last 800 thousands of years* 3

Figure 1.3: *Key mitigation strategies for reducing atmospheric CO_2 emissions from 57 Gt to 14 Gt, over the next 40 years.* 5

Figure 2.1: *Oceanic crustal age* 14

Figure 2.2: *Modified version of Penrose oceanic crust stratigraphy* 15

Figure 2.3: *Heat flow and ocean depth measurements as a function of age* .. 17

Figure 2.4: *Data and models for heat flow and ocean depth* 18

Figure 2.5: *Schematic illustration of observed and estimated heat flow, with difference defined as a hydrothermal flux* 20

Figure 2.6: *Phase diagram of CO_2 for temperatures from -100 to 50 °C, and pressures from 0.01 and 1000 MPa* 22

Figure 2.7: *Densities of seawater and carbon dioxide as a function of temperature between 0 and 100 °C, and pressure between 0 and 60 MPa.* 24

Figure 2.8: *Histograms of thermal conductivity measurements for marine sediments from the IODP-ODP database, and the global compilation* 26

Figure 2.9: *Map of density difference $\Delta\rho$ between CO_2 and seawater at the sediment-basement interface, generated using the GDH1 model, with $K_s = 1$ W/(m K)* 30

Figure 2.10: *Map of density difference $\Delta\rho$ between CO_2 and seawater at the sediment-basement interface, generated using the HSCM model, with Ks = 1 W/(m K)* 30

Figure 2.11: *Tectonic setting of the Juan de Fuca Plate* 32

Figure 2.12: *Schematic cross section of the ODP Leg 168 drilling transect profile* 33

Figure 2.13: *Tectonic setting of the eastern equatorial Pacific Ocean.* 36

Figure 2.14: Schematic cross sections of the Holes 504B and 896A, and Hole 1256D..36

Figure 2.15: Density difference between CO_2 and seawater density as a function of pressure between 0 and 60 MPa, and temperature between 0 and 100 °C, with the phase diagram of CO_2 overlaid. JdFP and eePO data are shown....38

Figure 2.16: Comparison between estimated temperatures (from GDH1 model) in the eastern equatorial Pacific Ocean (eePO) and the Juan de Fuca Plate (JdFP), and measured downhole temperatures at the sediment-basement interface...39

Figure 3.1: Primary trapping mechanisms for the long-term storage of carbon dioxide in offshore basalts...44

Figure 3.2: Density difference between CO_2 and seawater density as a function of pressure between 0 and 60 MPa, and temperature between 0 and 100 °C, with the phase diagram of CO_2 overlaid...46

Figure 3.3: A cylindrical equal area map showing locations for gravitational trapping of CO_2, using the GDH1 model for heat flow estimations.............47

Figure 3.4: Sediment thickness versus oceanic floor age..............................48

Figure 3.5: Density difference between CO_2 and seawater at the sediment-basement interface as a function of plate age and sediment thickness using the GDH1 model to determine both water depth and thermal conditions....49

Figure 3.6: A cylindrical equal area map showing locations for physical trapping of CO_2 in the seafloor 50

Figure 3.7: A cylindrical equal area map showing locations for stable geological sequestration of CO_2...52

Figure 3.8: A cylindrical equal area map showing locations for stable geological sequestration of CO_2 at 300 m into the basement.....................................53

Figure 3.9: Map of density difference Δρ between CO_2 and seawater at (a) the Juan de Fuca Plate (with K_s = 2 W/(m K)) and (b) the eastern equatorial Pacific Ocean (with K_s = 1 W/(m K))...57

Figure 3.10: Tectonic setting of the offshore Western Australia 58

Figure 3.11: An equal area map showing the potential target ***a*** for CO_2 storage...59

Figure 3.12: *Single-Channel Seismic (SCS) reflection profiles RC1403 and ELT45, with correspondent locations on topographic map* 62

Figure 3.13: *Bathymetric map showing the potential target* ***a*** *for CO_2 storage. Suitable locations for gravitational trapping ($\Delta\rho > 0$ kg/m^3)* 64

Figure 4.1: *Grain size distribution for all the ground samples (63-125 µm) before the dissolution experiments.* 79

Figure 4.2: *SEM images from PTS-polished thin sections, and from stubs* 80

Figure 4.3: *Summary of eight batch type experiments on three type of rocks: JdF, CD80WP132, and G1* 81

Figure 4.4: *Experimental setup for the CO_2-seawater-oceanic rock dissolution experiments* 83

Figure 4.5: *pH, alkalinity and DIC trends throughout all the duration of the experiments* 85

Figure 4.6: *Si and Ca concentrations overtime during the dissolution experiments* 87

Figure 4.7: *Ca/Si and ΔCa/ΔSi ratios in all the aqueous solutions, expressed as a function of time during the dissolution experiments* 88

Figure 4.8: *Best fitting curves of silicon and calcium concentrations for all the experimental runs.* 89

Figure 4.9: *Si and Ca release rate as a function of time during the dissolution experiments.* 90

Figure 4.10: *Grain size distribution analyses and SEM images for all the JdF samples, before and after the experiments* 91

Figure 4.11: *Grain size distribution analyses and SEM images for all the CD80WP132 basalts and G1 gabbro, before and after the experiments* 92

Figure 4.12: *Rock dissolution extents (Si and Ca) in % vs. time for all the samples used in the experiments. All the mass is considered as "reactive"* 94

Figure 4.13: *Si and Ca dissolution rates as a function of time normalized to the initial geometric surface area of rock for all experimental runs* 97

Figure 4.14: *Sketch of rock dissolution within the HDPE reactor used in this study, considering only the top-surface area of the sample as reactive.* 99

Figure 4.15: Mineral average distribution in the basalts of JdF and MAR, and in the ophiolitic gabbro G1. 102

Figure 4.16: Si release rates "surface corrected" as a function of pH, for all the experimental runs of this study at 40 °C and for SWC-Cl series from Wolff-Boenisch et al. [2011] 108

Figure 4.17: Whole rock Si dissolution rates "surface corrected" for all the experimental runs as a function of pH, compared to experimental results of Critelli et al. [2014], Gudbrandsson et al. [2011] at 25 °C, and Wolff-Boenisch et al. [2011] 110

Figure 4.18: Whole rock Ca dissolution rates "surface corrected" for all the experimental runs as a function of pH, compared to the experimental results of Gudbrandsson et al. [2011] at 25 °C. 110

Figure 5.1: Network of CO_2 offshore transport via ship, from two point-sources (2 * 10 Mt CO_2/yr) along the coastline to a storage site at 500, 1000, or 1500 km from shore 117

Figure 5.2: Bathymetric map of all the ocean, with contours every 2500 m. Locations for stable geological sequestration of CO_2 at the sediment-basement interface are shown 124

Figure 5.3: Bathymetric map of all the ocean, with contours every 2500 m. Locations for gravitational trapping of CO_2 ($\rho_{CO2} > \rho_{seawater}$) at the sediment-basement interface are shown. 125

Figure 5.4: Summary of drilling times for several scenarios of water depth, sediment and basement thickness 126

Figure 6.1: Summary of cost estimations for the transport and storage of 20 Mt of CO_2, in 25 years-long CCS projects. Six scenarios are shown as a function of distance from shore (500 or 1500 km), water depth (2500 or 5000 m), and number of injection wells (7 or 40). 137

DECLARATION OF AUTHORSHIP

I, **CHIARA MARIENI**

declare that this thesis and the work presented in it are my own and has been generated by me as the result of my own original research.

GEOLOGICAL STORAGE OF CARBON DIOXIDE IN OCEANIC CRUST

I confirm that:

1. This work was done wholly or mainly while in candidature for a research degree at this University;
2. Where any part of this thesis has previously been submitted for a degree or any other qualification at this University or any other institution, this has been clearly stated;
3. Where I have consulted the published work of others, this is always clearly attributed;
4. Where I have quoted from the work of others, the source is always given. With the exception of such quotations, this thesis is entirely my own work;
5. I have acknowledged all main sources of help;
6. Where the thesis is based on work done by myself jointly with others, I have made clear exactly what was done by others and what I have contributed myself;
7. Parts of this work have been published as: *Marieni et al. [2013].*

Signed: ....

Date:...

Acknowledgements

I would first like to thank my supervisor Damon Teagle for his guidance and support over the last four years. I particularly thank him for the perseverance on my English, the determination to develop my scientific mind, and the sharing of his immense knowledge on the oceanic crust. Unbelievably, you managed to deal with my stubbornness and “Italianism”.

As well as every apple has its half, my PhD project had Juerg Matter. I would like to thank him for appearing two years ago in Southampton with a great deal of thought and enthusiasm, and for always managing to make me feel positive about my work.

Also, I would not have managed to publish my first paper without the priceless help of Tim Henstock. I will never forget his look at me when I dared to prefer MATLAB to GMT. Never again Tim, I promise!

A special thank goes to Matt Cooper, because he taught me all the basics of how to “behave” in a geochemical lab, spending a considerable amount of time to deal with a whole new line of experiments. Despite the “trouble” nickname that you gave to me, I know you had a lot of fun too!

As Yoda would say, “numerous are the people who collaborated with me” for the success of this thesis: Steve Roberts (great Panel Chair), Martin Palmer (geochemistry), Catriona Menzies (lab techniques and English, just to say a couple…), Bob & John – now John & Dan (thin sections and jewellery), Kate Peel (IC, ICP-OES), Pavel Gaca (IC), Richard Pearce (SEM), James Hunt (Mastersizer), Greeshma Gadikota (BET, Columbia University, NY), Alex Webber (scientific, or not, discussions), Michelle Harris (carbonate veins world), and Nick Woodman (my first baby steps in geoengineering). Overall, thanks for having gone along with me and my ideas!

Finally, we all know that I am way too chatty, so a list of friends and family to fit in two lines will be reductive to describe all the experiences and emotions that I shared with you. However, thanks to Valtellina’s people (si mamma, tu sei in questo gruppo), housemates (tons in four years), 12.30-lunch mates, volleyball players, geochemistry group, Italian and Taiwanese crews, and all the NOC people who had the misfortune to ask me the routinely “how are you doing?” question and got trapped to listen to my actual state of mind.

And of course, thanks to you Si.

List of accompanying material

A-CHAPTER 1

CH1-1 *Marieni et al. [2013]* **145**

A-CHAPTER 2

CH2-1A Heat flow map generated with the GDH1 model **151**

CH2-1B Heat flow map generated with the HSCM model **152**

CH2-2 NOAA National Geophysical Data Center (NGDC) sediment thickness map [*Divins, 2003*] **153**

CH2-3A Map of temperature at the sediment-basement interface, generated with the GDH1 model **154**

CH2-3B Map of temperature at the sediment-basement interface, generated with the HSCM model **155**

CH2-4 General Bathymetric Chart of the Oceans (GEBCO) – gridfive world bathymetry map [*IOC et al., 2003*] **156**

CH2-5 Map of hydrostatic pressure at the sediment-basement interface **157**

CH2-6 Comparison between estimated temperatures in the eastern equatorial Pacific Ocean (eePO) and the Juan de Fuca Plate (JdFP), and measured downhole temperatures at the sediment-basement interface [Marieni et al., 2013] **158**

A-Chapter 3

CH3-1 Density difference between CO_2 and seawater at the sediment-basement interface as a function of plate age and sediment thickness using A- GDH1 and B- HSCM models to determine both water depth and thermal conditions **159**

CH3-2 Equal area map showing locations for stable geological sequestration of CO_2 using the HSCM model **160**

CH3-3 Equal area maps showing locations for stable geological sequestration of CO_2 using the GDH1 model, for several sediment thickness intervals **161**

A-Chapter 4

Methods

CH4-1 Alkalinity titration **166**

CH4-2 ICP-OES, cations **167**

CH4-3 IC, anions **170**

CH4-4 PTS terminology **172**

CH4-5 ICP-MS on whole silicate rock **173**

Analyses

CH4-6 SEM + SEM-EDS on whole rocks (63-125 µm, pre experiments) **176**

CH4-7 ICP-MS on whole silicate rocks (63-125 µm, and <63 µm) **179**

CH4-8 XRD on whole silicate rocks (63-125 µm, and <63 µm) **181**

CH4-9 XRF on whole silicate rocks (63-125 µm, and <63 µm) **182**

CH4-10 SEM-EDS on single grains (63-125 µm, pre experiments) **184**

CH4-11 SEM + SEM-EDS on whole rock (63-125 µm, post experiments) **186**

CH4-12 ICP-OES and IC (original + corrected for evaporation effect) **191**

Samples

CH4-13 Juan de Fuca, IODP U1362 A **197**

CH4-14 MAR, CD80WP132 **200**

CH3-15 Ophiolitic gabbro, G1 **201**

Abbreviations

A_{BET}	BET surface area
Ac	carbon Alkalinity
A_{geo}	geometric surface area
B€	Billions of euro ($x10^9$)
barg	bar gouge (bar-1)
BET	Brunauer-Emmett-Teller (surface area analysis)
CAPEX	CAPital EXpenditure
CCS	Carbon Capture and Storage
CDR	Carbon Dioxide Removal
CO_2	carbon dioxide
COP21	Conference Of Parties – 21st
DIC	Dissolved Inorganic Carbon
DSDP	Deep Sea Drilling Project
eePO	eastern equatorial Pacific Ocean
EOR	Enhanced Oil Recovery
EPR	East Pacific Rise
FLNG	Floating Liquefied Natural Gas
FPSO	Floating Production Storage and Offloading system
GDH1	Global Depth and Heat flow model -1
GEBCO	GEneral Bathymetric Chart of the Ocean
GMT	Generic Mapping Tool
GSA	Geometric Surface Area analysis
GSD	Grain Size Distribution
Gt	Giga tons ($x10^9$)
HSCM	Half Space Cooling Model
IAPSO	International Association for the Physical Sciences of the Oceans
IC	Ion Chromatography
ICP-MS	Inductively Coupled Plasma-Mass Spectrometry
ICP-OES	Inductively Coupled Plasma-Optical Emission Spectrometry
IEA GHG	International Energy Agency Greenhouse Gases
IODP-1	Integrated Ocean Drilling Program
IODP-2	International Ocean Discovery Program
IPCC	Intergovernmental Panel on Climate Change
JdF	Juan de Fuca
K_s	thermal conductivity of sediments
LNG	Liquid Natural Gas
LOI	Loss Of Ignition
M€	Millions of euro ($x10^6$)
Ma	Millions of year ago ($x10^6$)
MAR	Mid-Atlantic Ridge

mbsf	meters below seafloor
mbsl	meters below sea-level
MORB	Mid-Ocean Ridge Basalt
Mt	Mega tons (x10^{6})
Mtpa	Millions of tonne per annum (x10^{6})
Myr	Millions of year
NIST	National Institute of Standards and Technology
NOAA	National Oceanic and Atmospheric Administration
ODP	Ocean Drilling Program
OPEX	annual OPerational EXpenditure
P	Pressure
pCO_2	partial pressure of carbon dioxide
ppm	parts per million
PSM	Parsons and Sclater's Model
PTS	Polished Thin Section
RCB	Rotary Core Barrel
RTJ	RodriguezTriple Junction
S	Salinity
SCS	Single-Channel Seismic
SEM	Scanning Electron Microscope
SEM-EDS	SEM with x-ray spectroscopy
STL	Submerged Turret Loading
SWIR	South-West Indian Ridge
T	Temperature
TA	Total Alkalinity
TLT	Temperature Logging Tool
XRD	X-Ray Diffraction
XRF	X-Ray Fluorescence
yr	year
ZEP	Zero Emissions Platform
$\Delta\rho$	difference of density
ρ	density

Chapter 1: Introduction

1.1 Anthropogenic CO_2 emissions into the atmosphere

"*Warming of the climate system is unequivocal*" [*IPCC*, 2013], and "*most of the observed increase in global average temperatures since the mid-20th century is extremely likely due to the observed increase in anthropogenic greenhouse gas concentrations*" [*IPCC*, 2014b].

Carbon dioxide (CO_2) is the primary greenhouse gas emitted through human activities. But, how can we distinguish the anthropogenic sources of CO_2, essentially due to the burning of fossil fuels, from the natural components? The key factor is the isotopic signature of the carbon (C) in CO_2. Among the three naturally occurring isotopes of carbon on Earth (^{12}C, ^{13}C, and ^{14}C), carbon-12 and -13 are stable. Their isotopic ratio ^{13}C:^{12}C (usually expressed as $\delta^{13}C$ relative to a reference material) can be used to distinguish atmospheric carbon sources. For example, plants have less ^{13}C relative to the seawater because during photosynthesis plants more easily take in ^{12}C over the heavier ^{13}C isotope. Carbon-14 (^{14}C or radiocarbon) is a radioactive carbon isotope, with a half-life of about 5730 years. Its decay permits reliable age determination of samples up to 50k years old because after ~10 half-lives the quantity of ^{14}C remaining is <0.1% and difficult to detect. Hence, younger natural sources of CO_2 are relatively rich in ^{14}C and ^{13}C, whereas fossil fuels, which are usually millions of years old, are depleted in ^{13}C and contain little to no traces of ^{14}C. Considering this difference, the origin of CO_2 concentrations can be differentiated, making mapping of the global carbon budget possible.

The global carbon budget is the balance of the exchanges (inputs and outputs) of carbon between carbon reservoirs (carbon cycle) or within one specific loop (such as atmosphere – biosphere exchange). The Earth's oceans, soils, plants, animals and volcanoes are all natural sources of carbon dioxide emissions, whereas human CO_2 inputs into the atmosphere include fossil fuel combustion (i.e. power plants, transport, and gas flaring), cement production, and land use (i.e. deforestation, logging and intensive cultivation of cropland soils). Natural and anthropogenic exchanges of carbon dioxide (CO_2) between oceans, atmosphere and land are shown in Figure 1.1, as average values calculated between 2004 and 2015 [*Canadell et al.*, 2007; *IPCC*, 2007; *Le Quere et al.*, 2009; *Le Quéré et al.*, 2014; *Le Quéré et al.*, 2015; *Sabine et al.*, 2004]. The total amount of CO_2 currently stored into the atmosphere is approximately 3100 Gt (~400 ppm). According to ^{14}C measurements, 2200 Gt (~280 ppm) are from natural sources, whereas 900 Gt (~115 ppm) are derived from human activities [www.esrl.noaa.gov, *Hofmann et al.*, 2009]. At present, global CO_2 anthropogenic emissions are estimated to be 36 Gt/yr [www.cdiac.ornl.gov]. Of this, 30% is absorbed by terrestrial plants and soils ("*land sink*"), 26% by the oceans ("*ocean sink*"), with 44% remaining in the atmosphere. This leads to an annual growth of 16 Gt of CO_2 in the atmosphere.

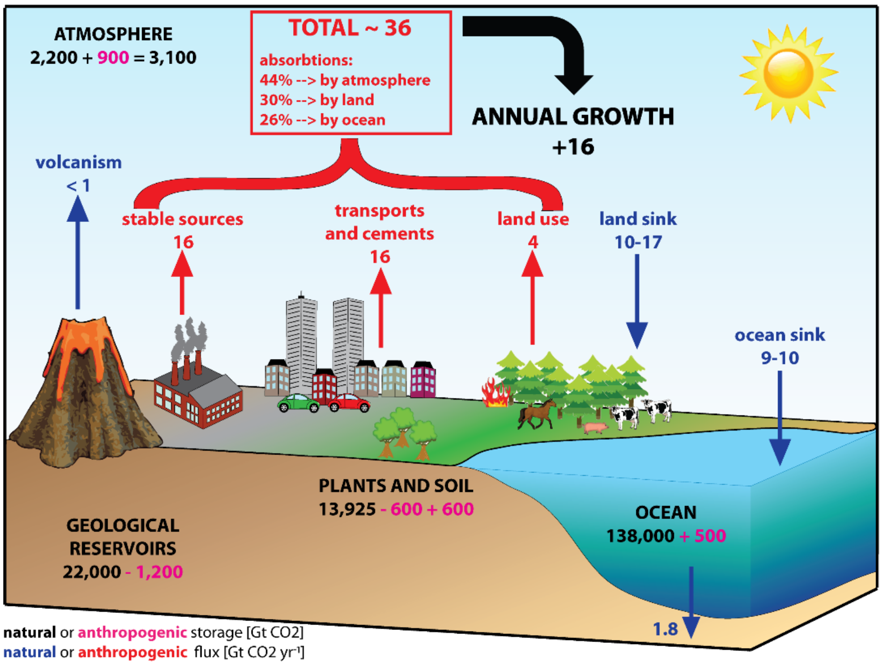

Figure 1.1: Global carbon budget shown as average values between 2004 and 2015 [Canadell et al., 2007; IPCC, 2007; Le Quere et al., 2009; Le Quéré et al., 2014; Le Quéré et al., 2015; Sabine et al., 2004]. CO_2 fluxes are expressed in Gt/yr with red (anthropogenic flux) and blue (natural flux) arrows. The sum of these exchanges leads to an annual growth of 16 Gt of CO_2 to the atmosphere. Natural and anthropogenic reservoirs of Gt of CO_2 in the Earth are shown in black and pink, respectively.

However, the atmospheric CO_2 annual growth is an average value in constant evolution. The current high concentration of CO_2 in the atmosphere is the result of an exponential increasing trend registered worldwide over the last 200 years (Figure 1.2). Records of atmospheric CO_2 concentrations measured in air bubbles trapped in ice cores [*Barnola et al.*, 1987; *Luthi et al.*, 2008] over the last 800 thousand years show a cyclic trend, corresponding to glacial and interglacial periods, with peaks and troughs always below the threshold of 300 ppm (Figure 1.2). Since the beginning of industrialisation in ~1800 AD, atmospheric CO_2 concentrations have risen rapidly. High CO_2 concentrations (>300 ppm) are only present in significantly older records. For example, during the Early Carboniferous (320-360 Ma) the atmospheric concentration of carbon dioxide was ~1000 ppm, whereas during the Late Carboniferous (270-320 Ma) CO_2 levels were “as low” as they are today [*Franks et al.*, 2014].

To summarize: several CO_2 concentration excursions during the history of our planet have been documented and dated with several geochemical proxies but no peaks above 300 ppm have occurred in the last 800 thousand years. The CO_2 mass in the atmosphere has constantly grown over the last 200 years, leading to a current annual increase of 16 Gt. The starting point and the development of this exponentially increasing trend coincides with the industrial use of fossil fuels on a global scale.

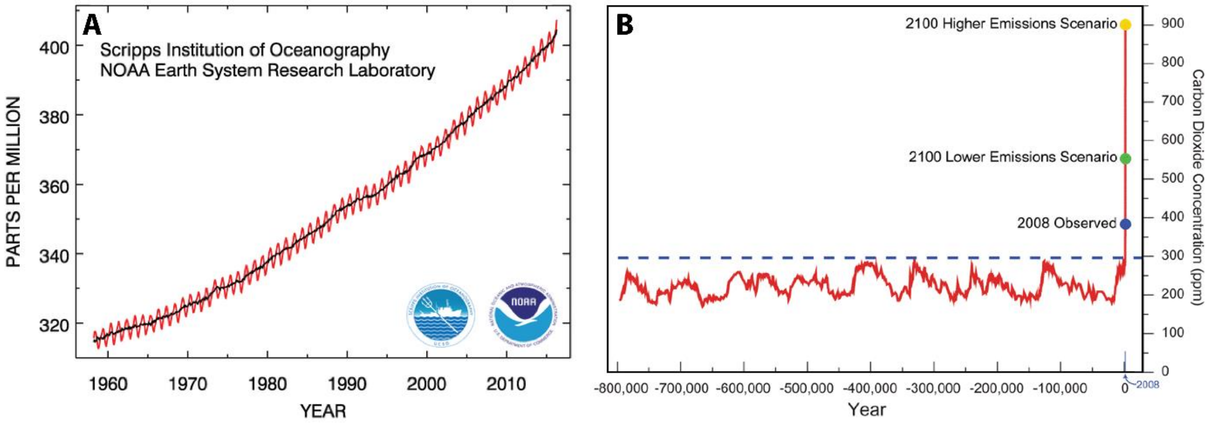

*Figure 1.2: Trends of carbon dioxide concentration into the atmosphere (1 ppm of CO_2 = 7.84 Gt of CO_2), in the last 200 years (**A** – “Keeling Curve” Mauna Loa Observatory May 2016, www.esrl.noaa.gov/gmd/ccgg/trends/full.html), and over the last 800 thousands of years (**B** – www.ncdc.noaa.gov), using data from ice core records and more recent direct measurements.*

1.2 Mitigation strategies

Climate change mitigation has the characteristics of a collective action problem at the global scale, with the goal of reducing the carbon dioxide content of the atmosphere. In the past 20 years, scientists, politicians, and economists have suggested mitigation strategies and new "green" policies to minimise the effect of this greenhouse gas on global climate and the environment (e.g. ocean acidification) [*Bryant*, 1997; *IPCC*, 2014a]. Repeated warnings sent by the United Nations Intergovernmental Panel on Climate Change, specifically in the report *IPCC* [2007], concluded that yearly reductions of at least 50% in global CO_2 emissions compared to 2000 levels will need to be achieved by 2050 (from ~30 to 14 Gt CO_2) to limit the long-term global average temperature rise to between 2.0 and 2.4 °C relative to pre-industrial levels. The temperature limit is based on models that demonstrate how ocean circulation, weather patterns, and marine ecosystem cycles, will be irreversibly perturbed beyond this threshold [*Frölicher and Joos*, 2010; *Prentice et al.*, 2001; *Solomon et al.*, 2009], with severe implications for humans and the environment. At the Paris climate conference in 2015 (COP21), governments agreed to endeavour to limit the increase to 1.5 °C [*Conference of the Parties Twenty-first Session*, 2015]. On the other hand, *Allen et al.* [2009] and *IPCC [2013*] have noted that cumulative anthropogenic CO_2 emissions may provide a better constraint on temperature rise than CO_2 emission rates. Anthropogenic CO_2 emissions are expected to peak at 3.67 trillion tons of CO_2 (~470 ppm), about half of which has already been emitted, and will most likely induce a warming of 2 °C above pre-industrial temperatures, with a 5–95% confidence interval of 1.3–3.9 °C.

Various approaches have been proposed to reduce anthropogenic CO_2 emissions, including reducing energy demand, improving technology efficiency, and increasing the contribution of nuclear and low carbon renewable energy. An additional approach is to increase the carbon sinks, for example through Carbon Capture and Storage (CCS) of CO_2 in reservoirs that safely preclude the re-emission of anthropogenic CO_2 into the atmosphere [*Hoffert et al.*, 2002; *IPCC*, 2005b; *Pacala and Socolow*, 2004]. The implementation of one strategy does not preclude the deployment of others. In order to halve the current anthropogenic CO_2 emissions (~36 Gt/yr) and reach the target of 14 Gt/yr of CO_2 into the atmosphere by 2050, as indicated by the *IPCC reports*, we should apply all the possible low-carbon technologies (Figure 1.3) [*IEA*, 2012]. CCs is one of the most promising strategies because it could be implemented while fossil fuels remain the dominant source of energy, and renewable energies are being developed. Looking at the impact of these strategies, CCS could potentially contribute to a ~19% reduction in total CO_2 emissions over the next 40 years, based on the current direct emissions from industry (e.g. iron and steel, cement, chemical and petrochemical). CCS generally requires the separation of CO_2 from an industrial gas stream or directly from the atmosphere (Capture), compression and transport via pipelines or ships (Transport), and injection of fluids into underground geologic reservoirs (Storage).

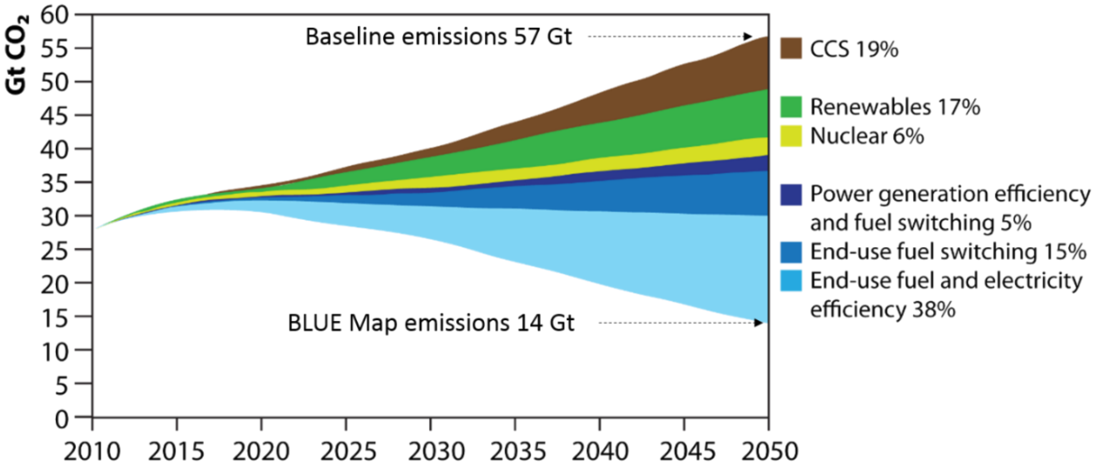

Figure 1.3: Key mitigation strategies for reducing atmospheric CO_2 emissions from 57 Gt (Baseline emissions) to 14 Gt (BLUE Map emissions), over the next 40 years [modified version of IEA, 2010].

1.3 Geological storage of CO_2

Pore space in deep geological rock formations may provide a secure location to store anthropogenic CO_2 emissions. Several geological formations/reservoirs, such as deep saline aquifers, depleted oil and gas reservoirs, and unmineable coal seams are being investigated as possible CO_2 storage reservoirs [*Bachu et al.*, 2007; *IPCC*, 2005a]. However, the effectiveness of these reservoirs depends on their storage capacity, reservoir stability, risk of leakage, and retention time [*Benson and Cole*, 2008; *Hawkins*, 2004; *Rochelle et al.*, 2004].

The injection of CO_2 into deep saline sedimentary aquifers [*Eccles and Pratson*, 2012; *House et al.*, 2006; *Levine et al.*, 2007; *Schrag*, 2009] is a particularly promising approach due to their large storage capacity, the natural presence of low permeability cap rocks, and the common proximity to major industrial sources. For example, at the Sleipner Project (240 km West of Stavanger, Norway) more than 15 million tons of CO_2 have been injected into a subsea saline formation in the North Sea since 1996 [www.statoil.com/en/TechnologyInnovation/NewEnergy/Co2CaptureStorage/Pages/SleipnerVest.aspx].

Depleted oil and gas reservoirs have also been proposed due to their large storage capacity, existing infrastructure, and because injection of gases such as carbon dioxide can be used for enhanced oil recovery [*Bachu*, 2000; *Jessen et al.*, 2005]. The IEA GHG Weyburn-Midale CO_2 Monitoring and Storage Project (Canada) is an example of CCS applied to enhanced oil recovery (EOR). This site is currently the world's largest carbon capture and storage project with over 25 million tons of injected anthropogenic CO_2 since the project start in 2000, and with about 2.8 million tons of CO_2 being stored annually [www.ptrc.ca/projects/weyburn-midale].

The *IPCC report [2005]* estimates that deep saline aquifers have a storage capacity of at least 1000 Gt CO_2 and depleted oil and gas reservoirs could store 675–900 Gt CO_2, although the storage capacity of unminable coal formations is uncertain, with estimates up to 200 Gt CO_2. Considering that ~1840 Gt of CO_2 have already been emitted into the atmosphere (see Section 1.2.), the potential reservoir storage capacity of "conventional" formations is unlikely to accommodate future CO_2 anthropogenic emissions.

Hence, mafic and ultramafic formations are starting to be considered as potential sites suitable for carbon sequestration [*Dessert et al.*, 2003; *Gislason and Oelkers*, 2014; *Gislason et al.*, 2010; *Godard et al.*, 2011; *Kelemen and Matter*, 2008; *Oelkers et al.*, 2008; *Power et al.*, 2013]. This research is still at the experimental stage, and for this reason these formations are often described as "*unconventional reservoirs*" [*Matter and Kelemen*, 2009].

1.4 Unconventional reservoirs

Mafic and ultramafic rocks are igneous rocks rich in magnesium and iron, with 40-90% and >90% of mafic minerals (such as olivine, and pyroxene), respectively.

The importance of these rocks in carbon sequestration strategies is linked with their high content of divalent cations (Ca^{2+}, Mg^{2+}, and Fe^{2+}). These positively charged ions, once in contact with CO_2-rich fluids, can react with the bicarbonate (HCO_3^-) and carbonate (CO_3^{2-}) ions in solution, and precipitate as carbonate minerals ("mineral carbonation"), providing the permanent fixation of CO_2 as a stable solid phase [e.g. *Lackner et al.*, 1995; *Seifritz*, 1990; *Sipilä et al.*, 2008].

Mineral carbonation can be done *ex situ* or *in situ [IPCC, 2005b; Oelkers et al., 2008]*. The *ex situ* scenario is part of an industrial process where suitable initial material has to be transported to a "carbonation reactor", ground, and heated up to precipitate the solid CO_2-rich end product. This methodology of carbonate phase formation in silicate rocks is thermodynamically favourable, but encounters numerous challenges in terms of transport, efficiency, and economic feasibility [*Gerdemann et al.*, 2007]. An example is the multi-step mineral carbonation that involves the extraction of divalent metal oxides from silicates (e.g. serpentine minerals) using industrial waste residues, and the production of carbonates using CO_2 captured from stable sources located in close proximity [*Dri et al.*, 2014].

The *in situ* option overcomes the need of rock transport, by injecting a CO_2-rich solution directly into porous rocks. This requires critical choices on the type of host rock formation, and the reservoir location, which should be fairly accessible and should have abundant water availability for carbonation [*Kelemen and Matter*, 2008].

Several studies have confirmed the natural occurrence of mineral carbonation in mafic and ultramafic rocks through the observation of carbonate veins as products of hydrothermal alteration processes in the seafloor [*Alt and Teagle*, 1999; *Coggon et al.*, 2010; *Shibuya et al.*, 2013] and/or surface chemical weathering [*Brady*, 1991]. Hence, the efficiency of mineral carbonation is the key difference between CO_2 storage in unconventional reservoirs versus conventional reservoirs in sedimentary basins. As shown by *Dessert et al.* [2003], natural carbonation of continental basalt consumes ~0.18 Gt of CO_2 per year globally. Also, multiple experiments and numerical modelling studies on CO_2 precipitation rates within (ultra) mafic rocks suggest that mineral carbonation could happen in the order of years [*Gysi and Stefánsson*, 2008; *McGrail et al.*, 2006; *Paukert et al.*, 2012; *Rosenbauer et al.*, 2012; *Schaef and McGrail*, 2009; *Schaef et al.*, 2010]. In sedimentary systems, however, the mineralization process would likely take from hundreds to thousands of years, due to the lack of reactive Ca, Mg, and Fe-rich silicate minerals [*Benson and Cole*, 2008; *Gunter et al.*, 1997], allowing the gas to potentially escape back into the atmosphere due to earthquakes or incomplete seals.

In the last decade, carbon dioxide injections into mafic and ultramafic formations have started to be considered as a valid unconventional alternative to the industrial CO_2 sequestration into more conventional sedimentary basins. Most of the sites recognised so far as unconventional reservoirs are located on land and characterised as flood basalts [*Goldberg et al.*, 2010; *Matter et al.*, 2007; *McGrail et al.*, 2006; *Schaef et al.*, 2010; 2011; *Van Pham et al.*, 2012], basaltic glasses [*Galeczka et al.*, 2014; *Gislason et al.*, 2010; *Oelkers and Gislason*, 2001], exposed peridotites [*Kelemen and Matter*, 2008; *Kelemen et al.*, 2011; *Olsson et al.*, 2014], or mine tailings [*Harrison et al.*, 2012; *Power et al.*, 2013; *Wilson et al.*, 2006b]. However, only two field-scale pilot CO_2 injection projects have been conducted in basalts: the CarbFix Project in Iceland and the Big Sky Carbon Sequestration Partnership (BSCSP) project in U.S. [*Gislason and Oelkers*, 2014; *Tollefson*, 2013]. The CarbFix Project at the Hellisheidi geothermal power plant in SE Iceland started in 2007*,* and is an attempt to combine the capture of CO_2 from a geothermal power plant with its storage in a nearby basaltic formation (www.carbfix.com). The gaseous CO_2 is dissolved in water before being injected into the subsurface formation [*Alfredsson et al.*, 2008; *Gislason et al.*, 2010; *Matter et al.*, 2009; *Matter et al.*, 2011; *Oelkers et al.*, 2008]. The pilot test involved the injection of 175 tons of pure CO_2. Subsequent monitoring showed that, 95% of the injected CO_2 has been mineralized to carbonate minerals within less than 2 years [*Matter et al.*, 2015; *Matter et al.*, 2013; *Matter et al.*, 2016].

In the BSCSP project *[McGrail et al., 2006]*, near Wallula – Washington State, 1000 tons of supercritical CO_2 was injected into continental flood basalts at more than 800 m depth (www.bigskyco2.org). In contrast to the CarbFix Project, in the BSCSP project the CO_2 is slightly less dense than reservoir water, making the presence of impermeable rock layers above the injection zone essential to keep the CO_2 trapped, and allow time for mineralization to occur. The first results from the fluid samples collected at the injection zone show elevated concentrations of elements such as calcium and magnesium that indicate that the injected CO_2 has reacted with the host rocks [*McGrail et al.*, 2014].

Only a few studies have focused on deep-sea basalts [*Goldberg and Slagle*, 2009; *Goldberg et al.*, 2008; *Goldberg et al.*, 2013; *Slagle and Goldberg*, 2011; *Takahashi et al.*, 2000]. These studies have evaluated the theoretical storage capacity based on physical properties of mid-ocean ridge flanks, and identify several potential locations for *in situ* CO_2 injections. However, they do not consider the phase stability of CO_2 and its consequences for the trapping mechanisms. No field-scale offshore pilot projects have yet been developed. Such investigations on offshore carbon sequestration are still at an early stage, leaving unsolved a series of questions:

- What are the thermodynamic conditions at the sediment-basement interface of mid-ocean ridge flanks?
- Can CO_2 sequestration be applied to the whole seafloor? What are the main constraints?
- Are the sites highlighted by previous studies the best locations in the oceanic crust for CO_2 geological storage? If so, what criteria is this based on (i.e. CO_2 stability over time, permeability, reduction in risk of leakages, seawater circulation…)?
- What is the effective geochemical reactivity of deep-sea basalts in a CO_2-rich system? And, are the experimental results available in literature representative?
- Is CCS applied to the oceanic crust a feasible or economically advantageous strategy?
- Considering the withdrawal of the £1 billion capital subsidy by the UK government (November 2015) for two CCS projects, Peterhead and White Rose [http://www.globalccs institute.com], how could CCS in deep-sea basalts be made more attractive on an industrial scale?

1.5 Deep-sea basalts

The oceanic crust, formed of erupted basaltic rocks placed on top of basaltic dikes and gabbro (mafic rocks), overlies peridotite (ultramafic rock) of the upper mantle. Both rock types can be found on land or offshore, with basalts covering approximately 60 % of the Earth's surface.

Given the above mentioned open questions concerning storing CO_2 offshore in the ocean crust (Section 1.4), this study investigates the geological storage of CO_2 in marine volcanic formations, specifically in deep-sea basalts that form the uppermost lavas of the oceanic crust. Despite the challenges of working in the offshore environment (such as high costs, and difficulties in monitoring), these formations may have several advantages over other potential geological storage options. These include:

a) large reservoir capacities, since they form most of the seafloor;

b) *in situ* availability of seawater for gradual dissolution of CO_2 in porewaters into the basement [*Brady and Gíslason*, 1997] and for dissolved CO_2 injection [*Kelemen et al.*, 2011], following the requirement that CO_2 must be dissolved into an aqueous solution before carbonation can begin [*Gislason et al.*, 2014; *Gunter et al.*, 1993; *Sigfusson et al.*, 2015];

c) potentially fast mineral carbonation [*Elderfield et al.*, 1999], which in turn could guarantee fluid retention times greater than 500 years, reducing the time required for post-injection monitoring, and the possibility of accidental release [*Goldberg et al.*, 2008; *Lackner*, 2003; *Oelkers and Cole*, 2008];

d) low permeability sediment blankets are naturally available in some regions.

According to these parameters and the outcomes from experiments and numerical modelling on basalts, these rocks offer many of the necessary pre-requisites of extent, reactivity, and storage capacity for long-term CO_2 storage [*Gislason and Oelkers*, 2014; *Goldberg et al.*, 2010]. However, the important question remains: how much of this storage potential is practical to use [*Snæbjörnsdóttir et al.*, 2014]?

1.6 Chapter summaries

The objectives of this thesis are to constrain the physical parameters required for trapping CO_2 in deep-sea basalts in order to identify possible storage targets, and to improve the fundamental understanding of geochemical reactions involved in the offshore mineral carbonation of Mid-Ocean Ridge Basalts (MORB). A combination of analytical and experimental methods are used to investigate the exploitable potential of deep-sea basalts as a CO_2 sequestration media.

Chapter 2: The thermodynamic properties at the sediment-basement interface for the whole oceanic crust are investigated and related to the phase stability of carbon dioxide at this boundary. Two case studies in oceanic crust (Juan de Fuca and eastern equatorial Pacific Ocean) are described to compare model estimations with *in situ* measurements.

Chapter 3: The feasibility of carbon sequestration in deep-sea basalts is explored based on physical and gravitational properties at the sediment-basement interface. Suitable targets for offshore CO_2 injections are evaluated, together with sites that, contrary to previous suggestions, are gravitationally unsuitable.

A summary of the results described in Chapters 2 and 3 was published as a manuscript in *Geophysical Research Letters* – *Marieni et al.* [2013] (Appendix CH1-1).

Chapter 4: The geochemical reactions associated with the dissolution of oceanic rocks during carbon storage processes are investigated through batch dissolution experiments in a CO_2-seawater-rock system at CO_2 partial pressure of ~1 atm and 40 ˚C. For the first time, rocks from the upper oceanic crust and ophiolites have been used in CCS-mineral experiments.

Chapter 5: The costs related to the transport and storage of CO_2 offshore are analysed, providing several potential scenarios. Also, an attempt is made to link these cost estimations to the deep-sea basalt targets identified in the previous chapters, highlighting the technological and physical challenges.

Chapter 6: A general discussion on the main findings of this study and their implications in the CCS chain is carried out based on methodology, cost, and social issues. Limitations and future works are included to provide a background for further investigations of deep-sea basalt exploitation in climate change mitigation strategies.

Chapter 2: Thermodynamic properties of CO_2 at oceanic crust conditions

2.1. Introduction

Plate tectonic theory postulates that the lithosphere, which includes the crust and the uppermost mantle, is divided into plates that move around across the Earth's surface, driven by the gravity.

The oceanic crust forms by the rifting of the oceanic lithospheric plates at the *mid-ocean ridge*. The rifting of the 100-150 km thick lithosphere causes passive upwelling of the asthenosphere and partial melting of the mantle, to produce ~7 km of oceanic crust erupted or intruded at the mid-ocean ridge. The volcanic rocks erupted onto the ocean floor are rapidly cooled by seawater circulation, producing a highly permeable, fractured upper crust. As a result, the heated and chemically changed fluids expand until they rise buoyantly, transporting significant heat and elements from the crust into the oceans by advection. This extraction of heat, known as “*hydrothermal circulation*”, significantly affects the position and geometry of magma chambers, the chemical and physical alteration of oceanic rocks, and the composition of seawater.

Detailed explanations of oceanic crust structure, heat flow estimations, and effect of hydrothermal alteration on the carbon cycle are given in the next three sub-sections.

2.1.1. Oceanic crust

Our current knowledge of composition and structure of the oceanic crust derives from geophysical surveys of ocean ridges [*Raitt*, 1963; *Solomon and Toomey*, 1992], ocean floor dredging and drilling [*Auzende et al.*, 1989; *Becker et al.*, 1989; *Bonatti et al.*, 1975; *Cann and Funnell*, 1967; *Fox and Stroup*, 1981; *Francheteau et al.*, 1990], and studies of *ophiolites,* relicts of uplifted oceanic crust preserved on land [*Casey et al.*, 1981; *Coleman*, 1977; *Harper*, 1984; *Moores and Vine*, 1971; *Nicolas*, 1989].

The oceanic crust is the part of Earth that is formed at mid-ocean ridges, composed of mafic rocks, and geophysically defined to be on average 7.1 ± 0.8 km thick on the basis of the seismic velocity contrast with the mantle [*White et al.*, 1992]. The seismic boundary between crust and mantle is called *Mohorovičić discontinuity*, and marks a change of composition and density.

The oceanic crustal age spans from 0 to <200 Ma, with the oldest preserved in situ ocean floor found in the Western Pacific (Figure 2.1) [*Müller et al.*, 2008].

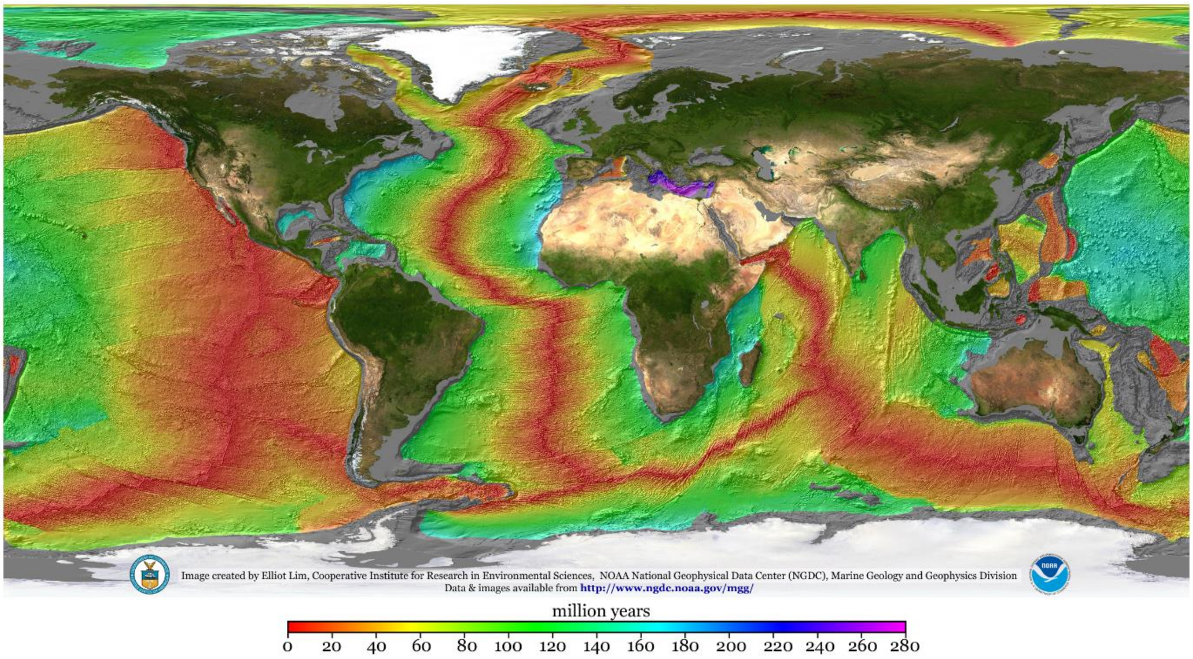

Figure 2.1: Oceanic crustal age [Müller et al., 2008]. Credit for images above: CIRES & NOAA/NCEI. Scale bar extends to 280 Ma to accommodate crustal ages in the Mediterranean Sea estimated from tectonic models.

The “ideal” structure of oceanic crust is based on the Penrose ophiolite assemblage [*Penrose Conference, 1972*] (Figure 2.2) that includes, from top to bottom, pelagic sediments (cherts), mafic volcanic complex (pillow lavas, massive flows, and breccias), mafic sheeted dike complex, and gabbroic rocks (with several textures). All the rocks below the sedimentary layer are defined as basement, and their contact is termed the “sediment-basement interface”. In terms of physical properties, this interface separates unconsolidated rocks with low densities (~1700 kg/m^3) [*Tenzer and Gladkikh*, 2014] and higher porosity (>30%) at the top [*Hamilton and Bachman*, 1982; *Nafe and Drake*, 1961] from crystalline rocks with higher density (~2900 kg/m^3) and lower porosity (10%) below [*Carlson and Herrick*, 1990; *Jarrard et al.*, 2003; *Johnson and Pruis*, 2003].

Studies of ophiolites also show that oceanic crust is underlain primarily by peridotite (Figure 2.2), called harzburgite, which is the tectonised residue left from the partial melting that produced the basalt and gabbro.

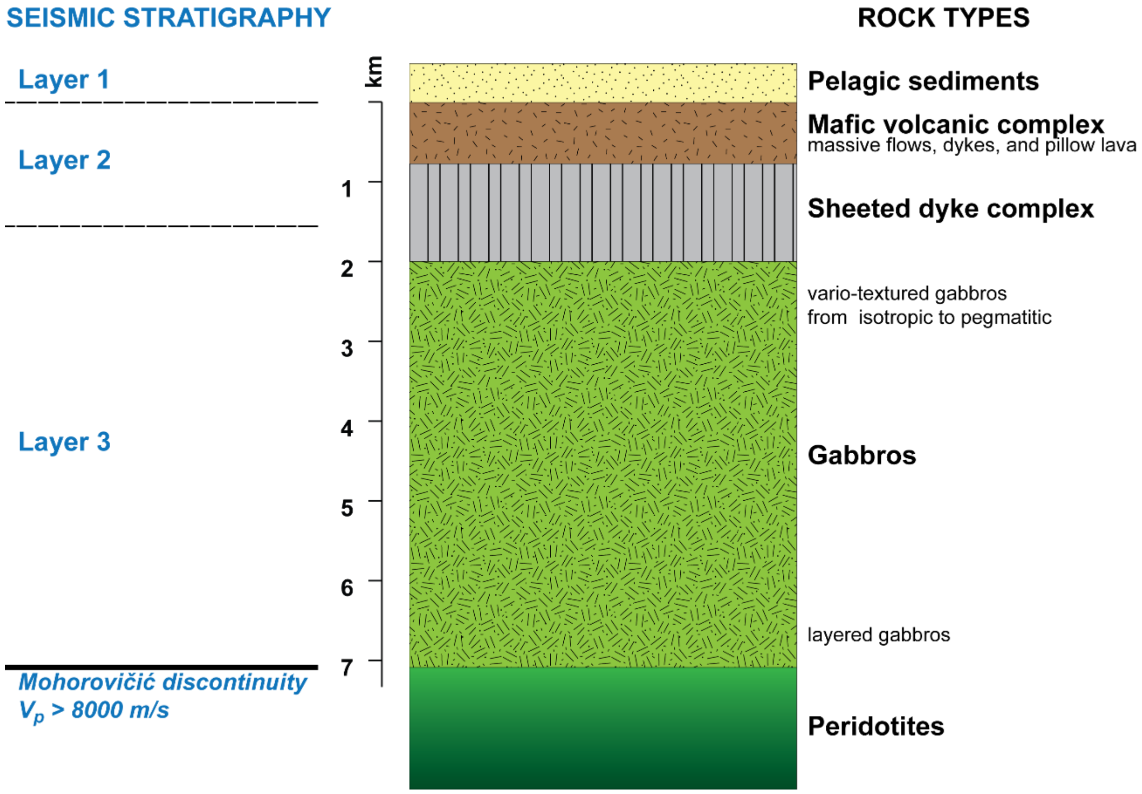

Figure 2.2: Modified version of Penrose oceanic crust stratigraphy [1972].

In general, the Penrose ophiolite model is appropriate for crust formed at fast spreading ridges, such as the East Pacific Rise, where the supply of molten material is enough to keep up with the extensional plate movements and allow compositional differentiation of lavas [*Sinton and Detrick*, 1992]. However, it cannot always be applied to the slow spreading oceanic crust formed at oceanic spreading rates <4 cm/yr (full rate), which comprises ≈50% of the global mid-ocean ridge system, such as the Mid-Atlantic Ridge (MAR) and the SW Indian Ridge (SWIR) [*Bach and Früh-Green*, 2010]. For example, at very slow spreading ridges, the low magma supply produces thinner crust, as confirmed by seismic and gravity data, promoting the tectonic exposure of deeper rocks [*Cannat*, 1993; 1996]. Hence, the oceanic spreading rate is responsible for the different topography and magma supply at mid-ocean ridges.

2.1.2. Heat flow in oceanic crust

Many studies have focused on the calculation of the heat budget through the oceanic crust to thermodynamically constrain the extent of conductive heat flow variation, the magnitude of the hydrothermal fluxes, and hydrothermal alteration in the basement [*Alt*, 1995; *Lister*, 1974; *McKenzie*, 1967; *Mottl and Wheat*, 1994; *Parsons and Sclater*, 1977; *Pollack et al.*, 1993; *Sclater and Francheteau*, 1970; *Sclater et al.*, 1980; *Stein and Stein*, 1992; 1994; *Stein et al.*, 1995; *Turcotte and Oxburgh*, 1967; *Turcotte and Schubert*, 2002]. Debate on the cooling of oceanic crust started when the first heat flow measurements at sea become available in the 1960's [*Langseth et al.*, 1966; *Von Herzen and Uyeda*, 1963], and 1070's [*Talwani et al.*, 1971; *Williams et al.*, 1974]. The main findings can be summarised as follows:

i) New oceanic lithosphere cools, deepens, and becomes denser as it spreads away from the mid-ocean ridges, as a function of age (Figure 2.3).

ii) The principal modes of heat transfer in the oceanic crust are conduction and advection, which can also be defined as "*hydrothermal circulation*".

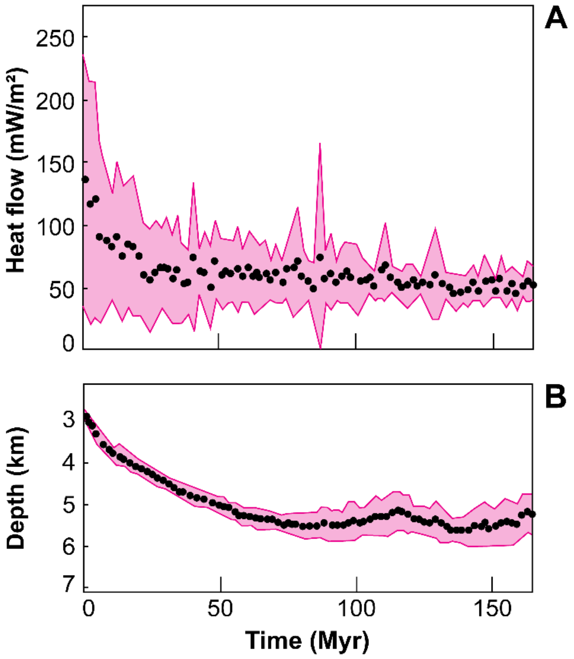

Figure 2.3: Heat flow (A) and ocean depth (B) measurements as a function of age [Stein and Stein, 1992]. Data (black dots) are averaged in 2-Ma bins, and one standard deviation about the mean value for each is shown by the contour plot (in pink).

Initially, *McKenzie* [1967] associated the systematic observation of the highest seafloor heat flow at mid-ocean ridges, together with the highest topographic relief, with a model explaining their exponential decrease with distance ("plate model"). Considering that the amount of cooling depends on time, *Sclater and Francheteau* [1970] described the data in terms of oceanic crust age rather than distance away from the ridge, providing the main constraint on the thermal structure and evolution of oceanic lithosphere. Also, *Parker and Oldenburg* [1973] showed that heat flow varies asymptotically as a function of $1/\sqrt{t}$, whereas depth increases as a function of $\sqrt{t}$, where t is the age of the oceanic plate.

Currently, there are three principal models to predict oceanic depth and conductive cooling in the lithosphere, and the first two are plate models with different parameters (Figure 2.4, Table 2.1):

- the Parsons and Sclater Model - PSM (in blue) [*Parsons and Sclater*, 1977];
- the Global Depth and Heat flow model - GDH1 (in red) [*Stein and Stein*, 1992];
- the Half Space Cooling Model - HSCM (in green) [*Turcotte and Schubert*, 1982; 2002].

Table 2.1: *Summary of the key parameters used in PSM, GDH1 model, and HSCM to calculate heat flow and oceanic depth.*

	model	HSCM	PSM	GDH1
Initial temperature	˚C	1300	-	-
Thermal conductivity	W/(m K)	3.3	3.1	3.1
Thermal expansivity	1/K	4 x 10^{-5}	3.3 x 10^{-5}	3.1 x 10^{-5}
Plate thickness	km	-	125	95
Basal temperature	˚C	-	1350	1450
Ridge depth	m	2500	2500	2600

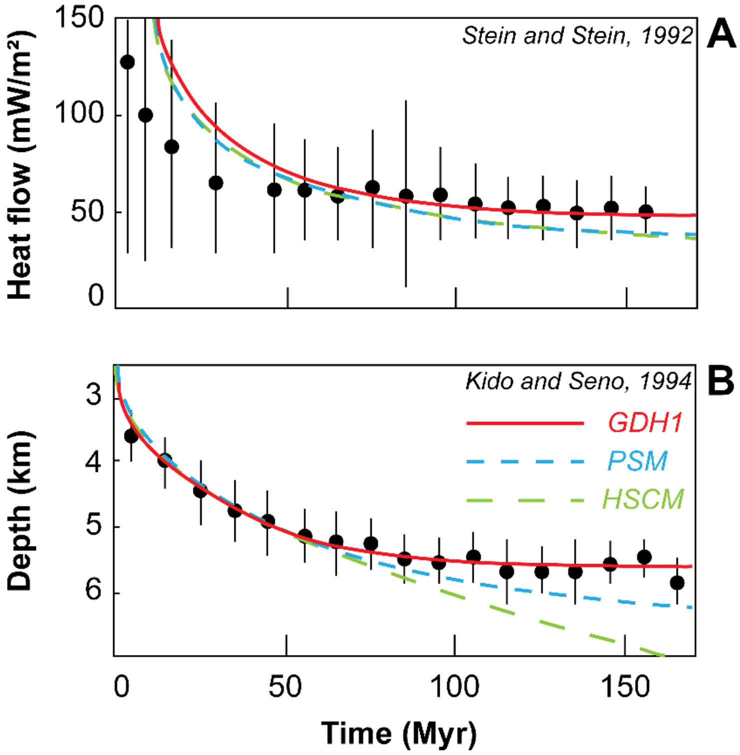

Figure 2.4: Data (black dots) and models (coloured lines) for A-heat flow and B-ocean depth as a function of age (modified from Kido and Seno [1994]; Stein and Stein [1992]; Stein et al. [1995]). The data standard deviations are represented as bars.

The PSM [*Parsons and Sclater*, 1977] improves on the *McKenzie* plate model in two main ways: data dependence on time, and slab thickness. In fact, the PSM presents the heat flow and bathymetry data as a function of the oceanic floor age (from 0 to 160 Ma) rather than distance from the ridge crest, highlighting the heat flow and depth flattening for lithospheric ages >50 Ma and >70 Ma, respectively. The PSM considers a lithosphere where basal temperature is 1350 ˚C, and thickness is ~125 km – rather than the previously proposed 50 km – based on the physical parameters calculated for the deepest parts of the Pacific Ocean. However, there are numerous anomalies that were excluded from the data analysis, and hence are not explained by the model (such as seamounts, plateaus, and islands), particularly for lithosphere older than 70-100 Ma and regions with anomalously thick sediment layers.

The GDH1 model [*Stein and Stein*, 1992] is conceptually similar to the PSM, and addresses the misfit of *Parsons and Sclater'*s model, using a larger heat flow dataset corrected for sediment thickness. As with PSM, the GDH1 model's key feature is the isothermal base of the lithosphere at a fixed depth, added to prevent the half space cooling from continuing at older ages. However, in the GDH1 model, a hotter (1450 ˚C at the base) and thinner lithosphere (95 km) satisfies many of the data that are anomalous in the PSM, especially for older lithosphere.

The HSCM [*Turcotte and Schubert*, 1982; 2002] proposes that the lithosphere is defined by a ~1300 ˚C isotherm within a cooling half space, which in this case is allowed to grow indefinitely. It also takes into account higher thermal coefficients of conductivity and expansivity of the crust than PSM and GDH1 models. The result is a model that shows a better agreement at younger ages (<80 Ma) than GDH1 model, but underestimates heat flow and overestimates depth for older ages. The continuing increase of depth with the age of the ocean floor defines the biggest difference with the other two models (PSM and GDH1).

In general, the GDH1 model gives a better fit on a global scale to ocean floor observations of depth and conductive heat flow than the PSM and HSCM (Figure 2.4). All models predict much higher conductive heat flow for oceanic crust <70 Ma. This discrepancy was the key evidence for the presence of heat transport by water circulation in the rocks (Figure 2.5) [*Lister*, 1974]. Accordingly to *Stein and Stein* [1994], ~34% (11 x 10^{12} W) of the total predicted global oceanic heat flux (32 x 10^{12} W) occurs by hydrothermal flow, including both “active near ridge” and “passive off-ridge” convective regimes that extends to a crustal age of ~65 Myr [*Elderfield and Schultz*, 1996]. Along the ridge axis, the temperature is >250 ˚C, and hydrothermal circulation is vigorous [*Lowell and Rona*, 1985; *Rosenberg et al.*, 1993; *Strens and Cann*, 1982]. On the ridge flanks, with temperature ≪200 ˚C, hydrothermal fluid flow is less intense, and generally restricted to the uppermost few hundred meters of permeable volcanic rocks. However, because of the vast expanse of the ocean ridge flanks, the more extended flank circulation accounts for ~70% of the total hydrothermal heat loss [*Becker et al.*, 1989; *Fehn et al.*, 1983; *Fisher et al.*, 1990; *Mottl and Wheat*, 1994].

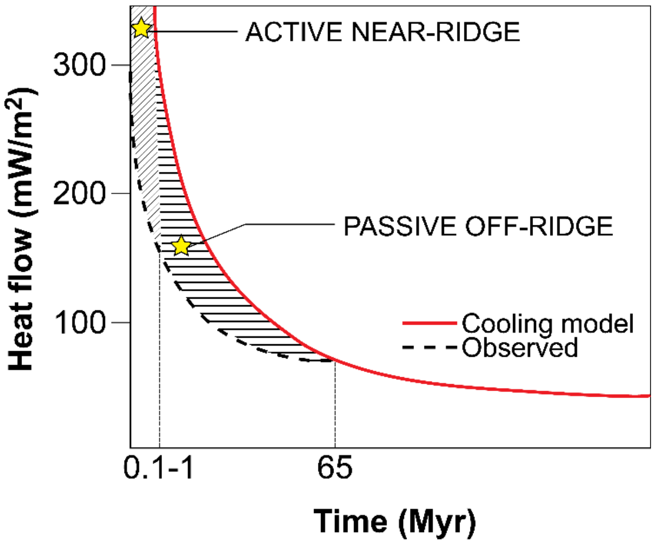

Figure 2.5: Schematic illustration of observed (dashed line) and estimated (red line) heat flow, with difference defined as a hydrothermal flux (dashed area) [modified from Stein and Stein, 1994].

The seawater flux necessary to produce the hydrothermal heat loss from the oceanic crust is ~1 x 10^{15} kg/yr [*Harris and Chapman*, 2004], where only ~7% of it is occurring at near-axial regions [*Stein and Stein*, 1994]. During hydrothermal alteration, seawater penetrates into the basement and reacts with volcanic rocks, resulting in major-ion composition changes in seawater dominated by: i) loss of Mg^{2+} – which is fixed in the crust as clay minerals, filling fractures and replacing volcanic glass, ii) addition of Ca^{2+} –

which is dissolved from basalts , iii) subsequent loss of alkalinity – due to the precipitation of secondary minerals, such as clays, sulphate, and carbonate minerals [*Fisher et al.*, 1990; *Mottl*, 1983; *Mottl and Wheat*, 1994].

2.1.3. Oceanic floor carbon uptake

Studies on basement fluids and secondary minerals in the oceanic crust have shown that one major effect of hydrothermal circulation is the uptake of carbon during the alteration of the volcanic section [*Alt and Teagle*, 1999; *Coggon et al.*, 2004; *Coogan and Gillis*, 2013; *Gillis and Coogan*, 2011; *Staudigel et al.*, 1989]. A portion of the carbon dioxide (CO_2) present in seawater is consumed by dissolution of oceanic crust silicates, and subsequent precipitation of carbonate minerals like calcite ($CaCO_3$).

Mass balance models indicate that the production rate of carbon in new crust due to volcanic outgassing at mid-ocean ridges is lower than the amount of carbon fixed in the oceanic crust per year, which is ~3 x 10^{12} mol C/yr (0.036 Pg C/yr) [*Alt and Teagle*, 1999; *Staudigel et al.*, 1989]. Consequently, the seafloor alteration is a net sink of carbon in oceanic crust (1.5-2.4 x 10^{12} mol C/yr, or 0.018-0.029 Pg C/yr) [*Alt and Teagle*, 1999], and plays an important role in the current debate on the global carbon cycle [*Kelemen and Manning*, 2015] raising a number of questions:

- How much CO_2 can be removed from seawater and mineralised?
- What are the optimal conditions for CO_2 consumption in the basement?
- What is the CO_2 phase stability in the seafloor?

In this chapter, I will consider the latter question, combining information from several global databases to determine the thermodynamic properties in the oceanic crust at the sediment-basement interface and to investigate the stability of carbon dioxide at this boundary.

2.2. CO_2 and seawater

Carbon dioxide is the most important greenhouse gas after water vapour in the Earth's atmosphere, and more than 98% of the carbon dioxide in the ocean-atmosphere system is stored in the oceans as dissolved inorganic carbon [*Zeebe and Wolf-Gladrow*, 1993]. CO_2 has no liquid state at pressures below 0.52 MPa. At 0.1 MPa (~1 atm), CO_2 condenses directly as a solid at temperatures below -78.5 ˚C, and vice versa the solid undergoes sublimation (Figure 2.6). The CO_2 triple point, where the three phases of CO_2 coexist in thermodynamic equilibrium, is at 0.52 MPa and -56.6 ˚C. The critical point, above which there is no phase boundary between gas and liquid, is at 7.38 MPa at 31.1 ˚C. Above this pressure and temperature limit, carbon dioxide behaves as a supercritical fluid, which combines properties of gas and liquid (Figure 2.6). A supercritical fluid has higher diffusivity, lower viscosity, and lower surface tension than the liquid phase. This means that supercritical CO_2 has, in general, better solvent properties than liquid CO_2.

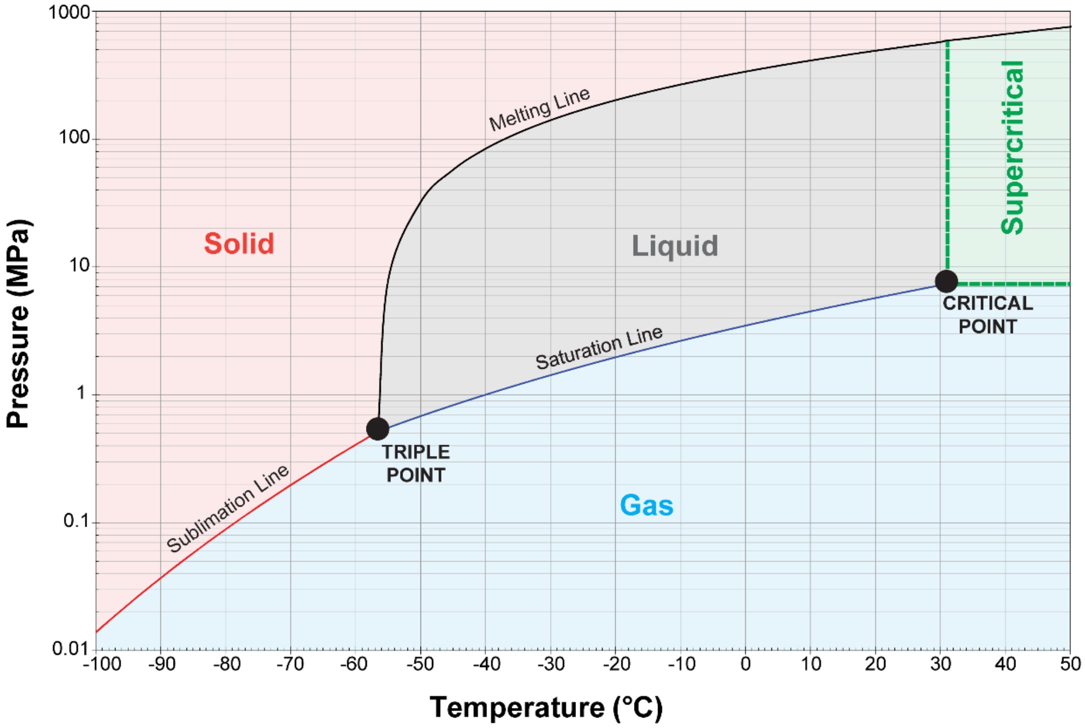

Figure 2.6: Phase diagram of CO_2 for temperatures from -100 to 50 ˚C, and pressures from 0.01 and 1000 MPa (modified from http://www.chemicalogic.com).

Seawater is a complex mixture of water, salts, and smaller quantities of other substances, including dissolved inorganic and organic materials and dissolved atmospheric gases. On average, seawater in the World's ocean has a salinity of ~35 practical salinity units – psu – or grams of salt dissolved in 1 kg of seawater [*Brown et al.*, 1995]. The six ions that make up 99% of all sea salts, from the most to the least abundant, are: *chloride* (Cl^-), *sodium* (Na^+), *magnesium* (Mg^{2+}), *sulfate* (SO_4^{2-}), *calcium* (Ca^{2+}), and *potassium* (K^+) [*Millero et al.*, 2008; *Summerhayes and Thorpe*, 1996]. Because of its salt content, seawater has different properties than fresh water, such as higher density and thermal conductivity, but lower specific heat capacity [*Sharqawy et al.*, 2010].

For the purpose of this thesis, the parameter that best describes the differences between CO_2 and seawater is density, which is directly affected by changes in temperature (T) or pressure (P). The densities of both compounds are calculated for pressures from 0 to 60 MPa and temperatures from 0 to 100 ˚C (Figure 2.7). The density of CO_2 (ρ_{CO2}) is determined by interpolating the online National Institute of Standards and Technology (NIST) database [*Linstrom and Mallard*, 2012], which is based on the equation of state by *Span and Wagner* [1996]. Seawater density ($\rho_{seawater}$) is estimated using the SeaWater MATLAB library [*Fofonoff et al.*, 1983], assuming a constant salinity of 35 psu [*Brown et al.*, 1995]. CO_2 density decreases dramatically with decreasing pressure and increasing temperature, compared to a near constant density for seawater (Figure 2.7). Furthermore, it is evident that carbon dioxide is denser than seawater only for pressures higher than 27 MPa (~2700 m of water) and temperature between 0 and 30 ˚C. Note that within this limited P-T window, liquid CO_2 is the thermodynamically stable phase. Liquid CO_2 has only a narrow range of densities - between 1040 and 1125 kg/ m^3, whereas the density of supercritical CO_2 varies from 140 kg/m^3 (at 100 ˚C, 8 MPa) to 1045 kg/m^3 (at 30 ˚C, 60 MPa).

In the next Section, the phase stability of CO_2 and seawater at the sediment-basement interface throughout all the oceans is determined as a function of the actual temperatures and pressures. Also, the effect of heat flow and sediment thickness variations at the top of the basement, in a world-wide scenario, is evaluated.

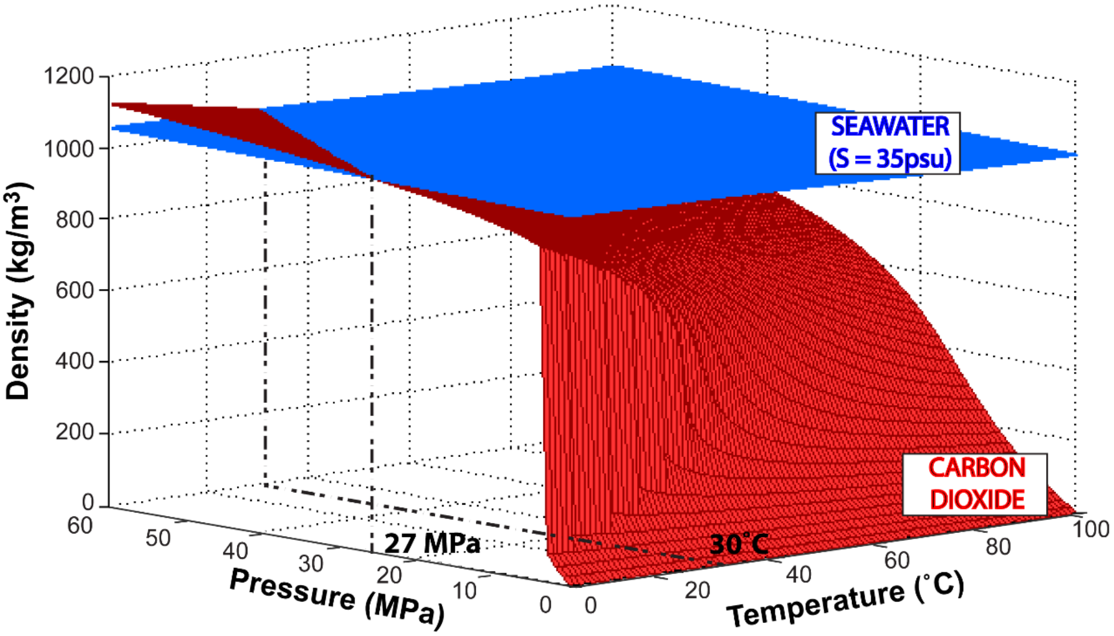

Figure 2.7: Densities of seawater (in blue) and carbon dioxide (in red) as a function of temperature between 0 and 100 ˚C, and pressure between 0 and 60 MPa.

2.3. Thermodynamic properties of oceanic crust

2.3.1. Heat flow estimation for the oceanic lithosphere

As previously described in Section 2.1.2, it is widely recognized that the GDH1 model provides a significantly better fit to observed conductive heat flow data, especially for older lithosphere where GDH1 gives values of heat flow higher than the estimates from the HSCM (Figure 2.4). Hence, in this study, GDH1 is considered the most appropriate model to evaluate the effect of heat flow at the sediment-basement interface throughout the world oceans. The PSM is not considered because the GDH1 model represents a development of the PSM. Conductive heat flow has been calculated for the global oceanic floor using the models GDH1 and HSCM.

The equations to calculate heat flow and bathymetry are listed for the GDH1 and HSCM models in Table 2.2. Oceanic crustal age is the only required input for the GDH1 model, whereas the HSCM also requires knowledge of lithospheric thermal conductivity (assumed to be 3.3 W/(m K)), temperature difference between the base and top of the lithosphere (assumed to be 1300 K), and thermal diffusivity (assumed to be 10^{-6} m^2/s).

Table 2.2: Summary of the equations used by GDH1 (left) and HSCM (right) to calculate heat flow and bathymetry.

	GDH1 *[Stein and Stein, 1992]*	**HSCM** *[Turcotte and Schubert, 1982; 2002]*
Heat flow	$\begin{cases} t \leq 55\,Ma, & q_0 = 510/\sqrt{t} \\ t > 55\,Ma, & q_0 = q_a + 96 exp\overline{\sqrt{-0.0278 * t}} \end{cases}$	$q_0 \ = \ K\ (T_1 - T_0)/\ \sqrt{\pi k t}$
	q_0: surface heat flow [mW/m^2] t: oceanic crustal age [Ma] q_a: asymptotic heat flow [48 mW/m^2]	q_0: surface heat flow [mW/m^2] K: lithospheric thermal conductivity [3.3 W/(m K)] $(T_1 - T_0)$: thermal difference between base and top of the lithosphere [1300 K] k: thermal diffusivity [10^{-6} m^2/s] t: oceanic crustal age [Ma]
Bathymetry	$\begin{cases} t < 20\,Ma, & \mathrm{dw} = dr + 365\sqrt{t} \\ t \geq 20\,Ma, & \mathrm{dw} = 5651 - 2473 exp\overline{\sqrt{-0.0278 * t}} \end{cases}$	$dw \ = \ dr + 350\,\sqrt{t}$
	dw: bathymetry [m] t: oceanic crustal age [Ma] dr: ridge depth [2600 m]	dw: bathymetry [m] t: oceanic crustal age [Ma] dr: ridge depth [2500 m]

To determine the heat flow at the sediment-basement interface for the whole oceanic lithosphere, the oceanic crustal age database [*Müller et al.*, 2008] has been adapted for a grid with 6 minute resolution (measurement nodes every ~10 km) (Figure 2.1). The consequent age-derived heat flow values, generated from both the HSCM and GDH1 models, have been considered only if they are below a reasonable threshold of 500 mW/m^2 (the mean value of oceanic heat flow measurements is 101 mW/ m^2), and plotted on global maps, using the GMT-*Generic Mapping Tools software* (Appendices CH2-1 A and B).

2.3.2. Temperature at the sediment-basement interface of the oceanic lithosphere

Following *Heberling et al.* [2010], from both the heat flow databases (GDH1 and HSCM), the geothermal gradient has been calculated for a grid of 6' x 6' using Fourier's Law:

$$\frac{dT}{dz} = \frac{q_0}{K_s}$$

where *dT/dz* is the geothermal gradient [K/m], q_0 the heat flow [W/m^2], and K_s the thermal conductivity of marine sediments, taken as 1 W/(m K). To calculate the temperature at the sediment-basement interface from the geothermal gradient, which is the rate of increasing temperature with respect to depth, knowledge of sediment thickness is required. Hence, the sediment thickness for all the oceanic crust has been computed from the NOAA-gridfive dataset [*Divins*, 2003] (Appendix CH2-2), and the temperature at the top of the basement has been extrapolated from both HSCM and GDH1 model and presented as global maps (Appendices CH2-3A and B, respectively). In general, the calculation with the GDH1 model gives temperatures higher than with the HSCM due to different lithospheric isothermal constraints associated with each model (Section 2.1.2).

The use of K_s as a constant value (1 W/(m K)) is based on two major global databases of marine sediment thermal conductivities: **A)** the IODP-ODP database with the most up to date data [*International Ocean Discovery Program*, 2015] and **B)** the historical global compilation of *Pollack et al.* [1993]. These databases give the global average values of K_s = ~1.3 and ~1 W/(m K), respectively (Figure 2.8).

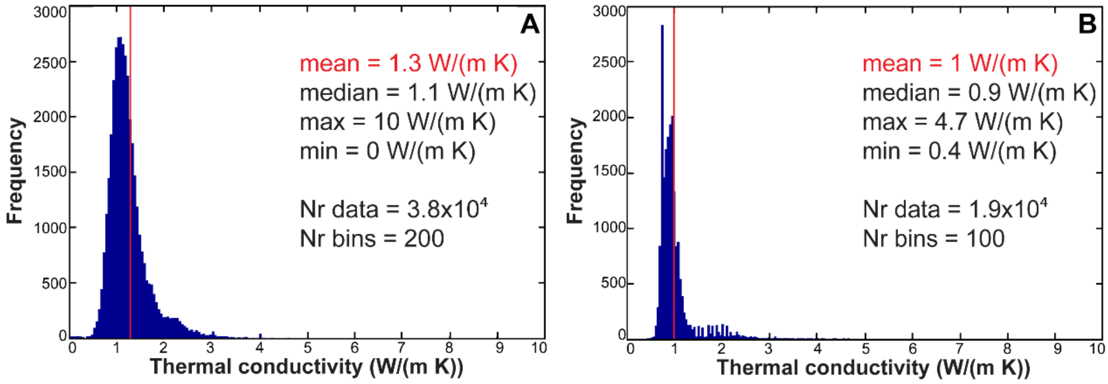

Figure 2.8: Histograms of thermal conductivity measurements for marine sediments from A) the IODP-ODP database [International Ocean Discovery Program, 2015], and B) the global compilation [Pollack et al., 1993]. The red line shows the mean, which is close or equal to 1 W/(m K) for both databases.

2.3.3. Pressure at the sediment-basement interface of the oceanic lithosphere

In general, there are two approaches to estimate the pressure at the sediment-basement interface, depending on the assumption of hydrostatic or lithostatic load above the basement.

1) Hydrostatic, considers all the load as water column: $u = g \cdot \rho_w \cdot (d_w + d_s)$;
2) Lithostatic, considers both overlaying rock mass and water column:

   $u = (g \cdot \rho_w \cdot d_w) + (g \cdot \rho_s \cdot d_s)$;

where g is the gravity constant of 9.81 m/s^2, ρ_w and ρ_s the seawater and sediment density [kg/m^3], respectively, d_w the water depth [m], and d_s the sediment thickness [m] [*Mann and Mackenzie*, 1990]. Based on *Brown et al.* [1995], seawater has been considered in its average conditions, with a constant density of 1030 kg/m^3, and a constant salinity of 35 psu. Measured marine sediment density values are on average 1700 kg/m^3 [*Tenzer and Gladkikh*, 2014]. Consequently, the lithostatic pressure increases more rapidly with sediment thickness than hydrostatic pressure.

This difference between pressure assumptions based on the sediment thickness highlights the importance of the choice on the pressure assumption to use. The chosen pressure should represent the vertical stress to which the fluid (e.g., CO_2, seawater) would be subjected to in the pore spaces, assuming an interconnected fluid network. This type of pressure is defined as effective pore pressure in Terzaghi’s principle [*Terzaghi et al.*, 1996]:

$$\sigma = \sigma' + u$$

in which the total stress (σ) is composed of two parameters, σ’ the effective stress and u the effective pore pressure. More specifically, the effective stress is interpreted as the stress that the solid granules constituting the sediment exchange at the contact points. The effective pore pressure is defined as the stress acting on the water in every direction with equal intensity, and it is calculated in the same way as the hydrostatic pressure. Hence, the hydrostatic assumption will be used in all of the following calculations involving the pressure in the oceanic crust basement.

The water column thickness, taken to be the sum of the water depth and sediment thickness, has been calculated at each point on a 6-minute resolution grid by combining two databases:

- the General Bathymetric Chart of the Oceans (GEBCO) – gridfive world bathymetry map [*IOC et al.*, 2003] (Appendix CH2-4);
- the NOAA-gridfive sediment thickness database (Appendix CH2-2).

Although anomalies in seafloor topography due to seafloor abyssal hills and seamounts are not always detected by global altimetry and gravity analyses, the NOAA sediment thickness database is currently the best available. For this study, only sediment thicknesses between 0 and the reasonable threshold of 2000 m are considered. A water depth >0 m is the only requirement for the bathymetry. The resulting hydrostatic pressure calculated for the whole oceanic crust at the sediment-basement interface ranges from 0 to 104 MPa, and has been presented as a global map (Appendix CH2-5).

It should be noted that the pressure estimations are completely independent from the heat flow model chosen for the thermal calculations.

2.3.4. CO_2 density at the sediment-basement interface of the oceanic lithosphere

Density (ρ) is the parameter that best describes the buoyancy of CO_2 at the different temperature and pressure conditions calculated for the oceanic lithosphere. CO_2 density decreases dramatically with decreasing pressure and increasing temperature, compared to a near constant density for seawater (Figure 2.7).

Densities for CO_2 and seawater have been determined at the sediment-basement interface of the whole oceanic lithosphere, at each point on a 6’ x 6’ grid, applying the density databases described in Section 2.2 to the temperature and pressure values calculated with the GDH1 and HSCM models (using K_s = 1 W/(m K) for both). The relative density difference defined between CO_2 and seawater is calculated as a density difference ($\Delta\rho$) on global maps for both models (Figure 2.9 and 2.10, for map generated with GDH1 and HSCM, respectively). There is little significant difference between the two models. Positive $\Delta\rho$ ($\rho_{CO2} > \rho_{seawater}$) indicates more dense CO_2. This only occurs at hydrostatic pressure higher than 27 MPa and temperatures between 0 and 30 ˚C. These conditions are typical of old oceanic crust in deep oceans. In contrast, negative $\Delta\rho$ ($\rho_{CO2} < \rho_{seawater}$) describes low density CO_2, which occurs at low pressure and high temperature, characteristic of shallow, young crust. The distribution of $\Delta\rho$ on the maps is controlled by a combination of basement heat flow and sediment thickness variations:

- high heat flow rate leads to high upper crustal temperature;
- high sediment thickness corresponds to high pressure, but also to high temperature, due to the hydrologic isolation effect of rapidly sedimented pelagic deposits that with their low-permeability trap the heat at the sediment-basement interface [*Davis et al.*, 1992; *Fisher and Davis*, 2000; *Langseth et al.*, 1988; *Stein et al.*, 1995].

Hence, most of the areas close to a ridge axes – loci of freshly created oceanic crust – or nearby continental margins – regions of thick layers of sediments – show negative $\Delta\rho$ conditions. However, there are some exceptions; for example, at the Rodriguez Triple Junction (RTJ) in the Indian Ocean, where the wide depression created by the cross of three rift valleys at water depth >3600 m and sediment thickness <100 m [*Munschy and Schlich*, 1989] causes a unique P-T environment, enabling the density of CO_2 to be greater than seawater at the ocean floor.

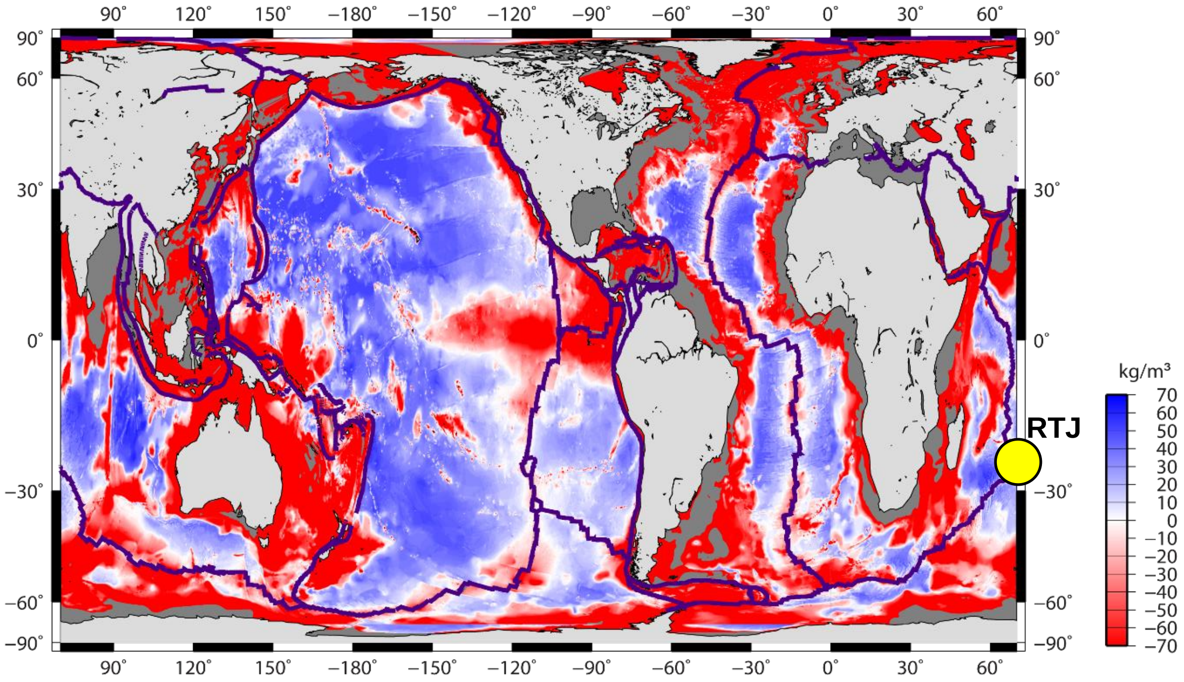

Figure 2.9: Map of density difference Δρ between CO_2 and seawater at the sediment-basement interface, generated using the GDH1 model, with K_s = 1 W/(m K). The red shadings show negative Δρ ($\rho_{CO2} < \rho_{seawater}$); the blue show positive Δρ ($\rho_{CO2} > \rho_{seawater}$). The RTJ-Rodriguez Triple Junction is indicated with a yellow circle.

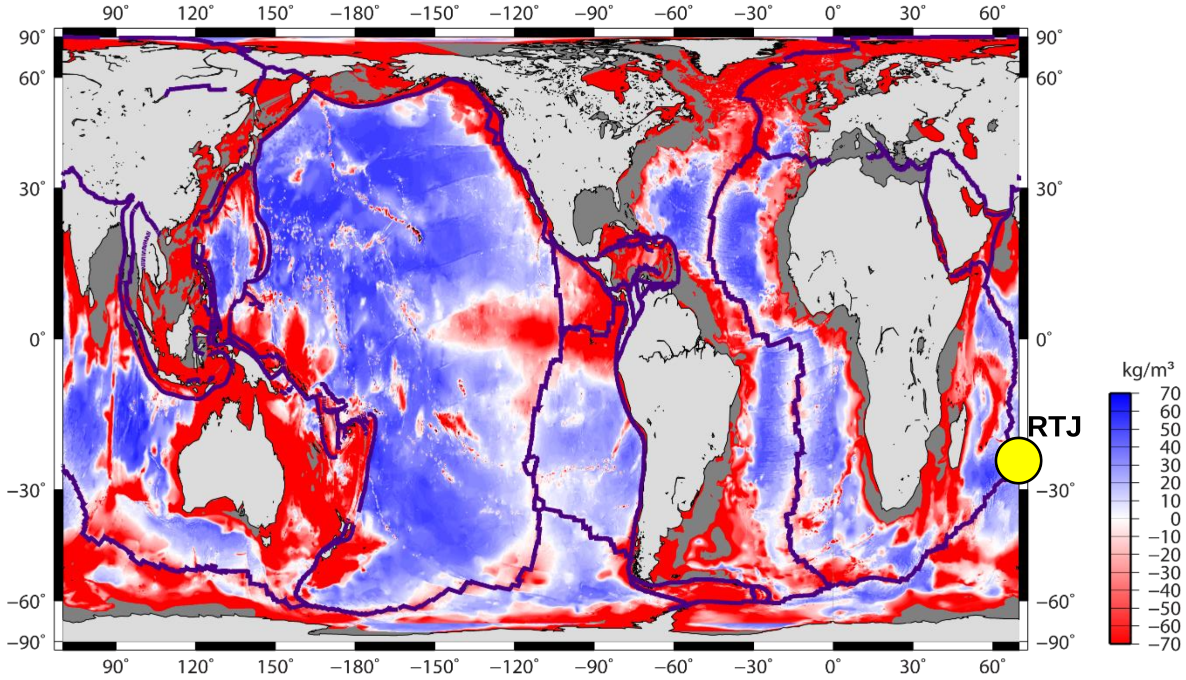

Figure 2.10: Map of density difference Δρ between CO_2 and seawater at the sediment-basement interface, generated using the HSCM model, with Ks = 1 W/(m K). The red shadings show negative Δρ ($\rho_{CO2} < \rho_{seawater}$); the blue show positive Δρ ($\rho_{CO2} > \rho_{seawater}$). The RTJ-Rodriguez Triple Junction is indicated with a yellow circle.

2.4. Thermodynamic properties of two case studies in oceanic crust

The previously described findings on T, P, and CO_2 densities at the sediment-basement interface in a world-wide scenario are the result of the application of heat flow models and the interpolation of several databases. To validate their interpretations, the model estimations have to be compared with actual measured temperatures and pressures at the sediment-basement interface. To address this issue, available *in situ* measurements, laboratory analyses and model outputs have been considered for two well-studied oceanic locations: the Juan de Fuca Plate (JdFP) and the eastern equatorial Pacific Ocean (eePO). Although there are numerous holes drilled into the oceanic crust by scientific ocean drilling, JdFP and eePO are the only locations where accurate temperatures close to the sediment-basement interface have been measured.

2.4.1. Juan de Fuca Plate

The Juan de Fuca Plate (JdFP – Figure 2.11), offshore Washington State and British Columbia (USA), has been the focus of conceptual studies of Carbon Capture and Storage (CCS) applied to deep sea basalt [*Goldberg et al.*, 2008] because it is one of the best studied mid-ocean ridge flanks, and it is near to major industrial regions of North America. The JdFP has been the locus of three scientific ocean drilling cruises (ODP Leg 168, and IODP Expeditions 301 and 327) and numerous other scientific experiments that have defined the regional thermal and hydrological regimes of the upper oceanic crust [*Becker et al.*, 2013; *Coggon et al.*, 2004; *Davis et al.*, 1997; *Fisher and Davis*, 2000; *Wheat and Mottl*, 2000; *Wheat et al.*, 2003].

The oceanic crust on this plate is relatively young, having formed at the Juan de Fuca Ridge between 0 and 11 million years-ago at intermediate spreading rate (5-7 cm/yr full rate) [*Govers and Meijer*, 2001], and occurs over a water depth range of 2200 to 3500 m. The pillow lavas that form the upper few hundred meters of the JdFP crust have high connected porosity (>10%), which allows to cold, unaltered seawater to enter the crust where basement is exposed at the seafloor [*Fisher*, 1998].

The ridge flank is blanketed by a very thick (from ~30 to >700 m) sequence of hemipelagic and turbiditic sediments derived from the North American continental margin during the Pleistocene (2.58 – 0.01 Ma) [*Fisher and Davis*, 2000].

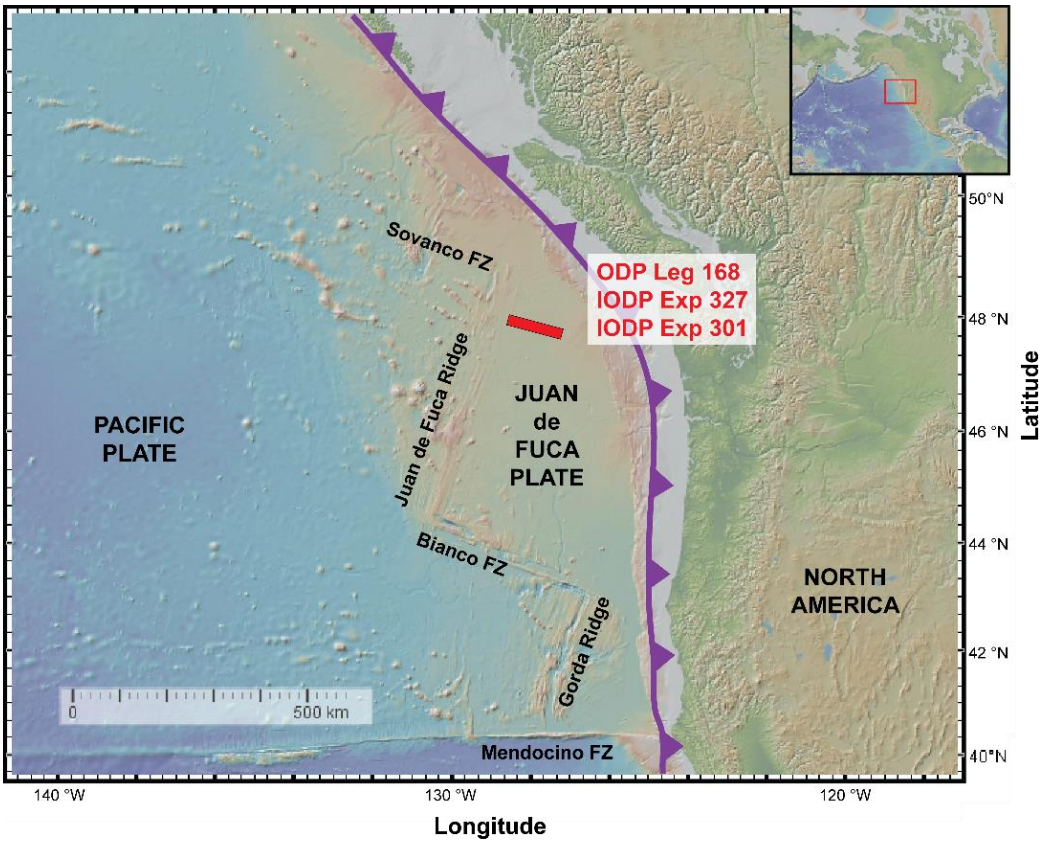

Figure 2.11: Tectonic setting of the Juan de Fuca Plate (JdFP). The sites of interest are highlighted in red.

The eastern ridge flank of the JdFP was investigated during the ODP Leg 168 (Figure 2.12). Ten sites were drilled between 20 and 100 km from the ridge axis, in crust ranging from 0.8 to 3.6 Ma, and sediment thickness increasing from 40 to 600 m (summary in Table 2.3). This relatively continuous and anomalously thick sediment cover has been found to be responsible for confining the hydrothermal fluids within the igneous basement for most of the ridge flank, and consequently affecting the thermal setting along the transect [*Davis et al.*, 1997].

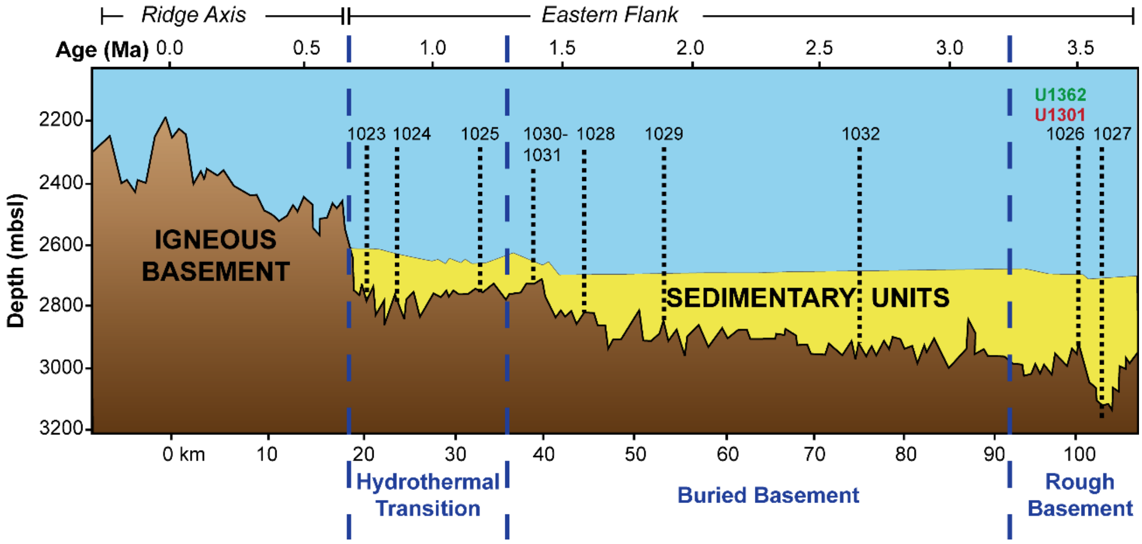

Figure 2.12: Schematic cross section of the ODP Leg 168 drilling transect profile (derived from seismic reflection), adapted from Davis et al. [1997]. Drill site locations of ODP Leg 168 (in black), IODP Exps 301 (in red) and 327 (in green), and inferred basement age are shown.

Temperature

The temperatures of pore water and basement fluids at the sediment-basement interface increase with distance from the ridge and range from 16° to 63°C (summary in Table 2.3) [*Coggon et al.*, 2004; *Elderfield et al.*, 1999; *Pribnow et al.*, 2000]. The high temperatures at the sediment-basement interface have been explained by the blanket effect of the anomalously thick sediment cover over young oceanic crust [*Davis et al.*, 2004; *Fisher et al.*, 2003; *Stein et al.*, 1995].

Pressure

As previously mentioned (Section 2.3.3), the hydrostatic pressure assumption is the most appropriate approach to describe the vertical stress to which the CO_2 would be subjected at the boundary between sediments and oceanic crust basement. Hence, the corresponding hydrostatic pressures of each ODP Leg 168 site at the sediment-basement interface have been determined, and compared to lithostatic estimations to highlight the pressure discrepancy.

The fundamental parameters considered in the calculations are:

- seawater density, locally calculated to be 1027 kg/m^3;
- sediment density, ranging between 1800 and 2000 kg/m^3 [*Davis et al.*, 1997];
- water depth, which on average corresponds to ~2600 m [*Davis et al.*, 1997];
- sediment thickness, which was measured for each site during the drilling expedition.

The hydrostatic and lithostatic pressures range from 26 to 33 MPa and from 26 to 39 MPa, respectively, showing a good agreement for most of the sites (summary in Table 2.3). The maximum pressure difference of 6 MPa has been obtained for a single site (Site 1027) characterised by sediment thickness greater than 600 m, whereas the average pressure difference for all the other sites, with sediment thickness below 300 m, is 1.4 MPa.

Table 2.3: Summary of the properties of the sites on JdFP drilled during the ODP Leg168. Pressure - P (MPa) and temperature (˚C) conditions are calculated at the sediment-basement interface. Distance from ridge axis, oceanic crustal age, water depth, and sediment thickness are also shown.

ODP Leg 168 Sites	**1023**	**1024**	**1025**	**1030**	**1031**	**1028**	**1029**	**1032**	**1026**	**1027**
Distance from ridge axis (km)	22.4	25.6	33.6	39.4	39.4	44.8	54.8	74.6	101.1	103.3
Oceanic crustal age (Ma)	0.86	0.97	1.24	1.43	1.43	1.62	1.95	2.62	3.51	3.59
Water depth (m)	2593	2614	2602	2574	2588	2659	2653	2645	2658	2657
Sediment thickness (m)	193	168	96.6	41.9	41.3	133	220	290	229	614
Temperature (˚C)	15.5	22.8	38.6	40.1	40.4	50.5	58.7	57.1	61.7	62.8
P hydrostatic (MPa)	28.1	28.0	27.2	26.3	26.5	28.1	28.9	29.6	29.1	32.9
P lithostatic (MPa)	29.8	29.5	28.1	26.7	26.8	29.3	30.9	32.0	31.3	38.9

2.4.2. Eastern equatorial Pacific Ocean

Other well studied upper oceanic crust sites that have been considered for CO_2 storage [*Slagle and Goldberg*, 2011] are in the eastern equatorial Pacific Ocean (eePO), specifically on the NE flank of the Cocos Ridge, and on the eastern flank of the East Pacific Rise (EPR) (Figure 2.13). Since 1970, numerous expeditions have provided a detailed characterisation of the extrusive section of this area (DSDP Leg 9, 16, 69, 70, 83, 92; ODP Leg 111, 137, 140, 148, 206; IODP Exp 309,312, 335) [*Alt and Teagle*, 1999; *Alt et al.*, 2010; *Alt et al.*, 1996; *Becker et al.*, 1988; *Cann et al.*, 1983a; *Davis et al.*, 2004; *Teagle et al.*, 2012; *Teagle et al.*, 2006; *Tominaga et al.*, 2009; *Walther*, 2003; *Wilson et al.*, 2003; *Wilson et al.*, 2006a]. The mid-ocean ridge basalts (MORB) in the eePO, extending in age from 0 to 26 Ma, are the result of several spreading events in a region with relatively simple tectonics [*Meschede and Barckhausen*, 2000]. The thermodynamic evaluation of this region focuses on the Sites 504, 896, and 1256 (Figure 2.13 and 2.14).

Sites 504 and 896, best represented by Holes 504B and 896A respectively, are located in ~7 Ma-old crust, at a water depth of 3460 m below sea-level, and are sited ~200 km south of the intermediate spreading rate Costa Rica Rift, the eastern segment of the Cocos-Nazca spreading Ridge (summary in Table 2.4) [*Alt et al.*, 1993; 1996; *Wilson et al.*, 2003]. Hole 896A was cored only to 469 mbsf, whereas 504B is the second deepest scientific hole drilled into oceanic crust at 2111 mbsf, coring most of the way through the sheeted dike complex.

Site 1256 formed ~15 Ma ago at the East Pacific Rise (EPR) during an episode of superfast oceanic spreading (full rate >20 cm/yr) [*Wilson*, 1996]. This site is located ~1100 km east of the EPR in 3645 m of water and Hole 1256D is 1522 m deep. Together with Hole 504B, it epitomises the most complete penetration into intact upper oceanic crust (summary in Table 2.4) [*Teagle et al.*, 2012; *Teagle et al.*, 2006; *Wilson et al.*, 2003; *Wilson et al.*, 2006a].

At all three sites, the overlaying 180 - 275 m of sediments are mainly chert, biogenic silica and carbonate [*Alt et al.*, 1996; *Wilson et al.*, 2003]. Also, ODP/IODP core porosity data and downhole measurements from the three extrusive sections highlight a similar porosity, which is on average 6-8% [*Becker et al.*, 2004; *Carlson*, 2010].

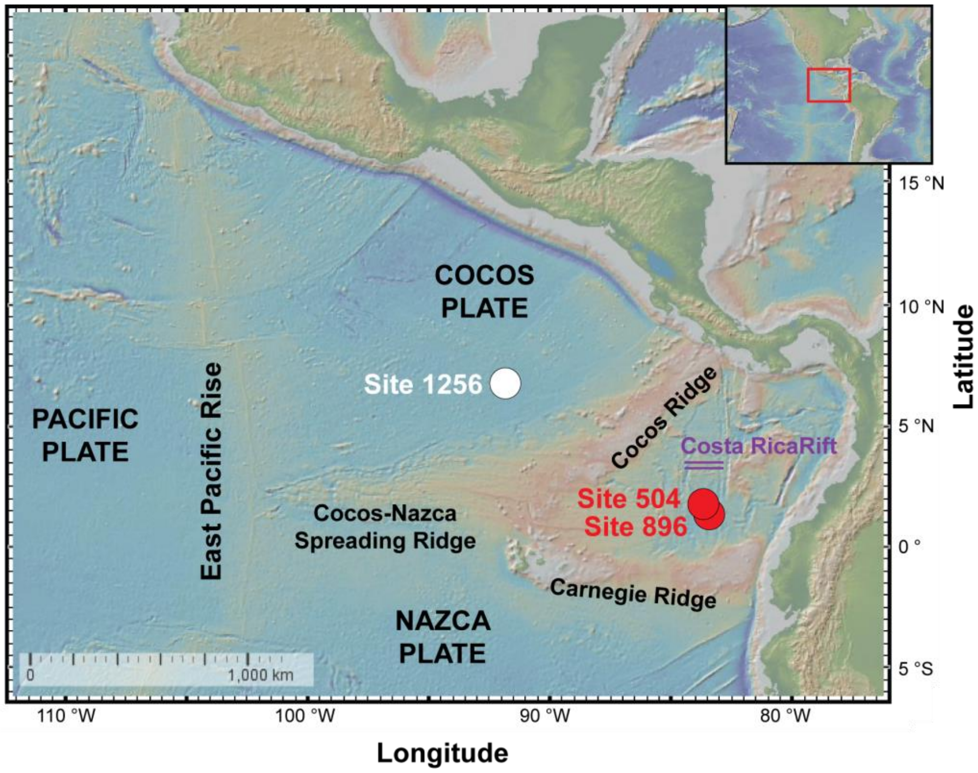

Figure 2.13: Tectonic setting of the eastern equatorial Pacific Ocean. The Sites of interest are shown in red (Site 504 and 896), and in white (Site 1256).

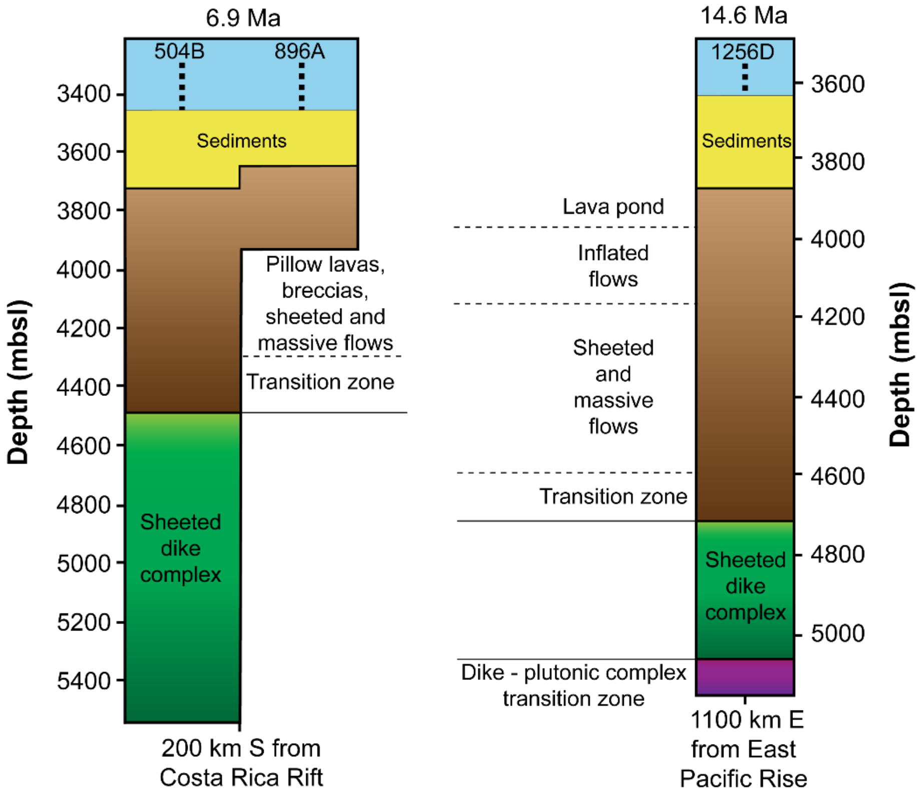

Figure 2.14: Schematic cross sections of the Holes 504B and 896A on the left (modified from Alt et al. [1996]), and Hole 1256D on the right (modified from Teagle et al. [2012]). Drill site locations and inferred basement age are shown at the bottom and top of each section, respectively.

Temperature

The long history of temperature profiles logged during more than 30 years of expeditions to these three sites has produced important datasets [*Becker et al.*, 2004; *Teagle et al.*, 2006]. However, down-welling cold seawater flow in open-hole conditions has often influenced the temperature. Hence, only measurements at equilibrium conditions, and recorded with a wireline installation after hole sealing, have been considered in this study.

The average temperatures at the sediment-basement interface are 45, 57, and 35 ˚C respectively for Sites 504 [*Guerin et al.*, 1996], 896 [*Becker et al.*, 2004] and 1256 [*Teagle et al.*, 2006] (summary in Table 2.4).

Pressure

Assuming an average water density of 1030 kg/m^3, the hydrostatic pressure at the sediment-basement interface for the Sites 504, 896, and 1256 is ~38, ~37, and ~39 MPa, respectively. As explained in Section 2.3.3, this pressure calculation is the most reasonable, but for completeness here the lithostatic-assumption outcomes are as follows (sediment density = 1400-1330 kg/m^3 [*Cann et al.*, 1983b; *Tominaga et al.*, 2009; *Wilson et al.*, 2003]): ~39 MPa for Site 504, ~37 MPa for Site 896, and ~40 MPa for Site 1256 (Table 2.4).

Table 2.4: Summary of the properties of the eePO Sites 504, 896 and 1256 drilled during several expeditions. Pressure - P (MPa) and temperature (˚C) conditions are calculated at the sediment-basement interface. Distance from ridge axis, oceanic crustal age, water depth, and sediment thickness are also shown.

eePO Sites	**504**	**896**	**1256**
Distance from ridge axis (km)	228	229	1100
Oceanic crustal age (Ma)	6.9	6.9	14.6
Water depth (m)	3474	3459	3635
Sediment thickness (m)	275	179	250
Temperature (˚C)	45	57	35
P hydrostatic (MPa)	37.9	36.8	39.4
P lithostatic (MPa)	38.9	37.4	40.0

2.4.3. Summary of two case studies

The JdFP and eePO P/T data are summarised in Figure 2.15, where the contour lines indicate the density difference ($\Delta\rho$) between CO_2 and seawater as a function of temperature and pressure, and the phase diagram of CO_2 is overlaid.

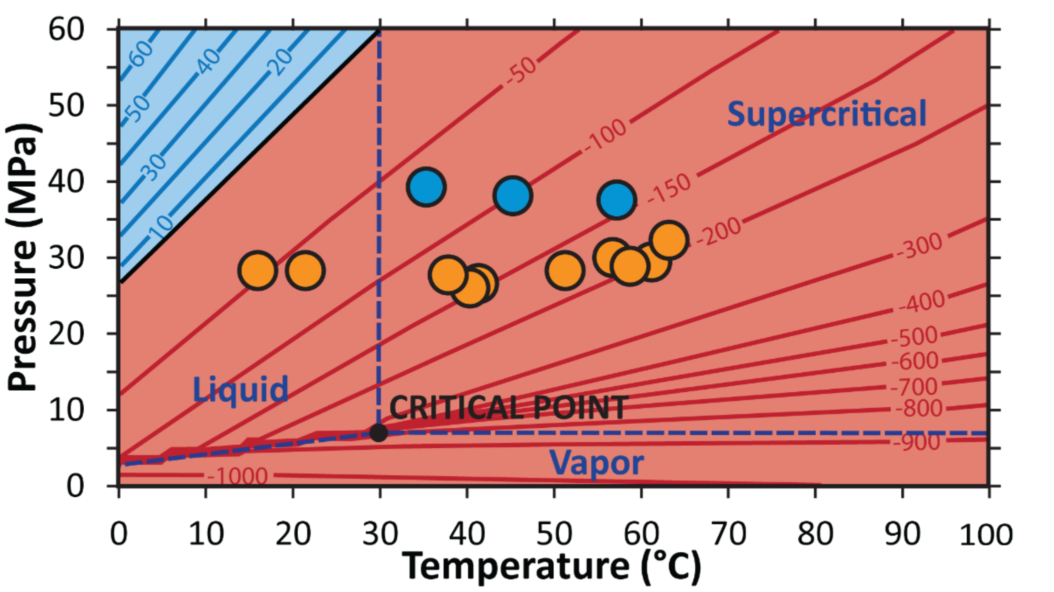

Figure 2.15: Density difference ($\Delta\rho = \rho_{CO2}-\rho_{seawater}$ in kg/m^3) between CO_2 and seawater density as a function of pressure between 0 and 60 MPa, and temperature between 0 and 100 °C, with the phase diagram of CO_2 overlaid (modified from Marieni et al. [2013]). Positive differences (ρ_{CO2} greater than $\rho_{seawater}$) are shown in blue, negative differences in red. JdFP and eePO data are illustrated with orange and blue circles, respectively.

From this figure, it is inferred that at the sediment-basement interface:

- CO_2 is mostly in a supercritical state, and is liquid only where the distance from the ridge axis is <30 km;
- at all sites, CO_2 is less dense than seawater;
- the pressures in the eePO case are higher than in the JdFP one due to the deeper water column;
- the temperatures are similar in both regions, even though JdF Sites are younger than eePO ones.

2.4.4. Validation process of temperature and pressure estimations

To validate the temperatures calculated for a world-wide scenario at the sediment-basement interface, the measured borehole temperatures at the two case-studies (JdFP and eePO) have been compared to the estimated temperature for the corresponding regions, calculated from the GDH1 model (Figure 2.16 – see Appendix CH2-6 for comparison with HSCM). The two areas have different trends of basement-sediment interface temperature as a function of age. In the eePO there is good agreement between estimated and measured temperature, whereas in the JdFP there is a discrepancy, with estimated values higher than actual measurements. The explanation lies in the sediment lithology and in the effect of the correspondent thermal conductivity (K_s) on the temperature. The chert, biogenic silica and carbonate sediments on eePO have thermal conductivity ~1 W/(m K) [*Alt et al.*, 1996; *Wilson et al.*, 2003], in agreement with the value assumed in this study with the GDH1 model. However, on the Juan de Fuca Plate, the recovered cores indicate the presence of terrigenous muddy and sandy turbiditic sediments, which have an higher measured thermal conductivity of ~2 W/(m K) [*Pribnow et al.*, 2000].

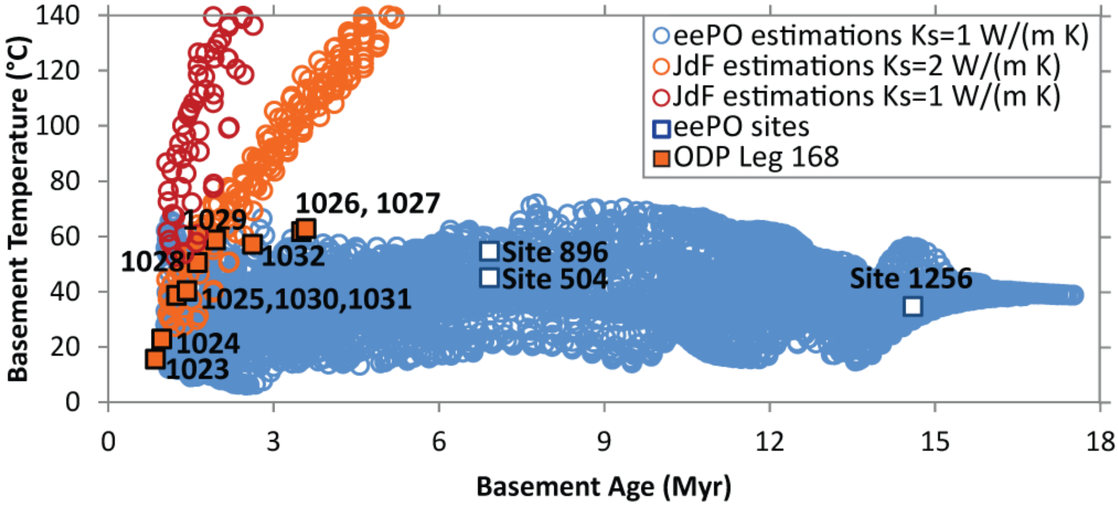

Figure 2.16: Comparison between estimated temperatures (from GDH1 model) in the eastern equatorial Pacific Ocean (eePO) and the Juan de Fuca Plate (JdFP), and measured downhole temperatures at the sediment-basement interface [Marieni et al., 2013]. White squares: data from eePO [Alt et al., 1993; Teagle et al., 2006]; orange squares: data from JdFP [Davis et al., 1997]. Circles: estimated values in the eePO (blue), and on the JdFP (red with K_s = 1 W/(m K); orange with K_s = 2 W/(m K)).

Consequently, the temperature-age curve resulting from the recalculations for the JdFP area, using K_s = 2 W/(m K) in the GDH1 model, shows a better fit with the majority of the temperatures at JdFP sites (Figure 2.16). On the other hand, at Sites 1026 and 1027, the measured temperatures are ~40 ˚C lower than predicted by the purely conductive heat flow model, and nearly identical despite the considerably different sediment thickness, which measures 229 and 614 m, respectively, (Table 2.2). This difference is justified by the local vigorous hydrothermal regime that redistributes the heat within the basement [*Hutnak et al.*, 2006; *Wheat et al.*, 2004], and is driven by very small lateral pressure gradients linked to surrounding basement outcrops (e.g., Baby Bear) [*Fisher et al.*, 2003; *Spinelli and Fisher*, 2004]. Also, this efficiency of lateral heat flow and hydrothermal circulation at the top of the igneous crust justifies the temperature similarity of JdF and eePO.

Hence, the temperature validation at the eePO and JdFP gives confidence in the calculations but emphasizes the need for verification of local physical properties.

Regarding the pressure estimations for the whole oceanic crust at the sediment-basement interface, no further validation is required because the hydrostatic calculations derive directly from well-constrained global datasets of sediment thickness and water depth [*Divins*, 2003; *IOC et al.*, 2003], and from seawater density, which show a narrow window of variations ranging from 1020 to 1050 kg/m^3 [*Brown et al.*, 1995]. Furthermore, the potential fluctuations in these parameters are not significant in this global context, where oceanic crust depth is on average ~3700 m, which corresponds to pressures of ~37 MPa [*Eakins and Sharman*, 2010]. In fact, a change of 100 m in sediment thickness or bathymetry produces a pressure modification of only ±0.1 MPa (~0.27% of average 37 MPa), whereas the maximum change in seawater density (from 1030 kg/m^3, average, to 1050 kg/m^3) yields to a maximum variation of +0.6 MPa (~1.6% of average 37 MPa).

2.5. Conclusions

This chapter illustrates the phase stability of carbon dioxide in the seafloor – a first step to better understand the potential of using the oceanic crust for storing CO_2. Existing global databases of crustal age, sediment thickness, and bathymetry have been investigated and combined with new studies on carbon dioxide and seawater at oceanic crust conditions. Specifically the stability of CO_2 has been determined at the sediment-basement interface, expressing it as a density difference between CO_2 and seawater.

The main findings are:

- the analysis on the thermodynamic properties of CO_2 and seawater highlights the importance of T, P, densities and phase diagrams in the evaluation of the overall behaviour of these two compounds;
- it is evident that carbon dioxide is denser than seawater only for pressures higher than 27 MPa (~2700 m of water) and temperature between 0 and 30 ˚C. It also means that within this small P-T window liquid CO_2 is the stable phase;
- comparison between two heat flow models confirms there are only negligible differences for the purposes of this study;
- the GDH1-based approach is a physically robust scoping study, but it presents uncertainties due to incomplete information on heat flow anomalies, local temperature irregularities, and thermal properties of sediments (i.e., thermal conductivity data);
- despite numerous holes drilled into the oceanic crust by scientific ocean drilling, the validation of the estimated temperature at the sediment-basement interface can only be assessed at thirteen sites, as they provide the only reliable drill hole temperature measurements;
- regions characterised by thermodynamically stable CO_2 are generally located in old oceanic crust covered by a relatively thin layer of sediments.

Chapter 3: Oceanic crust as a reservoir for CCS

3.1. Introduction

Geological trapping in mafic and ultramafic rocks is a proposed mitigation strategy to sequester anthropogenic CO_2 from the atmosphere on a long-term basis. As described in Chapter 1, several formations have started to be considered as potential CCS reservoirs. Most of these sites are located on land. A few theoretical studies have focused on offshore basalts [*Goldberg and Slagle*, 2009; *Goldberg et al.*, 2008; *Goldberg et al.*, 2013; *Slagle and Goldberg*, 2011], which cover approximately 60% of the Earth's surface, offering huge reservoir capacity, and show evidence, such as carbonate veins, for naturally occurring CO_2 mineralisation [*Alt and Teagle*, 1999; *Coggon et al.*, 2010]. To date, no field-scale pilot projects have been developed, mainly due to uncertainties linked with scientific, technological, and economic feasibility of the sequestration method associated with oceanic reservoirs. Common questions on offshore CO_2 sequestration in oceanic crust can be summarised as follows:

- Can offshore basalt formations safely store CO_2?
- What are the trapping mechanisms?
- Are there suitable locations for CO_2 sequestration in the seafloor? And if so, how accessible are these reservoirs?

So far, the global variability of sediment thickness, pressure (P), and temperature (T), and consequently the relative density (ρ) of CO_2 and seawater have been considered at the sediment-basement interface of the oceanic crust (Chapter 2).

In this chapter, the oceanic crust properties described in Chapter 2, such as *in situ* density, sediment thickness, and water depth, are combined together to demonstrate the effectiveness of CO_2 sequestration in deep-sea basalts, and identify potential targets.

3.2. CO_2 trapping mechanisms in offshore basalts

There are three primary trapping mechanisms proposed for long-term storage of carbon dioxide in offshore basalts (Figure 3.1):

1- *Gravitational trapping* under pressure and temperature conditions where CO_2 is denser than seawater [*Levine et al.*, 2007] – Chapter 2.

2- *Physical or permeability trapping*, where the presence of ≥200 m of overlying low-permeability marine sediments isolates the CO_2 injected into the basalts from the oceans, so that any leakage is trapped in the sediments [*Goldberg and Slagle*, 2009] – Chapter 3.

3- *Geochemical trapping,* where CO_2 and water react with the basalt host rocks to form geologically stable carbonate minerals, which is a process also known as "*mineral carbonation*" [*Gislason et al.*, 2010; *Seifritz*, 1990] – Chapter 4.

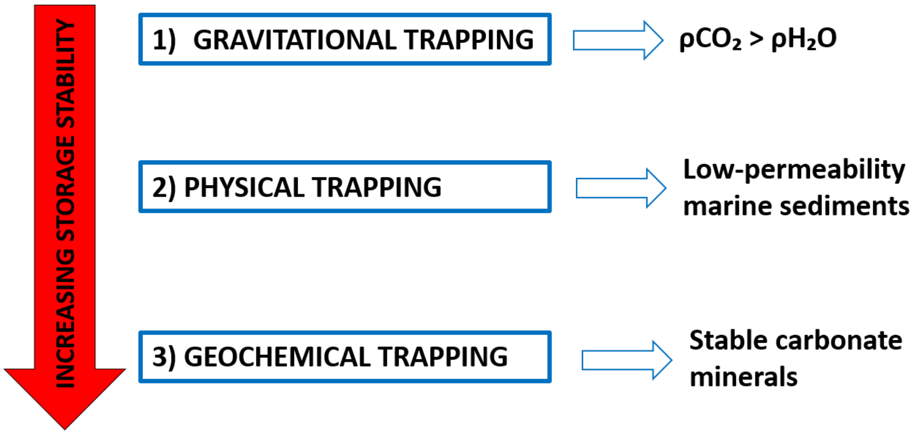

Figure 3.1: Primary trapping mechanisms for the long-term storage of carbon dioxide in offshore basalts.

Among these approaches, *carbon mineralisation* is the most permanent option (on the order of a thousand years) for CO_2 sequestration as the reaction products (Ca, Mg, and Fe carbonate minerals) are environmentally benign and stable, providing little possibility of accidental release and requiring little post-storage monitoring [*Lackner*, 2003; *Lackner et al.*, 1995; *Sipilä et al.*, 2008]. However, turning the carbon dioxide into a solid carbonate mineral in mafic and ultramafic rocks is not without challenges. These include the availability of water for carbonation, the possible mobilization of trace and toxic metals, and the consequent need for low-permeability cap rocks to prevent leakage of buoyant fluids at the seafloor (*physical trapping*) [*Oelkers et al.*, 2008]. Because CO_2 is generally less dense than water, buoyancy tends to drive CO_2 upwards back to the surface [*Oelkers and Cole*, 2008], although, under the right conditions, CO_2 can be dense enough to naturally stay within the basement rocks [*Levine et al.*, 2007] (Chapter 2). Hence, in offshore conditions, the theoretical maximum storage stability is reached with the combination of all three trapping mechanisms.

An additional trapping mechanism is *solubility trapping*. This involves the dissolution of CO_2 into formation water to create a CO_2-rich fluid that is slightly denser than the original CO_2-free water [*Gislason and Oelkers*, 2014; *Gunter et al.*, 1993]. As for *gravitational trapping*, solubility trapping eliminates the buoyancy that drives free CO_2 upwards with respect to the fluid. However, the solubility approach involves i) very large quantities of seawater, and ii) the presence of porous rocks to prevent over pressurisation of the reservoir with the huge amount of pumped water. The dissolution of one tonne of CO_2 at a partial pressure of ~2 MPa and 25°C requires ~27 t of fresh water [*Oelkers et al.*, 2008], or 31 t of seawater [*Gislason et al.*, 2010], whereas at ~25 MPa and 20°C the required mass of seawater is ~15 t [*Duan et al.*, 2006]. The process of dissolving CO_2 in solution prior to its injection would also increase the storage costs [*Gislason and Oelkers*, 2014]. Hence, solubility trapping is not considered viable for the geological storage of CO_2 in deep-sea basalts.

In the next sections, the most stable conditions for combined physical and gravitational trapping of CO_2 in deep-sea basalts are discussed. The rock dissolution reactions involved in geochemical trapping are considered in Chapter 4.

3.3. Gravitational trapping

As illustrated in Chapter 2, if CO_2 is denser than seawater ($\rho CO_2 > \rho_{seawater}$), it will tend to sink into the oceanic crust, becoming gravitationally trapped. This condition is met within a narrow P-T window, with hydrostatic pressures higher than 27 MPa (>2700m of water) and temperatures between 0 and 30°C (Figure 3.2).

The map of the positive density difference ($\Delta\rho > 0\ kg/m^3$) between CO_2 and seawater at the sediment-basement interface, calculated using the GDH1 heat flow model, highlights how areas with suitable PTρ conditions for CO_2 storage are found in old oceanic crust and in the deep ocean (Figure 3.3). Most of the ridge flanks or sites close to continental margins show negative $\Delta\rho$ conditions, due to high heat flow and thick piles of thermally isolating sediments, respectively.

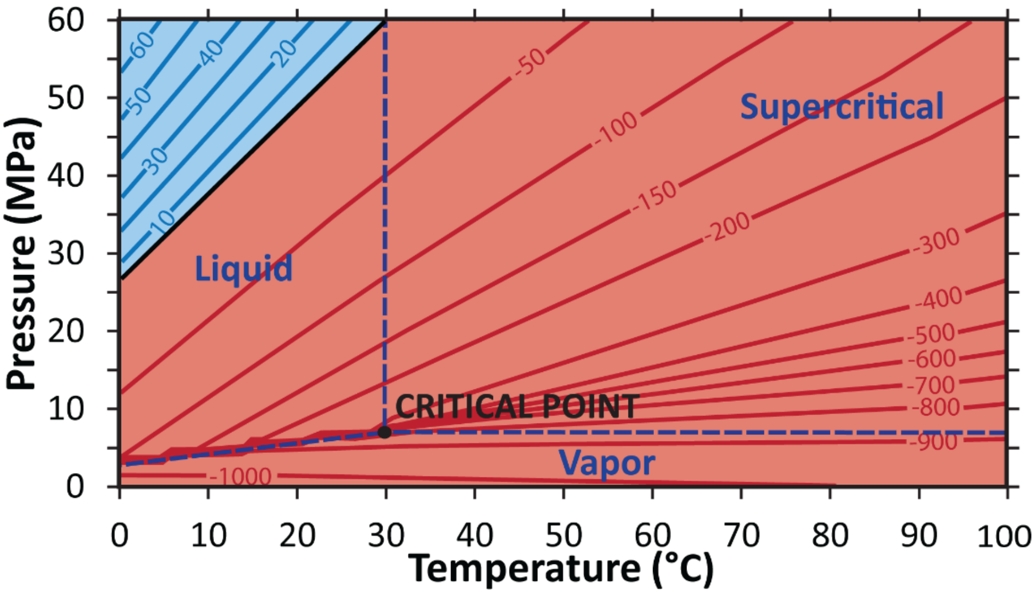

Figure 3.2: Density difference ($\Delta\rho = \rho CO_2 - \rho_{seawater}$ in kg/m^3) between CO_2 and seawater density as a function of pressure between 0 and 60 MPa, and temperature between 0 and 100 °C, with the phase diagram of CO_2 overlaid. Positive differences shown in blue indicate conditions for gravitational trapping [Marieni et al., 2013]. Modified version of Figure 2.15 in previous chapter.

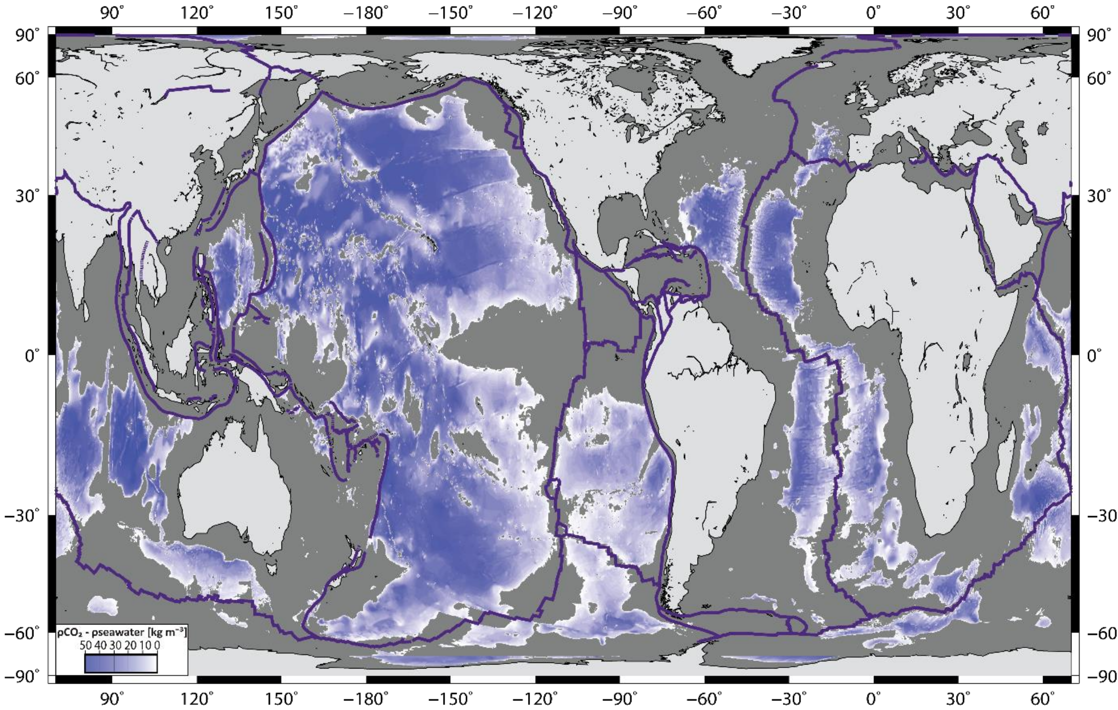

Figure 3.3: A cylindrical equal area map showing locations for gravitational trapping of CO_2, using the GDH1 model for heat flow estimations. Shading shows the positive difference in density between CO_2 and seawater ($\Delta\rho > 0$ kg/m^3).

3.4. Physical trapping

The physical trapping mechanism proposed by *Goldberg and Slagle* [2009] involves the presence of ≥200 m of overlying sediments to isolate the injected CO_2 in the basalts from the oceans, and to capture any leakage in the sediment pile. This retaining strategy is based on the low permeability of the sediments, which is the parameter that controls the extent of fluid flow through the sediments. In marine sediments, permeability is low, typically ranging from 10^{-19} to 10^{-12} m^2, and depends on sediment type and porosity (Table 3.1) [*Bryant and Rack*, 1990; *Spinelli et al.*, 2004]. Oceanic sediments can be divided into two main types: terrigenous (47 vol%) and pelagic (53 vol%); in turn, the pelagic sediments can be classified as calcareous (74 vol%), red clays (19 vol%), and biogenic siliceous (7 vol%) [*Hay et al.*, 1988]. In each group, permeability decreases with decreasing porosity, which decreases with depth. The permeability also has the tendency to increase with grain size; for example higher values are recorded in the sandy layers of turbidites (coarsest) than in red clays (finest).

Table 3.1: Oceanic sediment types (data from Hay et al. [1988]) and relative porosity and permeability (data from Spinelli et al. [2004]).

Oceanic sediments				**Porosity** %	**Permeability** m^2
47%	Terrigenous			20 - 85	10^{-19} - 10^{-13}
53%	Pelagic	Calcareous	74%	50 - 85	10^{-17} - 10^{-13}
		Red clays	19%	60 - 90	10^{-18} - 10^{-13}
		Biogenic siliceous	7%	45 - 90	10^{-19} - 10^{-12}

The NOAA-*gridfive* sediment database [*Divins*, 2003] has been used to determine the sediment thickness for all the areas with underlying oceanic crust (Appendix CH2-4). In general, the global distribution of sediment thickness is a function of oceanic lithosphere age [*Müller et al.*, 1997; *Spinelli et al.*, 2004]. If pairs of sediment thickness and lithospheric age values are grouped by age into 5 Ma bins, most of the bin-median values lie below 700 m and above 200 m (Figure 3.4). The average sediment thickness calculated from *Divins* [2003] database is ~400 m.

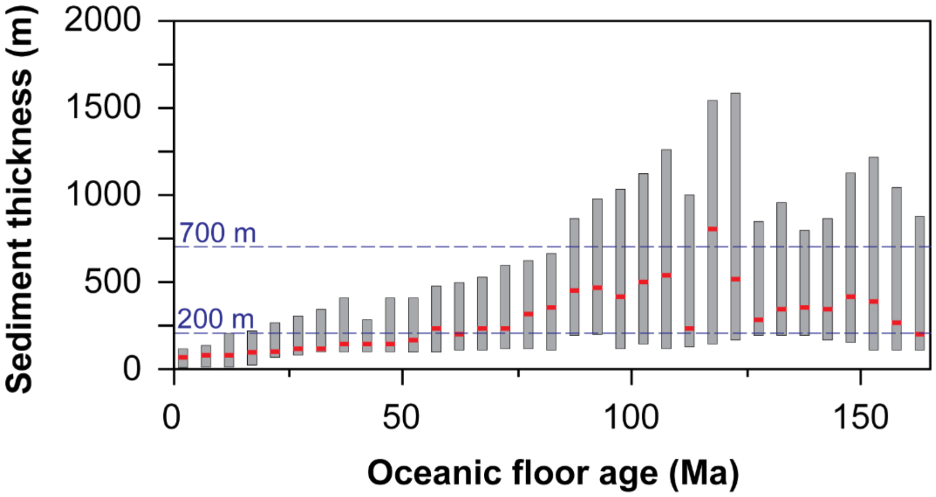

Figure 3.4: Sediment thickness (data from Divins [2003]) versus oceanic floor age (data from [Müller et al., 1997]) – modified from Spinelli et al. [2004]. Pairs of sediment thickness and lithospheric age values are determined on a grid with a spacing of 1.67 x 1.67˚, then grouped by age into 5 Myr bins. The box plot for each 5-Myr age bin shows the median sediment thickness (red horizontal line), the 25th and 75th percentile (bottom and top of the box, respectively), the 200 and 700 m limits (blue dashed lines).

In this study, based on the global distribution of sediment thickness, a minimum of 200 m has been chosen as the lowest physical trapping constraint to ensure a continuous low permeability blanket over minor basement topography such as faulted ridges or seamounts that might puncture the sediment cover and allow the ingress or egress of basement fluids [*Divins*, 2003]. This is consistent with recommendations for CO_2 storage in deep saline aquifers that require a caprock thickness of >100 m [e.g. *Chadwick et al.*, 2008].

To estimate the maximum sediment thickness, the density difference has been calculated for a wide range of lithospheric ages and sediment thicknesses using the GDH1 model for both water depth and heat flow, and assuming a hydrostatic sediment column (Figure 3.5). Based on global average conditions, GDH1 indicates a restricted zone where gravitational trapping is possible, and that anywhere with more than ~600 m of sediments CO_2 is likely to be gravitationally unstable due to the high temperatures. Using the HSCM (see Appendix CH3-1), the equivalent limit is ~1000 m. Hence, the upper sediment thickness limit has been set at 700 m.

From these constraints, a global map for the physical trapping strategy can be plotted for areas where sediment thicknesses is between 200 and 700 m (Figure 3.6).

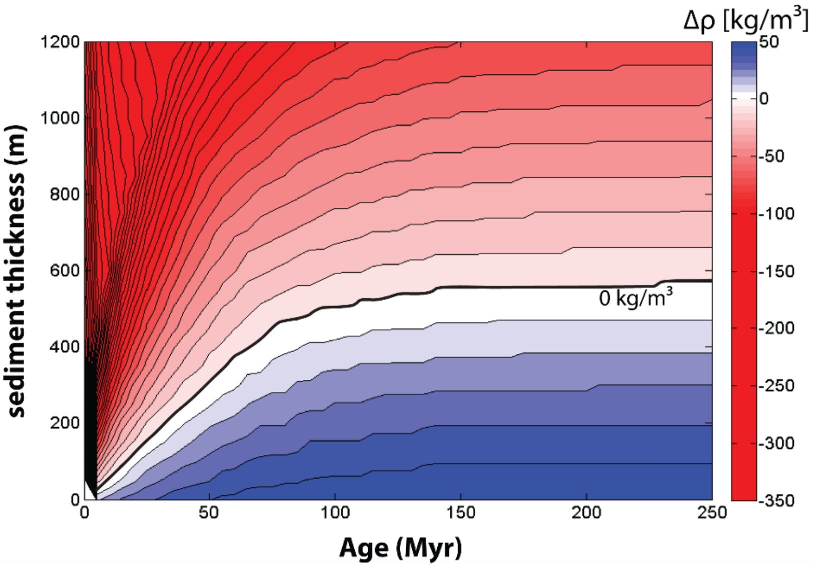

Figure 3.5: Density difference between CO_2 and seawater at the sediment-basement interface as a function of plate age and sediment thickness using the GDH1 model to determine both water depth and thermal conditions [Marieni et al., 2013]. Sediment thicknesses below the heavy black line show where positive density differences required for stable gravitational trapping are achieved.

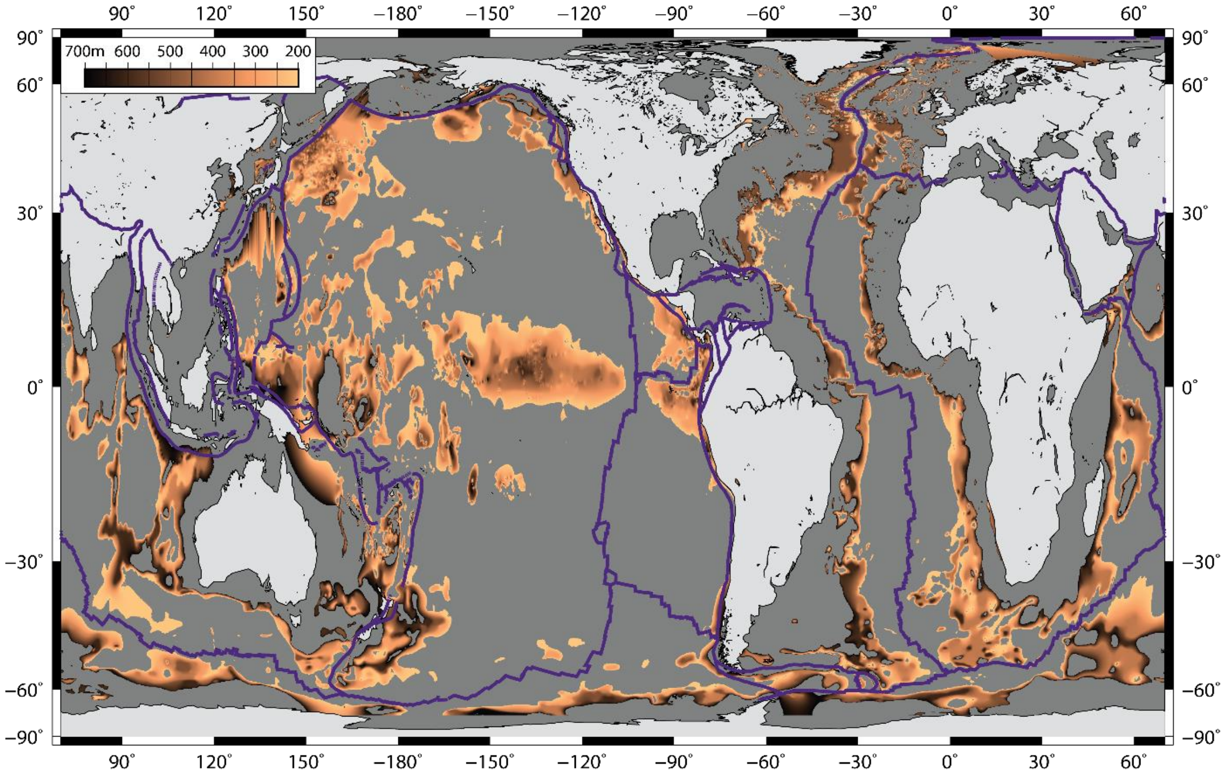

Figure 3.6: A cylindrical equal area map showing locations for physical trapping of CO_2 in the seafloor. Shading shows the sediment thickness between 200 and 700 m.

3.5. Offshore basalt targets

The optimal conditions for CO_2 storage in deep-sea basalts are reached by combining gravitational and physical trapping. The results from the individual analysis of each trapping mechanism have been merged in a global map (6 minute resolution), and expressed as density difference at the sediment-basement interface (Figure 3.7). A positive density difference identifies locations where 1) CO_2 is denser than seawater at the sediment-basement interface ($\rho CO_2 > \rho_{seawater}$) (Figure 3.3), and 2) the sediment thickness is between 200 m and 700 m (Figure 3.6). The global map produced using the HSCM is available in the Appendix CH3-2.

Much of the upper oceanic crust is not suitable for the geological sequestration of CO_2 by gravitational and physical trapping. However, five potential targets can be identified based on the positive $\Delta\rho$ between CO_2 and seawater, the oceanic crustal age, the sediment thickness, and the distance to major industrial CO_2 sources [*International Energy Agency Greenhouse Gas R&D Programme*, 2002]. All the targets are in water depths >5000 m. Selected reservoirs are in the Indian Ocean between Indonesia and Australia (inset **a**); in the northwest Pacific Ocean near the east coast of Japan and Russia (inset **b**), and south of the Aleutian Islands (inset **c**); and in the Atlantic Ocean near Bermuda (inset **d**) and close to South Africa (inset **e**) (Table 3.2). Other areas also have suitable conditions for carbon dioxide trapping, but these options have not yet been explored due to their smaller sizes and lower $\Delta\rho$, although some are closer to land. Potential storage volume for each target has been computed (Table 3.2), assuming an average porosity of 10% [*Carlson and Herrick*, 1990; *Johnson and Pruis*, 2003], even for old oceanic crust (e.g., ODP Hole 801C [*Jarrard et al.*, 2003]), and 300 m as a reasonable thickness of permeable pillow lavas for old crust. The storage capacity in each area is between ~13,800 and 127,800 Gt of CO_2. Given the ~1840 Gt of cumulative anthropogenic CO_2 emissions in the atmosphere since the Industrial Revolution [*Allen et al.*, 2009], and at the current global annual anthropogenic flux of ~36 Gt of CO_2 per year [*Le Quéré et al.*, 2015], even the smallest identified reservoir (inset **c**) could provide sufficient carbon dioxide sequestration capacity to accommodate past CO_2 emissions and also several centuries worth of future emissions (Figure 3.7).

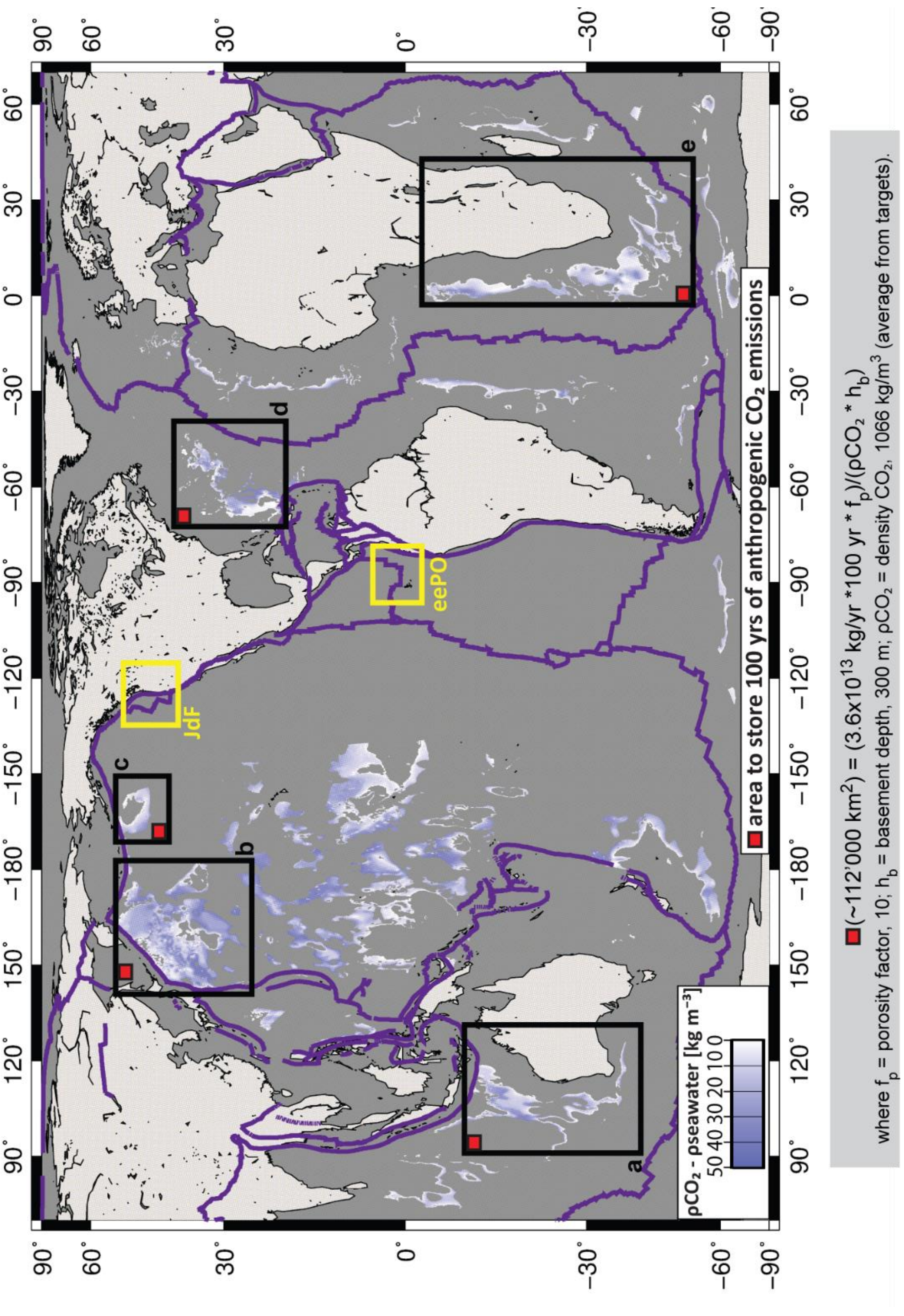

*Figure 3.7: A cylindrical equal area map showing locations for stable geological sequestration of CO_2 [modified from Marieni et al., 2013]. Shading shows the difference in density between CO_2 and seawater in areas where the sediment thickness is between 200 and 700 m and the CO_2 is denser than seawater. Five potential reservoirs (insets **a–e**) have been identified. As described in the equation at the bottom, the red box indicates the area required to store 100 yrs of current anthropogenic emissions of CO_2 (36 Gt/yr), assuming a pillow lava thickness of 300 m and 10% porosity [Carlson and Herrick, 1990; Jarrard et al., 2003; Johnson and Pruis, 2003]. Yellow boxes show regions in Figure 3.11, previously discussed in Chapter 2.*

Table 3.2: Properties of the five potential reservoirs. Δρ, in situ excess density of CO_2 over seawater; age from [International Energy Agency Greenhouse Gas R&D Programme, 2002; Müller et al., 2008]; sediment thickness from the NOAA database [Divins, 2003]. Distance of the reservoir from land is taken from the nearest stationary source of CO_2 according to the IEA GHG database [International Energy Agency Greenhouse Gas R&D Programme, 2002].

Code	**Location**	**Area** [x10^{6}km^{2}]	**Pore volume** [x10^{4}km^{3}]	**ρCO_2** [kg/m^{3}]	**CO_2** [Gt]	**Δρ** [kg/m^{3}]	**Age** [Ma]	**Sediment thickness** [m]	**Distance** [km]
a	Indian Ocean	1.47	4.42	1066	47,162	18	85	335	1500
b	NW Pacific	3.97	11.9	1073	127,870	24	100	310	1300
c	S-Aleutians	0.43	1.30	1063	13,791	15	60	275	1500
d	Bermuda	1.15	3.45	1066	36,780	17	80	320	1500
e	SE Atlantic	2.22	6.66	1062	70,701	14	85	290	1700

To confirm the assumption of 300 m as reasonable thickness of permeable old basalts, pressures and temperatures (using GDH1 model, with 2 W/(m K) as thermal conductivity of pillow lavas [*Clauser*, 2006]) have been calculated at 300 m into the basement for all the gravitationally and physically suitable locations. The density difference results are illustrated on a 6′×6′ global map (Figure 3.8).

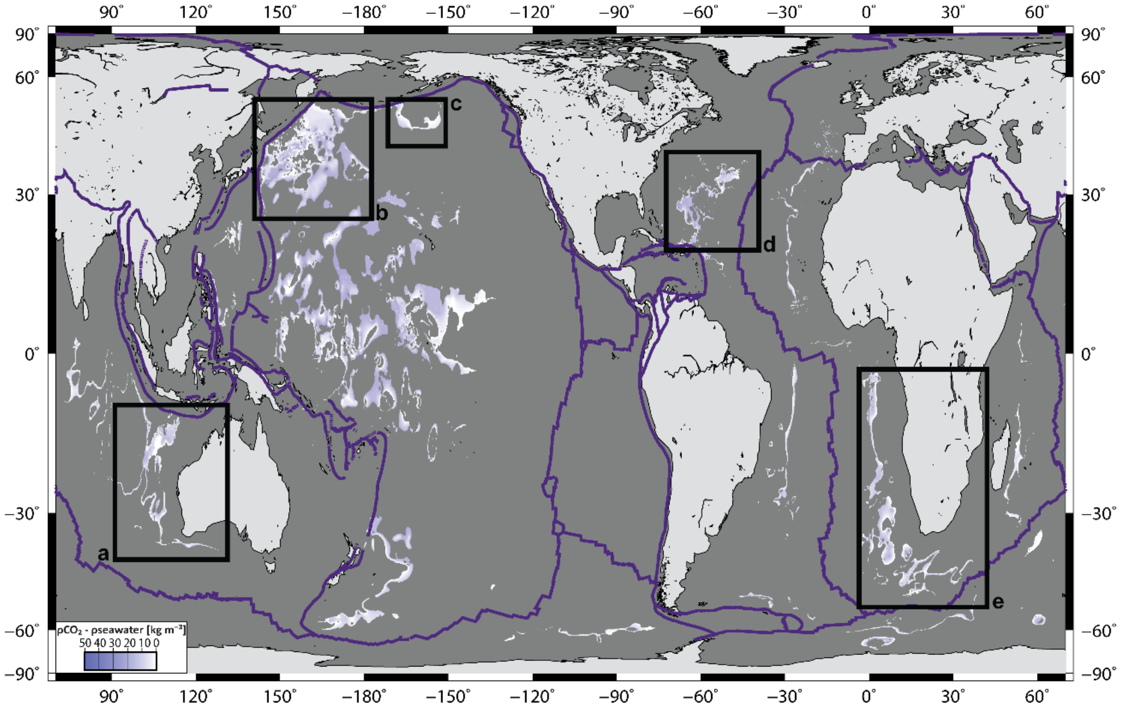

Figure 3.8: A cylindrical equal area map showing locations for stable geological sequestration of CO_2 at 300 m into the basement. Shading shows the difference in density between CO_2 and seawater in areas where the sediment thickness is between 200 and 700 m and the CO_2 is denser than seawater. 71% (by surface area) of the areas identified in Figure 3.7 are valid at this depth into the basement.

The size of the areas identified in these calculations are summarised in Table 3.3, expressed as a function of the total oceanic floor area, which is ~2.96x10^8 km^2 [*Müller et al.*, 2008]. If only physical trapping with sediment thickness between 200 and 700 m is considered at the sediment-basement interface (**1** in Table 3.3), the area of suitable oceanic crust for CO_2 storage is 31.5% of the total, and includes the sites where $\Delta\rho < 0$ kg/m^3 (seawater is denser than CO_2). If only gravitational trapping with $\Delta\rho > 0$ kg/m^3 (CO_2 is denser than seawater) is taken into account, the recommended locations cover 48.1% of the seafloor, with an average $\Delta\rho$ of ~26 kg/m^3 (**2** in Table 3.3). However, when both gravitational and physical trapping of CO_2 are combined, this area falls to only 7.5% at the sediment-basement interface (**3a** in Table 3.3) and 5.3% at 300 m into the basaltic crust (**3b** in Table 3.3), which is 71% of the area at the sediment-basement interface. Careful consideration of the behaviour of CO_2 in the crust is essential in selecting a suitable area for CO_2 storage.

Table 3.3: Surface area estimations as a function of type of trapping and sediment thickness. The relative area is calculated as a percentage of all the oceanic floor area (2.96x10^8 km^2) estimated with age [Müller et al., 2008].

Code	Type of trapping	Sediment thickness [m]	Location	Average Δρ [kg/m^3]	Area [km^2]	Relative area
1	physical	200 -700	sediment-basement interface		9.32x10^7	31.5%
2	gravitational		sediment-basement interface	26	1.42x10^8	48.1%
3a	gravitational + physical	200 - 700	sediment-basement interface	19	2.23x10^7	7.5%
3b	gravitational + physical	200 - 700	300 m into basement	11	1.57x10^7	5.3%
4	gravitational + physical	200 - 500	sediment-basement interface	19	2.19x10^7	7.4%
5	gravitational + physical	0 - 200	sediment-basement interface	28	1.17x10^8	39.4%
6	gravitational + physical	100-200	sediment-basement interface	29	5.07x10^7	17.1%
7	gravitational + physical	0 - 500	sediment-basement interface	27	1.42x10^8	48.0%
8	gravitational + physical	0 - 700	sediment-basement interface	26	1.42x10^8	48.1%

These calculations have all assumed a sediment thickness between 200 and 700 m (Section 3.4). However, in areas where the CO_2 is gravitationally stable and basement topography is low, 200 m of sediments may not be required to physically trap the CO_2 as theoretically the CO_2 would remain in the basalt even with no sediment cover. In order to better explore the effect of sediment thickness, five different scenarios have been considered (Table 3.3 and relative global maps in Appendices CH3-3 A, B, C, D, E): **4-** from 200 to 500 m; **5-** from 0 to 200 m; **6-** from 100 to 200 m; **7-** from 0 to 500 m; **8-** from 0 to 700 m. The results highlight the way in which the extent of CO_2 offshore reservoirs could be improved from 7.5 to 39.4% of the ocean floor if ≤ 200 m of marine sediments blanketed the gravitationally stable areas ($\Delta\rho$ of ~28 kg/m^3). Also, almost half of these locations are characterised by sediment thickness ranging from 100 to 200 m ($\Delta\rho$ of ~29 kg/m^3). Increasing the upper limit of sediment thickness from 500 to 700 m in gravitationally stable regions adds only 0.1% to the relative available area, and so increasing sediment thickness is relatively unimportant.

These evaluations, based on global data sets, show that CCS using subsea basalts as the storage medium has considerable potential, with many alternative storage conditions. However, regional investigations are required to determine local sediment properties, thicknesses, continuity, and seafloor thermal gradients. Drilling to facilitate detailed lithological, physical, thermal, and hydrological characterization of the sediment overburden and target basalt formations is essential.

In the next Section, case studies of unsuitable reservoirs (JdF and eePO in Figure 3.7), and an example of local investigations in the offshore region to the west of the Exmouth Plateau in NW Australia (*target* ***a*** in Figure 3.7) have been undertaken.

3.5.1. JdF and eePO as unsuitable CCS targets

As described in Section 2.4, the Juan de Fuca Plate (JdFP) and eastern equatorial Pacific Ocean (eePO) are two regions where the physical, geochemical, and structural properties of the upper oceanic crust are well characterised. Both regions have previously been proposed as potential offshore targets for carbon dioxide sequestration [*Goldberg et al.*, 2008; *Slagle and Goldberg*, 2011]. They have thick sediment layers on top of the basement, and show relatively high porosity (~10%) and permeability values ($10^{-17} – 10^{-13}$ m^2) in the upper 300 m of the crust [*Anderson et al.*, 1985; *Becker*, 1996; *Becker and Fisher*, 2000; *Davis and Becker*, 1998]. The JdFP has the advantage of being located at short pipeline distances to populated areas and CO_2 sources. In the evaluation of these sites, the advantages of long-term carbon sequestration via mineral carbonation, physical and gravitational trapping in oceanic crust were discussed. *Gravitational trapping* has been described for water depths greater than 2700 m, where injected CO_2 was assumed to be denser than seawater on the basis of *House et al.* [2006] density calculations. This trapping approach was supported by the outcomes of direct experiments on the ocean disposal of CO_2 carried out by *Brewer et al.* [1999], where CO_2 hydrate (~6 H_2O+CO_2) was forming from the injection of liquid CO_2 in the water depth range 2700 to 4500 m. The crystalline CO_2 hydrate is denser but less soluble than liquid CO_2 in seawater <2 ˚C, and its formation impedes the upward flow of the underlying CO_2 (liquid). However, in these previous studies on JdFP and eePO the phase relationships at the sediment-basement interface were not taken into account. The thick sediment blanket covering young oceanic crust results in high temperatures at the sediment-basement interface. Under these conditions CO_2 is a supercritical fluid, and consequently much less dense than seawater. Hence, contrary to previous suggestions, sites on the Juan de Fuca Plate and in the eastern equatorial Pacific Ocean are unsuitable for gravitational trapping of carbon dioxide (Figure 3.11) because the CO_2 will naturally tend to escape as a buoyant supercritical fluid.

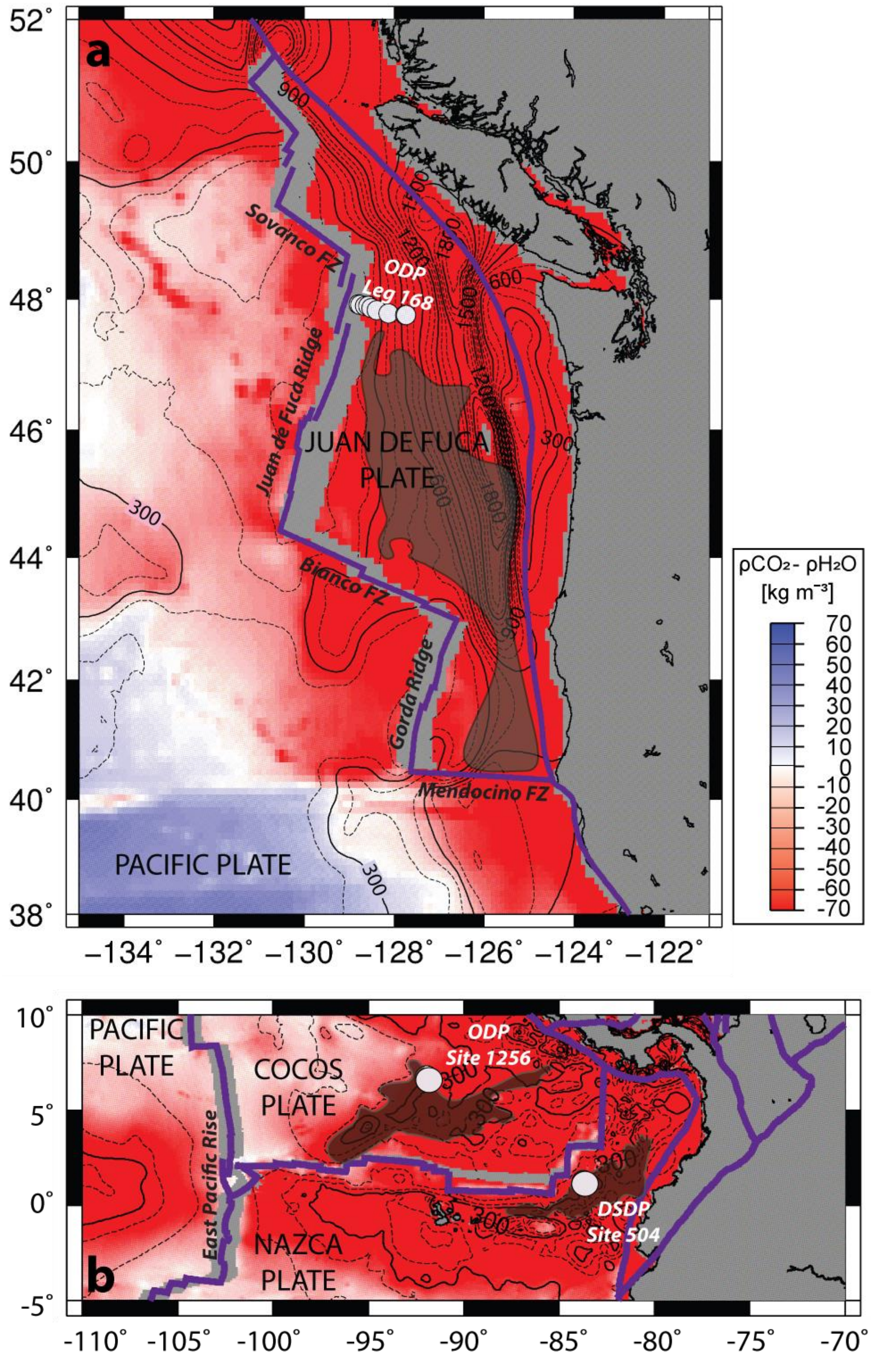

Figure 3.9: Map of density difference Δρ between CO_2 and seawater at (a) the Juan de Fuca Plate (with K_S = 2 W/(m K)) and (b) the eastern equatorial Pacific Ocean (with K_S = 1 W/(m K)). Sediment thicknesses [m] are shown by black contour lines. The dark shadows show the previously suggested regions for deep-sea basalt CO_2 sequestration [Goldberg et al., 2008; Slagle and Goldberg, 2011].

3.5.2. Target a: Indian Ocean

T*arget* ***a*** is located in the Indian Ocean, offshore Western Australia, between the Java Trench, the Ninetyeast Ridge, Broken Ridge, and the Diamantina Fracture Zone (Figure 3.10). This zone of the Indian Ocean is part of the Australian Plate, and is one of the oldest continent / ocean boundaries on Earth (~160 Ma) [*Gradstein et al.*, 1990]. The Exmouth plateau (Figure 3.10) is a major offshore petroleum province (e.g. Shell, and Woodside). This subsided continental platform is located ~300 km from the NW coast of Australia, and comprises ~10 km block-faulted Palaeozoic to Mesozoic (542-65 Ma) sedimentary rocks [*Exon and Willcox*, 1978]. The abundance of hydrocarbons in the sandstone formations of the area makes *target* ***a*** an economically interesting location to start more detailed investigations into the potential for deep-sea basalt CO_2 sequestration.

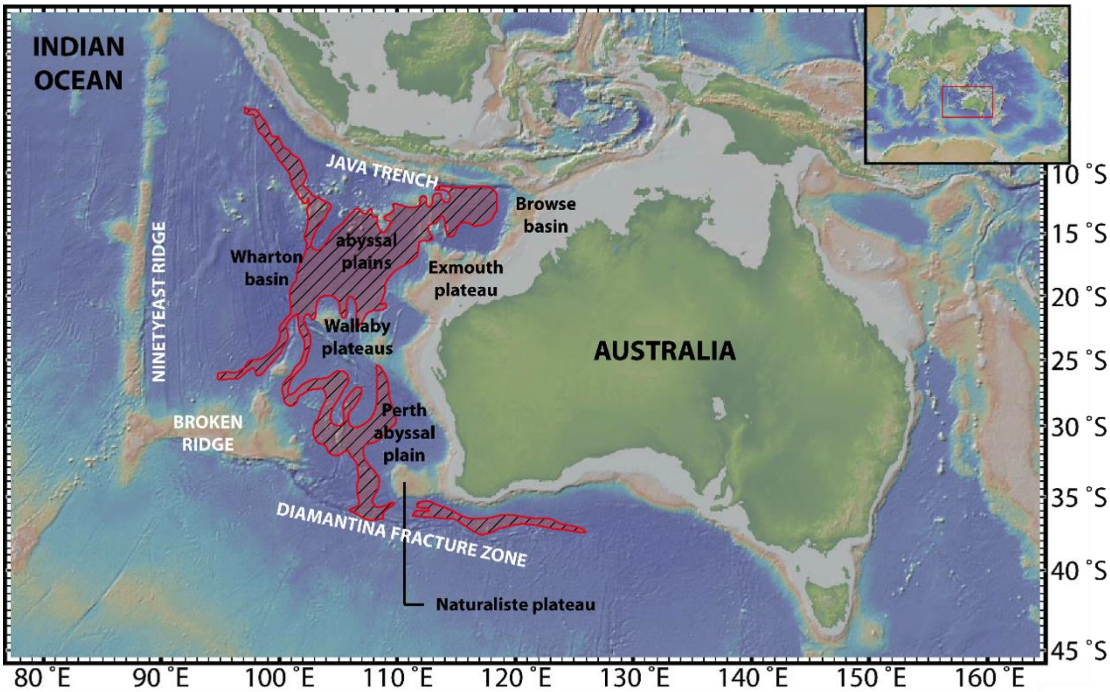

*Figure 3.10: Tectonic setting of the offshore Western Australia. The Indian Ocean target "**a**" is highlighted in red.*

Since the Jurassic (~200 Ma), many rifting events have occurred in this area, with at least three polar-wander path shifts influencing the oceanic spreading direction

[*Schettino and Scotese*, 2005]. As a consequence, numerous plateaus, ridges, basins, and abyssal plains characterise this region of the Indian Ocean. The area near *target* ***a*** has been the focus of five scientific ocean drilling cruises (DSDP Leg 26, 27, and 28; ODP Leg 122 and 123), which were all primarily focussed on the biostratigraphy of the sediments on top of the basement, and on the geodynamic reconstructions of the local paleogeography [*Gradstein et al.*, 1992; *Hayes et al.*, 1975; *Luyendyk and Davies*, 1974; *Veevers et al.*, 1974; *von Rad et al.*, 1992] (Figure 3.11). Hence, there are few data from the sediment-basement interface to characterise *target* ***a***, and to compare the empirical measurements with the oceanic crustal age-derived estimations, which have been carried out in this study.

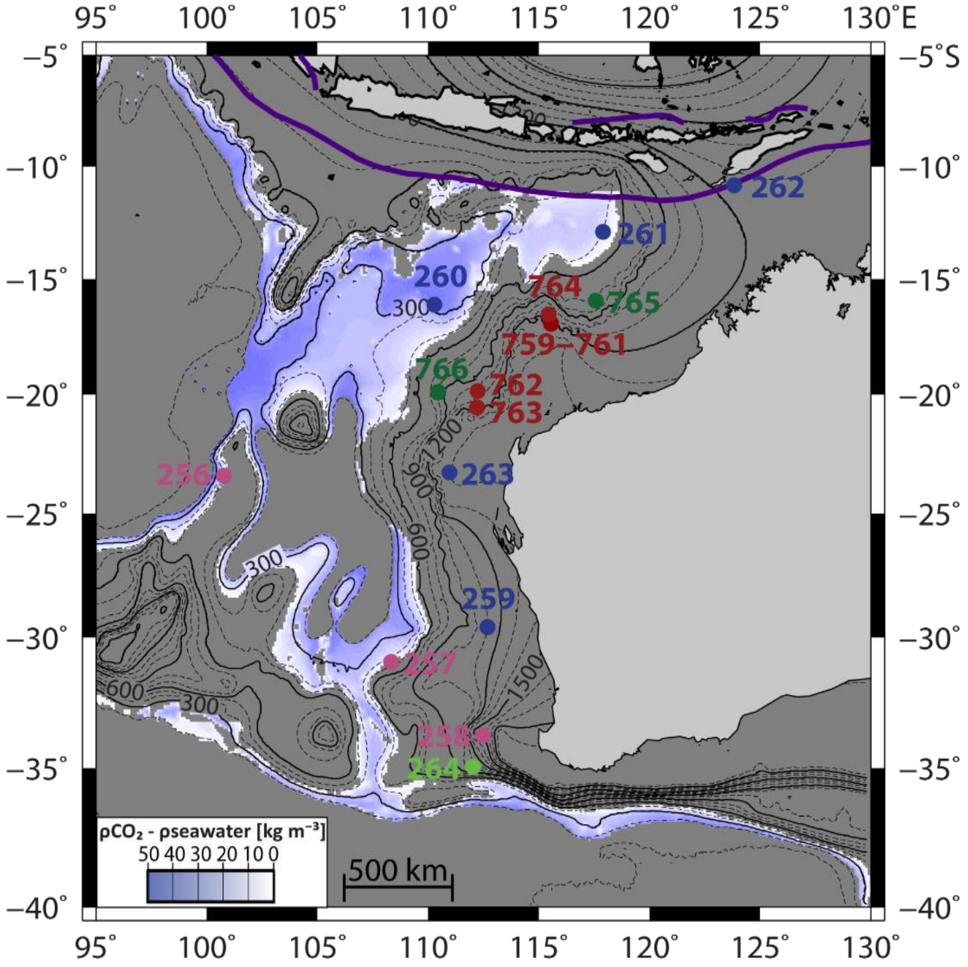

Figure 3.11: An equal area map showing the potential target ***a*** *for CO_2 storage. Shading shows the difference in density between CO_2 and seawater in areas where the sediment thickness is between 200 and 700 m and the CO_2 is denser than seawater. Sediment thicknesses [m] are shown with black contour lines [Divins, 2003]. The five scientific oceanic drilling cruises are also shown on the map (DSDP Leg 26 in pink; DSDP Leg 27 in blue; DSDP Leg 28 in light green; ODP Leg 122 in red; and ODP Leg 123 in dark green).*

3.5.2.1. Comparison between estimated and measured values

For each of the five scientific cruises, the results from drilling at representative sites are summarised in Table 3.4, together with the estimations of oceanic crustal age, water depth, sediment thickness, and temperature at the sediment-basement interface used in this study from global databases. The data relative to the ODP Leg 122 are also shown for comparison, even if the Sites are located on the continental margin.

Igneous basement was reached in three of the cruises (DSDP Leg 26, Leg 27, and ODP Leg 123), but only at one site (ODP Leg 123 – Site 765) temperature and porosity measurements were recorded [*Brereton*, 1992]. This was the first time a high resolution temperature tool (Temperature Logging Tool – TLT) was successfully used during scientific oceanic drilling. However, the temperature measurements at the sediment-basement interface were recorded several days after drilling through the basalts, and they were found to be lower than predicted by heat flow and thermal gradient measurements. *Castillo* [1992] attributed this cooling to the flow of cold seawater or formation fluids into the borehole during the open-hole conditions. The inferred temperature at the sediment-basement interface was then corrected from 26 to 37 ˚C using the Bullard method[1] [*Bullard*, 1947]. The crustal age of Site 765 was estimated to be 140 Ma, based on the oldest recovered sediment, but more recent age analysis using K/Ar on celadonite indicates it is 15 Myr older (155 Ma) [*Gradstein and Ludden*, 1992]. With this age of 155 Ma, the basalt at Site 765 is the oldest basement in the Indian Ocean.

In general, the data collected during these scientific drilling legs show the following: oceanic crustal ages on average older than 100 Ma; average thermal conductivity of ~1.3 W/(m K); bathymetry >5000 m; and sediment thicknesses between ~250 and ~1000 m (Table 3.4).

---

[1] The Bullard method is a technique used to estimate one dimensional, steady-state conductive heat flow in a layered medium, based on the temperature gradient and the summed thermal resistance of a number of depth intervals.

Table 3.4: Summary of drilling results (grey shading) and estimations from the global databases used in this study (yellow shading) for the representative sites of each scientific cruise. Blank spaces indicate not available measurements from cruises. Estimated values that show a significant difference (±20%) from the measurements are underlined.

	CRUISES	DSDP Leg 26		DSDP Leg 27		DSDP Leg 28	ODP Leg 122		ODP Leg 123
	SITES	256	257	260	261	264	759	763	765
Oceanic crustal age	Ma	103	109	129	153				155
		103	109	129	153	103			155
Bathymetry	m	5361	5278	5702	5687	2876	2092	1368	5730
		5268	5013	5677	5642	2821	2590	1350	5713
Deepest penetration	m	270	327	332	580	215	308	1037	1195
Sediment thickness	m	251	262	323	533	171	> 308	> 1037	936
		487	462	266	496	1040	1237	1201	710
Drill depth into basement	m	19	65	9	47	44			259
Sediment thermal conductivity (K_s)	W/(m K)	0.8	0.9				1.0-2.2	1.3-1.8	0.9-1.7
		1							
Basement porosity	%								5
		10							
T at sediment-basement interface	˚C								26 → 37
		28	26	16	27	58	63	61	37

The estimated values of oceanic crustal age (Figure 2.1, from *Müller et al.* [2008]) and bathymetry (Appendix CH2-4, from *IOC et al.* [2003]) are in good agreement with measured values. In contrast, sediment thickness (Appendix CH2-2, from *Divins* [2003]) shows differences of ~200 m, and up to ~900 m in the case of Site 264 (Table 3.4). The NOAA sediment thickness database used in this study [*Divins*, 2003] takes into account i) previously published isopach maps (e.g. *Divins and Rabinowitz* [1990]; *Hayes and LaBrecque* [1991]; *Ludwig and Houtz* [1979]; *Matthias et al.* [1988]), ii) ocean drilling results, and iii) archived seismic reflection profiles. However, the data interpolation is not a perfect process, especially along continental margins. To explore the validity of sediment thickness estimations in this area, the site specific measurements of scientific ocean drilling sites are compared to the scanned Single-Channel Seismic (SCS) reflection profiles collected on cruises of Lamont-Doherty's research vessels Robert D. Conrad (cruise RC1403), and Vema (cruise V2819) [http://www.geomapapp.org] (Figure 3.12). The seismic profiles show major changes in the acoustic basement depth in the space of a few kilometres for sites on or along the continental margin (e.g., Sites 759 and 765, respectively), suggesting that the sediment thickness discrepancies between measurements and estimations are the result of local variability. However, relatively constant sediment thickness observed around Site 260 confirms the validity of global estimations for mid-ocean ridge flanks.

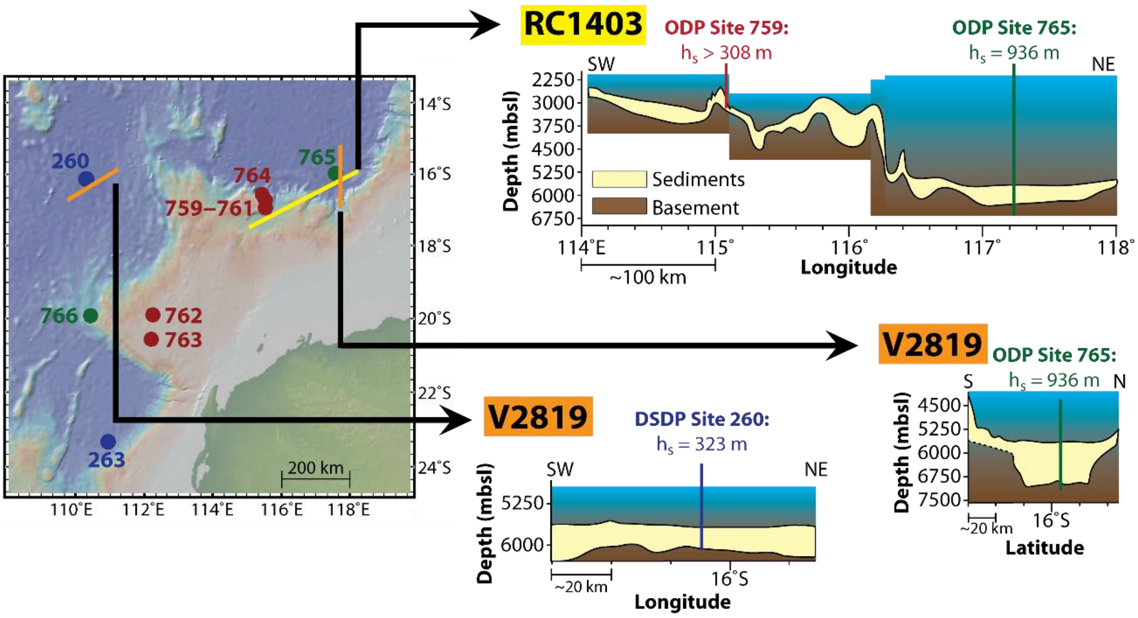

Figure 3.12: Single-Channel Seismic (SCS) reflection profiles RC1403 and ELT45, with correspondent locations on topographic map [modified from http://www.geomapapp.org]. The DSDP-ODP sites are highlighted with colours, and the corresponding measured sediment thickness is indicated as "h_S".

The equilibrium temperature at Site 765 (37 ˚C, Table 3.4) cannot be used in the validation of oceanic crustal age-derived temperature at the sediment-basement interface because it has been computed following the *Bullard method* [*Bullard*, 1947] based on a heat-conduction model, which in turn is at the base of the temperature estimations in this study. However, the temperature estimated with the GDH1 model at

Site 765, using K_s = 1 W/(m K), and interpolating values of sediment thickness, is ~37 ˚C (Table 3.4), in perfect agreement with the equilibrium value proposed by *Castillo* [1992] specifically for this location. The same temperature is calculated despite the ~200 m difference in sediment thickness between model and measurements, due to higher thermal conductivity considered by *Castillo* [1992] (~0.3 W/(m K) higher than GDH1 model).

3.5.2.2. Implications of target a for offshore CCS

*Target **a*** has been defined on the basis of combined gravitational ($\Delta\rho > 0$ kg/m^3) and physical trapping (sediment thickness between 200 and 700 m) (Figure 3.11). Its areal extent is ~1.47x10^6 km^2 (Table 3.2), but the water depth is on average greater than 5000 m, and a very limited part of the target is within 500 km of the Australian coastline. These characteristics make *target **a*** theoretically suitable for geological carbon sequestration, but practically incompatible with current technology and markets that are mostly interested in shallow reservoirs that are easy to monitor and have short transport distances [*Rubin*, 2008]. However, if only gravitational trapping is applied, *target **a*** almost doubles its size, including regions previously excluded because of sediment thicknesses below the 200 m threshold (Figure 3.13). In particular, not too far away from the southern coast of Western Australia, several square kilometres of oceanic crust become available (*target **a1*** in Figure 3.13), with sediment thickness between 100 and 200 m, but still located in deep waters (~5000 m). At these conditions, the liquid CO_2, naturally denser than seawater, would have the tendency to sink within the basement, and be stable with only a thin or absent sediment cover.

The potential carbon sequestration in *target **a***, by CO_2 storage in deep-sea basalts based on gravitational trapping, is not the first project suggesting injections of CO_2 in offshore Australia. The offshore region in NW Australia is an active region of natural gas production. For example, the Gorgon Project (Figure 3.13) is one of the largest natural gas projects ever undertaken in the world. It is located ~200 km from the northwest coast of Western Australia, and includes the injection and storage of CO_2 into a deep sedimentary formation sited 2.3 km below Barrow Island [https://www.chevronaustralia.com/our-businesses/gorgon]. The gas extracted from the Gorgon Field is separated from the naturally occurring reservoir CO_2 (~14%) before being liquefied in a facility capable of producing 15.6 Mt of liquid natural gas (LNG) per year. Liquefying natural gas to -162 ºC has the advantage of decreasing the volume of the gas 600 times, making shipping around the world more economical. The removed CO_2 will be transported via pipeline and injected beneath Barrow Island, migrating through the aquifer until it becomes trapped. According to preliminary estimations, this will reduce greenhouse gas emissions from the project by ~40% [https://www.chevronaustralia.com/our-businesses/gorgon].

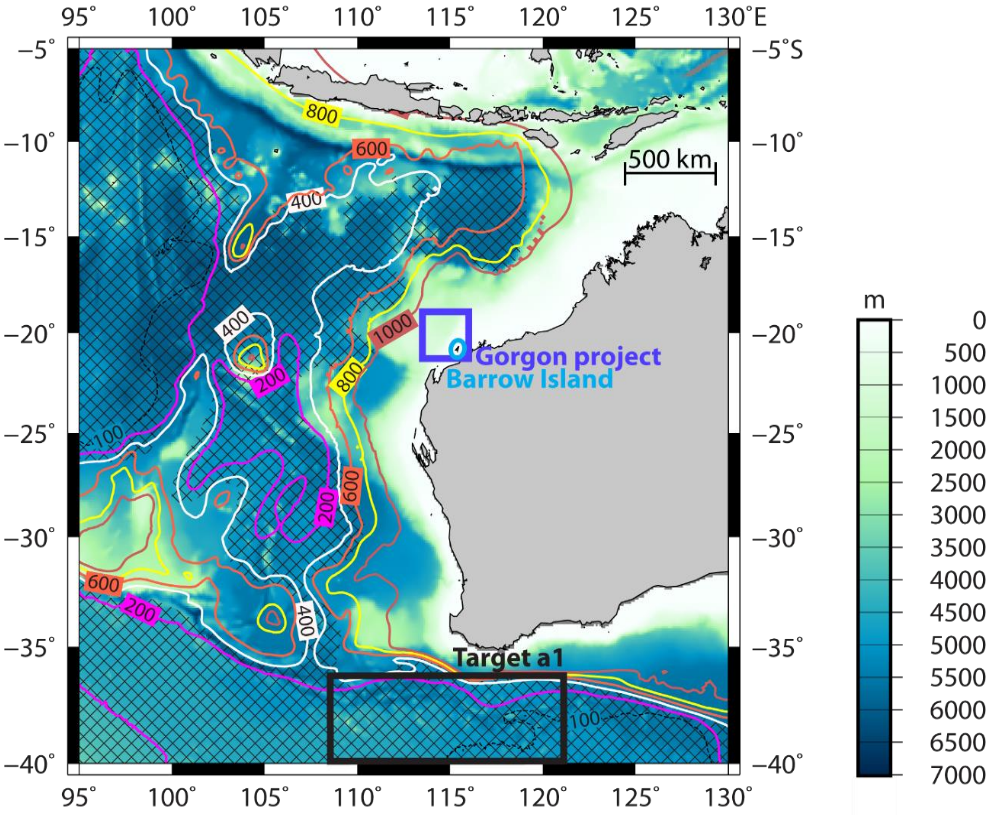

*Figure 3.13: Bathymetric map showing the potential target **a** for CO_2 storage. Suitable locations for gravitational trapping ($\Delta\rho > 0$ kg/m^3) are hatched, and target **a1** is shown in a black box. Sediment thickness is represented by coloured lines every 200 m, whereas the 100 m isoline is shown as a black dashed line. The location of the Gorgon Project is highlighted on the map with a blue square, and the position of Barrow Island with a light blue circle.*

Hence, considering both scenarios of CO_2 storage offshore, *target **a*** and the Gorgon Project, two main questions can be raised:

1) Is the shipping of liquefied gas used in the oil industry a viable options for CO_2 transport to offshore reservoirs?
2) Why has no CO_2 re-injection project been undertaken yet in oceanic crust, where the advantages derived from the presence of *in situ* gravitational trapping, a low-permeability sediment cap, and potentially highly reactive rock can be exploited?

An attempt to address these questions has been made in Chapter 5, analysing the CO_2 costs linked with CCS offshore projects.

3.6. Conclusions

The conceptual storage of carbon dioxide in mafic formations offshore is a mitigation strategy that is still developing.

In this chapter, limitations and constraints on its applicability have been given, considering gravitational and physical trapping in oceanic crust with the use of global databases. The results can be summarised as follows:

- the general carbon sequestration potential of oceanic crust must be evaluated starting from global scale studies on CO_2 stability at the sediment-basement interface, and proceeding towards more local analyses to better understand the relationships between observations at different scales;
- the extent of suitable areas for geological CO_2 sequestration depends on the level of physical and gravitational stability of CO_2 that is implemented in the evaluations;
- ~48% of the oceanic crust at the sediment-basement interface is suitable for gravitational trapping ($\Delta\rho_{CO2\text{-seawater}} > 0$ kg/m^3), and ~32% for physical trapping (sediment thickness between 200 and 700 m);
- the combination of gravitational and physical trapping reduces the oceanic crust suitable for CCS to ~8%; using these criteria, five potential targets have been selected;
- even the smallest identified reservoir could provide sufficient carbon dioxide sequestration capacity for several centuries;
- sites on the Juan de Fuca Plate and in the eastern equatorial Pacific Ocean are unsuitable for gravitational trapping of carbon dioxide because the CO_2 will naturally tend to escape due to the thermal conditions at the sediment-basement interface;
- specific investigations on *target **a*** (Indian Ocean) show the limitation of global scale studies. This highlights the need for detailed programs of local data acquisition (e.g., sediment thickness, heat flow, temperature, thermal conductivity, porosity, and permeability) to further develop the CO_2 trapping potential of this area.

Chapter 4: Low temperature batch dissolution experiments in a CO_2-seawater-rock system

4.1. Introduction

Among the several mitigation strategies proposed to sequester CO_2, *mineral carbonation* is one of the most promising [*Lackner*, 2003; *Seifritz*, 1990; *Sipilä et al.*, 2008]. As described in Chapter 3, mineral carbonation process is a g*eochemical trapping* mechanism, where purified CO_2 and water react with the surrounding rocks to form geologically stable carbonate minerals [*Lackner et al.*, 1995]. This may reduce the likelihood of accidental release and the need for post-storage monitoring [*Hawkins*, 2004; *Rochelle et al.*, 2004]. This mechanism has been found to be particularly efficient (time required <1000 yr) in mafic and ultramafic formations [*Galeczka et al.*, 2014; *Gislason et al.*, 2010; *Kelemen and Matter*, 2008; *Paukert et al.*, 2012; *Schaef et al.*, 2010; *Van Pham et al.*, 2012; *Xu et al.*, 2005]. Rocks rich in calcium and magnesium silicate minerals, such as basalts, can convert CO_2 to carbonate minerals by providing divalent cations, such as Ca^{2+}, Mg^{2+} and Fe^{2+} [*Goldberg*, 1999; *Matter et al.*, 2007].

Several reactions are involved with geochemical trapping in basaltic rocks [*Takahashi et al.*, 2000]. Carbon dioxide dissolves into formation waters through the following acidification reactions:

$$CO_2(aq) + H_2O \rightleftharpoons H_2CO_3 \rightleftharpoons HCO_3{}^- + H^+ \rightleftharpoons CO_3{}^{2-} + 2H^+ \quad (1)$$

The concentration of dissolved CO_2 in solution depends on CO_2 solubility, which in turn is a function of temperature, pressure and salinity of the formation water [*Portier and Rochelle*, 2005]. The products of CO_2 dissociation are bicarbonate (HCO_3^-) and carbonate (CO_3^{2-}) ions (Equation 1), which can precipitate as carbonate minerals if divalent cations are available in solution (Equations 2 and 3).

$$(Ca, Mg, Fe)^{2+} + 2HCO_3{}^{-} \rightleftharpoons (Ca, Mg, Fe)CO_3 + CO_2 + H_2O \quad (2)$$

$$(Ca, Mg, Fe)^{2+} + CO_3{}^{2-} \rightleftharpoons (Ca, Mg, Fe)CO_3 \quad (3)$$

The production of H^+ can be a limiting step in the precipitation of carbonates. Hence, further water-rock interactions are required to consume H^+ ions and drive reactions (1) and (2) to the right [*Matter and Kelemen*, 2009]. The dissolution of calcium plagioclase – anorthite $CaAl_2Si_2O_8$ – (Equation 4) is an example of a forward reaction that consumes hydrogen ions and produces Ca^{2+}:

$$CaAl_2Si_2O_8 + 2H^+ + H_2O \rightleftharpoons Ca^{2+} + Al_2Si_2O_5(OH)_4 \quad (4)$$

Oelkers et al. [2008] investigated the potential of anorthite, as well as other silicate minerals and basaltic glass, as a Ca-source for mineral carbonation. The results, based on mineral stoichiometry, suggest that 23.1 t of Ca-plagioclase are required to sequester a tonne of carbon as calcium carbonate - calcite $CaCO_3$, whereas only 8.76 t of basaltic glass are needed to convert the same amount of carbon in a suite of carbonate minerals (calcite, magnesite $MgCO_3$, and siderite $FeCO_3$).

Analyses of the upper oceanic crust show that interactions between seawater and basalt affect the global carbon budget, fixing dissolved CO_2 as carbonate minerals in rocks and veins at low temperature (<60 ˚C) [*Alt and Teagle*, 1999; *Coogan and Gillis*, 2013; *Coogan et al.*, 2016]. The net annual uptake rate of carbon as a result of oceanic crust alteration is ~1 x 10^{12} mol C yr^{-1}, and varies with oceanic crustal age and location [*Alt and Teagle*, 1999; *Gillis and Coogan*, 2011; *Staudigel et al.*, 1989]. Due to prolonged and extensive faulting, slow-spreading Atlantic crust can store higher quantities of carbonate in young crust, whereas fast-spreading Pacific crust shows a steady increase in carbonate abundance over time [*Rausch*, 2012]. These studies indicate that >80% of the carbonate minerals form during the hydrothermal alteration on the ridge flank within <25 Myr of oceanic crust formation [*Coogan et al.*, 2016; *Harris et al.*, 2014]. This means that, although fast in geological terms, these geochemical reactions proceed very slowly on human time scale. Hence, questions remain about whether the carbonation process can be speeded up, in order to exploit the oceanic crust for CO_2 storage in a relatively short period of time by mineral carbonation.

As shown by *Coogan and Gillis* [2013] comparing Mesozoic (higher atmospheric CO_2 concentration) and Cenozoic (lower atmospheric CO_2 concentration) silicate-carbonate weathering rates, the increase in alkalinity at high CO_2 concentration is due to the breakdown of igneous minerals and the consequent release of cations, which favours carbonate precipitation. In most cases though, silicate dissolution rates are slower than the corresponding carbonate precipitation rates, so accelerating the dissolution of silicate minerals is the key to optimize the mineralisation [*Oelkers et al.*, 2008].

Mineral dissolution rates in mafic and ultramafic rocks are enhanced by increasing the reactive surface area of the rock by grinding the material, by increasing temperature, and by adding acids and bases (such as H_2SO_4, HNO_3, NaOH, and $NaHCO_3$) [*Anbeek*, 1992; *Blum and Lasaga*, 1988; *Grandstaff*, 1978; *O'Connor et al.*, 2000; *Oelkers*, 2001a; *Teir et al.*, 2007]. Over the last two decades, a number of experiments have provided better understanding of the chemical processes controlling the dissolution of mafic and ultramafic rocks in CO_2-rich solutions, and in far-from equilibrium solutions. Particularly, experimental approaches include studies on crystalline basalt and basaltic glass at low temperature (25 – 75 ˚C) [*Galeczka et al.*, 2014; *Gislason and Oelkers*, 2003; *Gudbrandsson et al.*, 2011; *Gysi and Stefánsson*, 2012c; *Oelkers and Gislason*, 2001], and at high temperature (75 -250 ˚C) [*Gysi and Stefánsson*, 2012a; b]; on metabasalt [*Critelli et al.*, 2014]; on peridotite [*Andreani et al.*, 2009]; and on both basalt and peridotite in the presence of seawater [*Wolff-Boenisch et al.*, 2011]. More information on these experiments are provided in Table 4.1. In general, based on measurements of silicon release rates, it has been observed that under specific conditions (e.g., pH, pCO_2, and temperature) basalt dissolution rates may be nearly as high as those for peridotite [*Matter and Kelemen*, 2009; *Wolff-Boenisch et al.*, 2011] (Table 4.2).

Table 4.1: Summary of the experiments on mafic and ultramafic rocks carried out in the last two decades to investigate the rock dissolution potential.

	Reactor setup	Rock	Initial conditions			
			T ˚C	pCO_2 bar	pH	Solution
Andreani et al. [2009]	[a]flow-through	sintered peridotite	160	110	6.7	$H_2O + HCl + CO_2 + NaHCO_3$
Critelli et al. [2014]	[b]mixed flow	metabasalt	25	-	2-12	$H_2O + HCl + NaCl + NaOH$
Galeczka et al. [2014]	[a]flow-through	basaltic glass	22, 50	$10^{-5.7}$, 22	6.7	$H_2O + CO_2$
Gislason and Oelkers [2003]	[b]mixed flow	basaltic glass	6-150	-	2-11	$H_2O \pm HCl \pm NH_4Cl \pm NH_3$
Gudbrandsson et al. [2011]	[b]mixed flow	crystalline basalt	5-75	-	2-11	$H_2O \pm HCl \pm NH_4OH \pm NH_4Cl$
Gysi and Stefansson [2012]a,c	[c]mixed batch	basaltic glass	75-250	11-24	4.5-5.9	Vellankatla spring + CO_2
Gysi and Stefansson [2012]b	[c]mixed batch	basaltic glass	40	1-13	3.6-4.5	Vellankatla spring + CO_2
Oelkers and Gislason [2001]	[b]mixed flow	basaltic glass	25	-	3-11	$H_2O + HCl + NaOH + C_2H_2O_4 + AlCl_3$
Wolff-Boenisch et al. [2011]	[b]mixed flow	basaltic glass, crystalline basalt, peridotite	25	4	3.6	Seawater + CO_2

[a]flow-through: the solution passes through the reactor, and gets progressively discharged;
[b]mixed flow: the solution flows into the reactor, is mixed with a stirrer, and leaves the reactor;
[c]mixed batch: the solution is present from the beginning in the reactor, and is mixed with a stirrer.

Table 4.2: Summary of previous experimental results on rock dissolution potential, described as maximum silicon release rates, normalised to surface area. Experimental conditions are also shown.

	Rock	T ˚C	pCO_2 bar	pH	Surface area analysis	Si release rate log (mol/cm^2/s)
Critelli et al. [2014]	metabasalt	25	-	2-12	BET	from -14.3 to -15.9
Galeczka et al. [2014]	basaltic glass	50	22	4.4	geo	-13.2
Gislason and Oelkers [2003]	basaltic glass	50	-	2	BET, geo	-10
Gudbrandsson et al. [2011]	crystalline basalt	75	-	10.96	BET	-13.3
Oelkers and Gislason [2001]	basaltic glass	25	-	3	BET	-12.5
Wolff-Boenisch et al. [2011]	basaltic glass	25	4	3.76	geo	-12.42
	crystalline basalt	25	4	3.76	geo	-12.14
	peridotite	25	4	3.76	geo	-11.65

However, many of the uncertainties related to the CO_2-water-rock interactions are still under investigation; for example:

- Which mafic to ultramafic rocks provide the best physical and geochemical conditions for CO_2 sequestration?
- Is there any difference in reactivity between offshore and onshore basalts, and ophiolitic rocks?
- How complete and comparable are dissolution rate results obtained from different experiments?
- What are the implications related to the use of complex crystalline rocks during CO_2-experiments instead of mono-mineral or homogeneous (basaltic glass) materials?

In this chapter, primary rock dissolution rates and key reactions associated with CO_2 geochemical trapping in mafic rocks are investigated through batch dissolution experiments in a CO_2-seawater-rock system at CO_2 partial pressure (pCO_2) of ~1 bar and 40 ˚C. This temperature has been chosen because it is typical of ridge flank conditions for low temperature hydrothermal alteration, and comparable with other studies conducted on basalt in presence of seawater [*Crovisier et al.*, 1987; *Seyfried and Mottl*, 1982; *Wolff-Boenisch et al.*, 2011]. A major difference between this study and previous studies of CO_2-water–rock interactions is the nature of the experimental material. For the first time, rocks from the upper oceanic crust and ophiolitic rocks have been used in CO_2-mineral dissolution experiments.

4.2. Material and methods

4.2.1. Starting material

Reactive fluid

The seawater used in the experiments (CaribSea Inc) has a salinity of ~35 psu, and the composition is in agreement with IAPSO (International Association for the Physical Sciences of the Oceans) seawater [*Millero et al.*, 2008; *Summerhayes and Thorpe*, 1996]

(Table 4.3). It was stored at 4 ˚C in the dark and warmed up to room temperature overnight prior to its use in the experiments.

pH was measured with a semi micro plastic BNC electrode (Fisherbrand^{TM}), connected to a pH meter (Accumet AB 15/15+, Fisher Scientific^{TM}). The electrode accuracy was calibrated against standard buffer solutions, with a standard deviation of 0.03 pH units.

Total Alkalinity (TA) was determined with the Gran function using a modified titration methodology for a small-volume system (Appendix "*Methods*" CH4-1) [*Haraldsson et al.*, 1997].

Dissolved Inorganic Carbon (DIC) was calculated with the following equation:

$$DIC = \frac{Ac([H^+]^2/K_1 + [H^+] + K_2)}{[H^+] + 2K_2} \tag{5}$$

with $[H^+]$ derived from pH, Ac (carbon Alkalinity) assumed equal to TA, and the dissociation constants $K_1 = 1.89 \times 10^{-6}$ and $K_2 = 1.85 \times 10^{-9}$ estimated for T = 40 ℃, pCO_2 ~1 bar, and S = 35 psu, using the database available in *Millero et al.* [2006].

The Si, Na, Mg, Ca, K, and S concentrations in seawater were measured by inductively coupled plasma optical emission spectrometry (ICP–OES, Perkin-Elmer Optima 4300 DV). Fe was not measured due to potential issues with contamination from the stainless steel bubbler (see Section 4.2.3). The reproducibility of the ICP–OES analyses, determined by replicate analysis of the same sample is better than ± 3% for all elements. A detailed explanation on the preparation of samples and standards for ICP-OES analysis can be found in Appendix "*Methods*" CH4-2. Concentrations of SO_4 and Cl were measured by ion chromatography (IC, Dionex ICS2500). Repeat analysis of IAPSO seawater as well as single anion standards indicates that the reproducibility of the Cl and sulphate analyses is better than ±3%. A detailed explanation on the preparation of samples and standards for IC analysis can be found in Appendix "*Methods*" CH4-3.

Table 4.3: Chemical composition of the starting solution for the experimental work. Values are given in mmol/L.

	pH / ˚C	TA	DIC	Si	Na	Mg	Ca	K	S	SO_4	Cl
IAPSO reference*	8.10 / 20	2.30	1.94	0.10	469	53.1	10.3	10.2	28.2	28.2	546
IAPSO measured	7.66 / 20	2.38	2.23	0.11	468	52.6	10.5	10.0	28.1	27.5	555
SEAWATER measured	7.46 / 20	2.43	2.36	0.02	469	50.6	10.5	10.1	28.7	28.5	565

** from Summerhayes and Thorpe [1996], and Millero et al. [2008]*

Rocks

The rocks used in this study are mid-ocean ridge basalts from the Juan de Fuca and Mid-Atlantic Ridges, and a gabbro from the Troodos ophiolite in Cyprus. The mineralogy was determined by optical microscopy of polished thin sections (data summarised in Table 4.4), and confirmed by scanning electron microscope (SEM) analyses (Leo 1450VP SEM combined with Oxford Instruments X-Act 10mm^2 area SDD EDS Detector). Also, elemental line scans and mineral phase mapping were determined using the AZtec Energy software package connected to the SEM instrumentation. Percentages of phase concentrations are relative to the mapped area, which is ~10% of the whole thin section, and do not always reflect the actual volume of mineral in thin section, especially with cryptocrystalline texture. On the other hand, the maps provide SEM-EDS analyses of each phase present in the rock. Full SEM-EDS analysis results can be found in Appendix "*Analyses*" CH4-6.

The **Juan de Fuca** (JdF) samples consist of forty crystalline basalts collected during the scientific cruise *IODP Exp 327* from the *Hole U1362A*. They are heterogeneous multi-mineral solids that consist on average of 38 vol% labradoritic plagioclase, 23 vol% augitic clinopyroxene, 14 vol% mesostasis, 15 vol% secondary minerals, with minor olivine, iron oxides, and glass. The secondary mineralogy is composed of saponite, celadonite, oxides, and, if present, ~1 vol% calcite (Table 4.4). This suite is typical of low temperature hydrothermal alteration, and is mainly associated with groundmass replacement, vesicle fill, and alteration halos [*Fisher et al.*, 2011]. Due to the small volume of individual specimen (~12 cm^3 each), they were combined together to form three composite samples, on the basis of textural differences and composition. These composite samples, corresponding to cryptocrystalline, microcrystalline, and fine grained basalts, are identified as “JdF mix 1”, JdF mix 2”, and “JdF mix 3”, respectively. The complete list of samples and corresponding images, divided by textural group, is available in Appendix “*Samples*” CH4-13.

Table 4.4: Mineralogical composition of the MOR basalts (JdF mix 1, 2, 3, and CD80WP132) and ophiolitic gabbro (G1). The terminology definitions can be found in Appendix “Methods” CH4-4.

	JDF MIX 1	**JDF MIX 2**	**JDF MIX 3**	**CD80WP132**	**G1**
SAMPLING METHOD	drilling	drilling	drilling	dredging	fieldwork
LITHOLOGY	MOR basalt	MOR basalt	MOR basalt	MOR basalt	ophiolitic gabbro
GRAIN SIZE	cryptocrystalline[a]	microcrystalline[b]	microcrystalline[b] / fine[c]	cryptocrystalline[a]	medium[d]
TEXTURE	Intersertal glomeroporphyriticvariolitic	Intergranular glomeroporphyritic variolitic	Intergranular subophitic	Intersertal glomeroporphyritic vesicular	intergranular granoblastic
PRIMARY MINERALOGY %	**84**	**80**	**78**	**85**	**42**
PHENOCRYSTS %	19	15	6	35	-
Plagioclase-labrodorite	14	11	4	20	-
Pyroxene-augite	4	4	2	12	-
Olivine	1	trace	<1	3	-
GROUNDMASS %	65	65	72	50	42
Plagioclase-labradorite	28	30	28	11	-
Plagioclase-anorthite	-	-	-	-	40
Pyroxene-augite	19	20	20	5	2
Mesostasis	16	10	17	11	-
Opaques	2	5	5	-	-
Olivine	-	trace	-	3	-
Glass	-	-	2	20	-
SECONDARY MINERALOGY %	**13**	**13**	**19**	**<1**	**58**
Saponite	8	8	10	-	-
Celadonite	2	1	6	-	-
Oxides	3	3	3	<1	-
Calcite	1	1	-	-	-
Amphibole-actinolite	-	-	-	-	40
Plagioclase-albite	-	-	-	-	13
Chlorite	-	-	-	-	3
Talc	-	-	-	-	2
VESICLES MINERALOGY %	**4**	**7**	**3**	**15**	**-**
Minerals	celadonite, saponite, oxides	celadonite, saponite, oxides	celadonite, saponite, oxides	-	-
Filled	70%	60%	60%	<1%	-

[a] cryptocrystalline: crystals <0.1 mm; [b] microcrystalline: 0.1 mm < crystals < 0.2 mm; [c] fine grained: 0.2 mm < crystals < 1 mm; [d] medium grained: 1 mm < crystals < 5 mm.

The pillow basalt from the **Mid-Atlantic Ridge** (MAR) was dredged from the Reykjanes Ridge, SW of Iceland, during the *RRS Charles Darwin Cruise 80*, specifically at the *Way*

Point 132 (28.66˚W, 60.54˚N), and was provided for this study by Dr. Bramley J. Murton (*National Oceanography Centre, Southampton*). Mineralogically, the sample is a cryptocrystalline vesicular basalt consisting of 31 vol% labradoritic plagioclase, 20 vol% glass, 17 vol% augitic clinopyroxene, 11 vol% mesostasis, 6 vol% olivine, <1 vol% secondary minerals, and 15 vol% unfilled vesicles (Table 4.4). From now on, the MAR basalt is called "CD80132WP" (image available in Appendix "*Samples*" CH4-14).

The gabbro from the **Troodos ophiolite** (Cyprus) was sampled by Prof. Damon A.H. Teagle during a fieldwork in May 2014, close to the village of Kato Amiandos (32.93˚E, 34.93˚N). The rock shows a high degree of hydrothermal alteration, with mineralogy consisting of 40 vol% anorthitic plagioclase, 40 vol% actinolitic amphibole (replacing clinopyroxene), 13 vol% albitic plagioclase, 3 vol% chlorite, 2 vol% augitic clinopyroxene, and 2 vol% talc (Table 4.4). From now on, the Troodos gabbro will be called "G1" (image available in Appendix "*Samples*" CH4-15).

All solids were ground to obtain the 63 – 125 µm size fraction (Section 4.2.2.). The composition of 63-125 µm and <63 µm size fractions, were determined for each rock by inductively coupled plasma mass spectrometry (ICP-MS, Thermo Scientific X-Series 2), and X-ray diffraction (XRD) (Appendices "*Analyses*" CH4-7, and -8, respectively). A detailed description of the methodology used for ICP-MS analysis is available in Appendix "*Methods*" CH4-5. Furthermore, chemical analyses with X-ray fluorescence spectroscopy (XRF) were run at the University of St. Andrews (Scotland, UK), and are here summarised in Table 4.5 for 63-125 µm and <63 µm size fractions. The complete list of XRF analyses, with major and trace elements for both 63-125 µm and <63 µm size fractions, is available in Appendix "*Analyses*" CH4-9. The rock compositions in this study are considered from the XRF analyses, which show better accuracy and precision then ICP-MS analyses (Appendix "*Analyses*" CH4-9, and "*Methods*" CH4-5, respectively).

In general, rock compositions are similar to that of mid ocean ridge basalt – MORB – summarised by *GERM* [2000], as confirmed by ICP-MS analyses. No major differences are found between the two size fractions. Loss on ignition (LOI) is the percentage weight lost on sample ignition, due to the loss of volatile phases (for example H_2O, CO_2 and S) that may in part be compensated by a gain in mass due to oxidation of Fe^{2+} to Fe^{3+}. However, the dominant control on LOI is the concentration of water, which increases as a result of hydration of primary minerals during alteration. This effect is superimposed on the primary water content of the rocks compared to typical MORB (<0.2 wt% or less) [*Danyushevsky*, 2001]. In general, the LOI is <3% for all the samples.

Table 4.5: Summary of rock chemical compositions for 63-125 µm and <63 µm size fractions, expressed in percent (data from XRF analyses). Negative values are most probably due to gain in mass due to oxidation of Fe^{2+} to Fe^{3+}.

ID	**JdF mix 1**		**JdF mix 2**		**JdF mix 3**		**CD80WP132**		**G1**	
%	63-125 µm	<63 µm	63-125 µm	<63 µm	63-125 µm	<63 µm	63-125 µm	<63 µm	63-125 µm	<63 µm
SiO_2	49.6	48.3	48.6	49.6	50.1	49.6	49.0	50.9	44.9	47.4
TiO_2	1.93	2.03	1.66	1.60	1.70	1.95	1.24	1.05	0.0928	0.103
Al_2O_3	13.6	13.3	13.7	14.3	13.7	14.2	12.5	13.7	17.2	14.4
Fe_2O_3	11.7	12.4	11.2	10.6	11.6	12.2	14.5	12.6	5.54	6.44
MnO	0.233	0.237	0.200	0.190	0.200	0.208	0.222	0.190	0.109	0.126
MgO	6.47	6.82	7.40	7.18	6.79	6.35	7.65	7.57	11.1	13.2
CaO	12.4	12.9	13.9	13.4	12.9	12.8	12.9	12.3	17.1	14.1
Na_2O	2.35	2.20	2.15	2.09	2.12	2.05	1.70	1.51	0.949	1.08
K_2O	0.204	0.210	0.117	0.111	0.179	0.135	0.0248	0.0238	0.0426	0.0517
P_2O_5	0.149	0.118	0.0739	0.0493	0.0589	0.0555	0.0539	0.0597	<0.0110	<0.0110
SO_3	0.102	0.0977	0.133	0.135	0.0780	0.110	0.244	0.212	<0.0300	<0.0300
LOI	1.33	1.33	0.930	0.690	0.580	0.350	-0.180	-0.380	2.70	2.90
TOT	100	100	100	100	100	100	99.8	99.6	99.7	99.6

4.2.2. Sample preparation

Most studies on mineral dissolution and carbon sequestration have been performed on finely ground samples, in order to achieve measurable results within a laboratory-scale time frame [*Galeczka et al.*, 2014; *Harrison et al.*, 2012; *Oelkers and Gislason*, 2001; *Rosenbauer et al.*, 2012; *Shibuya et al.*, 2013]. *Gadikota et al.* [2014b] described in detail a sample preparation protocol, highlighting the importance of accurate particle size characterisation, and the implications of smaller particles in the samples. The presence of very fine particles increases the reactive surface area and extent of dissolution, giving false mineral reaction rates that cannot be compared to literature values. Hence, the current study attempted to utilise freshly ground rocks, which were ground following a multistep cleaning protocol, and provides a detailed physical description of the particles.

All the samples were ultrasonically cleaned and dried overnight at 60 ˚C, before being crushed with a laboratory ring mill (Rocklabs®) to reach a *fine sand* size fraction. To constrain the particle size between 63 and 125 µm and remove most of the fine particles produced during the grinding phase, a modified version of the cleaning procedure proposed by *Gadikota et al.* [2014b] was followed. The ground material was sieved using two stainless steel sieves of 63 and 125 µm, respectively (*dry sieving 1*), and cleaned in batches of 25 g. The 63-125 µm subsample obtained was then placed in the 63 µm sieve, previously positioned within a beaker, covered by deionized (DI) water, and cleaned ultrasonically for 5 minutes. At the end of the ultrasonication, the fine particles in suspension were removed and the sample still contained in the 63 µm sieve was flushed with DI water (*wet sieving*). This cycle of "ultrasonic bath-wet sieving" was repeated until no fine particles were observed. The final 63-125 µm sample was dried on a flat glass dish at 60℃ overnight in a vacuum oven, to eliminate reaction between the cleaned minerals and air. A second dry sieving step at 63 µm was carried out (*dry sieving 2*) to ensure that no fine particles were still trapped in the sample. Once declared "fine particle-free", the sample was weighed and stored in an amber glass bottle, which, in turn, was placed within a plastic bag to avoid any oxidation due to air contact.

The material loss for this type of cleaning procedure is quite high (~70%), because ~300 g of initial sample are needed to obtain ~80 g with a grain size fraction between 63 and 125 µm. This is a consideration to take into account in the selection of the starting material. Among all the samples used in this investigation, the ones from dredging (CD80WP132) and fieldwork (G1) were relatively easier to collect in big quantities (>1 kg) and no problem due to the loss of material emerged during the preparation. On the other hand, every specimen from oceanic crust drilling (JdF) was at least two orders of magnitude smaller (~30 g each) than the other rocks, resulting in a significant sample loss. Also, in the powdered oceanic core samples, a higher abundance of fine particles (<10 μm) was observed, most probably due to the presence of secondary minerals, such as clays, which have a lower hardness than basaltic glass. Hence, the JdF specimens were prepared taking into account the composition, and acknowledging the presence of fine particles.

In light of these technical difficulties, the ground material (63-125 μm) was subjected to multiple physical analyses, specifically to constrain the grain size and morphology.

The Brunauer-Emmett-Teller (BET) multipoint technique (Quantachrome NovaWin BET Analyzer via nitrogen, Columbia University in the City of New York, USA) was used to determine the surface areas of the rock samples. Resulting BET surface areas (A_{BET}) are listed in Table 4.6, together with the corresponding specific geometric surface areas (A_{geo}) that were calculated assuming the grains are spherical (Equation 6):

$$A_{geo} = \frac{6}{(d \times \rho)} \tag{6}$$

where A is the total area (cm^2/g), d the average particle diameter (cm), and ρ the density (g/cm^3) [*Cubillas et al.*, 2005; *Gautier et al.*, 2001; *Guy and Schott*, 1988; *Wolff-Boenisch et al.*, 2004].

Table 4.6: Surface areas measured with BET (A_{BET}) and geometrically calculated (A_{geo}) for each of the five samples. Volumetric weighted means used as particle diameter averages in the A_{geo} calculations are shown. Density is assumed to be 2.9 g/cm^3 for all the samples.

	A_{BET} [cm^2/g]	A_{geo} [cm^2/g]	Volumetric weighted mean of particles [μm]
JdF mix 1	57240	406	51
JdF mix 2	123420	489	42
JdF mix 3	8760	781	27
CD80WP132	22140	188	110
G1	12670	191	108

In a theoretical sample, ground to the size fraction 63-125 µm, with 94 µm as particle diameter mean and density of 2.9 g/cm^3, the total geometrical surface area is 220 cm^2/g. However, the abundance of clay and silt sized particles in the sample affects the average particle diameter and in turn the A_{geo}, which has to be defined sample by sample through more detailed analyses. Hence, grain size distribution (GSD) and relative particle diameter average were measured for each of the five samples using a Malvern Mastersize analyser (University of Southampton, UK) after shaking the samples overnight in a 0.05% Calgon solution to disaggregate the grains. GSD results are shown in Figure 4.1, whereas the volumetric weighted means used for A_{geo} calculations are reported in Table 4.6. Polished thin sections (PTS), and stubs were prepared for all the ground samples (63-125 µm) to further investigate and confirm the particle size distribution, composition and morphology by scanning electron microscopy (Leo 1450VP SEM combined with Oxford Instruments X-Act 10mm^2 area SDD EDS Detector) (Figure 4.2). Complete SEM analyses on ground samples, including EDS and elemental mapping data, are available in Appendices "*Analyses*" CH4-10, and -11, respectively.

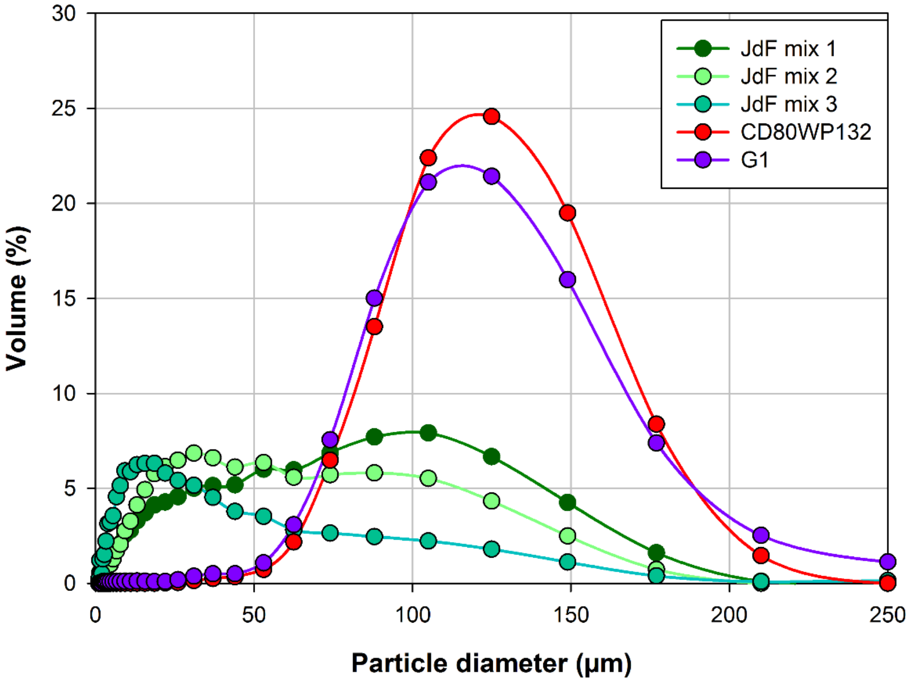

Figure 4.1: Grain size distribution (GSD) for all the ground samples (63-125 µm) before the dissolution experiments.

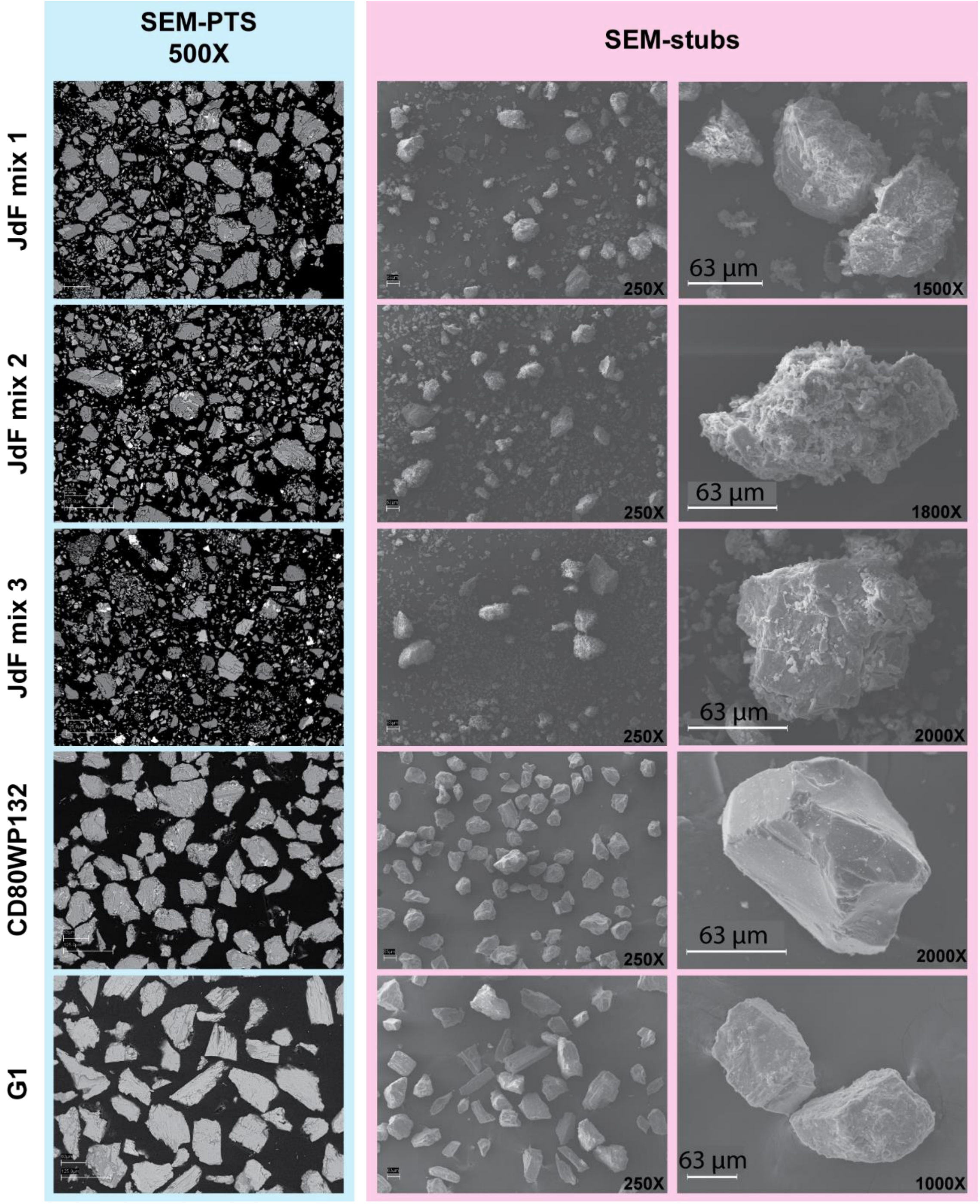

Figure 4.2: SEM images from PTS-polished thin sections (on the left, in the light blue box), and from stubs (on the right, in the pink box). The magnification for the PTS images is of 500X for all the samples, whereas the magnification for the stubs is indicated on each image.

4.2.3. Experimental setup

The same experimental design was adopted in eight batch type experiments to determine the dissolution reaction rate of the three different rocks: JdF, CD80WP132, and G1. Based on the solid mass used in each experiments, three subseries can be identified: 80, 65, and 30 g. A schematic representation of all the performed experiments is shown in (Figure 4.3). The subseries of 80 g represents the standard initial rock mass following the method proposed by *Gysi and Stefánsson* [2012c] for moderate CO_2 concentrations, and involves five experiments: JdF mix 1, JdF mix 2, JdF mix 3, CD80WP132-A (a subsample of CD80WP132), and G1-A (a subsample of G1). The subseries of 65 g (JdF mix 2bis, CD80WP132-Abis) and 30 g (CD80WP132-B, subsample of CD80WP132) were run to better quantify the role of reactive surface area and fine particles during dissolution. Both JdF mix 2bis and CD80WP132-Abis experiments were performed on samples that had been previously used in the 80 g experiments (JdF mix 2 and CD80WP132-A, respectively), to further investigate the reactivity of these rocks in progressive dissolution experiments.

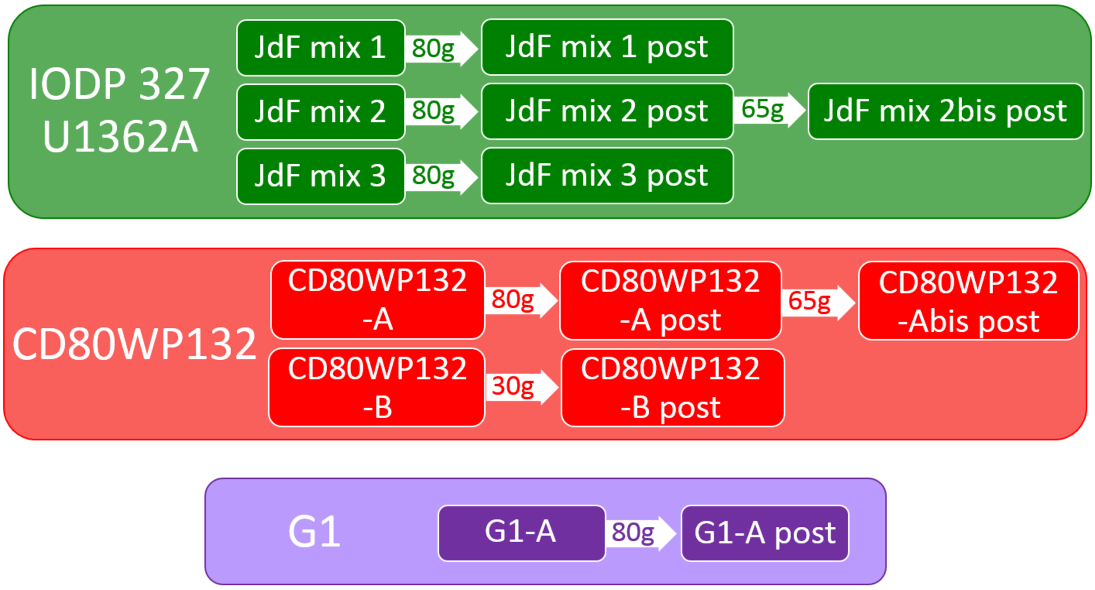

Figure 4.3: Summary of eight batch type experiments on three type of rocks: JdF (in green), CD80WP132 (in red), and G1 (in purple).

Several runs, lasting in total from 11 to 24 days, were carried out at 40℃ and pCO_2 ~1 bar, in a three-phase system, consisting of oceanic rocks, seawater and gaseous CO_2 in the headspace. The overall design is shown in Figure 4.4. Table 4.7 provides further details about the initial settings of each experiment.

For each run, 4 fluorinated HDPE 1000 mL bottles were positioned in a 25 L stainless steel water bath (MEDLINE BS-11). Each bottle was sealed with a Ley Rubber Ltd RB049/1H stopper with 4 holes: two of them for the inward and outward CO_2 flux, respectively; one for the pH electrode (Fisherbrand^{TM}); and the last one served as a sampling port. In each bottle, 500 ± 10 mL of seawater (CaribSea Inc) were added and warmed to 40℃. Once the temperature was reached, the CO_2 cylinder (BOC 270008-J, 50 L) was opened to start saturating the seawater with respect to CO_2. The pressure was regulated by a BOC Laboratory Series 8500 Multi-stage regulator (with maximum outlet pressure of 2 bar) at 0.25 bar. The CO_2 flux into each reaction bottle was regulated by a gas flowmeter (Cole-Parmer® Brass fittings, 1.2 LPM Air), and singularly controlled with gas valves (Swagelok®) positioned on the four gas lines. The CO_2 injection rate was set at 0.2-0.4 L/min. To homogeneously disperse the CO_2 (g) within the seawater, a stainless steel bubbler (0.5 µm pores) was positioned at the end of each gas line. A progressive oxidation process was observed on the bubbler, raising concerns about the measurements of Fe in solution (i.e. additional dissolved Fe in solution), and required a careful cleaning after each run.

The saturation process was monitored through pH measurements, using an electrode (Fisherbrand^{TM}) connected to a pH meter (accumet™ AB15+, Fisher Scientific™). The electrode was calibrated before each sample was taken using commercial buffer solutions, and stored in a KCl solution (Fisher Chemical). Once seawater reached saturation with respect to dissolved CO_2 (1-3 days from the beginning of the experiments), 80 to 30 g of ground rock was added to each of the 3 bottles. The fourth bottle was left with CO_2-saturated seawater but without any rock, in order to have a reference chemical composition throughout the duration of the experiments. After each run, bottles, tubing, and other materials used in the experiments were cleaned with 10% HNO_3 and then rinsed with DI water.

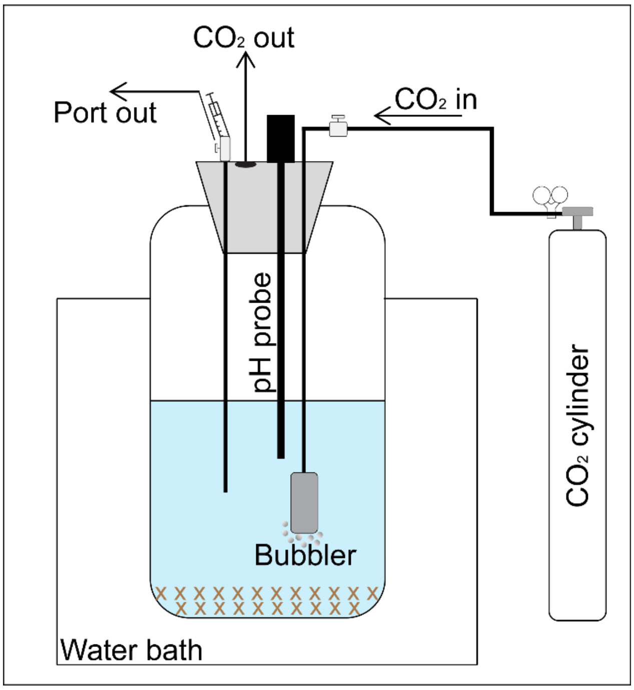

Figure 4.4: Experimental setup for the CO_2-seawater-oceanic rock dissolution experiments. The brown crosses at the bottom of the HDPE bottle represent the ground sample.

Table 4.7: Summary of the initial conditions for the CO_2-seawater-oceanic rock dissolution experiments. The reference solutions without any sample are the "Blank", and are shown at the top of each run.

		Initial conditions						**Saturated conditions**				
	Total Duration	**T**	**pH**	**TA**	**DIC**	**pCO_2**	**Saturation**	**T**	**pH**	**TA**	**DIC**	**pCO_2**
Sample	[days]	[℃]		[mM]	[mM]	[x10^{-3} bar]	[days]	[℃]		[mM]	[mM]	[bar]
Blank 2	11	13.5	7.35	2.51	2.47	1.93	1	40	4.62	2.83	38.75	1.76
JdF mix 1	11	13.5	7.35	2.51	2.47	1.93	1	40	4.63	2.66	35.54	1.62
JdF mix 2	11	13.5	7.35	2.51	2.47	1.93	1	40	4.62	2.58	35.29	1.60
JdF mix 3	11	13.5	7.35	2.51	2.47	1.93	1	40	4.67	2.95	36.32	1.63
Blank 3	24	16.2	7.69	2.46	2.17	7.47	3	40	4.79	2.91	27.84	1.22
CD80WP132-A	23	16.2	7.69	2.32	2.17	7.47	2	40	4.81	2.83	26.01	1.13
G1	24	16.2	7.69	2.32	2.17	7.47	3	40	4.86	3.10	25.67	1.10
Blank 4	13	15	7.64	2.46	2.32	9.05	3	40	4.74	3.05	32.39	1.43
JdF mix 2bis	13	15	7.64	2.46	2.32	9.05	3	40	4.78	2.98	29.12	1.28
CD80WP132-Abis	13	15	7.64	2.46	2.32	9.05	3	40	4.76	2.80	29.13	1.29
CD80WP132-B	13	15	7.64	2.46	2.32	9.05	3	40	4.77	2.97	29.63	1.30

Fluid samples were regularly taken out directly from each bottle, opening the sampling ports one at the time, temporarily closing the CO_2 gas line, and using a fresh syringe for each sample. For each sampling, 1 mL of solution was taken out: 0.5 mL was immediately analysed for pH and alkalinity (Appendix "*Methods*" CH4-1), whereas the other 0.5 mL was kept in the refrigerator for ICP-OES and IC analyses (Appendix "*Methods*" CH4-2, and -3, respectively). To preserve the major cation content (Ca, K, Mg, Na, S, Si, and Sr) in the ICP-OES samples, a drop of SB conc. HNO_3 was added. DIC was calculated from each couple of alkalinity and pH measurements, as described in Equation 5. The corresponding pCO_2 was calculated using Henry's Law for CO_2 solubility in water (Equation 7):

$$[CO_2] = K_0 * pCO_2 \tag{7}$$

where $[CO_2]$ is the aqueous CO_2 concentration in mol/L, and K_0 is Henry's constant. The aqueous CO_2 concentration was calculated from carbon alkalinity (Ac) as follows:

$$[CO_2] = \frac{A_c}{(K_1/[H^+] + 2 * K_1 * K_2/[H^+])} \tag{8}$$

To determine K_0 at room temperature and 40 ˚C, the following expression proposed by *Weiss* [1974] was used:

$$\begin{aligned} lnK_0 = 9345.17/T - 60.2409 + 23.3585\ln(T/100) + S[0.023517 \\ - 0.0023656T + 0.0047036(T/100)^2] \end{aligned} \tag{9}$$

where T is the temperature in Kelvin, and S is the salinity (35 psu).

Considering the initial seawater volume of 500 ± 15 mL, and an average total sampling volume of 12 mL, the original rock/water ratio was not significantly modified.

4.3. Results

4.3.1. Fluid chemistry

The variations in solution chemistry (pH, alkalinity, and DIC) as a function of time are illustrated in Figure 4.5. All the experiments show similar composition trends. The compositions of reference seawater solutions (blanks 2, 3, and 4) demonstrate how saturation conditions were reached at pH ~4.8, and alkalinity ~3.3 mmol/L, with a slight oversaturation during the first day of experiment highlighted by the calculated DIC. In general, dissolved CO_2 concentrations were <40 mmol/L (Figure 4.5). Experiments utilising rocks show a rapid increase in pH and alkalinity during the first five days, from initial values of 4.6 and ~2.5 mmol/L, respectively, to the maximum of 5.2 and ~5.0 mmol/L, respectively (Figure 4.5).

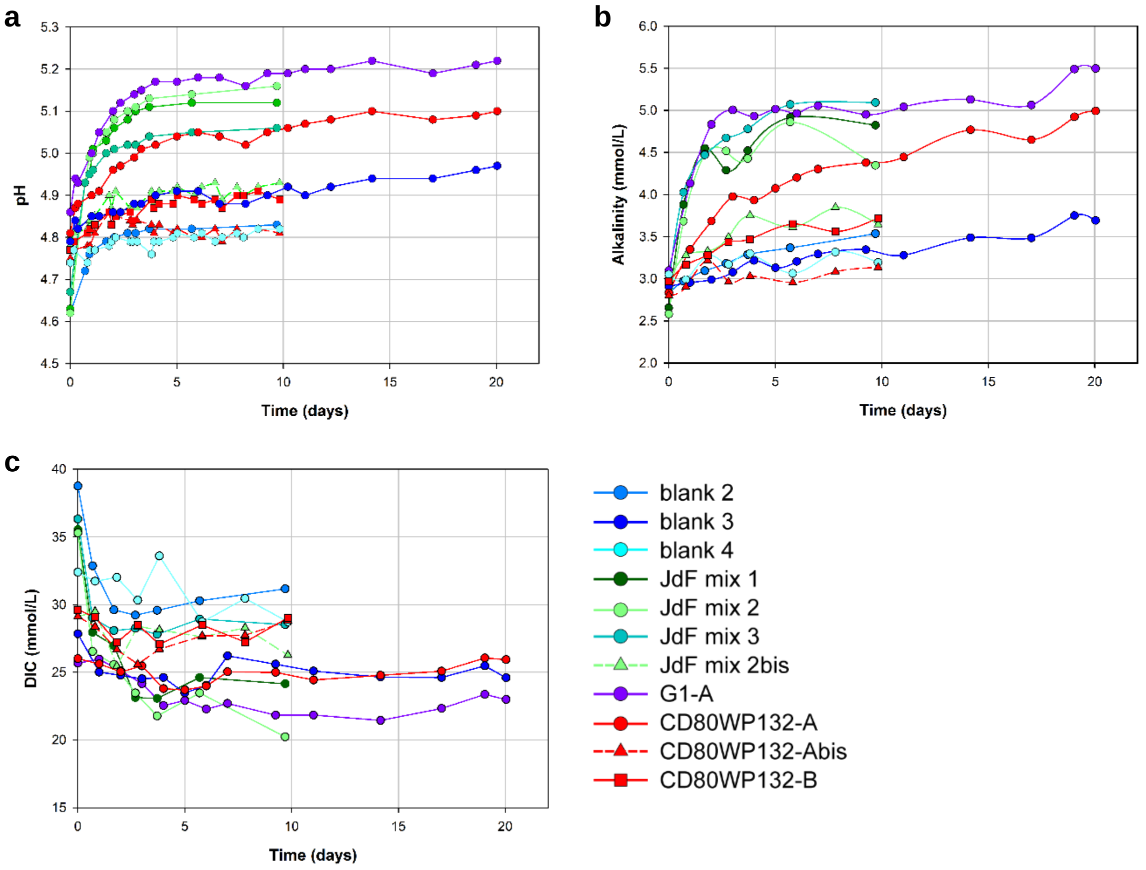

*Figure 4.5: pH (**a**), alkalinity (**b**) and DIC (**c**) trends throughout all the duration of the experiments. For each run, the first output refers to the measurement taken at time "zero", just before adding the solid sample, when the seawater is CO_2-saturated. All the reference solutions are shown in blue and identified as blank 2, 3, and 4, respectively.*

Because even the reference solutions showed an increases in pH and alkalinity, the mass change was further investigated, weighing the bottles before and after each experiment. The data, summarised in Table 4.8, confirmed the progressive evaporation of seawater during the experiments, determining a mass loss from 1 to 20% in each bottle. Assuming a linear evaporation effect, the concentrations of Na, Mg, Ca, K, Si and S in the fluids have been recalculated averaging the evaporation corrections from chlorine (Cl^-), sulphate (SO_4^{2-}) and total sulphur (S) analyses. The concentrations of Na, Mg, Ca, K, and S have been corrected from the "zero" day, whereas Si concentrations only from the "silicate rock addition" day because of silicon absence in seawater.

Table 4.8: Summary of evaporation effect measured via weight, anion concentrations (Cl^- and SO_4^{2-}), and total sulphur concentration (S), and linearized for cations and Si concentration corrections.

	EVAPORATION (%)				MAXIMUM LINEAR EVAPORATION CORRECTION (%)	
Sample	**weight**	**Cl^-**	**SO_4^{2-}**	**S (total)**	**Average for cations**	**Average for Si**
Blank 2		9.52	8.08	5.52	9.65	8.22
JdF mix 1		2.04	2.15	1.92	1.21	1.03
JdF mix 2		4.01	3.78	2.85	2.91	2.48
JdF mix 3		4.25	3.94	1.72	2.58	2.19
Blank 3	15.62	18.77	20.05	13.95	19.51	16.00
CD80WP132-A	9.71	10.09	9.21	6.94	10.15	8.32
G1	4.31	4.44	4.06	3.96	3.92	3.21
Blank 4	3.20	2.53	4.76	3.26	2.64	1.93
JdF mix 2bis	3.39	3.58	6.15	3.62	3.56	2.61
CD80WP132-Abis	1.48	1.22	2.37	1.89	1.56	1.14
CD80WP132-B	5.14	4.70	6.78	4.13	3.84	2.81

The original solution compositions measured with ICP-OES and IC, and the corresponding corrected concentrations, are shown in Appendix "*Analyses*" CH4-12.

The rock reactivity or cation release rates determined in the current study are based on the release of silicon and calcium. This choice was made for several reasons. First, both element concentrations present consistently increasing trends over time (Figure 4.6). Secondly, Si is recognised as a key element in silicate mineral dissolution reactions, because it holds together the mineral framework [*Oelkers*, 2001b]. Furthermore, the absence of Si and relatively low concentration of Ca in seawater make the chemical changes easier to detect in laboratory experiments. Other dissolved ions are either present in very small quantities (e.g. Al), or do not show any consistent variations in the solutions with time (e.g. Na, Mg, and K). The Ca concentrations appear to reach steady-state after ~5 days, whereas Si concentrations continue to increase throughout the experiments (Figure 4.6).

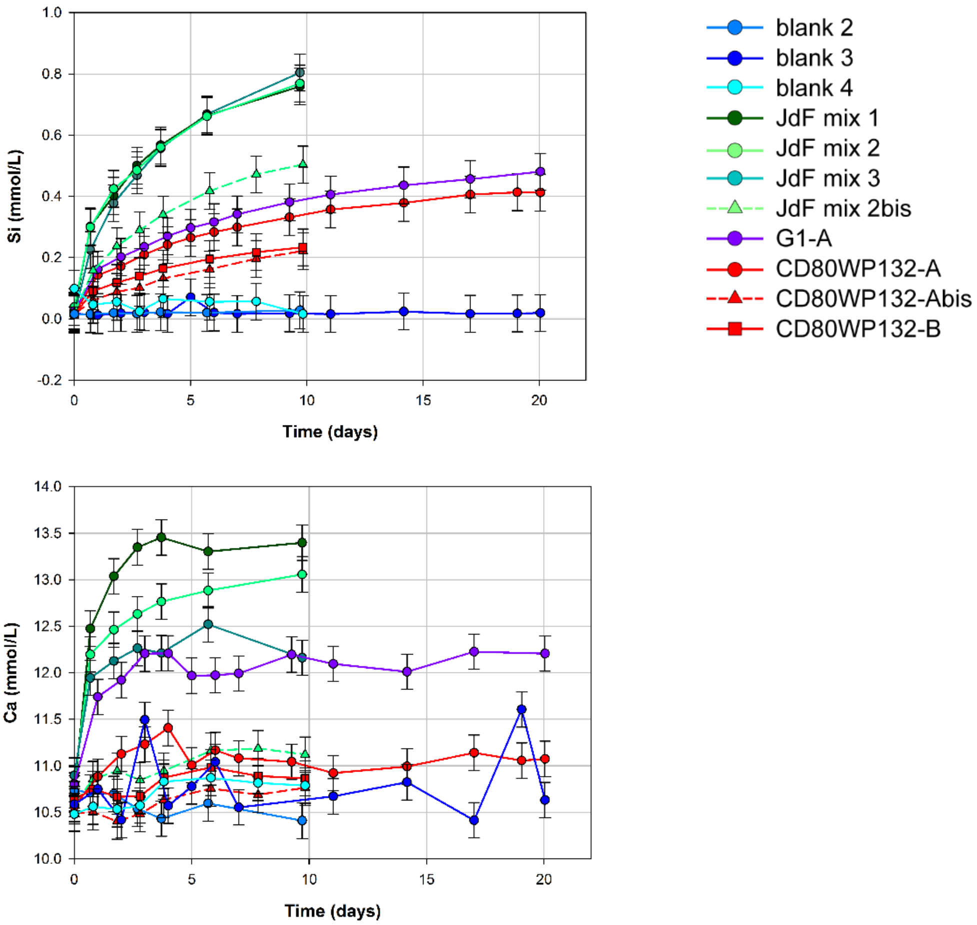

Figure 4.6: Si (top) and Ca (bottom) concentrations overtime during the dissolution experiments. Error bars represent the average 1σ (0.060 and 0.19 mmol/L for Si and Ca, respectively). For each run, the first output refers to the measurement taken at time "zero", just before adding the rock, when the seawater is CO_2-saturated. All the reference solutions are shown in blue and identified as "blank".

Aqueous absolute (Ca/Si) and relative (ΔCa/ΔSi) ratios have been calculated for all the solutions, to better characterise the reaction stoichiometry (Figure 4.7). The Ca/Si ratio expresses the elemental concentration variations with time, whereas the ΔCa/ΔSi ratio takes into account the initial solution composition, using:

$$\Delta Ca/\Delta Si \ = (Ca_x - Ca_0)/(Si_x - Si_0) \qquad (10)$$

where *"x"* is the relative time in days, and *"0"* represents the initial concentration measured at time zero, just before adding the rock.

The Ca/Si stoichiometric ratio for basalts and gabbro used in these experiments is ~0.25, whereas for seawater is ~500.

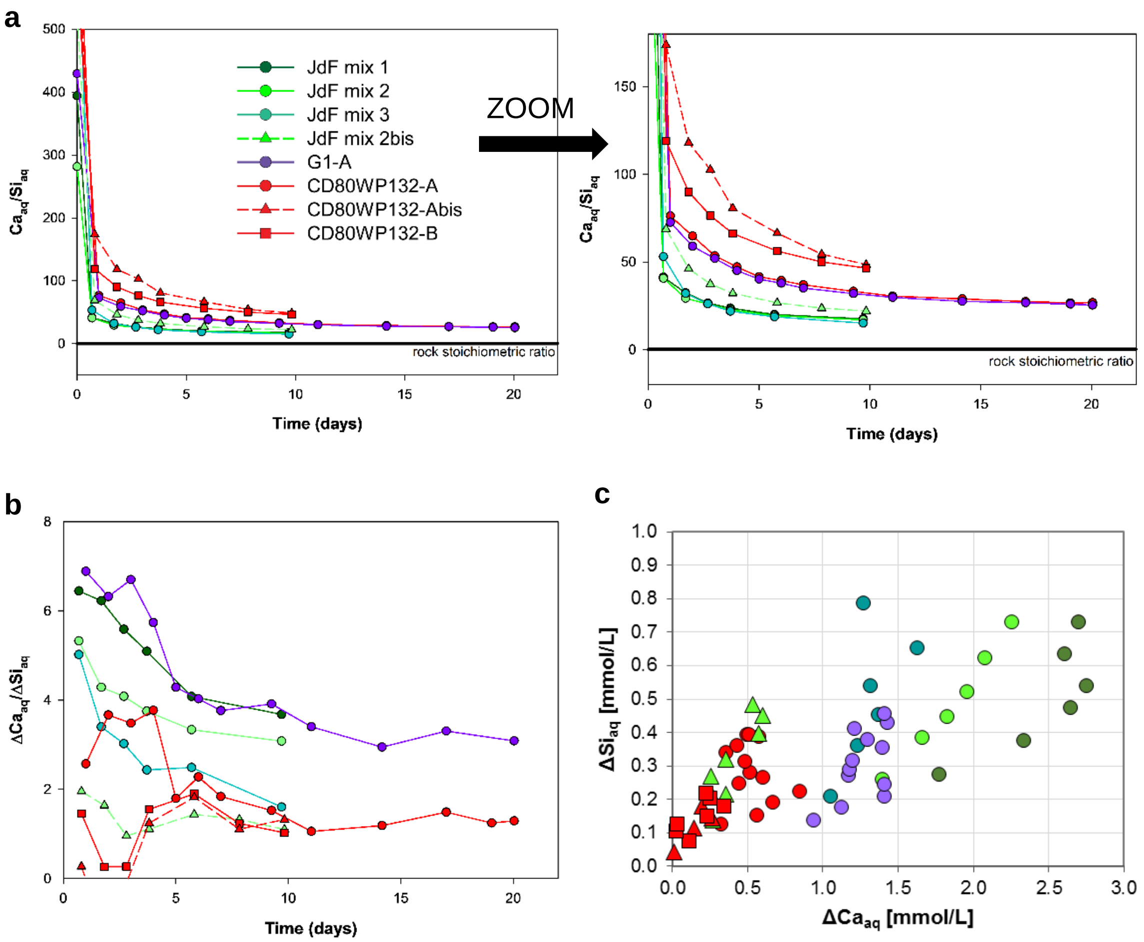

*Figure 4.7: Ca/Si (**a**) and ΔCa/ΔSi (**b**) ratios in all the aqueous solutions, expressed as a function of time during the dissolution experiments. Also, ΔSi is shown as a function of ΔCa (**c**). The rock stoichiometric ratio is indicated with a black line.*

Si and Ca release rates have been calculated fitting the experimental aqueous concentrations with an equation that best describes the compositional trend for each experiment (Figure 4.8), and differentiating the outputs with respect of time. These rates determine the elemental release differences between the samples, and quantify the incremental Si and Ca concentrations in solution over time (Figure 4.9). The R-squared coefficient, which range from 0 (the model fits no data) to 1 (the model fits all data), is used to described how well the data are fitted by the regression curve (Table 4.9). For the silicon concentrations all R-squared coefficients are >0.97, showing a very good agreement between curve and data. For the calcium concentrations, which show more variability among the samples, R-squared is >0.89 for JdF samples, 0.45< R-squared >0.77 for CD80WP132 samples, and >0.91 for G1.

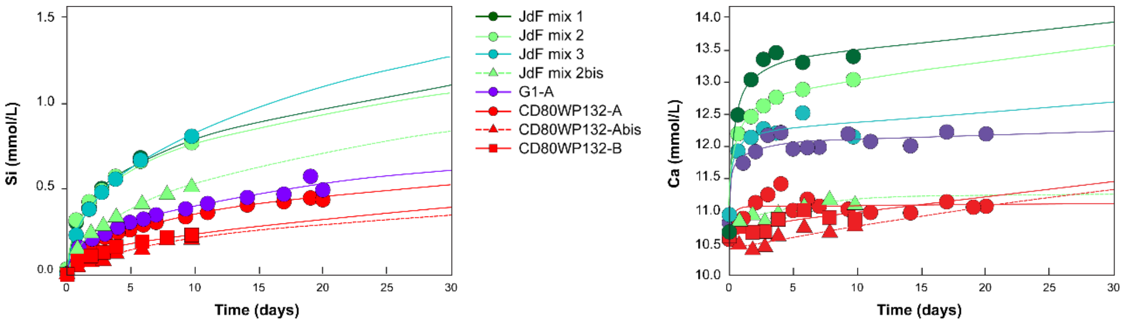

Figure 4.8: Best fitting curves of silicon (left) and calcium (right) concentrations for all the experimental runs.

Table 4.9: Summary of the R-squared coefficients for the regression curves applied to silicon and calcium concentrations in aqueous solution, for all the experimental run.

	R-squared	
	Silicon	**Calcium**
JdF mix 1	0.9976	0.9813
JdF mix 2	0.9990	0.9986
JdF mix 2bis	0.9986	0.8941
JdF mix 3	0.9984	0.9464
G1-A	0.9798	0.9156
CD80WP132-A	0.9966	0.4589
CD80WP132-Abis	0.9974	0.7629
CD80WP132-B	0.9979	0.6567

The differentiation has been done considering that the best fit is given by an exponential function at power two in every case (Equation 11, and its derivative Equation 12):

$$f(x) = ax^{b} + c \tag{11}$$

$$f'(x) = ab\, x^{b-1} \tag{12}$$

where $f(x)$ is the element concentration in mmol/L, x is the time ranging from 0 up to 30 days, $a, b,$ and c the constant values obtained with the best fit equation for each experiment, and $f'(x)$ the element release rate in mmol/L/day. The results of both Ca and Si release rates are shown in Figure 4.9. During the first two days the release rates range from 0.24 to 0.04 mmol/L/day for Si, and from 1.07 to 0.03 mmol/L/day for Ca. After 5 days, both Si and Ca release rates asymptotically decrease towards values <0.02 mmol/L/day. In general, the Si release rates among all the samples show similar trends, whereas the calcium ones display more variability.

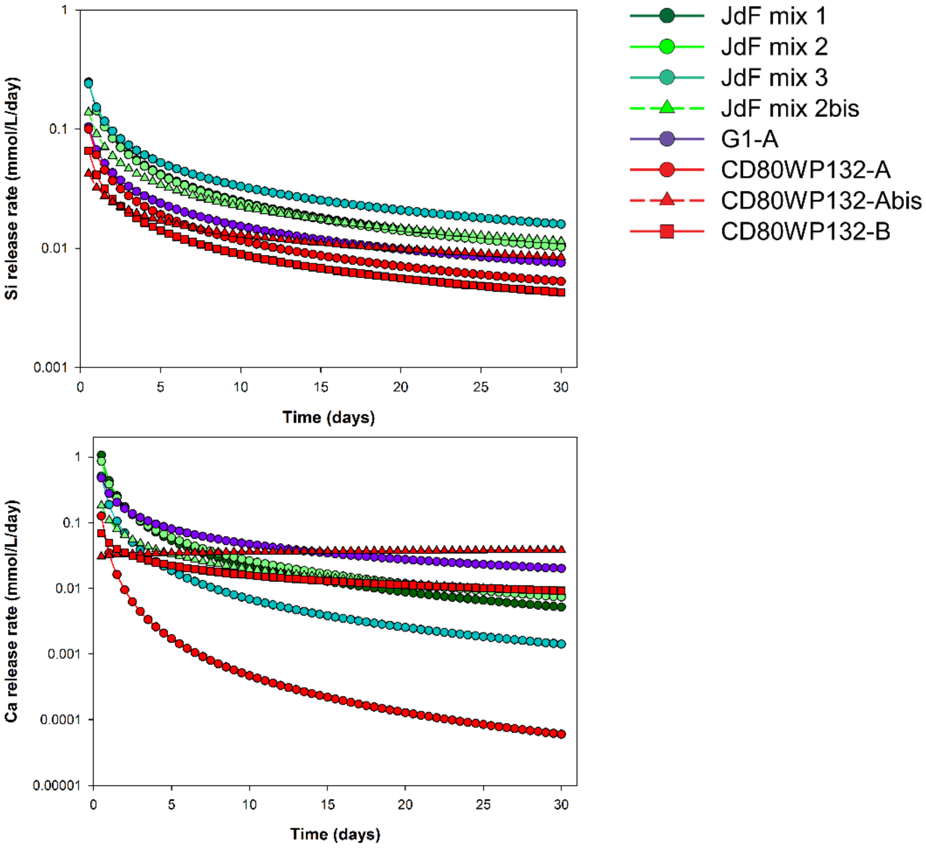

Figure 4.9: Si (top) and Ca (bottom) release rate as a function of time during the dissolution experiments.

4.3.2. Fine particle removal

Figures 4.10 (for JdF) and 4.11 (for G1 and CD80WP132) show GSD measurements, and the associated SEM images, for the samples before and after the experiments.

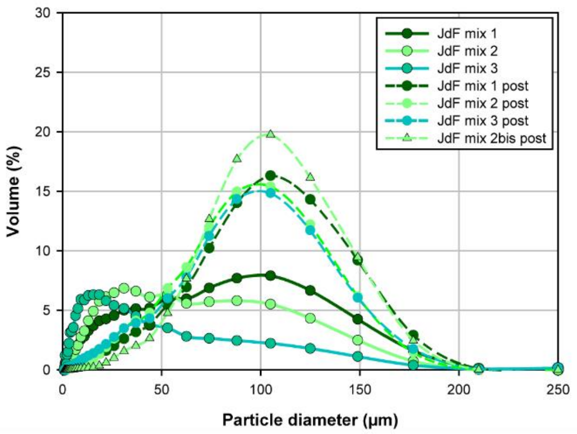

	VOLUME [%]				
	<11 µm	11-25 µm	25-30 µm	30-50 µm	>50 µm
JdF mix 1	17.57	18.90	5.16	15.33	43.05
JdF mix 1 post	3.85	6.44	2.60	11.05	76.06
JdF mix 2	16.39	25.97	7.14	18.37	32.14
JdF mix 2bis	2.36	6.73	3.48	14.09	73.34
JdF mix 2bis post	0.56	2.12	1.52	7.97	87.83
JdF mix 3	39.03	28.92	5.48	11.70	14.88
JdF mix 3 post	4.73	8.56	3.50	12.83	70.37

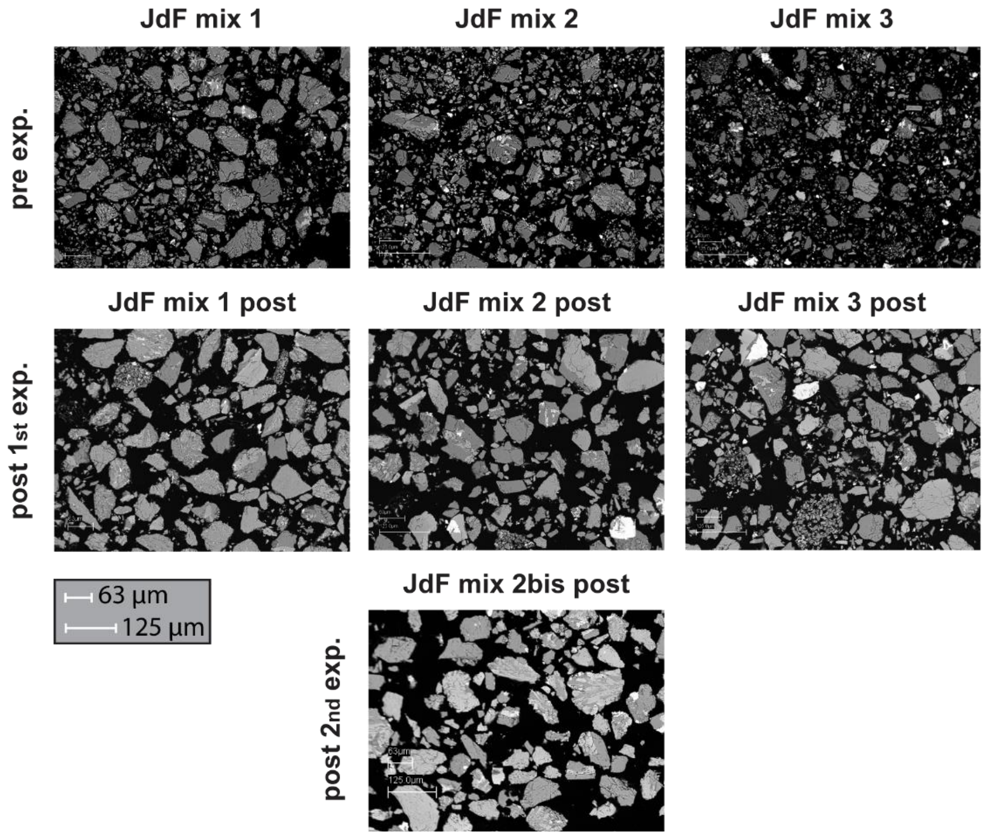

Figure 4.10: Grain size distribution analyses (top) and SEM images (bottom) for all the JdF samples, before and after the experiments (pre and post, respectively). The SEM images were taken with 500x of magnification. During the first set of experiments, 80 g of material was used for each run, whereas during the second set 65 g of already reacted material.

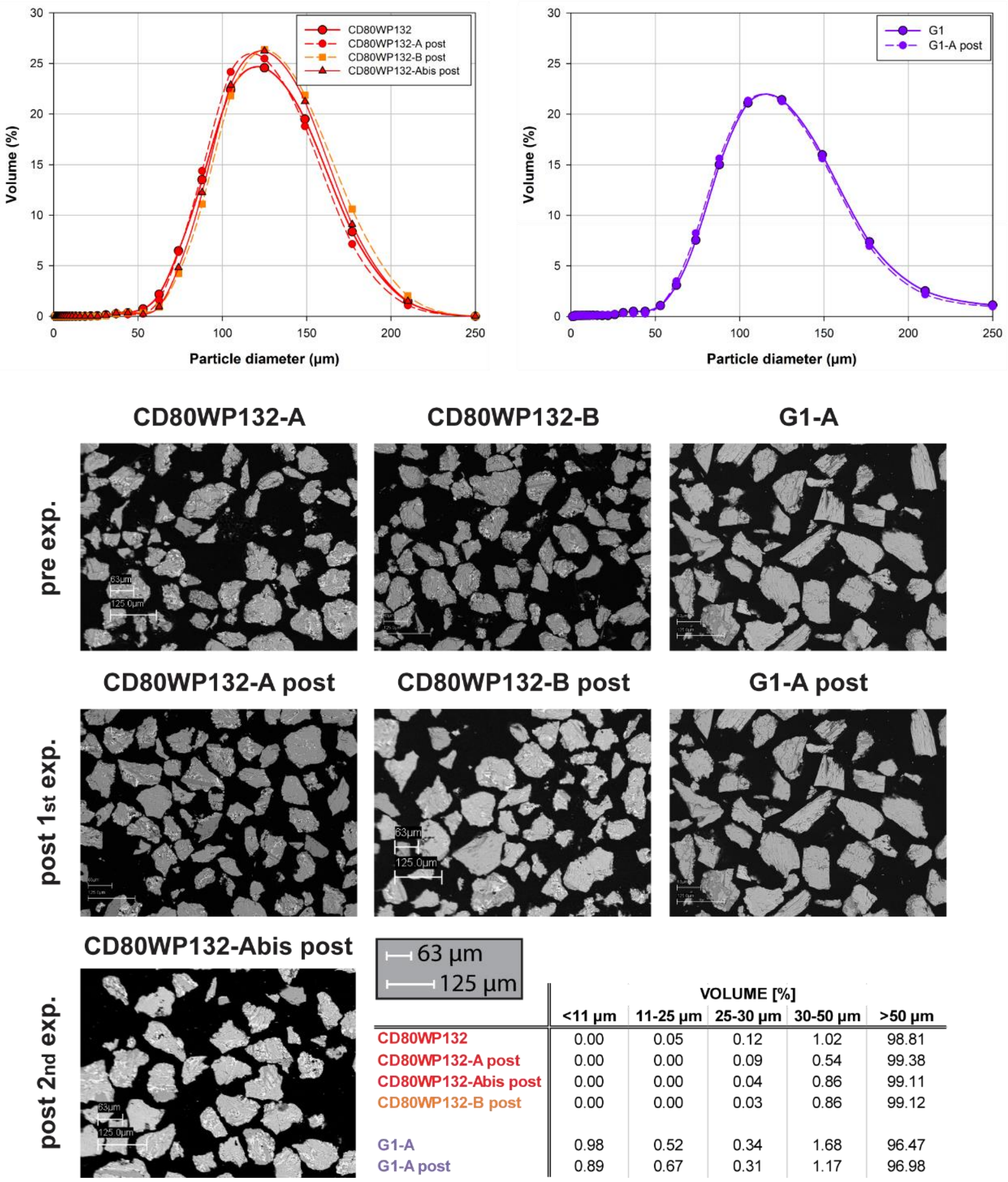

	VOLUME [%]				
	<11 µm	11-25 µm	25-30 µm	30-50 µm	>50 µm
CD80WP132	0.00	0.05	0.12	1.02	98.81
CD80WP132-A post	0.00	0.00	0.09	0.54	99.38
CD80WP132-Abis post	0.00	0.00	0.04	0.86	99.11
CD80WP132-B post	0.00	0.00	0.03	0.86	99.12
G1-A	0.98	0.52	0.34	1.68	96.47
G1-A post	0.89	0.67	0.31	1.17	96.98

Figure 4.11: Grain size distribution analyses (top) and SEM images (bottom) for all the CD80WP132 basalts (left) and G1 gabbro (right), before and after the experiments (pre and post, respectively). The SEM images were taken with 500x of magnification. During the first set of experiments, 80 g of material was used for each run, whereas during the second set 65 g of already reacted material was used. The experimental run on the sample CD80WP132-B was executed with only 30 g.

Importantly, the absence of fine particles (<10 µm) in G1 and CD80WP132 confirms that the dissolution of these samples has to be related to the effective size fraction between 63-125 µm, for all the experiments (Figure 4.11). Different scenarios are presented by the analyses of JdF samples. Both GSD and SEM analyses on samples JdF mix 1, 2, and 3 before the dissolution experiments indicate the presence of 16 to 40% in volume of fine particles. Analyses of the corresponding samples that underwent the first experimental run show a decrease in clay-sized material of 2-5% in volume (Figure 4.10, JdF mix 1, 2, and 3 post). This means that the fast kinetics expressed by Si and Ca release rates of JdF samples are most probably related to their higher reactive surface area, in agreement with the observations in previous studies [*Andreani et al.*, 2009; *Gadikota et al.*, 2014b; *Helgeson et al.*, 1984]. On the other hand, the second experimental run on the already used JdF mix 2 sample does not have such an abundance of fine particles, and the dissolution rates measured can be directly compared with other experiments with similar grain size fraction between 63-125 µm (Figure 4.10, JdF mix 2bis post).

Considering the change in grain size as a critical parameter in the kinetic rate interpretation, particle diameters and corresponding geometric surface areas (A_{geo}) of each sample are summarised in Table 4.10, before and after the dissolution experiments.

Table 4.10: Particle diameters and correspondent geometric surface areas (A_{geo}) for each sample, before and after the dissolution experiments. The elapsed time is specified.

	PRE EXPERIMENT		**Elapsed time**	**POST EXPERIMENT**	
Sample	GSD mean µm	A_{geo} cm^2/g	days	GSD mean µm	A_{geo} cm^2/g
JdF mix 1	50.95	406	9.7	79.44	260
JdF mix 2	42.35	489	9.7	74.05	279
JdF mix 2bis	74.05	279	9.8	86.88	238
JdF mix 3	26.50	781	9.7	72.61	285
G1	108.44	191	20.0	107.25	193
CD80WP132-A	109.89	188	20.0	109.82	188
CD80WP132-Abis	109.82	188	9.8	112.84	183
CD80WP132-B	103.72	199	9.8	114.94	180

4.3.3. Rock dissolution

The term “rock dissolution” refers to the maximum degree of dissolution to which a rock is characterised by. Usually, this level is reached with the steady-state ion release rate, which is defined as a condition where dissolution rates are time independent and where dissolution is stoichiometric [*Oelkers*, 2001b]. Although an almost constant pH is reached after five days in all the experimental runs, the steady-state condition is not fully reached in this study (Section 4.4.2).

The extent of rock dissolution is shown as a function of time in Figure 4.12 and summarised in Table 4.11. The percentages have been calculated as a ratio between aqueous concentration difference, and whole rock content, for both Si and Ca. The data for the whole rock content have been taken from XRF and SEM-EDS bulk rock analyses. All the mass of the samples used during the experiment is considered as “reactive”.

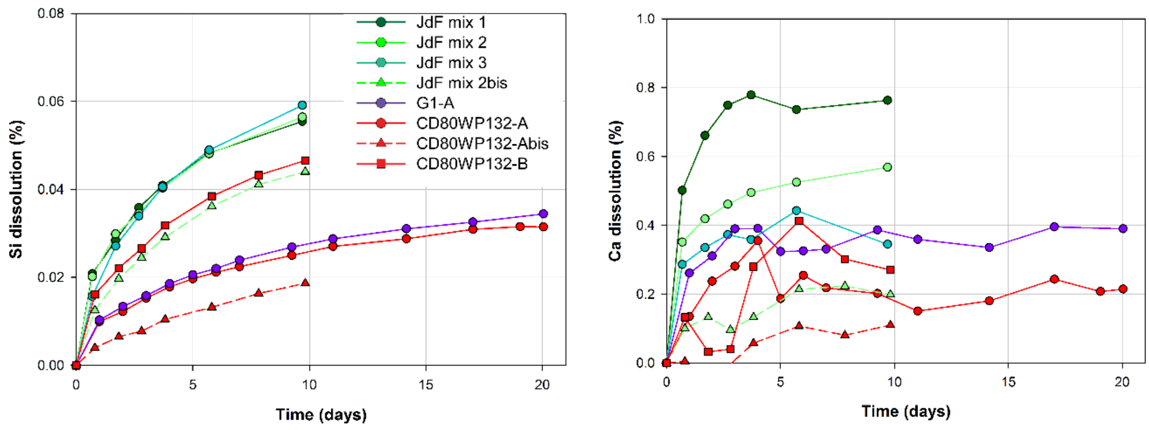

Figure 4.12: Rock dissolution extents (Si and Ca) in % vs. time for all the samples used in the experiments. All the mass is considered as “reactive”.

In general, the greatest extent of dissolution in terms of mass lost was achieved in the JdF samples, rich in fine particles, followed by the ophiolitic gabbro. The lowest extent of dissolution was observed in the MAR sample subjected to consecutive experimental runs (CD80WP132-Abis). The sample JdF mix 2bis (lower fine particle content) shows intermediate dissolution extent similar to fresh MAR basalt (CD80WP132-A and B). In particular, the comparable calcium dissolution extents of CD80WP132-A and B, which weigh 80 and 30 g respectively, highlight the apparent non-dependence on sample mass. This observation leads to the hypothesis that the reactivity is focused only on the top-surface layer of rock samples in the reactors (further explanations in Section 4.4.2.2).

Table 4.11: Rock dissolution extent in % using Si and Ca concentrations for all the samples used during the experiment. All the rock is considered to be "reactive".

				AQUEOUS CONCENTRATIONS		*ROCK DISSOLUTION*	
Sample	**Mass** [g]	**Type**	**Elapsed time** [days]	**ΔSi in 500 mL** [mmol]	**ΔCa in 500 mL** [mmol]	**Si** [%]	**Ca** [%]
JdF mix 1	80	fresh	9.7	0.37	1.35	0.06	0.76
JdF mix 2	80	fresh	9.7	0.37	1.13	0.06	0.57
JdF mix 2bis	65	re-run	9.8	0.24	0.27	0.04	0.20
JdF mix 3	80	fresh	9.7	0.39	0.63	0.06	0.35
G1-A	80	fresh	20.4	0.23	0.70	0.03	0.39
CD80WP132-A	80	fresh	20.4	0.20	0.26	0.03	0.22
CD80WP132-Abis	65	re-run	9.8	0.10	0.14	0.02	0.11
CD80WP132-B	30	fresh	9.8	0.11	0.11	0.05	0.27
Average	-	-	-	-	-	0.04	0.33

4.4. Discussion

4.4.1. Characterisation of physical properties

The surface area available for reaction is one of the most important factors determining the rate and extent of reaction for a given rock volume and time. Fine particles (<10 µm) have a higher ratio of surface area to volume, which in turn leads to high rock dissolution rates. Therefore, it is essential to carefully characterise the particle size and the corresponding reactive surface area in order to avoid overestimating the dissolution rates.

To address this issue, a clear procedure to prepare the samples was defined [*Gadikota et al.*, 2014b], and analyses on the grain size distribution (GSD) and on the surface area (GSA and BET) have been carried out. In general, BET analyses with nitrogen give a good measurement of specific surface area higher than 1 m^2/g, whereas krypton is more suitable for specific surface area <1 m^2/g [*Lowell and Shields*, 2013]. However, BET surface area may be a poor estimate for water-rock experiments because it is not representative of the actual contact area between fluid and rocks [*Brantley and Mellott*, 2000; *Lüttge and Arvidson*, 2008]. On the other hand, surface roughness is not taken into account in the geometric surface area calculations, which assume the presence of smooth spheres [*Cubillas et al.*, 2005]. Many studies have demonstrated how the geometric rather than BET surface area may be more accurate for estimating dissolution rates [*Gautier et al.*, 2001; *Gysi and Stefánsson*, 2012c; *Wolff-Boenisch and Gíslason*, 2002; *Wolff-Boenisch et al.*, 2004; *Wolff-Boenisch et al.*, 2011]. Rates in this study were normalized to the geometric surface area (Section 4.4.2), which was found to be more consistent with the SEM observations on particle size than BET measurements carried out with nitrogen (Table 4.6).

4.4.2. Rock dissolution characterisation

The interaction of CO_2-rich seawater and mafic rocks results in changes in solution chemistry, that are dependent on several factors including the CO_2 concentration, temperature, rock mineralogy, and sample grain size.

With respect to CO_2 sequestration, the primary interests of this experimental study are related to the determination of the rock dissolution rates (Section 4.4.2.1), the reactive mass within the sample – top-surface only hypothesis (Section 4.4.2.2), the type of mass transfer from rock to solution – congruent and/or incongruent dissolution (Section 4.4.2.3), and the calcium sources within the rocks (Section 4.4.2.4).

4.4.2.1. Rock dissolution rates

Considering the grain size distribution differencies between the samples, the dissolution rates have been normalised to the geometric surface area (Figure 4.13), following the equation:

$$r_X = \log\left[\Delta X/(\mathrm{Ageo} * t)\right] \tag{13}$$

where r_X is the dissolution rate of element X expressed as log [mol/cm^2/s], ΔX is the differential aqueous concentration of element X in mol/kg, A_{geo} the sample-specific geometric surface area pre-experiment in cm^2/kg (Table 4.10), and t the elapsed time in seconds [*Gysi and Stefánsson*, 2012c].

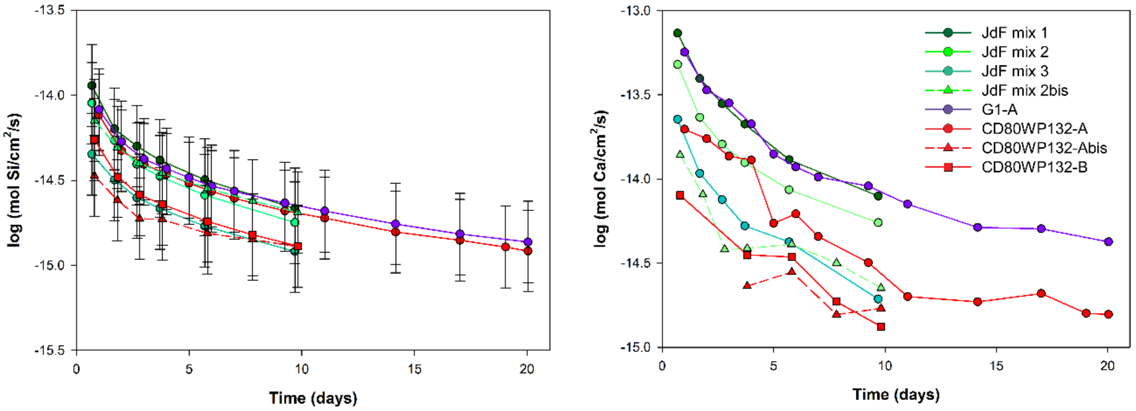

Figure 4.13: Si (on the left) and Ca (on the right) dissolution rates as a function of time normalized to the initial geometric surface area of rock for all experimental runs. Ca dissolution rates for CD80WP132-Abis (days 0.8, 1.8, and 2.8) and CD80WP132-B (days 1.8 and 2.8) have not been plotted due to analytical errors (values available in Table 4.12). Error bars (Si) or size of symbols (Ca) correspond to a ±0.2 or ±0.01 log unit estimated uncertainty calculated from the precision of Si and Ca concentrations measurements, respectively (Appendix "Methods" CH4-2, IAPSO error).

The dissolution rates in this study decrease with time, and trend towards the rock stoichiometric dissolution rate (Figure 4.7). In general, Si dissolution rates range from -13.94 to -14.92 log (mol/cm^2/s), whereas Ca dissolution rates range from -13.13 to -14.88 log (mol/cm^2/s) (Table 4.12). The dissolution rates for Si and Ca measured at the end of each experimental run are the closest to the stoichiometric dissolution, and range from -14.67 to -14.92 log (mol/cm^2/s), and from -14.10 to -14.88 log (mol/cm^2/s), respectively (Table 4.12).

The similarity among the dissolution rates confirms that the fastest kinetics related to fine particle abundance are overcome by the normalisation, making possible an appropriate comparison among samples. Overall, the ophiolitic gabbro shows dissolution rates higher or similar to the Jdf ones. The MAR basalts are characterised by a wider range of dissolution rates that are usually lower than JdF and gabbroic samples.

Table 4.12: Summary of rock dissolution rates, normalised to the geometric surface area, for all the experimental runs. Values of dissolution rate are given in log (mol/cm^2/s). For CD80WP132-Abis, the Ca dissolution rates for days 1.8 and 2.8 are not available due to analytical errors on Ca concentrations.

Elapsed time (days)	JdF mix 1		JdF mix 2		JdF mix 2bis		JdF mix 3		G1		CD80WP132 -A		CD80WP132 -Abis		CD80WP132 -B	
	Si	**Ca**	**Si**	**Ca**	**Si**	**Ca**	**Si**	**Ca**	**Si**	**Ca**	**Si**	**Ca**	**Si**	**Ca**	**Si**	**Ca**
0.7-0.8	-13.94	-13.13	-14.05	-13.32	-14.15	-13.86	-14.35	-13.65	-	-	-	-	-14.47	-15.05	-14.26	-14.10
1.0	-	-	-	-	-	-	-	-	-14.09	-13.25	-14.12	-13.71	-	-	-	-
1.7-1.8	-14.20	-13.40	-14.27	-13.63	-14.31	-14.09	-14.50	-13.97	-	-	-	-	-14.62	-	-14.48	-15.06
2.0	-	-	-	-	-	-	-	-	-14.27	-13.47	-14.33	-13.76	-	-	-	-
2.7-2.8	-14.30	-13.55	-14.41	-13.79	-14.40	-14.42	-14.60	-14.12	-	-	-	-	-14.73	-	-14.59	-15.16
3.0	-	-	-	-	-	-	-	-	-14.38	-13.55	-14.41	-13.86	-	-	-	-
3.7-3.8	-14.38	-13.68	-14.48	-13.90	-14.46	-14.41	-14.67	-14.28	-	-	-	-	-14.73	-14.64	-14.64	-14.45
4.0	-	-	-	-	-	-	-	-	-14.43	-13.67	-14.46	-13.89	-	-	-	-
5.0	-	-	-	-	-	-	-	-	-14.48	-13.85	-14.52	-14.26	-	-	-	-
5.7-5.8	-14.50	-13.89	-14.59	-14.06	-14.55	-14.39	-14.77	-14.37	-	-	-	-	-14.81	-14.55	-14.74	-14.46
6.0	-	-	-	-	-	-	-	-	-14.53	-13.93	-14.57	-14.21	-	-	-	-
7.0	-	-	-	-	-	-	-	-	-14.56	-13.99	-14.61	-14.34	-	-	-	-
7.8	-	-	-	-	-14.62	-14.50	-	-	-	-	-	-	-14.85	-14.81	-14.82	-14.73
9.3	-	-	-	-	-	-	-	-	-14.63	-14.04	-14.68	-14.50				
9.7-9.8	-14.67	-14.10	-14.75	-14.26	-14.69	-14.65	-14.92	-14.71	-	-	-	-	-14.89	-14.77	-14.89	-14.88
11.0	-	-	-	-	-	-	-	-	-14.68	-14.15	-14.72	-14.70	-	-	-	-
14.2	-	-	-	-	-	-	-	-	-14.76	-14.29	-14.80	-14.73	-	-	-	-
17.0	-	-	-	-	-	-	-	-	-14.82	-14.30	-14.85	-14.68	-	-	-	-
19.0	-	-	-	-	-	-	-	-	-	-	-14.89	-14.80	-	-	-	-
20.0	-	-	-	-	-	-	-	-	-14.86	-14.37	-14.92	-14.81	-	-	-	-

4.4.2.2. Reactive mass

For a fixed elemental concentration in solution, the key parameter to calculate the dissolution extent is the effective reactive mass in solution.

In section 4.3.3, a general estimation of dissolution extent is given, considering all the sample as reactive. However, it has been observed that a change in the sample mass used during the experiments (from 80 to 30 g) does not significantly affect the Ca and Si concentrations in solution. Therefore, the hypothesis has been advanced that the reactions are only focused on the top-surface layer of rock samples in the reactor. If this hypothesis is true, the dissolution extent should be higher, depending on the size of the top-surface area considered as reactive (Figure 4.14).

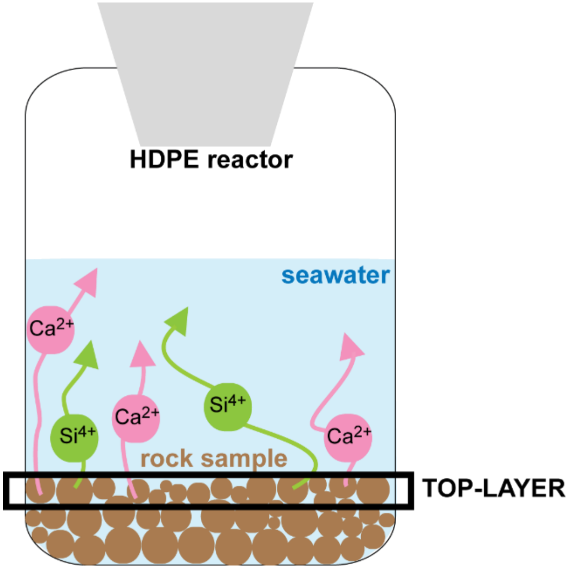

Figure 4.14: Sketch of rock dissolution within the HDPE reactor used in this study, considering only the top-surface area of the sample ("top-layer") as reactive.

An attempt has been made to quantify the top-layer weight (Equation 14), assuming the presence of unimodal grain size with diameter equal to the mean of the corresponding grain size distribution for each sample (Table 4.10).

$$M_{TL} = (A_{HDPE} * V_p * \rho_r) / A_p \tag{14}$$

where M_{TL} is the top-layer mass in g, A_{HDPE} the HDPE bottle area calculated for an actual radius of 4 cm, V_p and A_p the volume and area, respectively, occupied by a single particle (accordingly to GSD mean), and ρ_r the rock density assumed to be 2.9 g/cm^3.

On average, the top-layer weighs 0.76 g. Also, assuming 50 wt% SiO_2 (Si = 23.4 wt%) and 12 wt% CaO (Ca = 8.6 wt%) for each layer (averages for mafic rocks), it is possible to estimate the maximum Si and Ca release if the top-layer totally reacted, and compare it with the actual Si and Ca aqueous concentrations (Table 4.13). Calculations show that an average reactive mass of 0.76 g, lying on the top-surface always in contact with the CO_2-rich solution, is sufficient to supply the measured concentrations during the dissolution experiments. This means that the average values of Si and Ca dissolution extent for the whole sample mass of 0.04% and 0.33%, respectively (Table 4.11), would increase two orders of magnitude if all reactions are taking place from the top-surface only (Table 4.13). However, these preliminary considerations have to be further tested and confirmed by more experiments with different water/rock ratios, and stirred samples, in order to better constrain the dissolution extent and the reactive mass of these rocks.

*Table 4.13: Summary of top-surface reactive mass (**M_{TL}**) for all the experimental runs, with corresponding Si and Ca mass (**$M_{Si\text{-}TL}$** and **$M_{Ca\text{-}TL}$**, respectively). **ΔSi (aq)** and **ΔCa (aq)** are the differential moles of Si and Ca, respectively, measured in 500 mL of aqueous solution (Table 4.11). **Si_{TL}** and **Ca_{TL}** are the Si and Ca rock dissolution extent, respectively, considering only the top-surface area as reactive. Grey shading shows the sample averages for all the above mentioned parameters.*

Sample	M_{TL} [g]	$M_{Si\text{-}TL}$ [g]	$Mol_{Si\text{-}TL}$ [mol]	ΔSi (aq) [mol]	Si_{TL} [%]	$M_{Ca\text{-}TL}$ [g]	$Mol_{Ca\text{-}TL}$ [mol]	ΔCa (aq) [mol]	Ca_{TL} [%]
JdF mix 1	0.50	0.12	0.0041	0.0004	5.84	0.04	0.0011	0.0014	80.34
JdF mix 2	0.41	0.10	0.0034	0.0004	5.94	0.04	0.0009	0.0011	59.87
JdF mix 3	0.26	0.06	0.0021	0.0004	6.23	0.02	0.0006	0.0006	36.32
JdF mix 2bis	0.72	0.17	0.0060	0.0002	3.77	0.06	0.0015	0.0003	15.88
Average (JdF)	0.47	0.11	0.0039	0.0035	5.44	0.04	0.0010	0.0009	48.10
G1-A	1.05	0.25	0.0088	0.0002	3.63	0.09	0.0023	0.0007	41.06
CD80WP132-A	1.07	0.25	0.0089	0.0002	3.31	0.09	0.0023	0.0003	22.64
CD80WP132-B	1.01	0.24	0.0084	0.0001	1.84	0.09	0.0022	0.0001	9.96
CD80WP132-Abis	1.07	0.25	0.0089	0.0001	1.59	0.09	0.0023	0.0001	8.79
Average (CD80WP132)	1.05	0.25	0.0087	0.0001	2.25	0.09	0.0023	0.0002	13.79
Average (all samples)	0.76	0.18	0.0063	0.0003	4.02	0.07	0.0016	0.0006	34.36

4.4.2.3. Rock mass transfer

As shown in Figure 4.7, the extent of dissolution in terms of Ca/Si ratio decreases with rock dissolution progress, getting closer – and in some cases parallel – to the whole rock Ca/Si stoichiometric ratio (~0.25), but without reaching it. This means that all the experimental runs are characterised by incongruent dissolution. *Oelkers* [2001b] explained the “non-stoichiometry” as a result of the leached layer formation, which is commonly a provisional part of the dissolution process. Observations of this layer on olivine show that the leaching of cations and incongruent mineral dissolution result in the formation of a Si-rich mass-transfer-limiting passivation layer, which eventually limits the extent of mineral dissolution [*Béarat et al.*, 2006; *Daval et al.*, 2011; *Gadikota et al.*, 2014b]. In this study, the formation of a passivation layer is suggested by the observations of incongruent dissolution, and of a higher calcium dissolution extent than Si one (Tables 4.11 and 4.13). Also, the proximity of Ca and Si release rates to steady-state indicates that the reactions are extending beyond the passivation layer to the bulk rock, towards a more congruent dissolution (Figure 4.9).

4.4.2.4. Calcium source

The different release of calcium at pH ~5 from all the mafic rocks used during the experiments (Tables 4.11 and 4.13) suggests which of the calcium-rich minerals are the most susceptible to dissolution. In the rocks used in this study, calcium is abundant in glass, mesostasis, pyroxene, amphibole, plagioclase, and calcite (Table 4.14).

Table 4.14: Averages of mineral molar compositions [Deer et al., 1963; 1978; 1997], and relative stoichiometric Ca/Si ratios. Glass composition from USGS standard BHVO-2 [Wilson, 1997].

	Ca	Na	Mg	Fe	Ti	Al	Si	C	O	OH	Ca/Si
						mol					
Plagioclase, albite	-	1.0	-	-	-	1.0	3.0	-	8.0	-	-
Plagioclase, oligoclase	0.2	0.8	-	-	-	1.2	2.8	-	8.0	-	0.07
Plagioclase, andesine	0.4	0.6	-	-	-	1.4	2.6	-	8.0	-	0.15
Plagioclase, labradorite	0.6	0.4	-	-	-	1.6	2.4	-	8.0	-	0.25
Plagioclase, bytownite	0.8	0.2	-	-	-	1.8	2.2	-	8.0	-	0.36
Plagioclase, anorthite	1.0	-	-	-	-	2.0	2.0	-	8.0	-	0.50
Pyroxene, augite	0.9	0.1	0.9	0.2	0.10	0.4	1.9	-	6.0	-	0.42
Amphibole, actinolite	1.8	0.2	3.4	1.3	0.02	0.4	7.8	-	22	2	0.23
Calcite	1.0	-	-	-	-	-	-	1.0	3.0	-	-
Glass	0.2	0.1	0.2	0.2	0.03	0.3	0.8	-	2.9	-	0.25

In order to advance suggestions on which is the most reactive mineral among them, the mineral dissolution rates have to be compared. According to literature data, calcite, glass and olivine are the most susceptible phases to alteration, followed by pyroxene, amphibole, and plagioclase [e.g., *Banfield et al.*, 1991; *Crovisier et al.*, 1987; *Eggleton et al.*, 1987]. However, the alteration order of the last three minerals is not well established, because it mainly depends on pH, temperature, and mineral composition [e.g., *Fridriksson et al.*, 2001; *Gudbrandsson et al.*, 2011; *Nesbitt and Wilson*, 1992]. A list of mineral dissolution rates, together with the experimental conditions at which they have been measured, is available in Table 4.15. In general, these kinetic observations suggest that, for pH ~5, the mineral alteration order is calcite > olivine and glass > pyroxene > anorthitic plagioclase > amphibole hornblende > albitic plagioclase.

Given the mineral average distributions of the samples used in this study (Figure 4.15), there are several Ca-rich phases to be considered as potential Ca-sources. For the basalts, these phases are calcite, mesostasis, labradoritic plagioclase, and augitic pyroxene, with the addition of glass for the MAR samples, whereas for the ophiolitic gabbro G1, amphibole and anorthitic plagioclase.

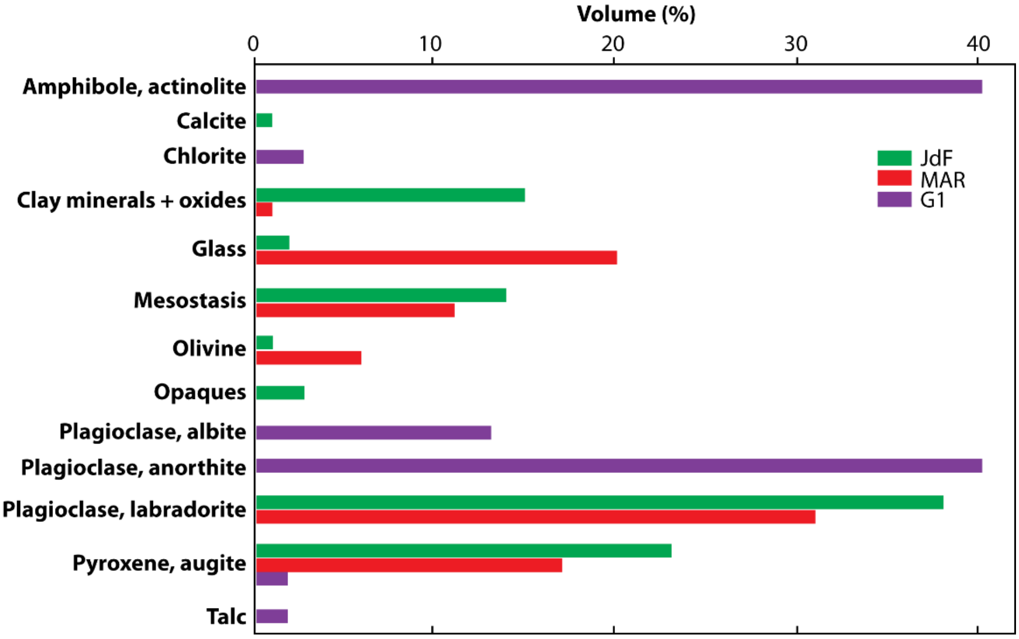

Figure 4.15: Mineral average distribution in the basalts of JdF and MAR, and in the ophiolitic gabbro G1.

The MAR and JdF basalts, despite the 15-30% of mesostasis and glass content, and ~20% of pyroxene, do not show particularly high dissolution rates (Table 4.12). However, the experimental run with the JdF samples "mix 1" and "mix 2", and the ophiolitic gabbro show the highest aqueous concentration of Ca. This higher Ca-reactivity from the basalts is justified by the presence of ~1% of calcite, which is recognised in literature as very reactive [*Cubillas et al.*, 2005] (Table 4.15). In contrast, considering that G1 had no calcite, and almost no pyroxene (~2%), the main mineral sources of Ca in the gabbro have to be amphibole and anorthitic plagioclase.

No experimental data have been found in literature on single-phase Ca dissolution rates of amphiboles (Table 4.15), but Si results from whole rock dissolution experiments on metabasalt with 50% of actinolite content are shown by *Critelli et al.* [2014]. These whole rock Si dissolution rates are in agreement with this thesis findings (see further discussion in section 4.4.3). On the other hand, several experiments were carried out on plagioclase, even if only a small number measured the Ca dissolution rates (Table 4.15) [*Berg and Banwart*, 2000; *Carroll and Knauss*, 2005; *Casey et al.*, 1991]. Overall, these single-phase investigations demonstrate that the plagioclase dissolution rates change as a function of the plagioclase composition. The more calcic fraction (An-anorthite) exhibits faster reaction rates at a range of pH and temperatures [*Blum*, 1994; *Casey et al.*, 1991; *Gudbrandsson et al.*, 2014; *Holdren and Speyer*, 1987; *Oelkers and Schott*, 1995; *Oelkers et al.*, 1994], than the more sodic fractions, from labradorite to albite [*Carroll and Knauss*, 2005; *Chou and Wollast*, 1985; *Gudbrandsson et al.*, 2014; *Oxburgh et al.*, 1994; *Stillings et al.*, 1996] (Table 4.15). Hence, the fast Ca release in the experimental run with gabbro is in agreement with literature data on anorthitic plagioclase, but does not exclude a Ca contribution from the amphibole. Also, the slower Ca dissolution rates in this thesis basalts (JdF mix 3 and CD80WP132) can be related to the labradoritic nature of the plagioclase and/or to the lack of amphibole and calcite.

Table 4.15: Summary of mineral dissolution rates and relative experimental conditions at which they have been measured [Berg and Banwart, 2000; Carroll and Knauss, 2005; Casey et al., 1991; Chou and Wollast, 1985; Cubillas et al., 2005; Golubev et al., 2005; Gudbrandsson et al., 2014; Knauss et al., 1993; Oelkers and Schott, 1995; Oxburgh et al., 1994; Pokrovsky and Schott, 2000].

Mineral	Reactor setup	T °C	pCO_2 bar	pH	Si release rate log (mol/cm²/s)	pH	Ca release rate log (mol/cm²/s)	Reference
Pyroxene diopside [$Ca_{0.99}Mg_{0.98}Fe_{0.02}Cr_{0.01}Si_2O_6$]	mixed flow[a]	25	0	1-12	from -14.12 to -15.32	1-4	from -14.04 to -14.75	*Golubev et al. [2005]*
			1	4.25	-14.62	4.25	-14.56	
Pyroxene diopside [$Ca_{0.97}Mg_{0.89}Fe_{0.08}Al_{0.04}Si_{1.99}O_6$]	flow-through[b]	25-70	atm	2-12	from -12.80 to -15.27	2-12	from -12.54 to -15.83	*Knauss et al. [1993]*
Amphibole hornblende [$Ca_2(Mg,Fe,Al)_5(Si,Al)_8O_{22}(OH)_2$]	mixed flow[a]	25	0	2-11	from -14.24 to -14.96	-	-	*Golubev et al. [2005]*
			1	4	-14.71	-	-	
Forsterite [Mg_2SiO_4]	mixed flow[a]	25	0	2-11	from -11.92 to -14.07	-	-	*Golubev et al. [2005]*
			1	4.16	-12.26	-	-	
Forsterite [Mg_2SiO_4]	mixed flow[a]	25	-	1-12	from -11.23 to -15.25	-	-	*Pokrovsky and Schott [2000]*
Calcite [$CaCO_3$]	mixed flow[a]	25	-	-	-	5.1-9.3	from -9.57 to -10.35	*Cubillas et al. [2005]*
Plagioclase Albite [$Na_{0.97}K_{0.01}Ca_{0.02}Al_{0.99}Si_{3.00}O_8$]	batch[c]	25	-	2	-14.97	2	-	*Casey et al. [1991]*
Plagioclase Andesine [$Na_{0.46}K_{0.05}Ca_{0.46}Al_{1.50}Si_{2.50}O_8$]			-		-14.16		-14.07	
Plagioclase Anorthite [$Na_{0.08}Ca_{0.92}Al_{1.90}Si_{2.09}O_8$]			-		-12.19		-12.25	
Plagioclase Albite [$NaAlSi_3O_8$]	fluidized bed[d]	25	atm	1-12	from -14.2 to -15.9	-	-	*Chou and Wollast [1985]*
Plagioclase Albite [$Na_{0.99}Ca_{0.01}Al_{1.04}Si_{2.97}O_8$]	mixed flow[a]	22	-	2-11	from -13.42 to -15.33	-	-	*Gudbrandsson et al. [2014]*
Plagioclase Labradorite [$Na_{0.34}Ca_{0.66}Al_{1.63}Si_{2.35}O_8$]			-	2-11	from -13.31 to -15.47	-	-	
Plagioclase Anorthite [$Na_{0.13}Ca_{0.87}Al_{1.83}Si_{2.14}O_8$]			-	2-11	from -12.05 to -14.62	-	-	
Plagioclase Anorthite [$Ca_{1.2}Al_{1.94}Si_{2.0}O_8$]	thin-film flow[e]	25	0.1	5.5-8.5	from -15.06 to -15.36	5.5-8.5	from -15.66 to -15.76	*Berg and Banwart [2000]*
Plagioclase Anorthite [$Na_{0.04}Ca_{0.97}Al_{1.94}Si_{2.04}Fe_{0.02}O_8$]	mixed flow[a]	45-95	-	2.4-3.2	from -10.55 to -11.52	-	-	*Oelkers and Schott [1995]*
Plagioclase Labradorite [$Na_{0.4}Ca_{0.6}Al_{1.6}Si_{2.4}O_8$]	mixed flow[a]	30-130	atm	3.2	from -11.66 to -14.57	3.2	from -11.69 to -13.40	*Carroll and Knauss [2005]*
			21.5		from -12.34 to -13.45		from -12.34 to -13.19	
Plagioclase Oligoclase [$Na_{0.87}Ca_{0.13}Al_{1.2}Si_{2.8}O_8$]	flow-through[b]	25	-	3.0-6.5	from -15.5 to -16.2	-	-	*Oxburgh et al. [1994]*
Plagioclase Andesine [$Na_{0.54}Ca_{0.46}Al_{1.4}Si_{2.6}O_8$]			-	3.0-6.5	from -14.2 to -14.8	-	-	
Plagioclase Bytownite [$Na_{0.24}Ca_{0.76}Al_{1.8}Si_{2.2}O_8$]			-	3.0-6.5	from -13.3 to -14.5	-	-	

[a] mixed flow: the solution flows into the reactor, is mixed with a stirrer, and leaves the reactor;

[b] flow-through: the solution passes continuously through the reactor, and gets progressively discharged;

[c] batch: the solution is present from the beginning in the reactor;

[d] fluidized bed: the solution passes continuously through a solid granular material at high velocities to suspend the solid, maximizing mixing and fluid-rock interaction;

[e] thin-film flow: the solution passes continuously through a thin membrane filter, where the powder is sitting on.

4.4.3. Comparison with previous rock dissolution experiments

Seawater has a high ionic strength and its use in batch dissolution experiments, especially at low temperature, complicates the detection of relatively small contributions of cations to solution as a result of CO_2-seawater-rock reactions. For this reason, at present, only a few experimental studies have investigated fluid-rock interactions in CO_2-rich seawater [*Crovisier et al.*, 1987; *Seyfried and Mottl*, 1982; *Wolff-Boenisch et al.*, 2011]. Among them, data from *Wolff-Boenisch et al.* [2011] are comparable to the current study results, due to similarities in the experimental setup (Table 4.1). In that study, similar mixed flow dissolution experiments on mafic and ultramafic rocks (45-125 µm) were carried out at 25 ˚C and pCO_2 of 4 bar, continuously re-circulating the CO_2 in the system. The purpose of the study was to compare the steady-state silica release rates from basaltic glass (G), crystalline basalt (X) of similar chemical composition, as well as dunitic peridotite (P). The composition of these rocks, together with JdF, CD80WP132, and G1 samples from these study are summarised in Table 4.16, normalized to one mole of silicon.

Table 4.16: Composition comparison between basalts (JdF mix 1, JdF mix 2, JdF mix 3, and CD80WP132), and gabbro (G1) used in this study with the rocks used by Wolff-Boenisch et al. [2011] ,Critelli et al. [2014] and Gudbrandsson et al. [2011](G-basaltic glass; X-crystalline basalt; P-peridotite; MB-metabasalt). All the chemical compositions have been normalized to one mole of silicon.

	This study					Gudbrandsson et al. [2011], Wolff-Boenisch et al. [2011]			Critelli et al. [2014]
	JdF mix 1	**JdF mix 2**	**JdF mix 3**	**CD80WP132**	**G1**	**G**	**X**	**P**	**MB**
Si	1.000	1.000	1.000	1.000	1.000	1.000	1.000	1.000	1.000
Ti	0.029	0.026	0.026	0.019	0.002	0.025	0.025		
Al	0.322	0.331	0.323	0.302	0.452	0.365	0.329	0.017	0.346
Fe_{tot}	0.178	0.173	0.175	0.222	0.093	0.194	0.193	0.120	0.233
Fe(II)							0.174	0.120	
Fe(III)							0.019		
Cr	0.001	0.001	0.001	0.0005	0.001			0.005	
Mn	0.004	0.003	0.003	0.004	0.002	0.003	0.003	0.002	
Mg	0.195	0.227	0.202	0.233	0.368	0.294	0.310	1.639	0.472
Ca	0.268	0.306	0.275	0.282	0.408	0.263	0.273		0.272
Na	0.092	0.086	0.082	0.067	0.041	0.081	0.061		0.063
K	0.005	0.003	0.005	0.001	0.001	0.008	0.007		0.002
P	0.003	0.001	0.001	0.001	<0.001	0.004	0.003		
S	0.002	0.002	0.001	0.004	0.001				
O	3.435	3.468	3.370	3.388	3.865	3.403	3.374	3.795	3.727

Among the several experimental series performed by *Wolff Boenisch et al.*, the “SWC” focussed on the effect of the chemical components of seawater on dissolution rates. The initial values of this series, called “SWC-Cl”, represent the steady-state composition of the solution, making them the most suitable data for comparison. The Si dissolution rates as a function of pH are summarised in Figure 4.16, together with the elemental rates from all the experimental runs of this study. The Si release rates in *Wolff-Boenisch et al*. were generated using:

$$r_{Si} = \log\left[F * C_{Si}/(\mathrm{Ageo}_i * m)\right] \qquad (15)$$

where r_{Si} is the dissolution rate of Si expressed as log [mol/cm^2/s], F is the pump flowrate equal to 2 mL/min, C_{Si} is the concentration of Si in the outlet fluids in mol/L, A_{geo} the initial geometric surface area of sample i in cm^2/g, and m the initial mass of material in the reactor in g. No grain size distribution analysis was performed on the ground materials, and no Ca dissolution rates were measured.

The mafic and ultramafic rocks from *Wolff-Boenisch et al*. exhibit significantly higher rates than oceanic rocks in this study, even if the major cation chemistry is relatively similar (Table 4.16). The explanation can be related to three crucial factors: pCO_2, water/rock ratio, and experimental setup itself (Table 4.17).

Table 4.17: Summary of experimental conditions of current study and previous works.

	Reactor setup	**T** ˚C	**pCO_2** bar	**DIC** mM	**pH**	**Water/rock ratio** mL/g
This study	batch, seawater	40	1	<40	4.8	6-17
Critelli et al. (2014)	mixed flow	25	-	-	2 - 12	67-300
Wolff-Boenisch et al. (2011)	mixed flow, seawater	25	4	114	3.5	60-75
Gislason and Oelkers (2003)	mixed flow	25 - 50	-	-	2 - 12	n.a.
Gudbrandsson et al. (2011)	mixed flow	5 - 75	-	-	2 - 11	60-300

In the case of mixed-flow experiments the 4 bar pCO_2 led to ~114 mM of dissolved inorganic carbon in solution, which is two orders of magnitude higher than in these new batch experiments, resulting in a much lower pH of 3.5 (Table 4.16). The lower the pH, the higher the activity of H^+, and the higher the dissolution rate [*Gislason and Oelkers*, 2003; *Wolff-Boenisch et al.*, 2004]. Also, *Golubev et al.* [2005] found that silicate dissolution rates can be affected by the presence of higher CO_2 in solution, independently from the pH.

The second factor potentially responsible for the rate discrepancies, the water/rock ratio, was ~60-75 mL/g in the mixed-flow reactors, whereas ~6-17 mL/g in the HDPE bottles of this study, where only the top-surface always in contact with seawater was most probably reactive (Section 4.4.2.2). This means that the higher the water/rock ratio is, the higher the solid surface in contact with the reactive solution is, potentially resulting in a higher dissolution rate. This highlights the major role of the reactive mass quantification in the understanding of the extent and rate of rock dissolution.

Finally, the importance of the experimental setup in the measurement of dissolution rates has been observed by many authors [*Clow and Drever*, 1996; *van Grinsven and van Riemsdijk*, 1992], who measured higher rates with stirred ("mixed") batch reactors than with column experiments ("flow-through") or non-stirred batch reactors.

The dissolution rate dependency on general experimental settings is further confirmed by *Gislason and Oelkers* [2003] for basaltic glass mixed flow experiments at 25 and 50 ˚C as a function of pH, in an aqueous CO_2-free solution with lower ionic strength than seawater (0.1 and 0.7 mol/kg, respectively) (Table 4.17, and Figure 4.16). The 25 and 50 ˚C elemental dissolution curves, which were obtained by a multioxide dissolution model, are closer to the dissolution rates of the samples used in this batch reactor study, and show slower rates than *Wolff-Boenisch et al.*, despite the common mixed flow setup (Figure 4.16).

Hence, all the previously listed factors are potentially affecting the dissolution rate, but this discrepancy seems to be mainly driven by the pCO_2 conditions.

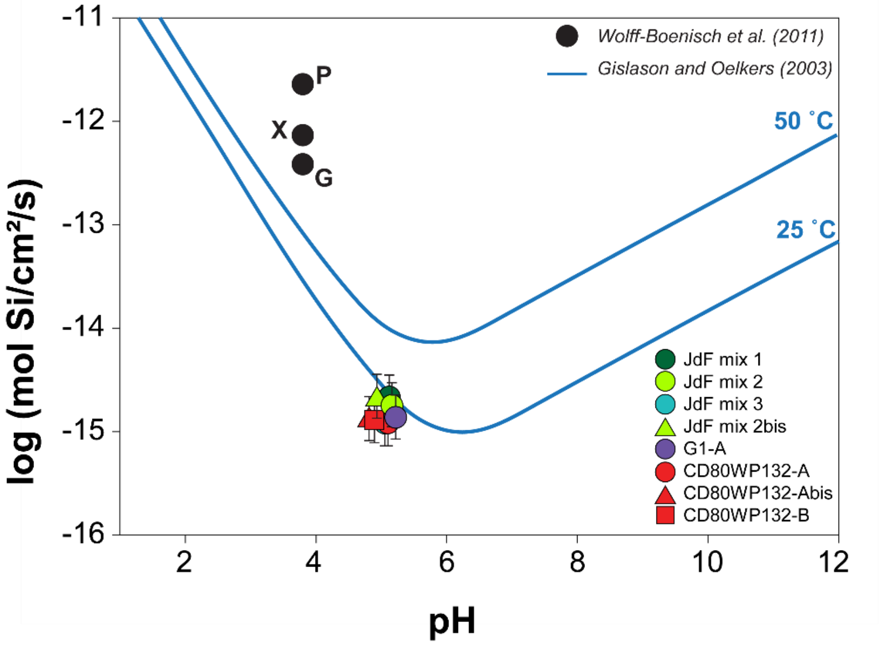

Figure 4.16: Si release rates "surface corrected" as a function of pH, for all the experimental runs of this study at 40 ˚C (coloured symbols) and for SWC-Cl series from Wolff-Boenisch et al. [2011], where G-basaltic glass, X-crystalline basalt, and P-peridotite. The blue lines indicate the overall dissolution rates proposed by Gislason and Oelkers [2003] for basaltic glass mixed-flow experiments at 25 and 50 ˚C as a function of pH, based on multioxide dissolution model. Error bars correspond to a ±0.2 log unit estimated uncertainty calculated from the precision of Si concentrations measurements (Appendix "Methods" CH4-2, IAPSO error).

The whole rock Si release rates "surface corrected" from this study can also be compared with the elemental release rates obtained by *Critelli et al.* [2014], and *Gudbrandsson et al.* [2011], following Equation 15 (Table 4.2, and Figure 4.17). The authors carried out mixed-flow dissolution experiments on a metabasalt from an ophiolitic sequence (Monte Reventino, Italy), and a crystalline basalt from the Stapafell Mountain (SW-Iceland), respectively, at pH from 2 to 12, temperatures from 5 to 75 ˚C, and water/rock ratio of ~60-300 mL/g, to investigate the steady state elemental release rates in a CO_2-free aqueous solution (Table 4.17). The rock mineralogy is summarised in Table 4.18, whereas the XRF bulk analyses, normalized to one silicon, are shown in Table 4.16. The crystalline basalt used by *Gudbrandsson et al.* is the same as the X-crystalline basalt described by *Wolff-Boenisch et al.*

Table 4.18: Summary of rock mineralogy for metabasalt [Critelli et al., 2014], and crystalline basalt [Gudbrandsson et al., 2014] used during dissolution experiments. The relative mineral content is given in wt% and vol%, respectively.

	Critelli et al. [2014]	***Gudbrandsson et al. [2011]***
Amphibole, actinolite	50.0	-
Calcite	1.0	-
Epidote	9.0	-
Glass	-	4.2
Iron oxides	-	4.7
Olivine	-	15.8
Phyllosilicate, chlorite	32.0	-
Phyllosilicate, phengite	1.0	-
Plagioclase, albite	7.0	-
Plagioclase, labradorite	-	41.3
Pyroxene	-	34.0

Figure 4.17 shows how the Si release rates from this study are broadly in agreement with the elemental rates measured at 25 ˚C by *Critelli et al.* [2014], and *Gudbrandsson et al.* [2011] for pH ~5, lying across the labradorite [*Gudbrandsson et al.*, 2011; *Oxburgh et al.*, 1994] and hornblende [*Golubev et al.*, 2005] dissolution curves estimated for 25 ˚C. These hornblende dissolution rates proposed by *Golubev et al.* are further confirmed by the actinolitic values computed by *Critelli et al.* from the whole rock rates.

Furthermore, *Gudbrandsson et al.* also proposed whole rock Ca dissolution rates for a range of pH (Figure 4.18). All the Ca release rates investigated in this thesis seem to be slightly faster than X-crystalline basalt, especially for the gabbro and the two JdF samples “mix 1” and “mix 2” (Figure 4.18). This rate difference is most probably related to the mineralogy (Figure 4.18). In general, this comparison confirms the preferential dissolution of Ca at pH ~5 in all the rocks investigated during the several experimental runs, and suggests a major role of calcite, and plagioclase and/or amphibole composition in Ca dissolution rates.

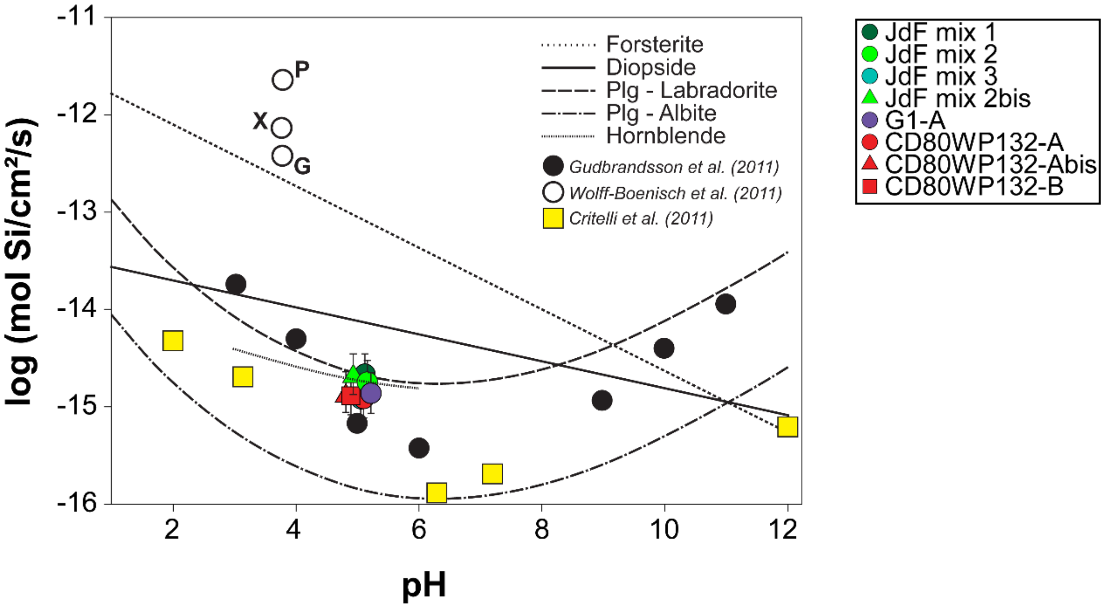

Figure 4.17: Whole rock Si dissolution rates "surface corrected" for all the experimental runs as a function of pH (coloured symbols), compared to experimental results of Critelli et al. [2014], Gudbrandsson et al. [2011] at 25 °C, and Wolff-Boenisch et al. [2011]. The forsterite, diopside, albite, and hornblende rates at 25 °C illustrated in this figure are taken from Pokrovsky and Schott [2000], Knauss et al. [1993], Chou and Wollast [1985], and Golubev et al. [2005], respectively. The labradorite curve was taken from Gudbrandsson et al. [2011], who in turn obtained it multiplying the albite dissolution curve of Chou and Wollast [1985] by 4 to fit the bytownite and andesine rate data taken from Oxburgh et al. [1994]. Error bars correspond to a ±0.2 log unit estimated uncertainty calculated from the precision of Si concentrations measurements (Appendix "Methods" CH4-2, IAPSO error).

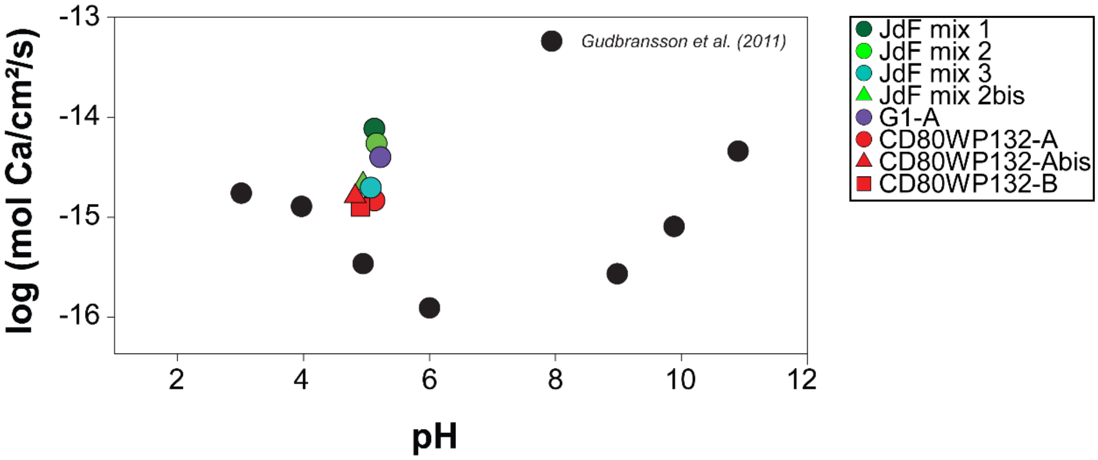

Figure 4.18: Whole rock Ca dissolution rates "surface corrected" for all the experimental runs as a function of pH (coloured symbols), compared to the experimental results of Gudbrandsson et al. [2011] at 25 °C. Size of symbols correspond to a ±0.01 log unit estimated uncertainty calculated from the precision of Ca concentrations measurements (Appendix "Methods" CH4-2, IAPSO error).

It should be noted that the Si dissolution rates measured by *Gudbrandsson et al.* [2011] (from -14 to -15 log (mol/cm^2/s)) are significantly lower than the one presented by of

Wolff-Boenisch et al. [2011] (-12 log (mol/cm^2/s)) (Table 4.2, Figure 4.17), even though they both conducted mixed flow experiments on crystalline rocks, using the same apparatus in the same laboratory, and a similar water-rock ratio (Table 4.17, and Figure 4.17). This means that, considering outputs at the same pH (i.e. pH ~3), the main factors potentially influencing this rate difference are pCO_2 [*Golubev et al.*, 2005], and the solution composition (Table 4.1). In fact, as described in Section 4.1, the behaviour of the NaCl contained in seawater, as well as a number of acids and bases in solution (such as H_2SO_4, HNO_3, F^-, NaOH, and $NaHCO_3$), and their catalytic effect on the Si dissolution rates, are described in a number of studies [*Gadikota et al.*, 2014a; *Kaszuba et al.*, 2005; *Oelkers*, 2001b; *Teir et al.*, 2007; *Wolff-Boenisch*, 2011; *Wolff-Boenisch et al.*, 2011].

The different experimental setup of *Gudbrandsson et al.* [2011] and *Critelli et al.* [2014] in comparison to this study (mixed flow and batch reactors, respectively) does not seem to significantly influence the experimental outcome (Figures 4.17 and 4.18).

Hence, further investigation on Si dissolution rates of JdF, CD80WP132, and G1 should be carried out with a variety of experimental setups, such as flow-through or stirred mixed-flow, varying pCO_2 values, and water/rock ratios, to have an improved perspective on their reactivity and to define the dependence on each experimental factor.

4.5. Conclusions

Geochemical trapping of CO_2 is part of a Carbon Capture and Storage mitigation strategy to reduce the CO_2 concentration in the atmosphere. This mechanism has been found to be more efficient (time required <1000 yr) in the presence of mafic and ultramafic formations, due to their fast cation release rates.

The aim of this chapter was to determine the dissolution rate in seawater-rock reaction experiments for oceanic rocks at low T (40˚C), and pCO_2 of 1 bar. The main findings are:

- the measurement of grain size distribution in the samples is essential for accurate interpretation of experimental results;
- the experimental setup adopted in this study lead to solution evaporation during the experimental run, resulting in a mass loss from 1 to 20% in each reactor. Therefore the evaporation extent has been measured using Cl, SO_4^{2-} concentrations, assuming these elements are conserved, and applied for correction to the resulting cation concentrations in solution;
- Si and Ca are the key elements to detect the release of cations from the solid to the seawater solution; other dissolved ions (e.g. Na, Mg, and K) do not show consistent chemical variations in the solutions with time due to their high concentrations in seawater;
- congruent dissolution was not reached most probably because of the formation of a passivation layer, enriched in Si and depleted in metals (e.g. Ca);
- incongruent dissolution during most of the elapsed time is due to reactions focussed on the surface of mineral grains;
- the mass balance calculations on Si and Ca concentrations suggest the presence of surface reaction mechanisms, showing that the top-surface only, with less than 1 g of rock involved in the reactions (assuming a full Si and Ca dissolution of grains with SiO=50 wt% and CaO = 12 wt%), could provide all the dissolved ions;

- at pH ~5, whole rock dissolution rates for Si and Ca range from -14.67 to -14.92 log (mol/cm^2/s), and from -14.10 to -14.88 log (mol/cm^2/s), respectively, and represents the closest rates to the stoichiometric dissolution;
- the similarity of Si release rate of ophiolitic gabbro and basalts, and the higher Ca release rate from the gabbro, JdF mix 1, and JdF mix 2 is perhaps one of the most significant observation of this study;
- the interpretation of Si and Ca dissolution rates identifies calcite, together with amphibole and plagioclase as main calcium sources in these batch dissolution experiments;
- overall, the crystalline samples used in this study show a similar or higher reactivity to Icelandic crystalline basalt [*Gudbrandsson et al.*, 2011], and metabasalt [*Critelli et al.*, 2014], both reacted in a mixed flow reactor at 25 ˚C, but lower than basaltic glass investigated by *Gislason and Oelkers* [2003], and *Wolff-Boenisch et al. [2011]*;
- solution composition, and pCO_2 conditions seem to affect the dissolution rate outputs from experiments carried out at similar temperature and pH, independently from the experimental setup;
- further investigations on JdF, CD80WP132, and G1 should be carried out with different experimental setups, such as flow-through or stirred mixed-flow, at varying solution compositions, pCO_2 and water/rock ratio conditions, to develop a more complete perspective on their reactivity and to define the extent of each experimental factors.

Chapter 5: Costs linked with offshore CO_2 sequestration projects in oceanic crust

5.1. Introduction

In the last decades, the strategy of storing carbon dioxide in geological formations to reduce anthropogenic CO_2 emissions to the atmosphere has started to be implemented, but is still developing scientifically and technologically [*IPCC*, 2005b]. To date, carbon storage is mainly undertaken in sedimentary formations, such as deep aquifer and depleted oil and gas fields – EOR [*Global CCS Institute*, 2015]. For instance, injection of CO_2 into the subsurface has been practiced for decades for EOR [*Al Eidan et al.*, 2015]. The cost of carbon storage is directly related to type of capture and transport facility, storage capacity, and reservoir utilisation [*Leung et al.*, 2014]. Among the studies and reports focused on the costs of CO_2 transport and storage in a CCS context (e.g. *Global CCS Institute* [2015]; *IEA* [2015]; *Rubin* [2008]), a growing number of articles consider offshore storage options (e.g. *Aspelund* [2010]; *Decarre et al.* [2010]; *Haugen et al.* [2009]; *McKinsey & Company* [2008]; *Rubin et al.* [2015]; *Svensson et al.* [2005]; *Torp and Brown* [2004]). However, in most studies, the scenarios and explanations are not sufficiently detailed to enable direct comparisons of proposed costs. The most comprehensive study on CCS costs has been carried out by the European Technology Platform for Zero Emission Fossil Fuel Power Plants (known as the ZEP – Zero Emissions Platform), which represents a coalition of stakeholders supportive of CCS [*ZEP*, 2011a].

Despite the potential advantages of carbon sequestration in mafic formations (Chapters 2, 3, and 4), the exploitation of oceanic crust for CCS purposes has not been considered because of the supposed high costs involved with offshore reservoirs. To the author's knowledge, there have been no publications to date that breakdown the expenditures associated with a CCS project in its entirety to allow the assessment of the economic feasibility of offshore strategies, leaving a number of questions unsolved. For example:

- What is the cost of offshore CO_2 sequestration?
- Specifically, what is the cost of offshore transport and storage of CO_2 in deep-sea basalts?
- What infrastructures are required?
- What are the main limitations related to offshore injection of CO_2?
- Are there economically feasible offshore locations for CCS projects in deep-sea basalts?

In this chapter, an attempt is made to address these questions, estimating the cost linked with offshore annual transport and storage of 20 Mt of CO_2 in the oceanic crust. The costs are considered for distances of 500, 1000, and 1500 km from the coast, and typical well injection rates of 0.5 to 3 Mt CO_2/yr. Finally, the overall costs related to a potential offshore CCS project in deep-sea basalts have been calculated for three scenarios, on the basis of water depth, with potential reservoirs located at 1000, 2500, and 5000 mbsl. Costs are giving in euros (€), and at the time of writing the exchange rate with US dollars is €1.00 = $1.13 [http://www.xe.com/currencyconverter/convert/?From=EUR&To=USD].

5.2. Costs for CO_2 transport offshore

Three distance-specific cases of CO_2 offshore transport are presented, with CO_2 costs based on ZEP estimations [*ZEP*, 2011a] and updated by Mr. Nils H. Eldrup (project manager at Tel-Tek and member of ZEP-transport working group). The ZEP report provides cost estimates for large-scale CCS, including costs for different pipes and ships for offshore networks.

Carbon dioxide from two point sources of 10 Mt/yr each (equal to 20x10^6 t/yr) is transported by ~10 km onshore feeders to a coastline port from where it is shipped to storage sites located 500, 1000, or 1500 km offshore (Figure 5.1). For example: a typical coal plant with a capacity of 1000 MW, is able to power up to 1 million houses, and produces ~6 Mt of CO_2 per year. Consequently, the shipping of 20 Mt/yr of CO_2 corresponds to the cumulative annual emissions of at least three of these power stations.

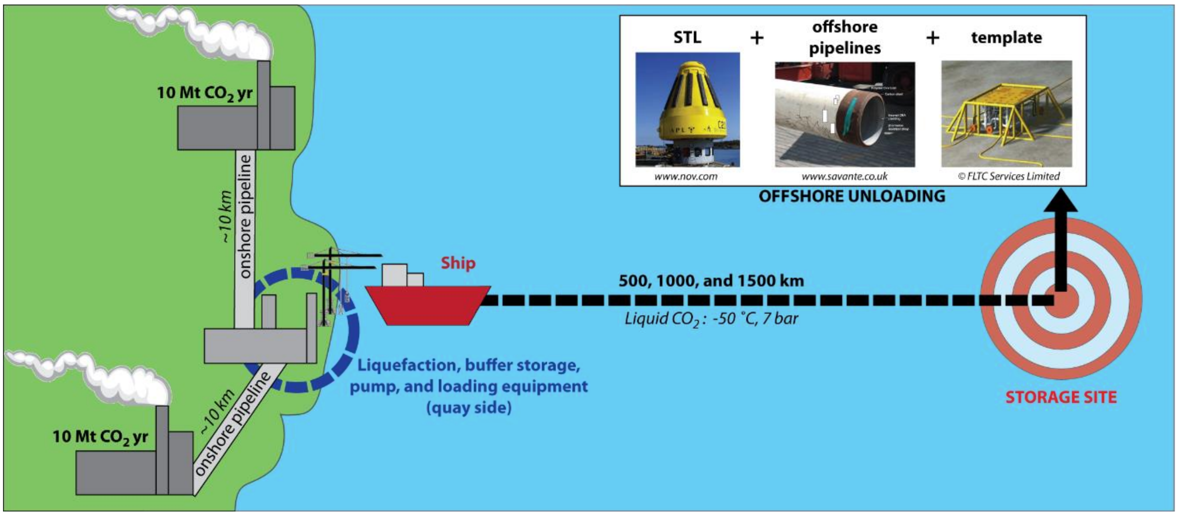

*Figure 5.1: Network of CO_2 offshore transport via ship, from two point-sources (2 * 10 Mt CO_2/yr) along the coastline to a storage site at 500, 1000, or 1500 km from shore. STL = Submerged Turret Loading.*

Ship transport costs have been estimated following the assumptions listed below [*ZEP*, 2011a]:

- the loading equipment and functional quay facilities are in existence, and the loading time is set at 12 h;
- the liquefaction plant on the coast delivers CO_2 at 7 bar (0.7 MPa) and -50 ˚C to the storage tanks; these pressure and temperature conditions have been chosen to meet the best cost/requirement ratio [*Svensson et al.*, 2005], and to avoid any risk of formation of dry ice;
- the transport process is assumed to deliver the CO_2 to the well-head at the storage site in the following condition:
    - temperature = ambient seawater temperature from 4 to 15 ˚C;

  - pressure = 60 barg (6 MPa) - barg, or “*gauge pressure*”, is equal to absolute pressure minus atmospheric pressure;
- the maximum cargo capacity per ship is equal to 40,000 m^3 (~1x10^9 mol of CO_2);
- the average ship speed is 12 knots (~22 km/h);
- no intermediate offshore storage is assumed to be necessary and results in an intermittent injection into the wells with a discharge time set at 48 h;
- CAPEX (capital expenditure) is calculated for a project lifetime of 25 years with an interest rate of 8%, based on the weighted average cost of capital (WACC);
- OPEX (annual operational expenditure) is based on actual operating cost experience: crew costs, maintenance, fuel costs, and port fees;
- Cost estimate accuracy = ±30%.

In addition to the cost of transport distance from shore, ship transport also includes the costs of liquefaction, a storage ship with dynamic positioning and unloading buoy (*STL-Submerged Tool Loading*™), and flexible pipelines to the seafloor limited to a first *template* (supporting structure on the seabed). Details on the transport facilities and relative transport costs are summarised in Tables 5.1 and 5.2, respectively.

The *STL system* consists of a conventional cargo tanker which connects/disconnects to a submerged cone-shaped turret buoy, which in turn is catenary moored to pile anchors [*Wall et al.*, 2002]. The mooring buoy can be simply disconnected from the transport ship, where it would float in an equilibrium position about 30 – 50 m below the sea surface. A vessel equipped with *STL* tools is capable of staying moored to the transfer system at a location offshore and perform its function even in severe weather conditions. In general, 3 to 4 buoys have been considered in the estimations for all the scenarios, but this number may be greater for larger scale projects, because it is a function of the number of wells and ships involved.

Both the *STL system* and offshore pipelines have been designed to be capable of holding at 250 barg, which corresponds to water depth of ~2500 m.

The *template* is a steel protection structure with integrated manifolds and wellheads, and is considered to be a four-slot subsea terminal with a 50 km control cable to a platform or an on-site vessel. A typical example of a vessel permanently moored to the seabed is the FPSO for LNG: Floating Production Storage and Offloading system for Liquefied Natural Gas. The LNG FPSO is a floating facility usually installed above or close to an offshore gas field in order to receive, process, liquefy, store and export natural gas. The first LNG platform, as well as the largest offshore facility (488 m long, 74 m wide) ever constructed is the "Prelude FLNG (Floating Liquefied Natural Gas)", located in the Browse Basin (NW Australia). At full load, it displaces more than 600,000 t (0.6 Mt), and cost ~€9 billion.

The costs for a platform or vessel, beside the cargo ships, are not taken into account in these estimations. The costs of manifolds for wells, drilling of standard injection wells, and connecting offshore pipelines are assumed to be part of the storage costs (Section 5.3, Table 5.3) [*ZEP*, 2011b].

Table 5.1: Details of the facilities and timings for which the cost estimations are based.

Distance	km	500 km	1000 km	1500 km
Ship	nº	7	9	12
Roundtrip per ship	nº/yr	70	50	39
Roundtrip time	days	5	7	9
Sailing time (one way)	h	22	45	67
STL Buoy	nº	4	3	3

Following the ZEP report assumptions, at ship transport conditions (-50 ˚C, 7 bar) CO_2 density is equal to 1155 kg/m^3, and the potential mass of transportable CO_2 for a ship with capacity of 40,000 m^3 is 0.046 Mt per journey. This means that a total of 435 discharges of full cargo ships are needed per year to achieve the target of 20 Mt of total annual injectivity. A fleet from 7 to 12 ships, together with an appropriate number of STL buoys, is required, depending on the reservoir offshore distance, to deliver the expected 20 Mt of CO_2 at the storage site (Table 5.1). Also, considering 48 h as the assumed constant discharge time, and one template, the injection rate in each of the four wells is ~240 t/h.

The transport of 20 Mt of CO_2 per year via ship at 500 km from the shore (Table 5.2) can be estimated using the following formulas (Equations 1 and 2):

$$Capital\ 1st\ year = CAPEX_{f+s} + OPEX_{f+s} + annuity \tag{16}$$

$$Capital\ following\ years = OPEX_{f+s} + annuity \tag{17}$$

where $CAPEX_{f+s}$ are the CAPEX costs for onshore feeders and ship transport [M€], $OPEX_{f+s}$ the OPEX costs for onshore feeders and ship transport [M€/yr], $annuity$ the fixed sum to be paid per year [M€/yr]. This type of transport requires at least ~€1233 M (€1233x10^6) during the first year (Equation 1), and ~€186 M for each of the following years (Equation 2). The correspondent transport costs for 1500 km as offshore distance are estimated to be ~€1845 M during the first year, and ~€254 M for each of the following years (Table 5.2). Hence, the transport of 20 Mt of CO_2 per year, for the whole project lifetime of 25 years, ranges from ~€5.70 to ~€7.95 B (Table 5.2).

*Table 5.2: Cost estimates for CO_2 offshore transport via ships, from two point-sources (2 * 10 Mt CO_2/yr) along the coastline to a storage site located 500, 1000, or 1500 km from shore.*

Distance	km	500			1000			1500		
		CAPEX M€	**OPEX** M€/yr	**Annuity** M€/yr	**CAPEX** M€	**OPEX** M€/yr	**Annuity** M€/yr	**CAPEX** M€	**OPEX** M€/yr	**Annuity** M€/yr
Feeders onshore	2*10 Mt/yr	30.1	0.1		30.1	0.1		30.1	0.1	
Ship transport		860.0	156.3	29.7	1071.0	178.9	38.1	1355.0	204.9	49.4
TOTAL	M€/yr	890.1	156.4		1101.1	179.1		1385.1	205.0	
TOTAL for 20 Mt/yr	M€/yr	5700			6710			7950		
TOTAL CO_2 costs	€/t	11.4			13.4			15.9		

5.3. Costs for CO_2 storage offshore

The storage cost estimations [*Eldrup, personal communication, February 2016*] (Table 5.3) take into account manifolds and corresponding templates for wells, connecting offshore pipelines, drilling and casing of injection wells.

Several scenarios, based on the more typical well injectivity ranging from 0.5 to 3 Mt/yr, are presented to estimate the costs of the required offshore storage facilities for a reservoir able to store 20 Mt of CO_2 per year.

The well properties and drilling costs are those for cased holes drilled into sedimentary formations, with depth up to 3000 mbsf, which are characteristic of hydrocarbon production fields [*ZEP*, 2011b].

Table 5.3: Cost estimates for four offshore scenarios, each able to store 20 Mt CO_2 per year, taking into account injection rate, number of wells, pipeline distance and template.

Annual injection rate	**Injection rate**	**Number of wells**	**Well cost**	**Pipeline distance**	**Pipeline cost**	**Pipeline end module cost**	**Template cost**	**Total CAPEX cost**
Mt/yr	t/h		M€	km	M€	M€	M€	M€
0.5	57	40	2000	276	414	380	1120	3914
1	114	20	1000	136	204	190	560	1954
2	228	10	500	60	90	76	280	946
3	342	7	350	36	54	38	196	638

If the annual well injectivity increases from 0.5 to 3 Mt CO_2, the injection rate must increase from 57 to 342 t/h, resulting in a decrease in the number of injection wells required. This approach is due to the reservoir pressure, which is one of the most limiting factors for large scale geological storage and directly depends on the injection rate, formation permeability, thickness of formation, viscosity and compressibility of CO_2 [*Maroto-Valer*, 2010; *Mathias et al.*, 2009]. The bottom-hole pressure should exceed the formation pressure to avoid the influx of *in situ* fluids into the wellbore [*Bachu and Gunter*, 2004]. However, to meet the safety criteria for prevention of hydraulic fracturing of the reservoir, regulations stipulate that the bottom-hole pressure should not exceed 90% of the fracturing pressure [*IEAGHG*, 2010], which is defined by *Hubbert and Willis* [1972] as (Equation 3):

$$Pfr = \sigma_{min} + Pf \qquad (18)$$

where Pfr is the fracturing pressure, σ_{min} the minimum principal stress, and Pf the formation pressure (hydrostatically calculated). The fracturing pressure is the pressure at which the rock breaks, and the variation of pressure required to induce a fracture with depth is called the fracture gradient. An increase in the fracture gradient (i.e. at greater depth) corresponds to an increase in the maximum injection pressure. Consequently, in the case of a field with high reservoir pressure, it is viable to inject more CO_2 (high injection rate of 342 t/h), and the number of wells needed is reduced, along with the relative costs [*IEAGHG*, 2010].

In order to reach the target of 20 Mt of CO_2 stored annually in offshore reservoirs, the number of wells required varies from 40 to 7, with relative injection rate of 57 to 342 t/h, respectively. However, at constant discharge time of 48 h (Section 5.2), the number of wells needed to accommodate the content of one ship cargo (0.046 Mt CO_2) varies from 17 to 3, respectively, depending on the injection rate.

The CAPEX for the storage of 20 Mt of CO_2 per year in 40 available injection wells, each with injectivity of 0.5 Mt CO_2/yr, is estimated to be at least ~€3914 M, whereas for an higher injectivity of 3 Mt CO_2/yr in 7 available injection wells it would be ~€638 M (Table 5.3). Although the last option offers a more cost-effective injection scenario, it will require reservoirs with particularly good hydraulic and physical properties to keep the site suitable for CO_2 storage.

5.4. Summary of costs for CO_2 transport and storage offshore

Theoretically, if the total costs associated with the transport of 20 Mt/yr of CO_2 at reservoirs located 500 km from the shore, are added to the storage costs of seven wells with 3 Mt CO_2/yr annual injection rate each, ~€1.7 B would be necessary during the first year. If the transport distance increases by 3 times to 1500 km, the first year required capital does not triple, but increases to ~€2.3 B. If the storage site is at 500 km offshore and the costs are related to forty wells, each with 0.5 Mt CO_2/yr as annual injection rate, ~€5.0 B would be necessary during the first year.

This means that the cheapest scenario for both transport and storage cost estimations includes a reservoir located 500 km from the shore, comprising seven injection wells each with 3 Mt CO_2/yr injection rate, and the 20 Mt of CO_2 per year delivered by a fleet of 7 ships (Table 5.4). On the other hand, the most expensive options involve a storage site at 1500 km from the coastline, with 40 wells that have 0.5 Mt CO_2/yr annual injection rate, and a fleet of twelve ships (Table 5.4). Hence, taking into account the project lifetime of 25 years, the transport and storage of 20 Mt of CO_2/per year offshore would require in total from ~€6.3 B to ~€11.9 B.

Table 5.4: Summary of cost estimations for transporting and storing 20 Mt of CO_2 per year, in a 25-years long offshore project. "Scenario A" represents the cheapest option, whereas "scenario B" the most expensive one.

	Transport distance km	**Number of ship**	**Number of wells**	**Annual injection rate** Mt/yr	**TOTAL COSTS** B€
SCENARIO A	500	7	7	3	~6.3
SCENARIO B	1500	12	40	0.5	~11.9

5.5. Costs for CO_2 sequestration in deep-sea basalts

The costs of transport and storage of 20 Mt/yr of CO_2 offshore have been estimated for reservoirs at water depth <2500 m and sediment thickness below the seafloor up to 3000 m [*ZEP*, 2011a; b]. No calculation has been found concerning reservoirs located in deeper waters, up to 5000 m. Yet, the majority of the oceanic crust areas highlighted for combined gravitational and physical CO_2 trapping are located at water depths greater than 5000 m (Figure 5.2).

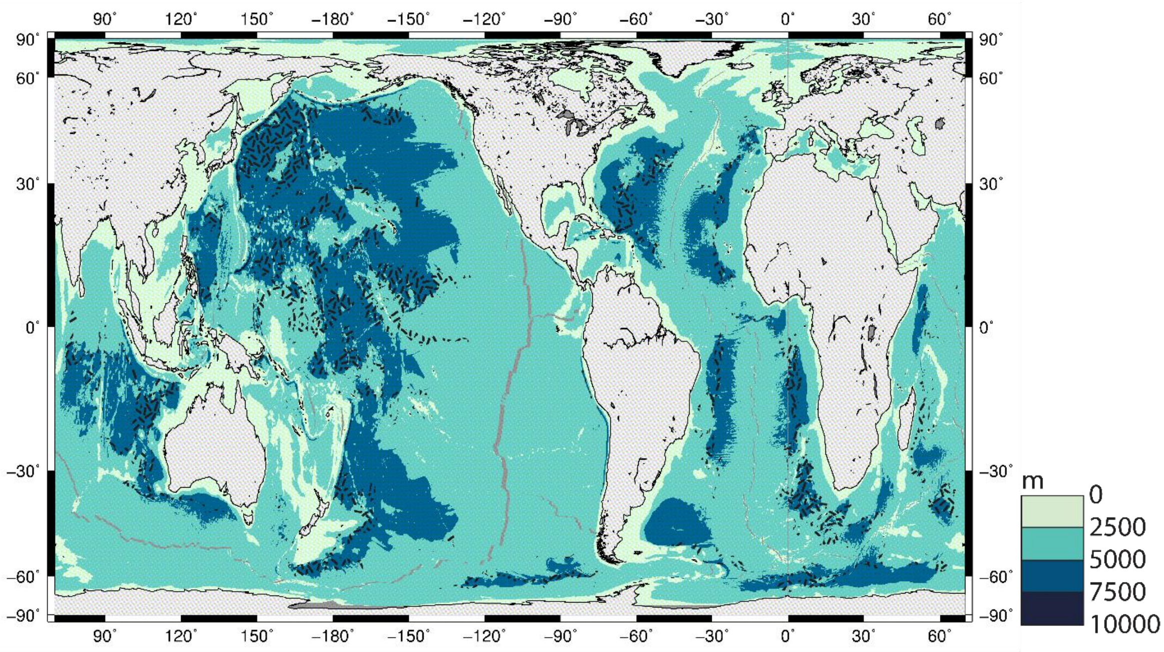

Figure 5.2: Bathymetric map of all the ocean, with contours every 2500 m. Locations for stable geological sequestration of CO_2 at the sediment-basement interface are shown by the black dashes.

However, if only gravitational trapping at the sediment-basement interface (Figure 5.3) is required, the extent of these areas potentially suitable for geological CO_2 storage in deep-sea basalts significantly increases. In particular, a new group of targets become available at shallower water depths, ranging from 2500 to 5000 m, but mostly further offshore. These depths are still greater than those considered in the cost estimations, but more accessible in terms of technological feasibility of CCS in offshore reservoirs.

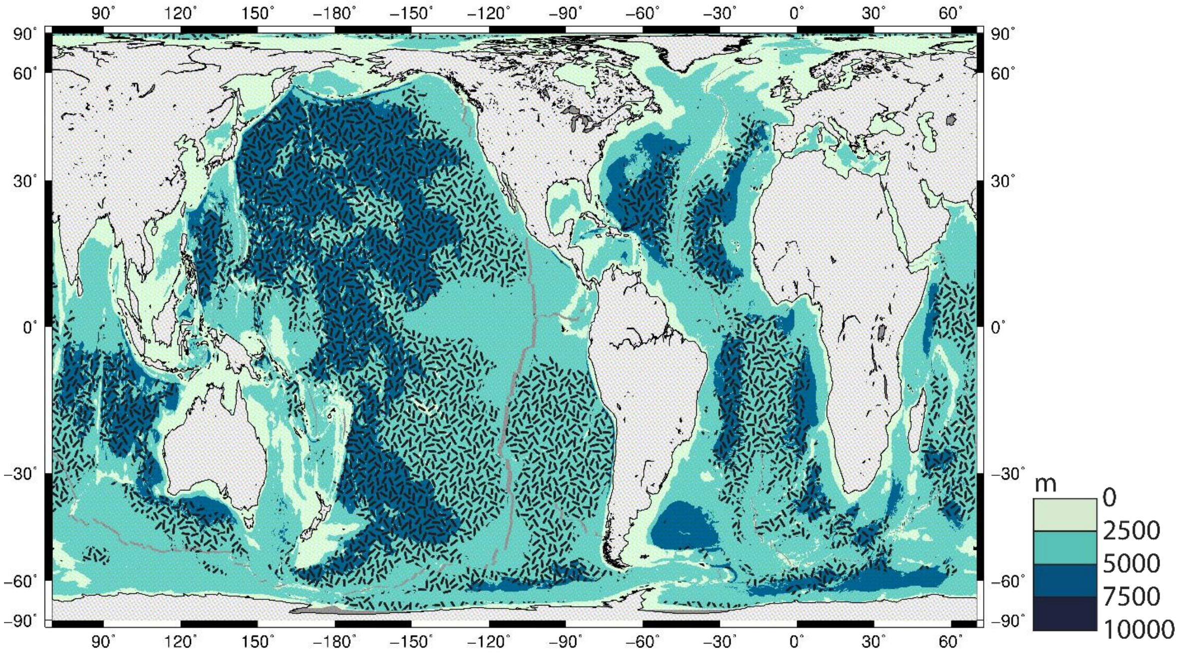

Figure 5.3: Bathymetric map of all the ocean, with contours every 2500 m. Locations for gravitational trapping of CO_2 ($\rho_{CO2} > \rho_{seawater}$) at the sediment-basement interface are shown by the black dashes.

In order to qualitatively scale up the cost estimations to deeper water depths, corresponding to locations for stable geological sequestration of CO_2 in deep-sea basalts, the IODP drilling time estimator [http://iodp.tamu.edu/participants/coring estimator.html] has been used to calculate several scenarios (Figure 5.4). This evaluation is based on the reasonable assumption that the total costs are proportional to the time spent for drilling wells at the storage site. Also, technological development is required to ensure the application of the transport facilities described in this study, particularly the STL system, for greater water depths, up to 5000 m.

For each of three water depths (1000, 2500, and 5000 m), three drilling conditions have been considered: **a-** 200 m of sediments and 300 m of basement, **b-** 3000 m of sediments, **c-** 700 m of sediments and 300 m of basement. Scenario **a** represents the minimum condition of combined gravitational and physical trapping (Chapter 3); scenario **b** the typical conditions of hydrocarbon production fields, which are included in the cost calculations (Section 5.3); scenario **c** the maximum amount of sediments for combined gravitational and physical trapping (Chapter 3).

To penetrate these rock thicknesses, the IODP calculations consider a rotary drilling (RCB) approach, with penetration rates decreasing from ~30 m/h (for sediments), to ~4.5 m/h (for the first 50 m of basement), ~3.0 m/h (for the next 100 m), and ~2.0 m/h (thereafter).

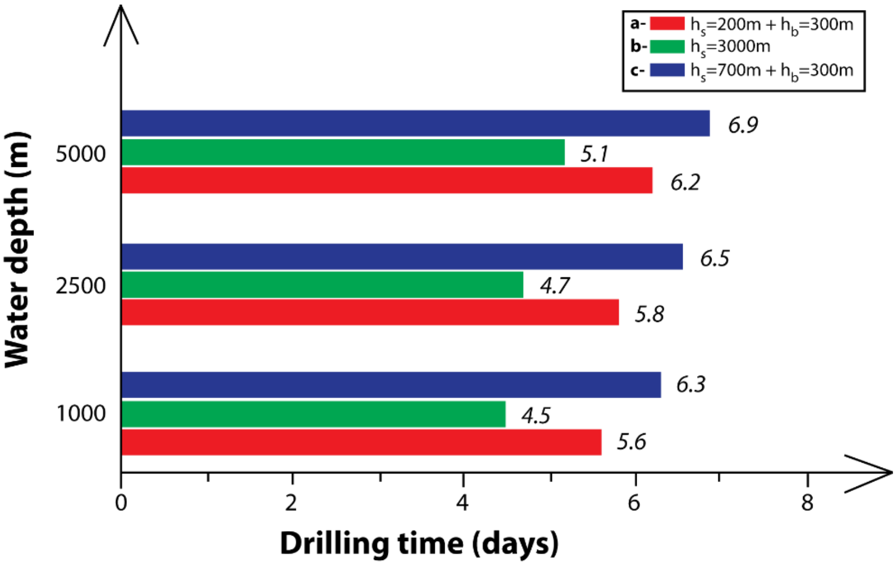

Figure 5.4: Summary of drilling times for several scenarios of water depth, sediment (h_S) and basement thickness (h_b) [http://iodp.tamu.edu/participants/coring estimator.html].

In general, the IODP drilling time results highlight that the cost associated with drilling of up to 3000 m of sediments (scenario **b**) are lower (~30%) than the costs associated with combined gravitational and physical trapping (scenarios **a** and **c**), for all water depths. On the other hand, the increase in water depth increases the drilling time. Particularly, the transition from 2500 to 5000 m of water leads to an increase in drilling time by a factor of ~1.1 on average (~10%).

Translated into costs, these results suggest that to scale a CCS project up to 5000 m water depth, as in the case of deep-sea basalts, capital costs should increase by ~1.4 times (~40% increase). For example, taking into account a project lifetime of 25 years, the transport and storage of 20 Mt of CO_2 at a reservoir located 500 km offshore, at ~5000 m of water depth, would require in total a minimum of ~€8.8x10^9 (Table 5.5), which almost corresponds to the cost of the Prelude FLNG (see Section 5.2.). Also, given the total volume of 500 Mt of CO_2, the cost of storing carbon dioxide for the 25 year-long project in deep-sea basalts at ~5000 m water depth ranges from ~18 €/t (500 km) to ~33 €/t (1500 km). Only the lowest estimation is comparable with the current injection costs in the Sleipner project that correspond to 17 $ per tonne of CO_2 (~15 €/t) [www.aapg.org/publications/blogs/energy-policy/article/articleid/12373], and in the Weyburn-Midale project that are 20 $ per tonne of CO_2 (~18 €/t) [www.sequestration.mit.edu/tools/projects/weyburn.html], with the difference that the latter two projects include the monitoring system. On the other hand, the costs associated with the *ex situ* mineral carbonation option have been estimated to be at least ~54 $ per tonne of CO_2 (~48 €/t), with separation and transportation costs for CO_2 not included [*Gerdemann et al.*, 2007]. *Rubin* [2008] determined that the CO_2 capture step accounts for up to ~80% of the whole CCS project costs. For example, the CO_2 captured through the most common post-combustion technique is estimated to cost between 48 and 68 $ per tonne of CO_2 (~42-60 €/t) [*Rubin et al.*, 2015].

More generally, it is also important to contextualise these cost estimations to better understand the potential CCS role within a global energy market. To date, the price for a barrel of crude oil (~0.136 t of crude oil) is ~$50 [www.nasdaq.com/markets /crude-oil], which corresponds to ~€315 per tonne of oil. Given that 1 tonne of crude oil produces ~3.2 t of CO_2 [*EPA*, 2015], 1 t of CO_2 is emitted for every ~€100 invested in crude oil. For comparison, the storage of that same tonne of CO_2 would cost between ~12.6 to ~33.3 €/t when associated with a 25 years transport and storage CCS project offshore. Furthermore, the global subsidies given to fossil fuel extracting companies in 2011 amounted to $4200x$10^9$ (~€3770x10^9), and increased to $5300x$10^9$ (~€4760x10^9) in 2015 [*Coady et al.*, 2015]. For purpose of comparison, the total costs needed during the first year of a CCS project, involving the transport and storage of 20 Mt of CO_2, at reservoirs located 500 km offshore, and with seven injection wells, at water depth of 2500 m, are ~€1.7x10^9; the same project has a total cost of ~€6.3x10^9 during its whole lifetime of 25 years (Chapter 5). These values corresponds to only ~0.03 and ~0.13%, respectively, of 2015 global subsides for fossil fuel extraction companies.

Table 5.5: Comparison of total cost estimations for transporting and storing 500Mt of CO_2 in 25 years in deep-sea basalts located at water depth of ~2500 and ~5000 m, for two distance scenarios (500 and 1500 km, respectively).

Distance from shore	**Water depth = 2500 m**		**Increasing factor**	**Water depth = 5000 m**	
	Total costs	**Cost CO_2**		**Total costs**	**Cost CO_2**
km	x10^9 €	€/t		x10^9 €	€/t
500	~6.3	~12.6	40%	~8.8	~17.6
1500	~11.9	~23.8		~16.7	~33.3

5.6. Conclusions

The majority of the information available to estimate the costs of geological storage of carbon dioxide offshore are restricted to sedimentary reservoirs for hydrocarbon production, due to the difficulties and high costs associated with offshore EOR projects. In this chapter, a general estimation of the costs for transport and storage of CO_2 offshore has been attempted, together with a number of limitations and constraints on its applicability on a broader scale. The results can be summarised as follow:

- the CO_2 costs linked with ship transport and storage in offshore formations can be estimated for reservoirs at water depth < 2500 m and assuming injection wells are drilled into sediments;
- the suitable sites for combined gravitational and physical trapping at the sediment-basement interface are located in water depths >5000 m, whereas some of the areas defined by gravitational trapping are characterised by bathymetry between 2500 and 5000 m;
- the total costs for a 25 year-long CCS project, involving the transport and storage of $20x10^6$ t of CO_2 per year at reservoirs located 500 to 1500 km offshore, in water depth up to 2500 m, are estimated to range from ~€$6.3x10^9$ to ~€$11.9x10^9$;
- assuming proportionality between cost and drilling time, the corresponding total costs for a 25 year-long CCS project scaled up to 5000 m of water depth have to be multiplied by a factor of ~1.4;
- the transport and storage of 500 Mt of CO_2 over 25 years in a deep-sea basaltic reservoir located 500 km offshore, at water depths of 5000 m, would require in total a minimum of ~€$8.8x10^9$ for capital and operational costs, and the cost of carbon dioxide for the whole project would be ~18 €/t.

Chapter 6: Discussion and conclusions

6.1. Results summary

The primary goal of this thesis was to better understand the potential of the oceanic crust as a reservoir to store anthropogenic CO_2. For this purpose, several methodologies were applied: A) to illustrate the phase relationship of carbon dioxide in the seafloor; B) to explore the feasibility of carbon sequestration in deep-sea basalts based on gravitational and physical trapping at the sediment-basement interface; C) to determine the dissolution extent and rate of dissolution of oceanic rocks in batch experiments at low T, pCO_2 of 1 atm, and using seawater as a solution; and D) to explore the economic costs of transport and storage of CO_2 in offshore reservoirs.

The main outcomes of this work are: 1) carbon dioxide is denser than seawater only for pressures greater than 27 MPa (~2700 m of water) and temperatures between 0 and 30 ˚C; 2) regions characterised by thermodynamically stable liquid CO_2 are generally located in old oceanic crust covered by a relatively thin layer of sediments; 3) the combination of gravitational and physical trapping limits the oceanic crust suitable for CCS to ~8% of its area, but highlights five potential targets where even the smallest identified reservoir could provide sufficient carbon dioxide sequestration capacity for several centuries of anthropogenic CO_2 output; 4) based on the low temperature batch experiments in a CO_2-seawater-rock system, Ca and Si are key elements detecting the dissolution of cations from the solid to the aqueous solution; 5) plagioclase and, if present, amphibole and calcite are the reactive minerals providing Ca in the batch dissolution experiments, and their composition determines the different Ca release rates of studied rocks; 6) the total costs for CCS projects with a lifetime of 25 years, involving the transport and storage of 20 Mt of CO_2 per year, in deep-sea basaltic reservoirs located 500 and 1500 km offshore, respectively, and in water up to 5000 m deep, are estimated to be ~€$8.8x10^9$, and ~€$16.7x10^9$, respectively; 7) the corresponding total costs per tonne of CO_2 transported and stored are estimated to be ~18 €/t, and ~33 €/t, respectively.

6.2. CO_2 trapping mechanism implications

The three trapping mechanisms proposed to geologically store the CO_2 in offshore mafic and ultramafic formations are: gravitational (Chapter 2), physical (Chapter 3), and geochemical. In this study, only the dissolution reactions involved with the early stages of geochemical trapping have been investigated (Chapter 4).

In this thesis, the maximum storage stability is reached with the combination of gravitational and physical trapping mechanisms (Chapter 3), but at these conditions the CO_2 sequestration in deep-sea basalt does not represent an economically viable option (Chapter 5, and Section 6.5). However, the advantages and disadvantages of these mechanisms are discussed individually.

If only a thick layer of sediments above the oceanic basement, ranging from 200 to 700 m (*physical trapping*), is considered as a trapping mechanism, ~32% of the seafloor is suitable for CO_2 storage in mafic formations (Chapter 3). However, much of this region is characterised by temperatures and pressures that make CO_2 much less dense than seawater at the sediment-basement interface (Chapter 2), due to the shallower bathymetry. This means that the CO_2 would have a tendency to rise towards the seafloor, driven by buoyancy, instead of sinking into the basement. Also, the locations showing effective physical trapping would have to be validated in terms of cap rock integrity, permeability, stratigraphy, and hydrodynamic fluid dispersion (Chapter 1).

On the other hand, if the only requirement for CO_2 storage is that CO_2 is denser than seawater at the sediment-basement interface (*gravitational trapping*), as much as ~48% of oceanic crust is available (Chapter 3). CO_2 injection at these sites would have the advantage of trapping the CO_2 in the basement. These circumstances, together with the presence of water depth up to ~5000 m for reservoirs ~500 km from the coast, or shallower water for reservoirs up to 1500 km from the shore, could represent more economically feasible scenarios for the application of CCS offshore (Chapter 5). For example, a more detailed investigation of *target **a*** (offshore Western Australia) highlights the presence of several square kilometres of oceanic crust, located <500 km from the southern coast of Western Australia in deep waters up to ~5000 m (*target **a1*** - Chapter 3), that satisfies the more economical conditions for gravitational trapping only (Chapter 5).

In this thesis, the application of combined physical and gravitational trapping in offshore reservoirs as a CO_2 storing mechanism, independently from the mineral carbonation potential of basalts, identifies numerous suitable locations (Chapter 3), with CO_2 stable in a liquid state. However, these locations would not provide ideal conditions for geochemically trapping the CO_2. The high pressures, low temperatures, and liquid phase of carbon dioxide described in this thesis (Chapter 2) would create solubility issues, based on literature data. In a liquid state, CO_2 takes over hundreds of years to dissolve in the formation brine [*Hirai et al.*, 1997; *House et al.*, 2006]. A potential way to overcome this problem is to accelerate the dissolution through mixing the CO_2 in seawater prior to its injection – solubility trapping (Chapter 3) [*Gislason and Oelkers*, 2014; *Matter et al.*, 2011]. This process was partially simulated in the batch experiments, where gaseous CO_2 was maintained fully dissolved in solution (Chapter 4). However, the suggested approach involves i) very large quantities of seawater, ii) the presence of porous rocks to not over pressurise the reservoir with the huge amount of pumped water, and iii) increase in storage costs due to the process of dissolving CO_2 in solution prior to its injection (Chapter 3).

6.3. Carbon sequestration on mid-ocean ridge flanks

One of the main reasons to look at the oceanic crust as a carbon storage reservoir is linked to the vast size of porous basement, where CO_2 can be fixed in mafic and ultramafic rocks through carbonate mineral formation (Chapters 2 and 4). Many studies on natural analogues, represented by carbonate veins within the basement, suggest the mid-ocean ridge flanks are potential locations for CO_2 sequestration offshore, because of hydrothermal circulation, and the sufficient porosity and permeability within the extrusive section (Chapters 1 and 2). Old oceanic crust in deep oceans shows a great potential for combined gravitational and physical CO_2 trapping (Chapters 2 and 3). On the other hand, most of the areas close to the ridge axis – which is characterised by hot, freshly created oceanic crust – or nearby continental margins – which generally include thick layers of sediments above the basement – are considered unsuitable for combined CO_2 trapping because of the negative $\Delta\rho$ conditions (Chapters 2 and 3).

A detailed investigation on the eastern flank of the Juan de Fuca (JdF) ridge, was done because it was proposed as a potential offshore target for carbon dioxide storage [*Goldberg et al.*, 2008; *Slagle and Goldberg*, 2011]. Previous studies have shown that carbonate veins formed from low temperature basement fluids (<70 ˚C) present in porous rocks [*Coggon et al.*, 2004], and therefore that carbon sequestration reactions occur naturally *in situ*. In this project, batch dissolution experiments carried out at 40 ˚C on JdF samples detected Ca and Si dissolution rates at pH ~5 (from -14.1 to -14.9 log (mol/cm^2/s), and from -14.7 to -14.9 log (mol/cm^2/s), respectively), which are comparable with highly reactive crystalline basalt from Iceland (from -15.0 to -15.5 log (mol/cm^2/s), and from -14.5 to -15.2 log (mol/cm^2/s), respectively) [*Gudbrandsson et al.*, 2011]

(Chapter 4). Another advantage put forward for JdF as potential offshore target is the presence of relatively continuous and anomalously thick sediment cover, particularly efficient for physical trapping (Chapter 2) [*Goldberg et al.*, 2008]. However, this study shows that the JdF site is not suited for CCS purposes, based on gravitational trapping, because the local conditions are too hot to keep the CO_2 within the basement ($\rho_{CO2} > \rho_{seawater}$, Chapter 3).

On this basis, the mid-ocean ridge flanks proximal (~500 km) to the ridge axes are rarely included in the maps proposed for the combined gravitational and physical trapping (Figure 3.7, Chapter 3). On the other hand, these same mid-ocean ridge flanks become suitable locations for CO_2 sequestration when only gravitational trapping is applied (Figure 3.3, Chapter 3). Despite sediment thicknesses <200 m, the high water depth at open ocean conditions (from 2500 and 7500 m) is sufficient to keep the pressure high enough for the CO_2 to be gravitationally stable. Nevertheless, these gravitationally suitable locations do not correspond to economic viable options due to the increased cost mainly associated with the distance from the coast (Chapter 5).

6.4. Batch CO_2 dissolution experiment implications

The experimental work conducted for this thesis provides important insight into the determination of dissolution reactions of basalts and gabbro from the modern ocean floor and ophiolites, respectively, in the presence of CO_2-rich seawater solution (Chapter 4). Batch reactor experiments (Chapter 4) revealed that the rate of dissolution of crystalline mafic rocks in a CO_2-rich seawater solution can be detected primarily through silicon concentrations, which is consistent with previous experiments, and also through calcium concentrations. This finding is a step forward in the understanding of mineral reactivity within the rock. In fact, the highest whole rock Ca dissolution rates were measured from the JdF samples with ~1% of calcite (mix 1 and mix 2), but also from the ophiolitic gabbro

(G1), for which the only Ca potential source is amphibole and plagioclase, as almost no pyroxene is present. This latter observation leads to the hypothesis that differencies in calcium release rates are related to calcite, amphibole and plagioclase content (Chapter 4). Also, anorthitic plagioclase (Ca ~1 mol) reacts faster than labradorite (Ca ~0.6 mol) and oligoclase (Ca ~0.2 mol), as shown in previous studies [e.g., *Casey et al.*, 1991; *Gudbrandsson et al.*, 2014; *Oxburgh et al.*, 1994]. Hence, plagioclase composition is a potential key factor defining the Ca-release rate (i.e. dissolution rates) during the low temperature (40 ˚C) experiments.

In a more general scenario, bearing in mind that the availability of cations (such as Ca, Mg, and Fe) in solution is considered one of the major challenges in the mineral sequestration of CO_2 [*Oelkers et al.*, 2008], this observation may lead to one of the most straightforward methods to distinguish which mafic formation should be taken into account for mineral carbonation for CCS purposes, offshore as well as on land. For example, the old oceanic crust (155 Ma) in the Indian Ocean – offshore Western Australia (*target **a***, Chapter 3), already identified to be suitable for combined physical and gravitational trapping – also shows a theoretically high geochemical potential. In fact, the basement of *target **a*** presents favourable characteristics highlighted above: cation sources provided by phenocrysts of olivine (fast reaction rates [*Kelemen and Matter*, 2008]) and plagioclase as calcic as An_{90} (90% anorthitic plagioclase) [*Ishiwatari*, 1992]; a nonpervasive low temperature alteration, typical of seafloor weathering, which confirms the past occurrence of carbonation reactions [*Gillis et al.*, 1992]; and a porosity on average around 5% [*Brereton*, 1992] to host the CO_2-rich fluids.

6.5. CO_2 cost implications for CCS offshore

Cost analysis of a potential CCS project with a reservoir located offshore highlighted two main factors that influence the estimations: 1) water depth, and 2) distance offshore.

Water depth is a major issue for the technologies considered in this study. In fact, ships with unloading buoys have been designed for bathymetric values up to 2500 m, but the proposed targets for CO_2 storage in basalts offshore are usually much greater than 2500 m for both cases of combined trapping and gravitational-only trapping (Chapters 3 and 5). Assuming improvements in future technology, and costs proportional to drilling time, the estimated costs for a CCS project in 5000 m of water depth were scaled up by a factor of 1.4 (Chapter 5). Consequently, a 25 year project involving the transport and storage of $20x10^6$ t of CO_2 per year to a reservoir located 500 km from the shore, at ~5000 m of water depth, with seven drilled wells, would require in total ~€$8.8x10^9$ (Figure 6.1). This estimation is ~€$5x10^9$ lower than the cost calculated for the corresponding option with 40 drilled wells (~€$13.4x10^9$), and ~$3x10^9$ lower than the option at 2500 m of water depth, 1500 km offshore, and 40 drilled wells (~€$11.9x10^9$) (Figure 6.1).

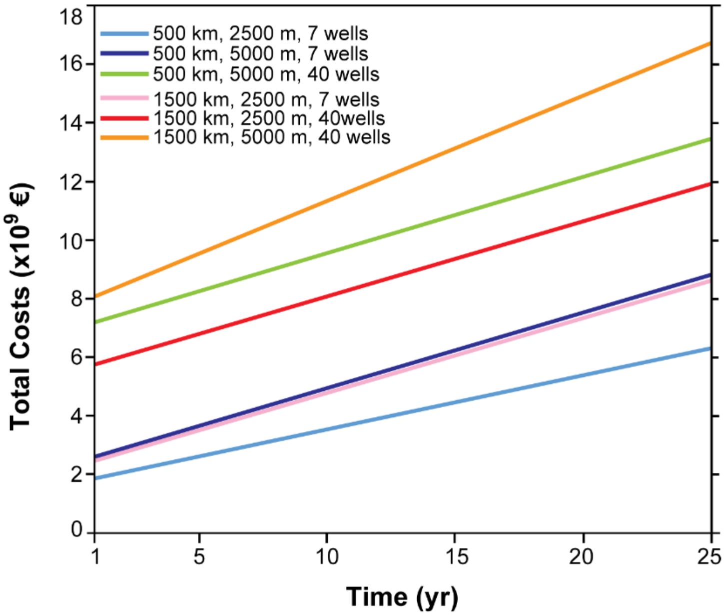

Figure 6.1: Summary of cost estimations for the transport and storage of 20 Mt of CO_2, in 25 years-long CCS projects. Six scenarios are shown as a function of distance from shore (500 or 1500 km), water depth (2500 or 5000 m), and number of injection wells (7 or 40).

Hence, these evaluations show that a CCS project is more economically viable when closer to the shore, even if in deeper waters, and using fewer wells, than if located further away, in shallower waters, and using many wells. The number of wells depends on the injection rate, which in turn is linked to the reservoir pressure and its permeability (Chapter 5). A high injectivity is required to reduce the number of wells, hence making deep water projects more attractive.

The influence of the distance from the coastline on the costs is intuitive: a greater distance to cover during the CO_2 transport corresponds to a higher number of ships required in the CCS fleet (Chapter 5), and therefore requiring larger volumes of fuel to operate them. Also, it is important to bear in mind that every step in the CCS chain also generates CO_2: for example, the transport of CO_2 via ship. The design of CO_2 carriers considered during the cost analyses (40,000 m^3, -50 ˚C, and ~7 bar – Chapter 5) is very similar to that of low temperature Liquid Petroleum Gas (LPG) carriers, which on average emit 43.5 g CO_2/tonne-km [*Second IMO GHG Study 2009*]. A one way journey of a ship involved in a CCS project (ship capacity of 0.046 Mt of CO_2 per journey) with targeted reservoir at 500 km offshore (~22 h journey) produces ~1000 t of CO_2.

Hence, the definition of the most economic location for a reservoir offshore is not straightforward, and further assessments are required to determine the capacity of specific reservoirs and their size. For example, assuming a basement thickness of 300 m and relative rock porosity of 10%, estimated for combined physical and gravitational trapping (Chapter 3), only 16 km^2 of mafic rocks would be required to store 500 Mt of CO_2 (at average density of 1066 kg/m^3) in 25 years.

6.6. Social implications

Anthropogenic CO_2 emissions into the atmosphere must be drastically reduced to limit the increase of global average temperature to less than 1.5 ˚C above pre-industrial levels [*Conference of the Parties Twenty-first Session*, 2015] (Chapter 1). This will require a combination of several strategies [*IPCC*, 2005b; 2014a]. Improved energy efficiency, and reduction in the use of fossil fuels as a source of energy are probably two of the wiser options, but the acceptance of the latter case by the general public, which is key for successful implementation, is a constant issue [*Judkins et al.*, 1993]. Increasing the carbon sink is an alternative strategy, and CCS is one of the most viable options [*IEA*, 2010; *Wright et al.*, 2014] (Chapters 1). However, little is known about the public perception of CCS as a mitigation strategy. Data on the topic have only been explored at small scale, and are technique-specific [*Shackley et al.*, 2009]. Also, most of the surveys are carried out for ongoing projects that are affiliated to Enhanced Oil Recovery – EOR, and deep-sedimentary aquifers [*Scott*, 2013]. These studies all found quite low levels of public awareness of CCS, and more generally of the perceived urgency of addressing climate change. Onshore CO_2 storage is suggested to cause the greatest concern, whereas, for the offshore projects, the main fears are associated with the CO_2 pipelines in the ocean. Overall, it appears that CCS would be more accepted when combined with other low-carbon strategies.

This thesis presents an unconventional approach to CCS independent from the petroleum industry, and by taking into account the stability of carbon dioxide in oceanic crust (Chapter 3). Also, an attempt to constrain the costs associated with CO_2 transport via ship, and its storage offshore, has been carried out to justify CCS strategies to a broader audience, comparing the main findings with oil industry costs (Chapter 5). Although the CO_2 costs for a whole transport-storage CCS project of 25 years is lower than current oil costs (Section 6.5), CCS strategies are still not playing a major role in the global market. The carbon tax on CO_2 emissions, so far implemented by only fifteen countries [www.worldbank.org/content/dam/Worldbank/document/Climate/backgroundnotecarbon-tax.pdf], ranges from 5 to 150 € per tonne of CO_2 equivalent (measure used to compare the emissions from various greenhouse gases based on their warming potential relative to that of carbon dioxide), and has been one of the main drivers for starting commercial CCS projects, besides EOR, such as the Sleipner project. Hence, is this carbon tax going to be applied worldwide? If so, will it be sufficient to boost the CCS market? Will its implementation change the public perspective on climate change?

The answers go beyond the scope of this thesis, but it is important to keep in mind the social implications of a research that focuses on such a complex challenge like the CCS.

6.7. Limitations

As this thesis research is focused on CCS offshore, a number of limitations are associated with the availability of relevant data (e.g. measurements from scientific drilling cruises). A series of reasonable assumptions was put in place to overcome this problem on a global scale, but further investigations are required. The database-related limitations are listed below, together with potential solutions.

1) *Temperature validation*: despite numerous holes drilled into the oceanic crust during scientific oceanic cruises, validation of the estimated temperature at the sediment-basement interface has only been done at thirteen sites (Chapter 2).
2) *Sediment thermal conductivity*: an average thermal conductivity value (K_s = 1 W/(m K)) was taken into account for all the sediment layers covering the whole oceanic crust, justified by global databases of marine sediment thermal conductivities (Chapter 2). An exception was made for the Juan de Fuca Plate, where more detailed investigations revealed a locally more appropriate thermal conductivity of 2 W/(m K) (Chapter 2).
3) *Basement permeability*: the volume of storable CO_2 in each of the identified targets was estimated assuming values of porosity (10%) and thickness (300 m) of basement, but without considering the permeability (Chapter 3), which within the uppermost few hundred meters of the igneous crust ranges from 10^{-22} to 10^{-9} m^2 [*Fisher*, 1998]. Its local variability and lack of measurements recorded during scientific cruises make its inclusion in the global investigations difficult.

In general, all the above limitations could be solved in the future with additional measurements from scientific cruises, more localised data analyses, and potential field-scale projects in the areas of interest.

Other important limitations of this study are associated with the experimental nature of the geochemical investigation (Chapter 4).

A) *Geochemical process*: the experiments were focused on dissolution reactions only to constrain the dissolution potential of oceanic rocks exposed at low temperature to a CO_2-rich seawater. Hence, in this far-from equilibrium setup, no further reactions, such as precipitation, were possible.

B) *Fine particles*: the decision to use oceanic cores involved the disadvantage of having less material available to start with, which in turn led to a compromise during the cleaning procedure, and the subsequent presence of fine particles in these samples. However, physical analyses were carried out to constrain the sample particle size, to account for their effect on the reaction kinetics, and to allow comparison with other experiments.

C) *Experimental settings*:

- the chosen temperature of 40 ˚C, and the continuous flux of CO_2 in and out of the reactor to maintain the saturation conditions led to the partial evaporation of the seawater. This was corrected by the consideration of the chloride concentration.
- the observation of corrosion on the stainless steel bubbler meant that analyses of iron and aluminium were compromised. Note that the only alternative gas distribution tube available in the market is made of borosilicate glass, which could compromise the measurement of silicon in the system;
- the reaction extent, most probably associated only with the top-surface of the samples, could be improved by stirring the solution, ensuring that no further decrease in the sample particle size will take place.

6.8. Future work

This research covers a number of scientific questions, ranging from the use of geophysical models for oceanic crust, to experimental work on geochemical reactions, and to economic evaluations on CCS feasibility offshore. This interdisciplinary approach has been chosen above a more specific one because of the CCS nature itself, which is complex and requires a broader assessment of risks, particularly for large-scale CCS decisions [*Choptiany et al.*, 2014]. Consequently, further work on each of these topics could be developed in the future.

Investigations on physical and gravitational CO_2 trapping at the sediment-basement interface for the whole oceanic crust show the sequestration potential of several areas on a global scale. However, more detailed analyses on Juan de Fuca Plate and eastern equatorial Pacific Ocean highlight the need of validating the general oceanic crust properties to a more localised level of research in order to define the real potential of each reservoir. As for the case of *target **a*** (NW Western Australia), all the other identified targets could undergo specific examinations. Also, more parameters could be included in the evaluation if, in any of the areas of interest, *in situ* measurements of permeability and sediment thermal conductivity become available.

The preliminary results from the experiments on several oceanic rocks highlighted the possibility of improving the experimental design, without major changes. For example, further experiments could be carried out as follows:

a) with 5-10 g of material, to have the sample always in contact with the CO_2-rich solution, and to better define the reactive mass;

b) with only anorthitic plagioclase, or actinolitic amphibole, to validate the hypothesis on the dependency of the mafic rock reactivity from these mineral compositions.

However, for a complete understanding of the rock reactivity, these samples should be exposed to different solutions, and type of experiments (such as flow-through, and combined dissolution-precipitation), but this latter option would require major efforts.

In general, a geochemical model based on the CO_2-seawater-oceanic rocks used during the dissolution experiments could provide more insight into the efficacy of mineral dissolution reactions, with particular attention to the behaviour of secondary minerals.

Regarding CO_2 costs, the only way to improve the theoretical estimations would be through the possibility to access information of already ongoing offshore CO_2 storage aspects, including those related to EOR, or being involved in an offshore field-scale injection project for CO_2 storage in mafic or ultramafic rocks.

6.9. Conclusions

At a time when environments are fast changing with global warming extremely likely due to the observed increase in anthropogenic greenhouse gas concentrations [*IPCC*, 2014b], mitigation strategies are the focus of increasing attention. The approaches proposed to counteract the levels of carbon dioxide in the atmosphere can be divided in “reducing emissions” methodologies (such as reducing energy demand, improving technology efficiency, and increasing the contribution of nuclear and low carbon renewable energy), and in “increasing carbon sinks” practices (such as Carbon Capture and Storage – CCS).

Understanding the advantages and limits of carbon capture and storage, from both economic and scientific perspectives, is essential for governments, stakeholders, academics, and the general public. In the last decades, CO_2 injections into mafic and ultramafic formations have started to be considered as an alternative to more conventional storage in sedimentary basins (e.g. CarbFix project, and Big Sky Carbon Sequestration Partnership). However, the storage capacity of these reservoirs has yet to be determined. The present thesis focused on the sequestration process of the CCS chain in a specific context, which involves the geological storage of carbon dioxide in deep-sea basalts. The thermodynamic properties at the sediment-basement interface for the whole oceanic crust, together with rock dissolution rates in a CO_2-seawater-oceanic rock system, and costs related to CO_2 transport offshore and relative underground storage were investigated. The outcomes constrained the viability of geological sequestration of CO_2 in oceanic crust via combined physical and gravitational trapping, proposing several suitable reservoirs, where even the smallest target could contribute to the reduction of several centuries of current anthropogenic CO_2 emissions (~36 Gt of CO_2 per year). On the other hand, this thesis also highlighted how much further work is required to turn this huge theoretical potential into a financially attractive option.

Appendix

A-Chapter 1

CH1-1: *Marieni et al. (2013)*.

Geological storage of CO_2 within the oceanic crust by gravitational trapping

Chiara Marieni,[1] Timothy J. Henstock,[1] and Damon A. H. Teagle[1]

Received 27 October 2013; accepted 4 November 2013.

[1] The rise of atmospheric carbon dioxide (CO_2) principally due to the burning of fossil fuels is a key driver of anthropogenic climate change. Mitigation strategies include improved efficiency, using renewable energy, and capture and long-term sequestration of CO_2. Most sequestration research considers CO_2 injection into deep saline aquifers or depleted hydrocarbon reservoirs. Unconventional suggestions include CO_2 storage in the porous volcanic lavas of uppermost oceanic crust. Here we test the feasibility of injecting CO_2 into deep-sea basalts and identify sites where CO_2 should be both physically and gravitationally trapped. We use global databases to estimate pressure and temperature, hence density of CO_2 and seawater at the sediment-basement interface. At previously suggested sites on the Juan de Fuca Plate and in the eastern equatorial Pacific Ocean, CO_2 is gravitationally unstable. However, we identify five sediment-covered regions where CO_2 is denser than seawater, each sufficient for several centuries of anthropogenic CO_2 emissions.

Citation: Marieni, C., T. J. Henstock, and D. A. H. Teagle (2013), Geological storage of CO_2 within the oceanic crust by gravitational trapping, *Geophys. Res. Lett.*, *40*, doi:10.1002/2013GL058220.

1. Introduction

[2] Human activities since the industrial revolution have increased atmospheric concentrations of greenhouse gases, in particular carbon dioxide (CO_2), requiring the development of mitigation strategies to minimize the effect on the global climate and potential ocean acidification [*Intergovernmental Panel on Climate Change*, 2007]. Various strategies have been proposed to reduce CO_2 emission including reducing energy demand, increasing renewable energy, and carbon capture and storage (CCS) underground. The effectiveness of geological reservoirs depends on their storage capacity, reservoir stability, risk of leakage, and the retention time [*Hawkins*, 2004; *Rochelle et al.*, 2004], with deep saline sedimentary aquifers [*Eccles and Pratson*, 2012; *House et al.*, 2006; *Levine et al.*, 2007; *Schrag*, 2009], and depleted oil and gas reservoirs [*Bachu*, 2000; *Jessen et al.*, 2005] receiving the greatest research attention. In addition, several mafic and ultramafic formations are under consideration for CO_2 storage including lava flows on Iceland [*Gislason et al.*, 2010; *Oelkers et al.*, 2008] and the Columbia River Basalts in the United States [*McGrail et al.*, 2006].

[3] This paper investigates the geological storage of CO_2 in the deep-sea basalts [*Goldberg et al.*, 2008, 2010; *Matter et al.*, 2007; *Slagle and Goldberg*, 2011] that form the uppermost igneous lavas of the oceanic crust and cover approximately 60% of Earth's surface. These formations may have advantages over other potential geological storage options: (a) large reservoir capacities; (b) low risk of postinjection leakage due to low permeability sediment blankets in some regions; (c) in situ availability of water; and (d) estimated fluid retention times greater than 500 years [*Goldberg et al.*, 2008]. The Juan de Fuca Plate (JdFP), offshore Washington State, has been the focus of conceptual studies of deep-sea basalt CCS [*Goldberg et al.*, 2008] because it is the best studied mid-ocean ridge flank with well-characterized regional thermal and hydrological regimes [*Fisher and Davis*, 2000]. The rocks on this plate are relatively young, having formed at the Juan de Fuca Ridge less than 11 Myr ago. The pillow lavas that form the upper few hundred meters of the JdFP crust have high connected porosity ($>10\%$) [*Fisher*, 1998], and the ridge flank is blanketed by a thick (from 30 to over 700 m) sequence of hemipelagic and turbiditic sediments derived from the North American continent.

[4] Other well-studied regions of the upper oceanic crust that have been considered for CO_2 storage [*Slagle and Goldberg*, 2011] are in the eastern equatorial Pacific Ocean (eePO) at Sites 504 and 1256 located in ~7 and 15 Myr old crust, respectively. Numerous studies on hydrothermal circulation provide detailed descriptions of physical properties and the porosity of the extrusive section of the ocean crust at these sites [*Alt et al.*, 1993; *Teagle et al.*, 2006; *Wilson et al.*, 2006].

[5] Three primary trapping mechanisms for the long-term storage of carbon dioxide in seafloor basalts have been proposed: (1) *Gravitational trapping* under pressure and temperature conditions where CO_2 is more dense than seawater [*Levine et al.*, 2007]. (2) *Physical or permeability trapping*, where the presence of $\geq$200 m of overlying low permeability marine sediments isolate the CO_2 injected into the basalts from the oceans, so that any leakage is trapped in the sediments [*Goldberg and Slagle*, 2009]. (3) *Geochemical trapping*, where the CO_2 and water react with the basalt host rocks to form geologically stable carbonate minerals [*Matter et al.*, 2007].

[6] In this study we consider the global variability of sediment thickness, pressure (p), and temperature (T), and consequently, the density (ρ) of CO_2 and seawater at the sediment-basement interface of the oceanic crust, to identify potential targets for combined gravitational and physical CO_2

Additional supporting information may be found in the online version of this article.

[1] Ocean and Earth Science, National Oceanography Centre Southampton, University of Southampton, Southampton, UK.

Corresponding author: C. Marieni, Ocean and Earth Science, National Oceanography Centre Southampton, University of Southampton, European Way, Southampton, SO14 3ZH, UK. (C.Marieni@noc.soton.ac.uk)

0094-8276/13/10.1002/2013GL058220

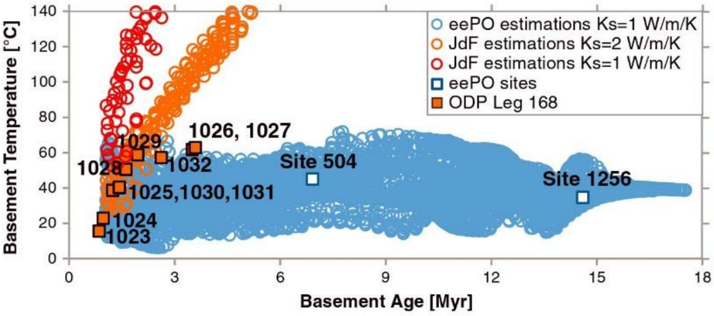

Figure 1. Comparison between estimated temperatures in the eastern equatorial Pacific Ocean (eePO) and the Juan de Fuca Plate (JdFP), and measured downhole temperatures at the sediment-basement interface. White squares: data from eePO [*Alt et al.*, 1993; *Teagle et al.*, 2006]; orange squares: data from JdFP [*Davis et al.*, 1997]. Circles: estimated values in the eePO (blue), and on the JdFP (red with $K_s = 1$ W/m/K; orange with $K_s = 2$ W/m/K).

sequestration. Although this is a physically robust scoping study, detailed programs of local data acquisition are imperative before any targets could be further developed.

2. Physical Parameters

[7] We have developed global maps of the density of seawater and CO_2 at the sediment-ocean crust interface. Pressure was estimated using the *NOAA-gridfive* sediment thickness database [*Divins*, 2003] combined with the General Bathymetric Chart of the Oceans (*GEBCO*)-*gridfive* world bathymetry map (both 6′ × 6′ grids) [*IOC et al.*, 2003]. The anomalies in the topography (e.g., abyssal hills and seamounts) are not always detected by global altimetry and gravity analyses, but the *NOAA* database is the currently best available. We assume a hydrostatic load to the top of basement, using a constant seawater density of 1030 kg/m^3 and a constant salinity of 35 psu (practical salinity unit) [*Brown et al.*, 1995]; this gives a lower bound on the pressure and the CO_2 density. We used the Global Depth and Heat flow model (GDH1) [*Stein and Stein*, 1992] to estimate the heat flow, and then the temperature, based on the oceanic crustal age [*Müller et al.*, 2008] (see supporting information "Text S1" for the equations). We use GDH1 because it is better for predicting the heat flow at old oceanic crustal ages than the Half Space Cooling Model (HSCM) [*Turcotte and Schubert*, 2002], and because the Global Heat Flow Database [*Pollack et al.*, 1993] is sparse and irregular. Nevertheless, our GDH1-based approach still presents uncertainties due to incomplete information on sediment thicknesses, local heat flow anomalies, and the thermal properties of sediments.

[8] From the heat flow we have calculated the geothermal gradient [*Heberling et al.*, 2010] and consequently estimated the temperature at the top of the basement (in °C), with the thermal conductivity of the sediments taken as $K_s = 1$ W/m/K [*Pollack et al.*, 1993; *Pribnow et al.*, 2000a] (see supporting information "Figure S2").

[9] We have validated our estimates of temperature at the sediment-basement interface by using borehole temperature logs from Sites 504 and 1256 [*Alt et al.*, 1993; *Teagle et al.*, 2006] and the Juan de Fuca Plate [*Davis et al.*, 1997] (Figure 1; supporting information "Figure S1" for comparison with HSCM). The two areas have different trends of basement-sediment interface temperature as a function of age. In the eastern equatorial Pacific Ocean there is good agreement between estimated and measured temperature. However, on the Juan de Fuca Plate, the temperatures at most sites are better fit using the higher measured thermal conductivity (K_s ~2 W/m/K) of the local muddy and sandy turbiditic sediments [*Pribnow et al.*, 2000b]. At Sites 1026 and 1027, the measured temperature is lower than predicted because of hydrothermal circulation [*Hutnak et al.*, 2006; *Wheat et al.*, 2004] linked to surrounding basement outcrops (e.g., Baby Bare) [*Fisher et al.*, 2003]. Although there are numerous holes drilled into the oceanic crust by scientific ocean drilling (Deep Sea Drilling Project (DSDP), Ocean Drilling Program (ODP), and Integrated Ocean Drilling Program (IODP)), eePO, and JdF are the only locations where the temperatures close to the sediment-basement interface are well constrained. The validation at the eePO and JdFP gives us confidence in our calculations but emphasizes the need for verification of local physical properties.

[10] The densities of CO_2 (ρ_{CO2}) and seawater ($\rho_{seawater}$) were calculated for pressures from 0 to 60 MPa and temperatures from 0 to 100°C. The CO_2 density was determined by interpolating the online National Institute of Standards and

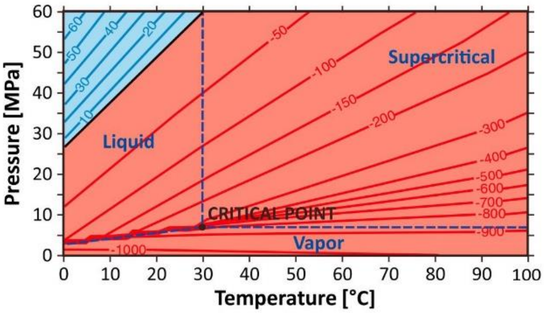

Figure 2. Density difference ($\Delta\rho = \rho_{CO2} - \rho_{seawater}$ in kg/m^3) between CO_2 and seawater density as a function of pressure between 0 and 60 MPa, and temperature between 0 and 100°C, with the phase diagram of CO_2 overlaid. Positive differences shown in blue indicate conditions for gravitational trapping.

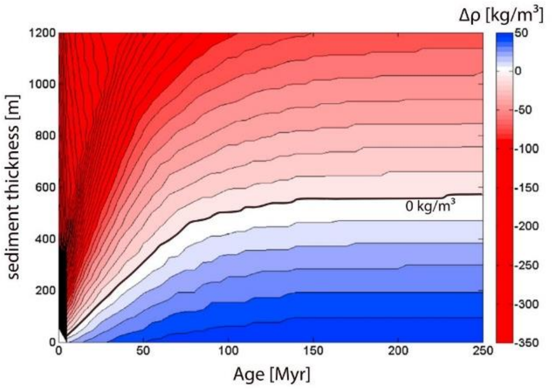

Figure 3. Density difference between CO_2 and seawater at the sediment-basement interface as a function of plate age and sediment thickness using the GDH1 model to determine both water depth and thermal conditions. Sediment thicknesses below the heavy black line show where positive density differences required for stable gravitational trapping are achieved.

Technology (NIST) database (Linstrom, P. J., and W. G. Mallard (Eds.), NIST Chemistry WebBook, NIST Standard Reference Database Number 69, National Institute of Standards and Technology, Gaithersburg Md, 20899, retrieved November 12, 2012, http://webbook.nist.gov), which is based on the equation of state by *Span and Wagner* [1996]. Seawater density was estimated using the SeaWater MATLAB library [*Fofonoff et al.*, 1983], assuming a constant salinity of 35 psu [*Brown et al.*, 1995]. Figure 2 shows the density difference between CO_2 and seawater as a function of temperature and pressure together with a phase diagram of carbon dioxide. Temperatures above 100°C are not considered because the density of CO_2 is too low to allow gravitational trapping.

[11] The density difference at the sediment-basement interface at each point in our $6' \times 6'$ global grids is calculated using the estimated temperature and pressure. We combined this with the sediment thickness map to identify locations where (1) CO_2 is denser than seawater at the sediment-basement interface (Figure 2), and (2) the sediment thickness is between 200 m and 700 m (Figure 3). We choose a minimum thickness of 200 m to ensure a continuous low permeability blanket over minor basement topography such as fault ridges or seamounts that might puncture the sediment cover and allow the egress of basement fluids. To estimate the maximum sediment thickness, we have calculated the density difference for a wide range of lithospheric ages and sediment thicknesses using the GDH1 model for both water depth and heat flow, and assuming a hydrostatic sediment column (Figure 3). Based on global average conditions, GDH1 indicates a restricted zone where gravitational trapping is possible, and that anywhere with more than ~600 m of sediments CO_2 is likely to be gravitationally unstable due to the high temperatures. Using the HSCM (see supporting information "Figure S3"), the equivalent limit is ~1000 m. Hence, we settle on an upper sediment thickness limit of 700 m.

3. Discussions

[12] Much of the upper oceanic crust does not provide suitable locations for the geological sequestration of CO_2 by gravitational and physical trapping. Gravitational trapping ($\rho_{CO2} > \rho_{seawater}$) requires pressures higher than 25 MPa

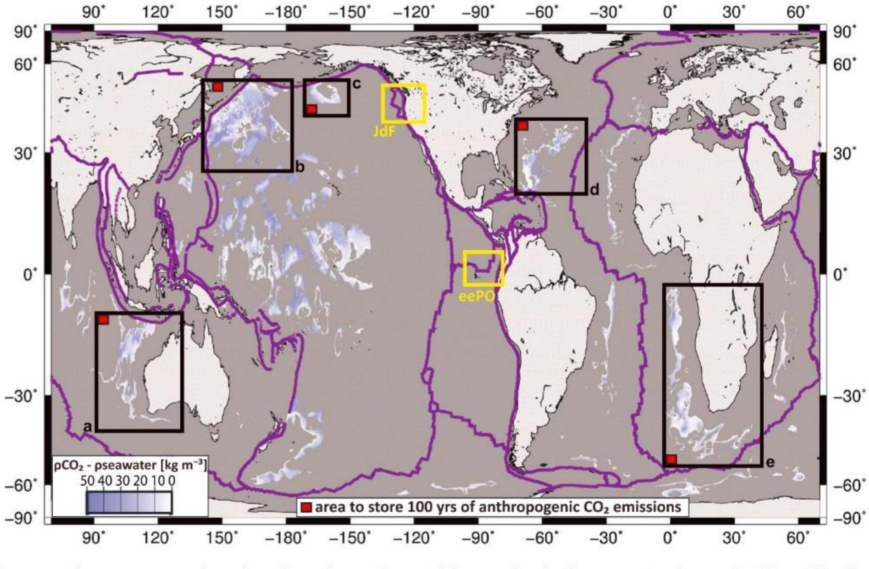

Figure 4. An equal area map showing locations for stable geological sequestration of CO_2. Shading shows the difference in density between CO_2 and seawater in areas where the sediment thickness is between 200 and 700 m and the CO_2 is denser than seawater. Five potential reservoirs (insets a–e) have been identified. The red box indicates the area required to store 100 yrs of current anthropogenic emissions of CO_2, assuming a pillow lava thickness of 300 m and 10% porosity [*Carlson and Herrick*, 1990; *Jarrard et al.*, 2003; *Johnson and Pruis*, 2003]. Yellow boxes show regions in Figure 5.

Table 1. Properties of the Five Potential Reservoirs[a]

Code	Location	Area [$\times 10^6$ km^2]	Pore Volume [$\times 10^4$ km^3]	ρCO$_2$ [kg/m^3]	CO$_2$ [Gt]	Δρ [kg/m^3]	Age [Myr]	Sed. Thickness [m]	Distance [km]
a	Indian Ocean	1.47	4.42	1066	47,162	18	85	335	1500
b	NW Pacific	3.97	11.9	1073	127,870	24	100	310	1300
c	S-Aleutians	0.43	1.30	1063	13,791	15	60	275	950
d	Bermuda	1.15	3.45	1066	36,780	17	80	320	1500
e	SE Atlantic	2.22	6.66	1062	70,701	14	85	290	1700

[a] Δρ, in situ excess density of CO$_2$ over seawater; age from [*Müller et al.*, 2008]; sediment thickness from the NOAA database [*Divins*, 2003]. Distance of the reservoir from land is taken from the nearest stationary source of CO$_2$ according to the IEA GHG database [*International Energy Agency Greenhouse Gas R&D Programme*, 2002].

(~2500 m of water) and temperature between 0 and 30°C (Figure 2). The density of CO$_2$ decreases dramatically with decreasing pressure and increasing temperature, compared to a near constant density for seawater. The combination of high pressure and low temperature requires old ocean crust with relatively thin sediments. Note that within this *p-T* window liquid CO$_2$ is the thermodynamically stable phase, with densities between 1040 and 1125 kg/m^3 compared with 140 kg/m^3 (at 100°C, 8 MPa) to 1045 kg/m^3 (at 30°C, 60 MPa) for supercritical CO$_2$.

[13] Suitable reservoirs where physical (sediment between 200 and 700 m) and gravitational ($\rho_{\mathrm{CO2}} > \rho_{\mathrm{seawater}}$) trapping can be combined are shown on the global map (Figure 4); the global map produced using the HSCM is available in the supporting information "Figure S4". Selected potential reservoirs are in the Indian Ocean between Indonesia and Australia (inset a); in the northwest Pacific Ocean near the east coast of Japan and Russia (inset b), and south of the Aleutian Islands (inset c); and in the Atlantic Ocean near Bermuda (inset d) and close to South Africa (inset e) (Table 1).

[14] We have identified these sites based on the positive $\Delta\rho$ between CO$_2$ and seawater, the oceanic crustal age, the sediment thickness, and the distance to major industrial CO$_2$ sources [*International Energy Agency Greenhouse Gas R&D Programme*, 2002] (Table 1). Other areas also have suitable conditions for carbon dioxide trapping, but we have not yet explored these options due to their smaller sizes and lower $\Delta\rho$, although some are closer to land. We have computed the potential storage volume for each target (Table 1), assuming 300 m as reasonable thickness of permeable pillow lavas for old crust. Given an average porosity of 10% [*Carlson and Herrick*, 1990; *Johnson and Pruis*, 2003], even for old oceanic crust (e.g., ODP Hole 801C [*Jarrard et al.*, 2003]), we determine the potential pore volume. The storage capacity in each area is between ~13,800 and 127,800 Gt of CO$_2$. At the current global annual anthropogenic flux of ~35 Gt of CO$_2$ per year [*Le Quere et al.*, 2009], even the smallest identified reservoir (inset c), could provide sufficient carbon dioxide sequestration capacity for several centuries (Figure 4).

[15] Contrary to previous suggestions [*Goldberg et al.*, 2008; *Slagle and Goldberg*, 2011], sites on the Juan de Fuca Plate and in the eastern equatorial Pacific Ocean are unsuitable for gravitational trapping of carbon dioxide (Figure 5) because thick sediment covering young oceanic crust results in high temperatures at the sediment-basement interface, that renders CO$_2$ less dense than seawater.

[16] Our evaluation based on global data sets shows that CCS using subsea basalts as the storage medium has considerable potential. However, regional investigations are needed to determine local sediment properties, thicknesses, continuity, and seafloor thermal gradients. Drilling to facilitate detailed lithological, physical, thermal, and hydrological characterization of the sediment overburden and target basalt formations is essential.

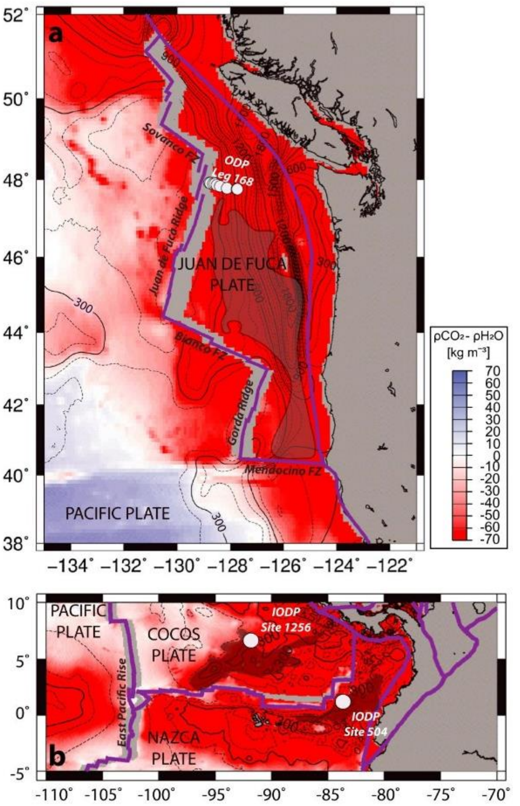

Figure 5. Map of density difference $\Delta\rho$ between CO$_2$ and seawater at (a) Juan de Fuca Plate (with K$_s$ = 2 W/m/K) and (b) at eastern equatorial Pacific Ocean (with K$_s$ = 1 W/m/K). Sediment thicknesses are shown with black contour lines. The dark shadows show the previously suggested regions for deep-sea basalt CO$_2$ sequestration [*Goldberg et al.*, 2008; *Slagle and Goldberg*, 2011].

4. Conclusions

[17] Offshore basalt formations have been previously suggested as sites for geological carbon dioxide sequestration. We have used global data compilations to calculate the density of CO$_2$ in the pressure-temperature regime at the top of the basement throughout the world's oceans, and identified regions where CO$_2$ is denser than seawater. Previously suggested young sites on the eastern flank of the JdF Ridge and in the eastern equatorial Pacific (Sites 504, 1256) are not suitable for storing CO$_2$ because it is gravitationally unstable ($\Delta\rho_{CO2-seawater}=0$ to $<-70\,kg/m^3$). However, we identify five large regions of old seabed where gravitational stability of stored CO$_2$ coincides with physical trapping by 200–700 m thickness of sediments. Using conservative assumptions about the porosity available, the smallest of these regions can store several centuries of anthropogenic CO$_2$ emissions.

[18] **Acknowledgments.** This research used data provided by the Integrated Ocean Drilling Program (IODP), the Ocean Drilling Program (ODP), and the Deep-Sea Drilling Project (DSDP). Funding for this research was provided by the University of Southampton Vice Chancellor's Scholarship to C. M., and NERC grant NE/I006311/1 to D.A.H.T. We thank Juerg M. Matter, Nick Woodman, and Martin R. Palmer for their discussions that assisted in the development of these ideas. We thank the Editor Peter Strutton, Robert Harris and a second anonymous reviewer for their constructive comments that have improved the paper.

[19] The Editor thanks Robert Harris and an anonymous reviewer for their assistance in evaluating this paper.

References

Alt, J. C., et al. (1993), *Proc. ODP, Init. Repts., 148*, Ocean Drilling Program, College Station, Tx.

Bachu, S. (2000), Sequestration of CO$_2$ in geological media: Criteria and approach for site selection in response to climate change, *Energy Convers. Manage.*, *41*(9), 953–970.

Brown, E., A. Colling, D. Park, J. Phillips, D. Rothery, and J. Wright (1995), *Seawater: Its Composition, Properties, and Behaviour*, 2nd ed., pp. 166, Elsevier Ltd., Oxford, U.K.

Carlson, R. L., and C. N. Herrick (1990), Densities and porosities in the oceanic crust and their variations with depth and age, *J. Geophys. Res.*, *95*(B6), 9153–9170.

Davis, E. E., M. J. Mottl, A. T. Fisher, and J. Firth (1997), *Proc. ODP, Init. Repts., 168*, pp. 470, Ocean Drilling Program, College Station, Tx.

Divins, D. L. (2003), *Total Sediment Thickness of the World's Oceans and Marginal Seas*, NOAA National Geophysical Data, Center, Boulder, Colo.

Eccles, J. K., and L. Pratson (2012), Global CO$_2$ storage potential of self-sealing marine sedimentary strata, *Geophys. Res. Lett.*, *39*, L19604, doi:10.1029/2012GL053758.

Fisher, A. T. (1998), Permeability within basaltic oceanic crust, *Rev. Geophys.*, *36*(2), 143–182.

Fisher, A. T., and E. E. Davis (2000), An introduction to the scientific results of Leg 168, in *Proc. ODP, Sci. Results, 168*, edited by A. T. Fisher, E. E. Davis, and C. Escutia, pp. 3–5, Ocean Drilling Program, College Station, Tx.

Fisher, A. T., et al. (2003), Hydrothermal recharge and discharge across 50 km guided by seamounts on a young ridge flank, *Nature*, *421*(6923), 618–621.

Fofonoff, N. P., R. C. J. Millard, and United Nations Educational, Scientific, and Cultural Organization, Paris (France). Div. of Marine Sciences (1983), Algorithms for computation of fundamental properties of seawater. Endorsed by UNESCO: SCOR/ICES/IAPSO Joint Panel on Oceanographic Tables and Standards and SCOR Working Group 51. UNESCO Technical Papers in Marine Science, No. 44/ N. P. Fofonoff and R. C. Millard, Jr, distributed by ERIC Clearinghouse [Washington, D.C.].

Gislason, S. R., et al. (2010), Mineral sequestration of carbon dioxide in basalt: A pre-injection overview of the CarbFix project, *Int. J. Greenhouse Gas Control*, *4*(3), 537–545.

Goldberg, D. S., and A. L. Slagle (2009), A global assessment of deep-sea basalt sites for carbon sequestration, *Energy Procedia*, *1*(1), 3675–3682.

Goldberg, D. S., T. Takahashi, and A. L. Slagle (2008), Carbon dioxide sequestration in deep-sea basalt, *Proc. Natl. Acad. Sci.*, *105*(29), 9920–9925.

Goldberg, D. S., D. V. Kent, and P. E. Olsen (2010), Potential on-shore and off-shore reservoirs for CO$_2$ sequestration in Central Atlantic magmatic province basalts, *Proc. Natl. Acad. Sci.*, *107*(4), 1327–1332.

Hawkins, D. G. (2004), No exit: Thinking about leakage from geologic carbon storage sites, *Energy*, *29*(9-10), 1571–1578.

Heberling, C., R. P. Lowell, L. Liu, and M. R. Fisk (2010), Extent of the microbial biosphere in the oceanic crust, *Geochem. Geophys. Geosyst.*, *11*, Q08003, doi:10.1029/2009GC002968.

House, K. Z., D. P. Schrag, C. F. Harvey, and K. S. Lackner (2006), Permanent carbon dioxide storage in deep-sea sediments, *Proc. Natl. Acad. Sci.*, *103*(33), 12,291–12,295.

Hutnak, M., A. T. Fisher, L. Zühlsdorff, V. Spiess, P. H. Stauffer, and C. W. Gable (2006), Hydrothermal recharge and discharge guided by basement outcrops on 0.7–3.6 Ma seafloor east of the Juan de Fuca Ridge: Observations and numerical models, *Geochem. Geophys. Geosyst.*, *7*, Q07O02, doi:10.1029/2006GC001242.

International Energy Agency Greenhouse Gas R&D Programme (2002), Building the cost curves for CO$_2$ storage, Part 1: Sources of CO$_2$*Rep.*, Cheltenham, U.K.

IOC, IHO, and BODC (2003), Centenary edition of the GEBCO digital atlas, published on CD-ROM on behalf of the Intergovernmental Oceanography Commission and the International Hydrographic Organization as part of the General Bathymetric Chart of the Oceans, edited by BODC, Liverpool, U.K.

Intergovernmental Panel on Climate Change (2007), *Climate Change 2007: Synthesis Report. Contribution of Working Groups I, II and III to the Fourth Assessment Report of the Intergovernmental Panel on Climate Change*, edited by Core Writing Team, R. K. Pachauri, and A. Reisinger, pp. 104, IPCC, Geneva, Switzerland.

Jarrard, R. D., L. J. Abrams, R. Pockalny, R. L. Larson, and T. Hirono (2003), Physical properties of upper oceanic crust: Ocean Drilling Program Hole 801C and the waning of hydrothermal circulation, *J. Geophys. Res.*, *108*(B4), 2188, doi:10.1029/2001JB001727.

Jessen, K., A. R. Kovscek, and F. M. Orr Jr. (2005), Increasing CO$_2$ storage in oil recovery, *Energy Convers. Manage.*, *46*, 293–311.

Johnson, H. P., and M. J. Pruis (2003), Fluxes of fluid and heat from the oceanic crustal reservoir, *Earth Planet. Sci. Lett.*, *216*(4), 565–574.

Le Quere, C., et al. (2009), Trends in the sources and sinks of carbon dioxide, *Nat. Geosci.*, *2*(12), 831–836.

Levine, J. S., J. M. Matter, D. Goldberg, A. Cook, and K. S. Lackner (2007), Gravitational trapping of carbon dioxide in deep sea sediments: Permeability, buoyancy, and geomechanical analysis, *Geophys. Res. Lett.*, *34*, L24703, doi:10.1029/2007GL031560.

Matter, J. M., T. Takahashi, and D. Goldberg (2007), Experimental evaluation of in situ CO$_2$-water-rock reactions during CO$_2$ injection in basaltic rocks: Implications for geological CO$_2$ sequestration, *Geochem. Geophys. Geosyst.*, *8*, Q02001, doi:10.1029/2006GC001427.

McGrail, B. P., H. T. Schaef, A. M. Ho, Y.-J. Chien, J. J. Dooley, and C. L. Davidson (2006), Potential for carbon dioxide sequestration in flood basalts, *J. Geophys. Res.*, *111*, B12201, doi:10.1029/2005JB004169.

Müller, R. D., M. Sdrolias, C. Gaina, and W. R. Roest (2008), Age, spreading rates and spreading symmetry of the world's ocean crust, *Geochem. Geophys. Geosyst.*, *9*, Q04006, doi:10.1029/2007GC001743.

Oelkers, E. H., S. R. Gislason, and J. M. Matter (2008), Mineral carbonation of CO$_2$, *Elements*, *4*(5), 333–337.

Pollack, H. N., S. J. Hurter, and J. R. Johnson (1993), Heat flow from the Earth's interior: Analysis of the global data set, *Rev. Geophys.*, *31*(3), 267–280.

Pribnow, D. F. C., M. Kinoshita, and C. A. Stein (2000a), Thermal data collection and heat flow recalculations for ODP Legs 101-180Rep. 0120432, Institute for Joint Geoscientific Research, GGA, Hanover, Germany.

Pribnow, D. F. C., E. E. Davis, and A. T. Fisher (2000b), Borehole heat flow along the eastern flank of the Juan de Fuca Ridge, including effects of anisotropy and temperature dependence of sediment thermal conductivity, *J. Geophys. Res.*, *105*(B6), 13,449–13,456.

Rochelle, C. A., I. Czernichowski-Lauriol, and A. E. Milodowski (2004), The impact of chemical reactions on CO$_2$ storage in geological formations: A brief review, *Geol. Soc. London Spec. Publ.*, *233*(1), 87–106.

Schrag, D. P. (2009), Storage of carbon dioxide in offshore sediments, *Science*, *325*(5948), 1658–1659.

Slagle, A. L., and D. S. Goldberg (2011), Evaluation of ocean crustal Sites 1256 and 504 for long-term CO$_2$ sequestration, *Geophys. Res. Lett.*, *38*, L16307, doi:10.1029/2011GL048613.

Span, R., and W. Wagner (1996), A new equation of state for carbon dioxide covering the fluid region from the triple-point temperature to 1100 K at pressures up to 800 MPa, *J. Phys. Chem. Ref. Data*, *25*(6), 1509–1596.

Stein, C. A., and S. Stein (1992), A model for the global variation in oceanic depth and heat flow with lithospheric age, *Nature*, *359*(6391), 123–129.

Teagle, D. A. H., J. C. Alt, S. Umino, S. Miyashita, N. R. Banerjee, D. S. Wilson, and The Expedition 309/312 Scientists (2006), *Proc. IODP, 309/312*, Integrated Ocean Drilling Program Management International, Inc., Washington, D. C.

Turcotte, D., and G. Schubert (2002), *Geodynamics*, 2nd ed., pp. 456, Cambridge University Press, Cambridge, U.K.

Wheat, C. G., M. J. Mottl, A. T. Fisher, D. Kadko, E. E. Davis, and E. Baker (2004), Heat flow through a basaltic outcrop on a sedimented young ridge flank, *Geochem. Geophys. Geosyst.*, *5*, Q12006, doi:10.1029/2004GC000700.

Wilson, D. S., et al. (2006), Drilling to gabbro in intact ocean crust, *Science*, *312*(5776), 1016–1020.

A-Chapter 2

CH2-1A: Heat flow map generated with the GDH1 model.

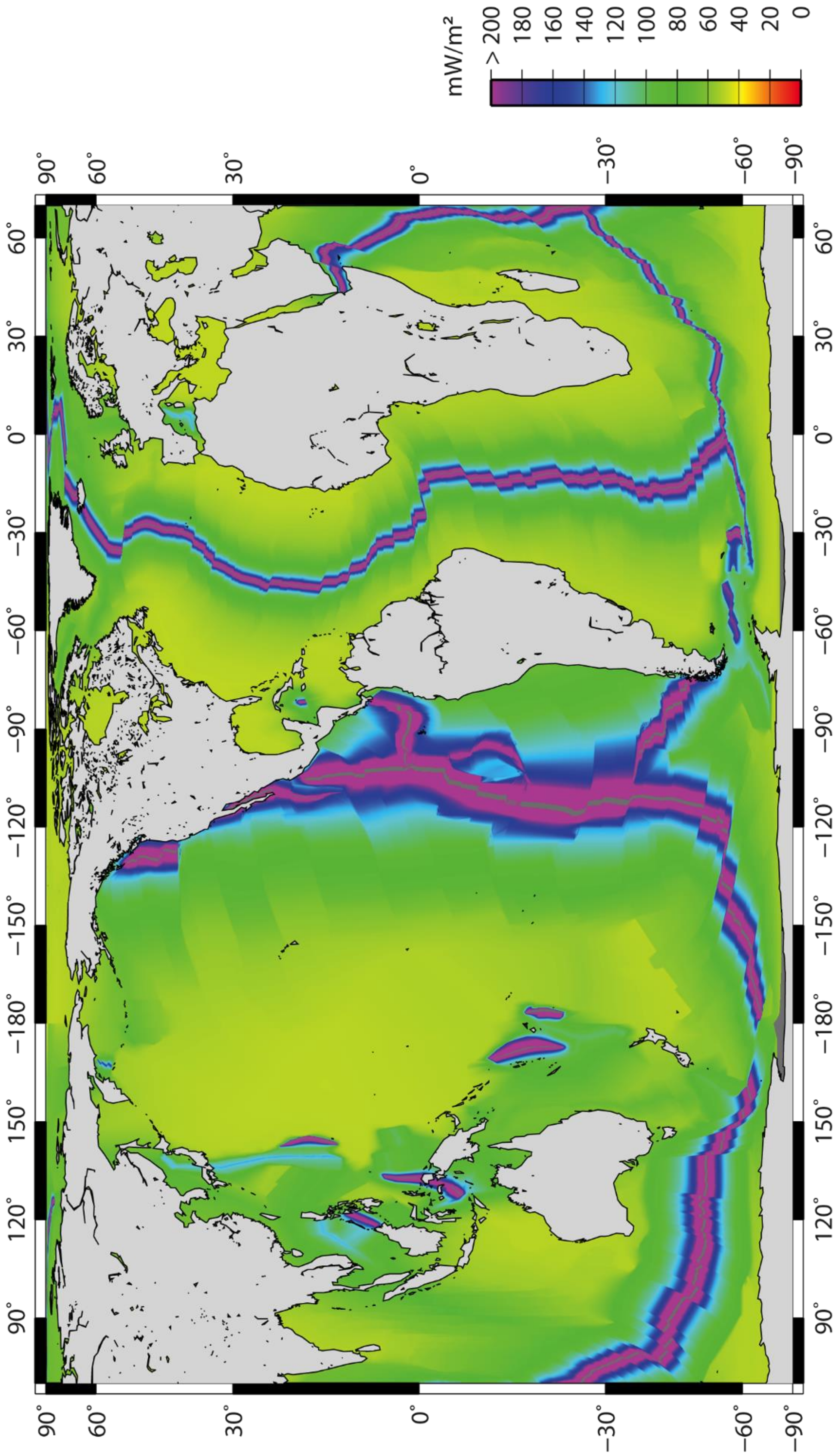

CH2-1B: Heat flow map generated with the HSCM.

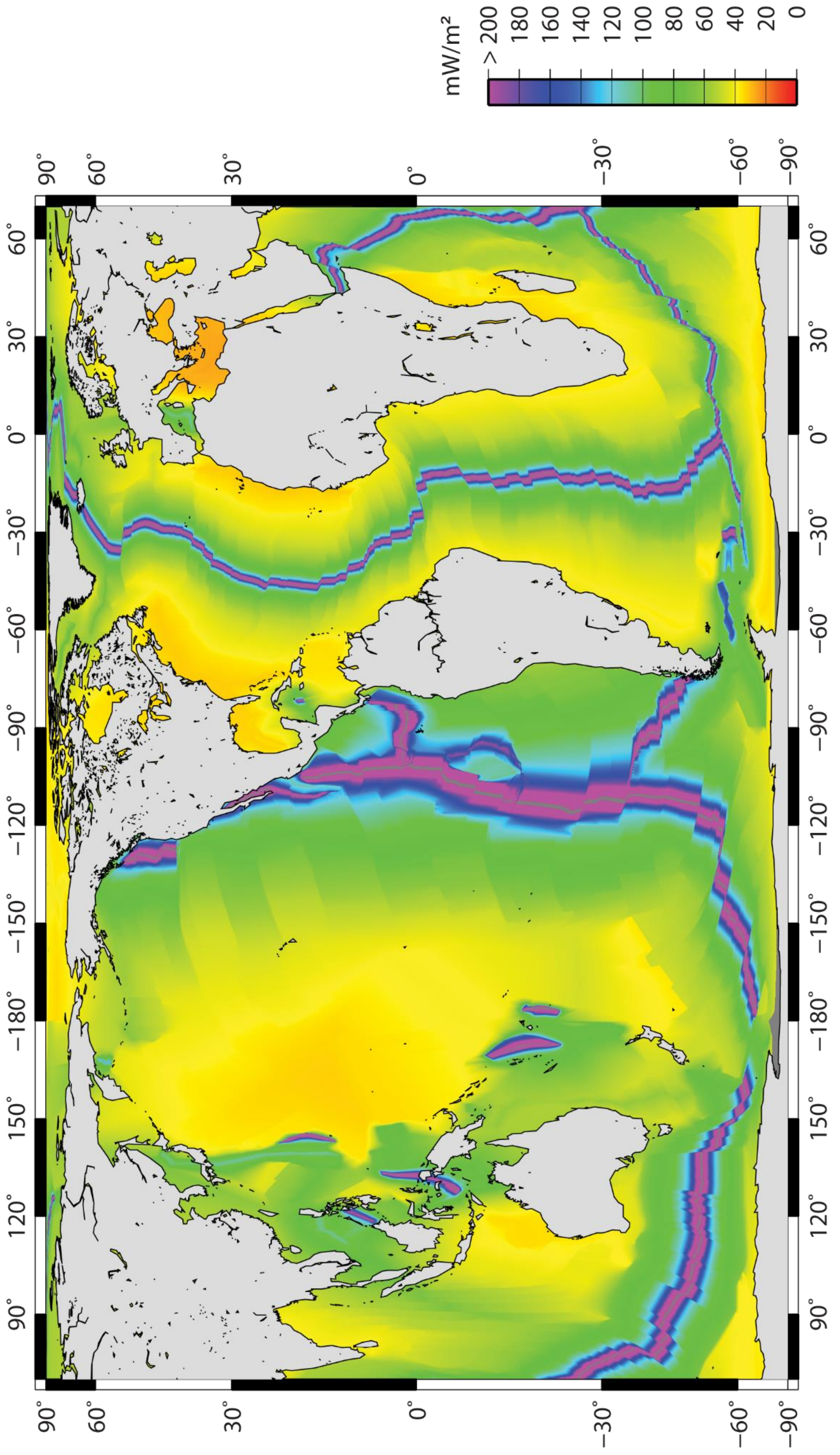

CH2-2: NOAA National Geophysical Data Center (NGDC) sediment thickness map [*Divins, 2003*]. The data were gridded with a grid spacing of 5 arc-minutes by 5 arc-minutes.

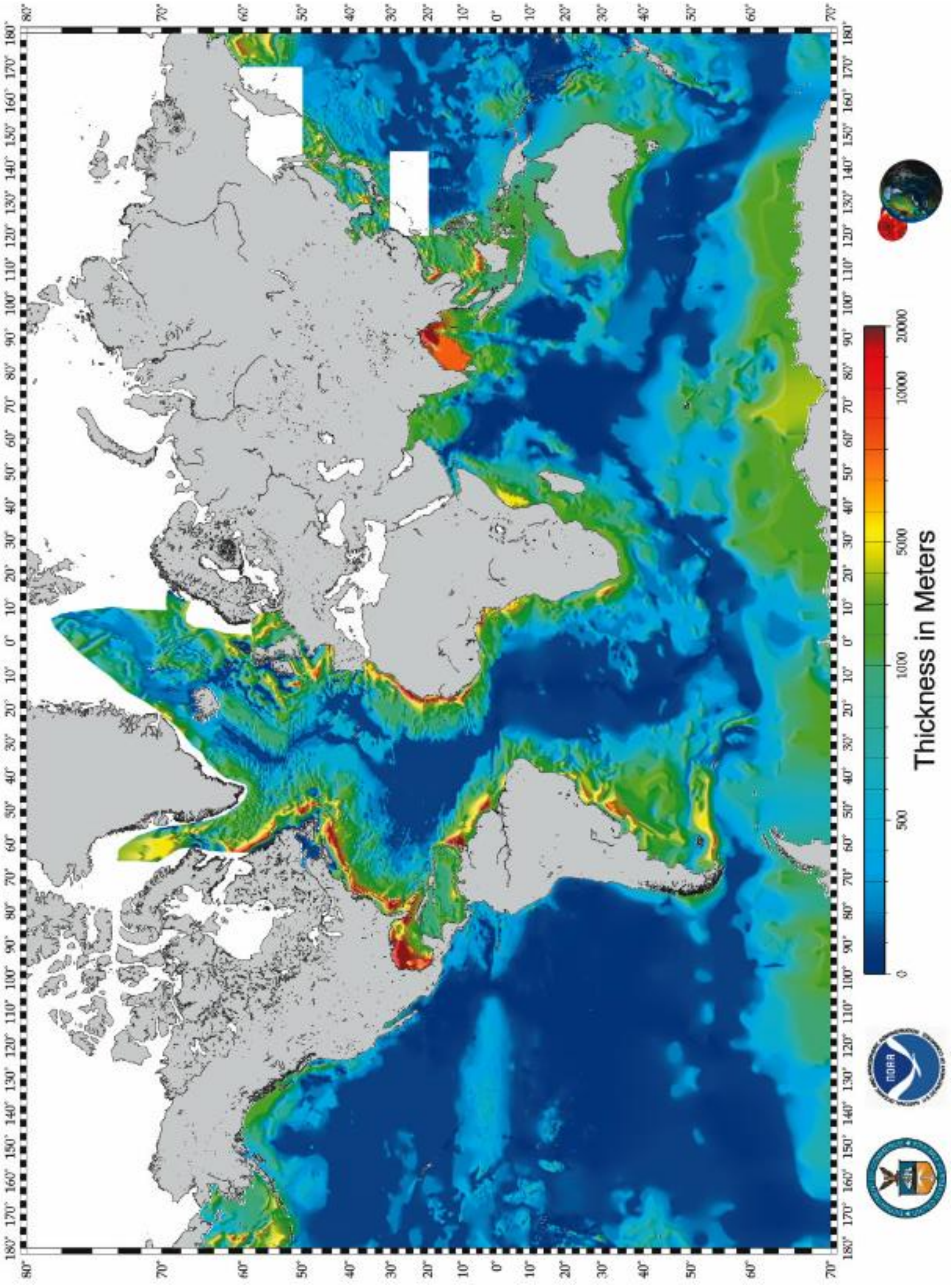

CH2-3A: Map of temperature at the sediment-basement interface, generated with the GDH1 model.

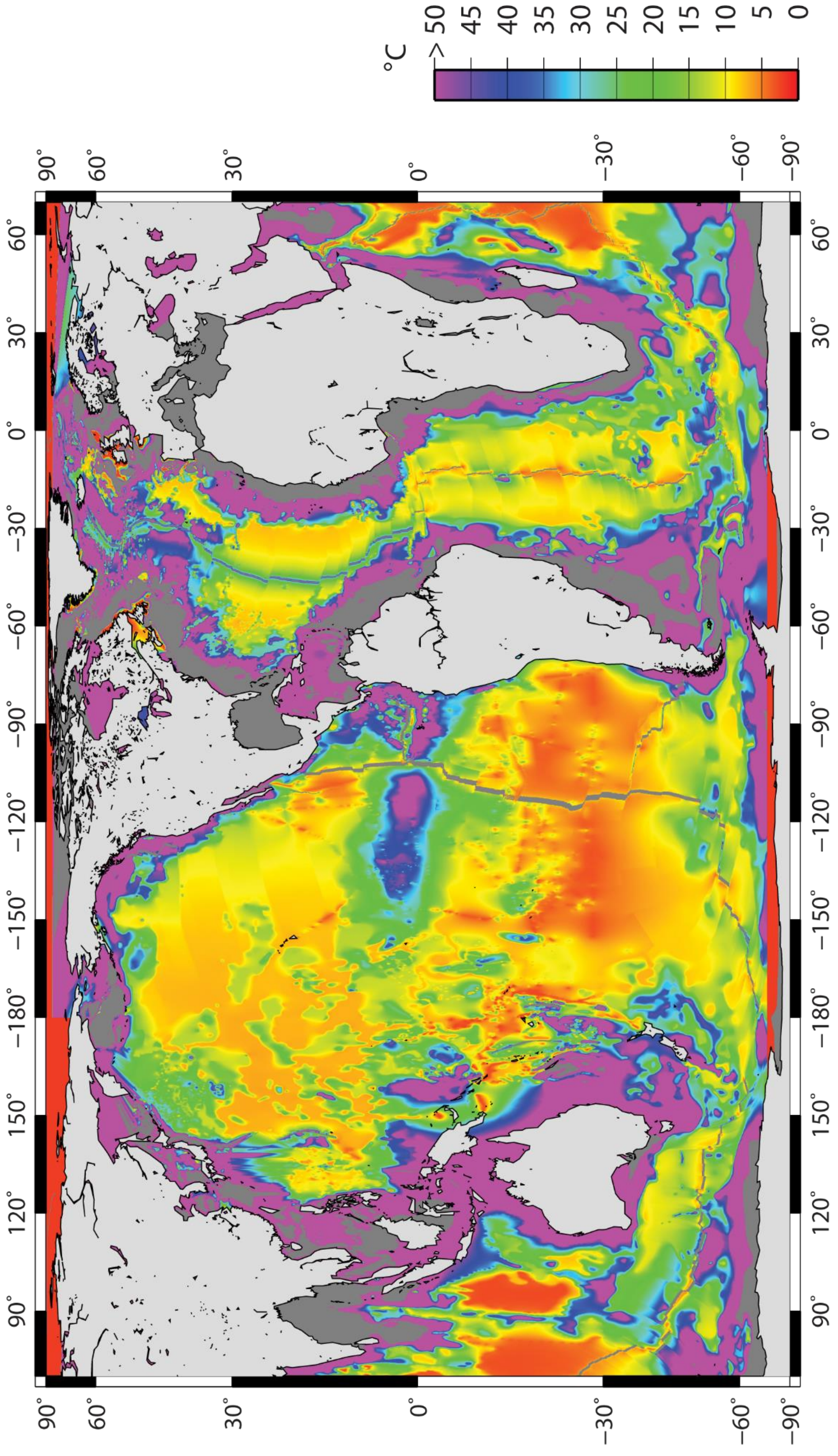

CH2-3B: Map of temperature at the sediment-basement interface, generated with the HSCM.

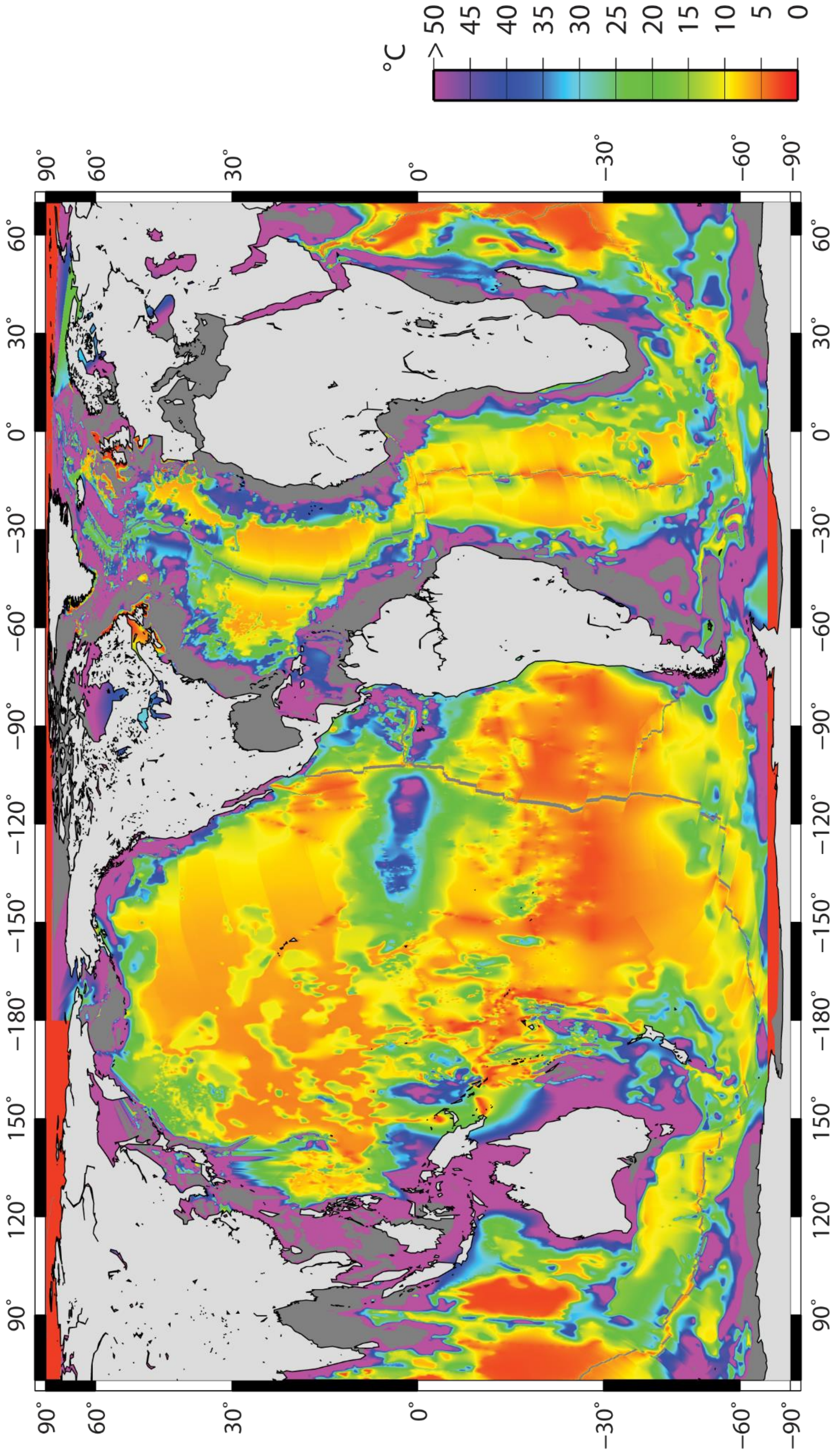

CH2-4: General Bathymetric Chart of the Oceans (GEBCO) – gridfive world bathymetry map [IOC et al., 2003].

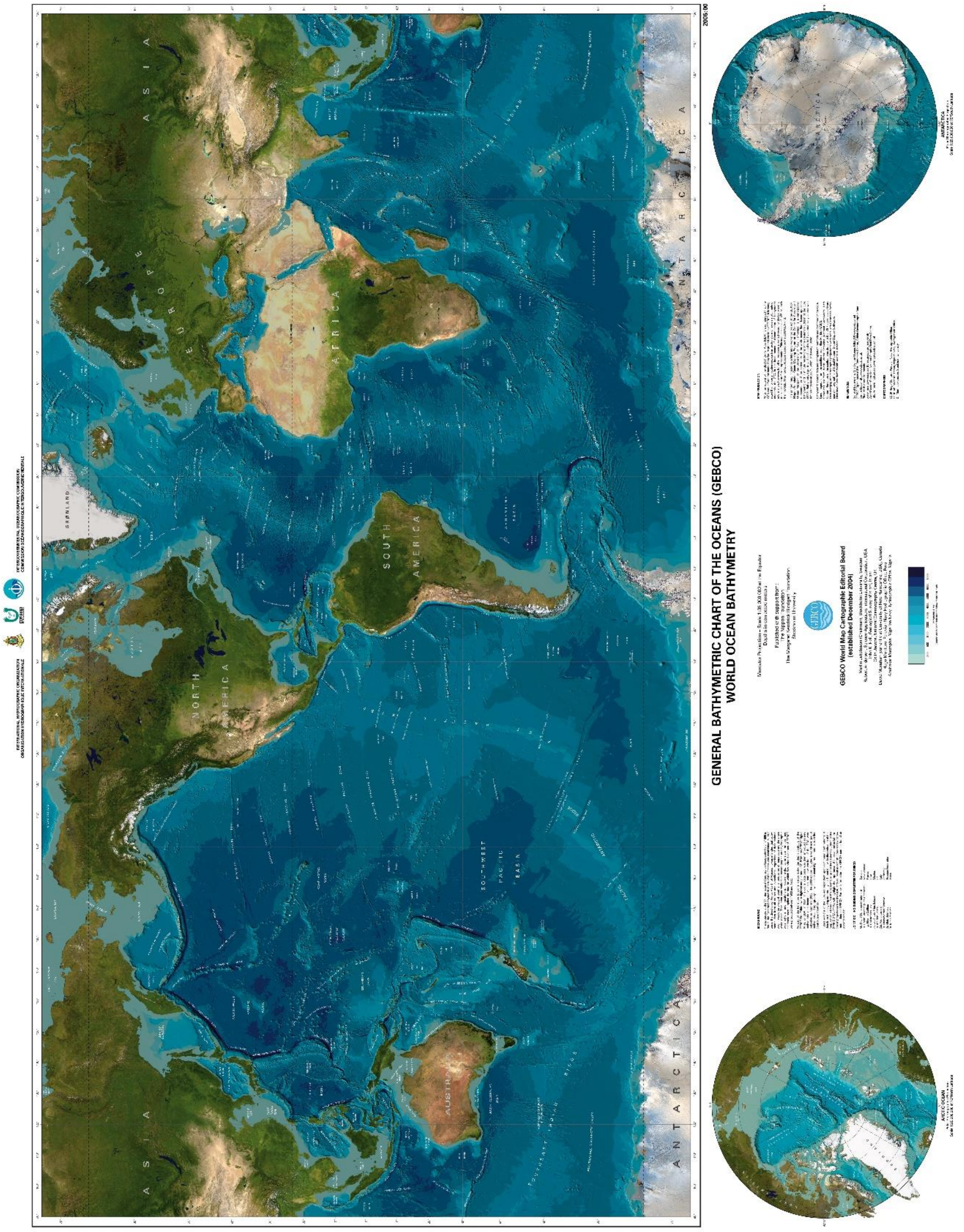

CH2-5: Map of hydrostatic pressure at the sediment-basement interface.

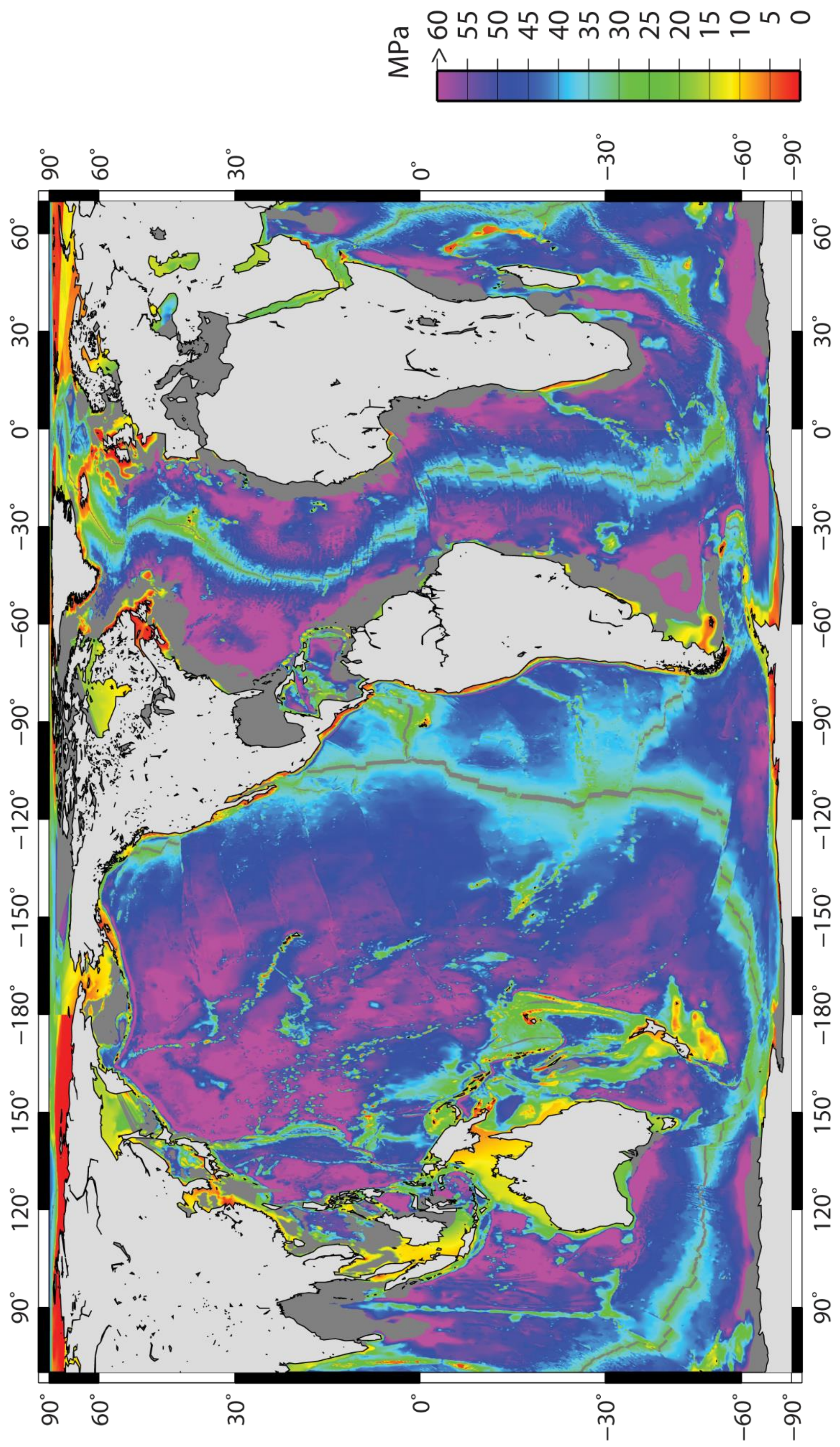

CH2-6: Comparison between estimated temperatures (from GDH1model at the top, and from HSCM at the bottom) in the eastern equatorial Pacific Ocean (eePO) and the Juan de Fuca Plate (JdFP), and measured downhole temperatures at the sediment-basement interface *[Marieni et al., 2013].* White squares: data from eePO *[Alt et al., 1993; Teagle et al., 2006];* orange squares: data from JdFP *[Davis et al., 1997].* Circles: estimated values in the eePO (blue), and on the JdFP (red with K_s = 1 W/(m K); orange with K_s = 2 W/(m K)).

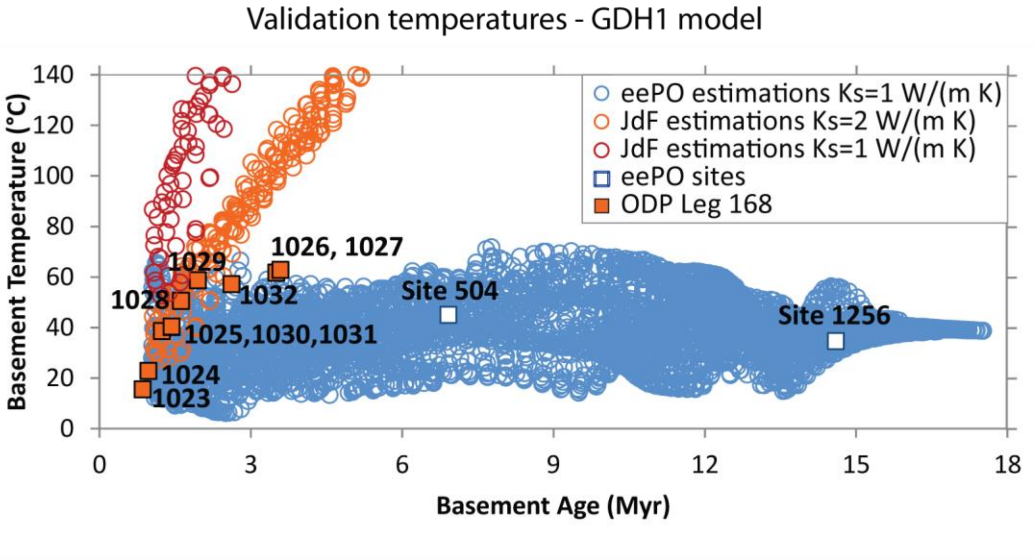

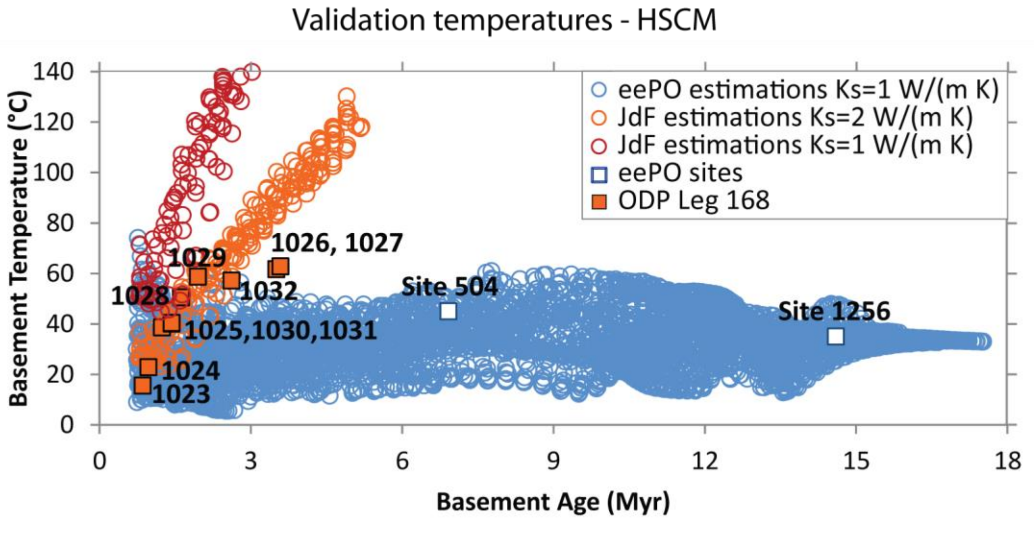

A-Chapter 3

CH3-1: Density difference between CO_2 and seawater at the sediment-basement interface as a function of plate age and sediment thickness using **A-** GDH1 and **B-** HSCM models to determine both water depth and thermal conditions. Sediment thicknesses below the heavy black line show where positive density differences required for stable gravitational trapping are achieved.

A - GDH1 model

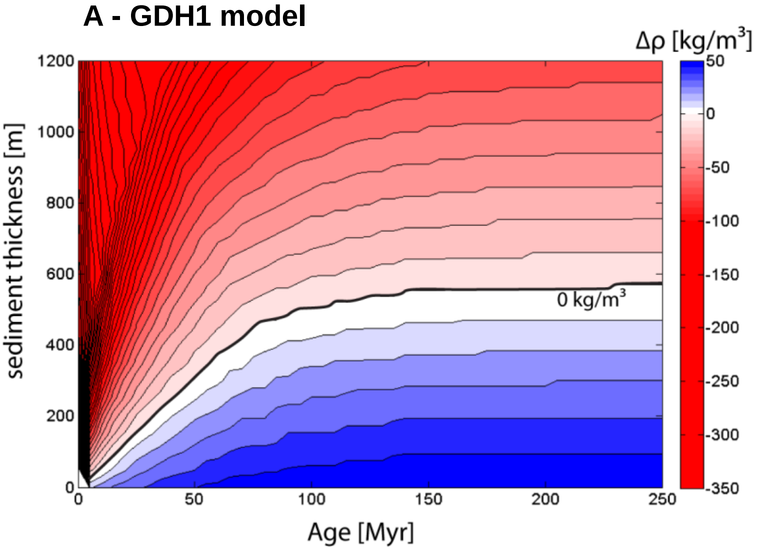

B - HSCM

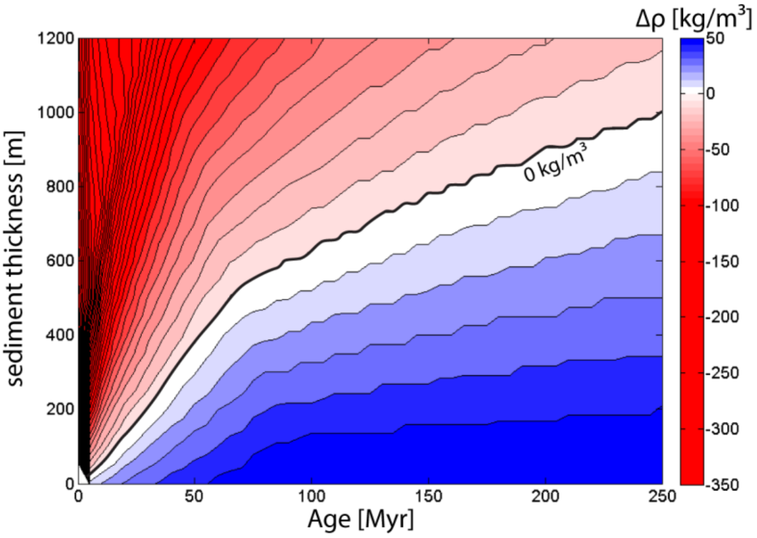

CH3-2: An equal area map showing locations for stable geological sequestration of CO_2 using the HSCM. Shading shows the difference in density between CO_2 and seawater in areas where the sediment thickness is between 200 and 700 m and the CO_2 is denser than seawater. Five potential reservoirs (**a**/**b**/**c**/**d**/**e**) have been identified. The red box indicates the area required to store 100 yrs of current anthropogenic emissions of CO_2, assuming a pillow lava thickness of 300 m and 10% porosity [*Carlson and Herrick, 1990*; *Jarrard et al., 2003; Johnson and Pruis, 2003*]. Yellow boxes show the eePO and JdF regions.

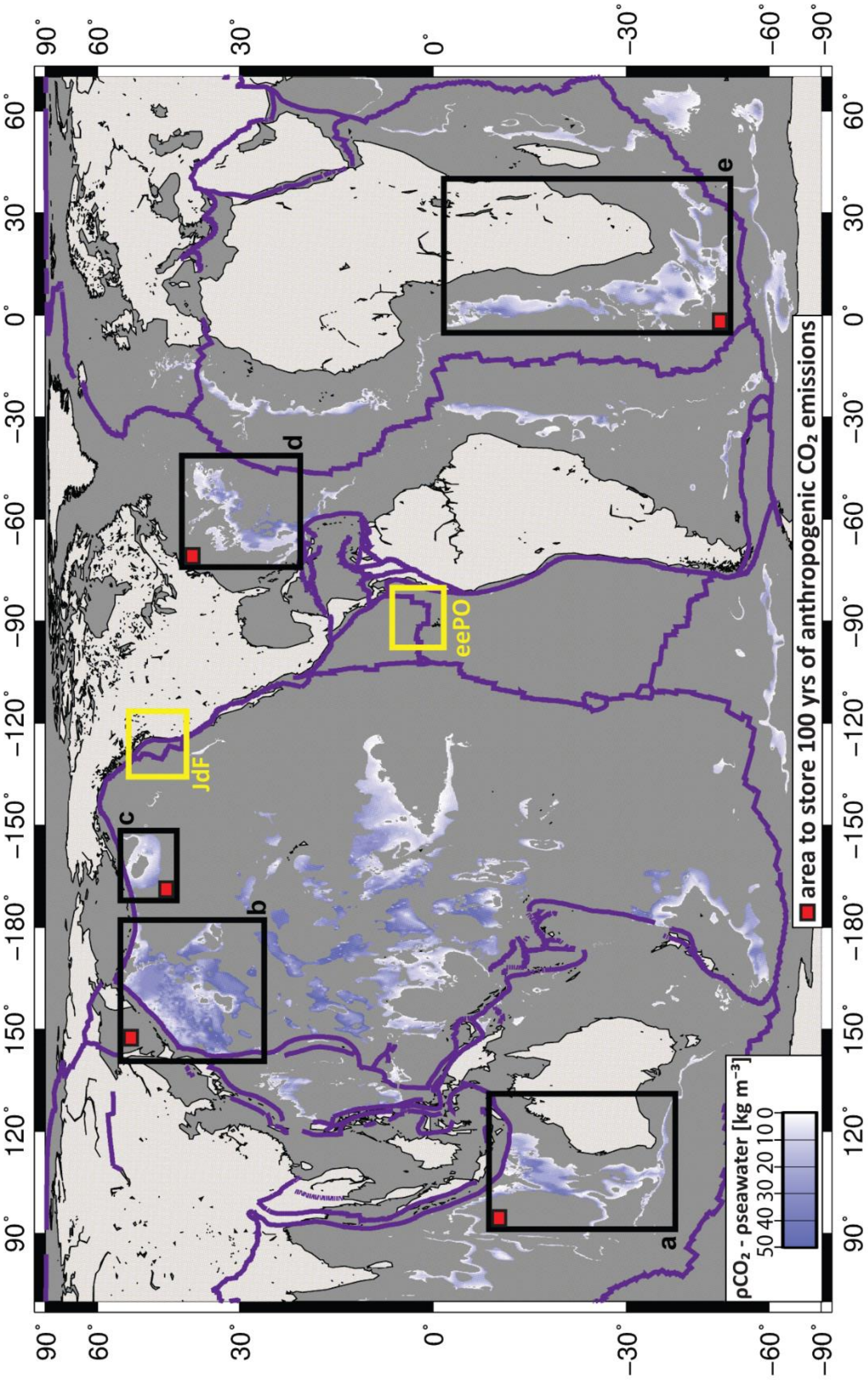

CH3-3: An equal area map showing locations for stable geological sequestration of CO_2 using the GDH1 model. Shading shows the difference in density between CO_2 and seawater in areas where CO_2 is denser than seawater, and the sediment thickness is **A**- between 200 and 500 m; **B**- between 0 and 200 m; **C-** between 100 and 200 m; **D**- between 0 and 500 m; and **E**- between 0 and 700 m.

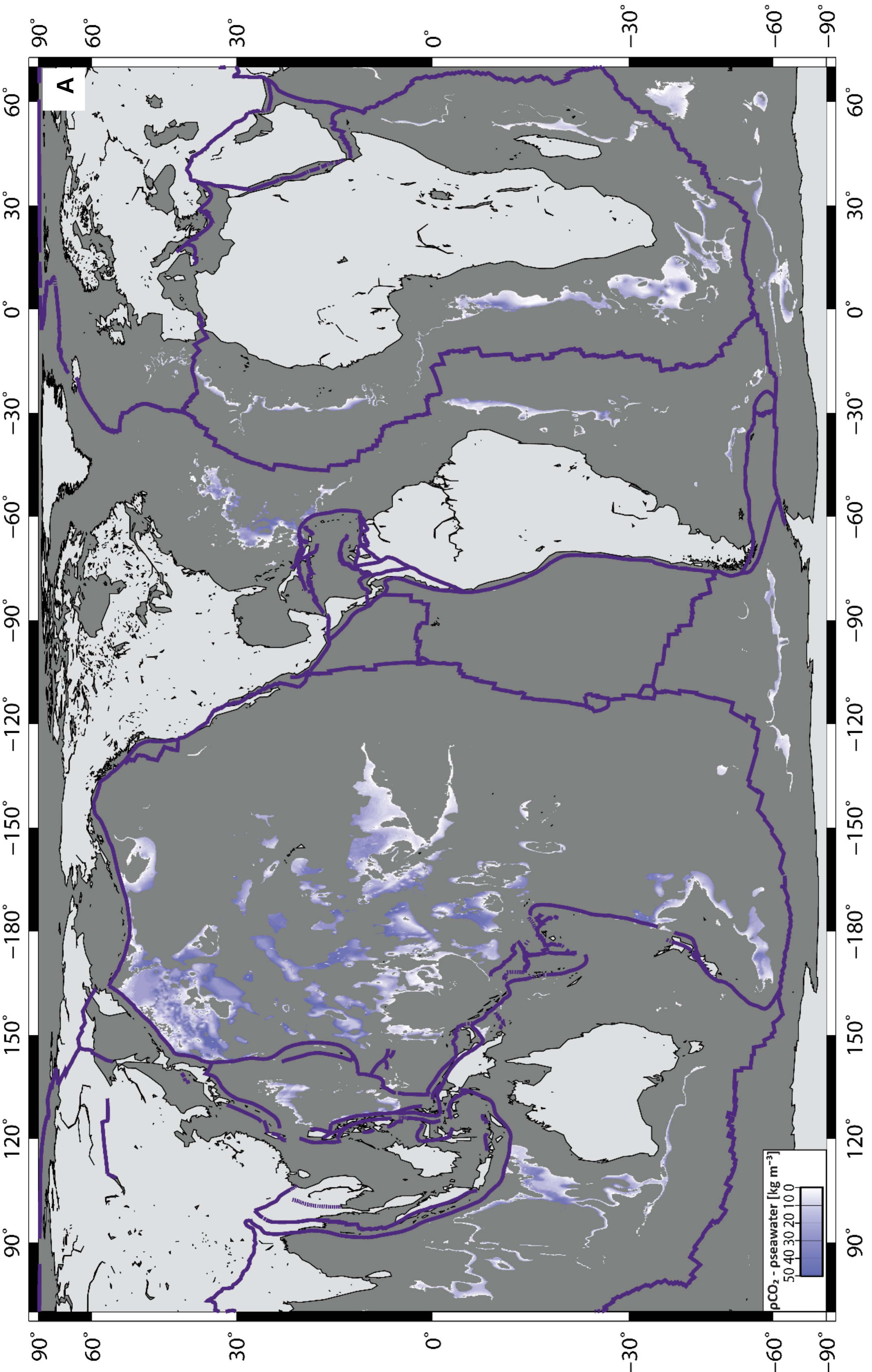

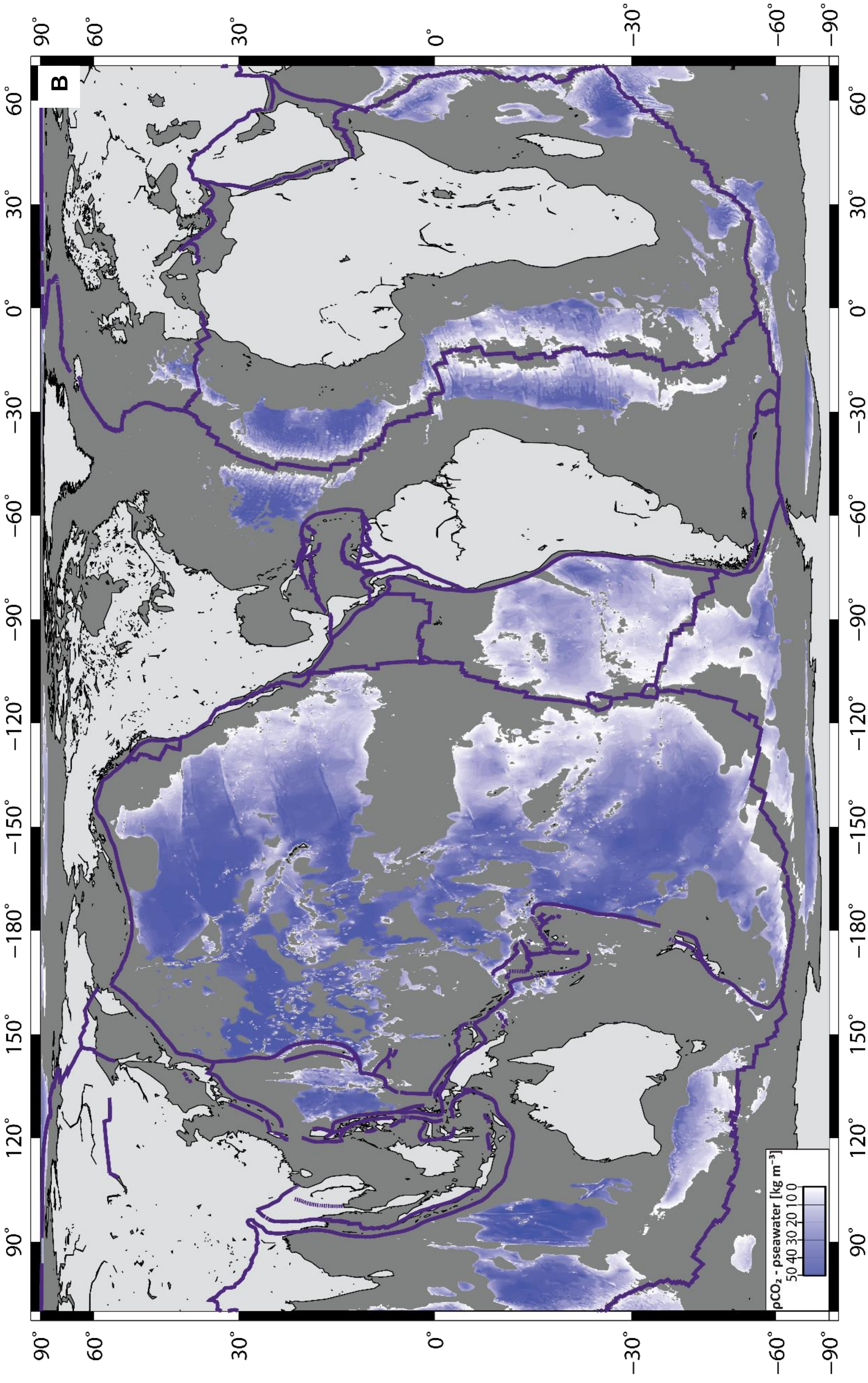
B
90°
60°
30°
0°
−30°
−60°
−90°
60°
30°
0°
−30°
−60°
−90°
−120°
−150°
−180°
150°
120°
90°
ρCO₂ - ρseawater [kg m⁻³]
50 40 30 20 10 0

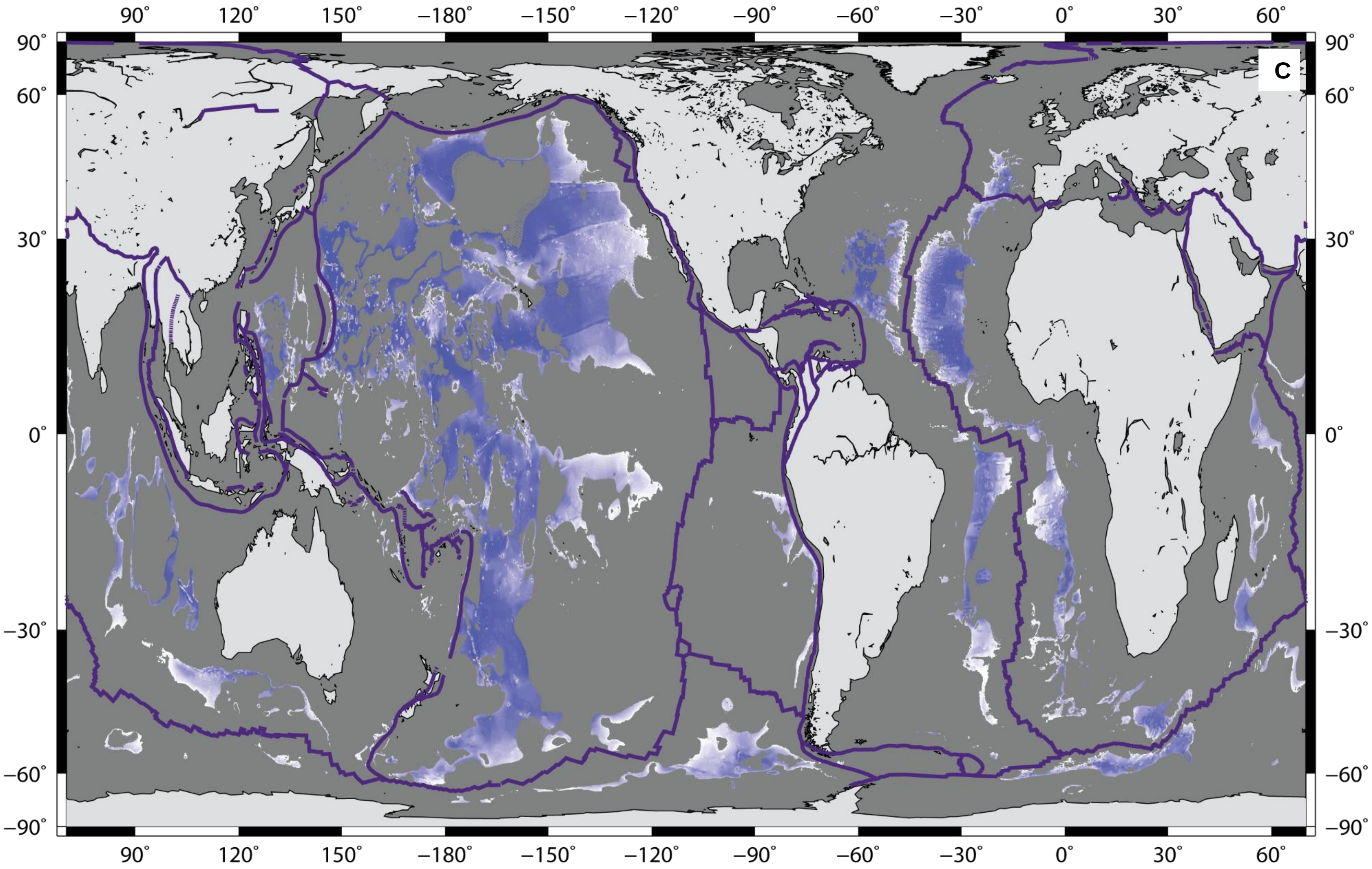
c
90°
120°
150°
−180°
−150°
−120°
−90°
−60°
−30°
0°
30°
60°
90°
60°
30°
0°
−30°
−60°
−90°

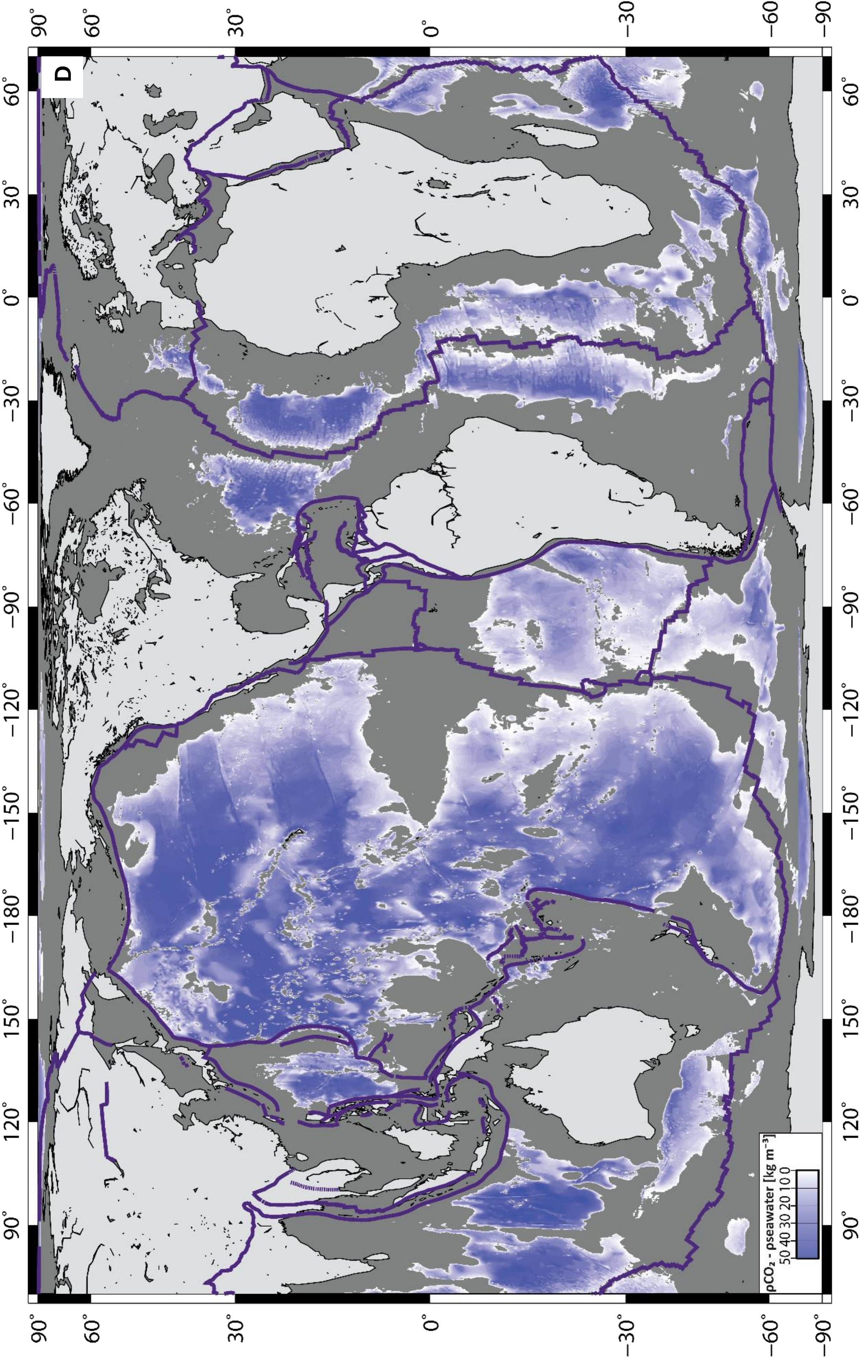
D
ρCO2 - ρseawater [kg m−3]
50 40 30 20 10 0
60°
30°
0°
−30°
−60°
−90°
−120°
−150°
−180°
150°
120°
90°
90°
60°
30°
0°
−30°
−60°
−90°

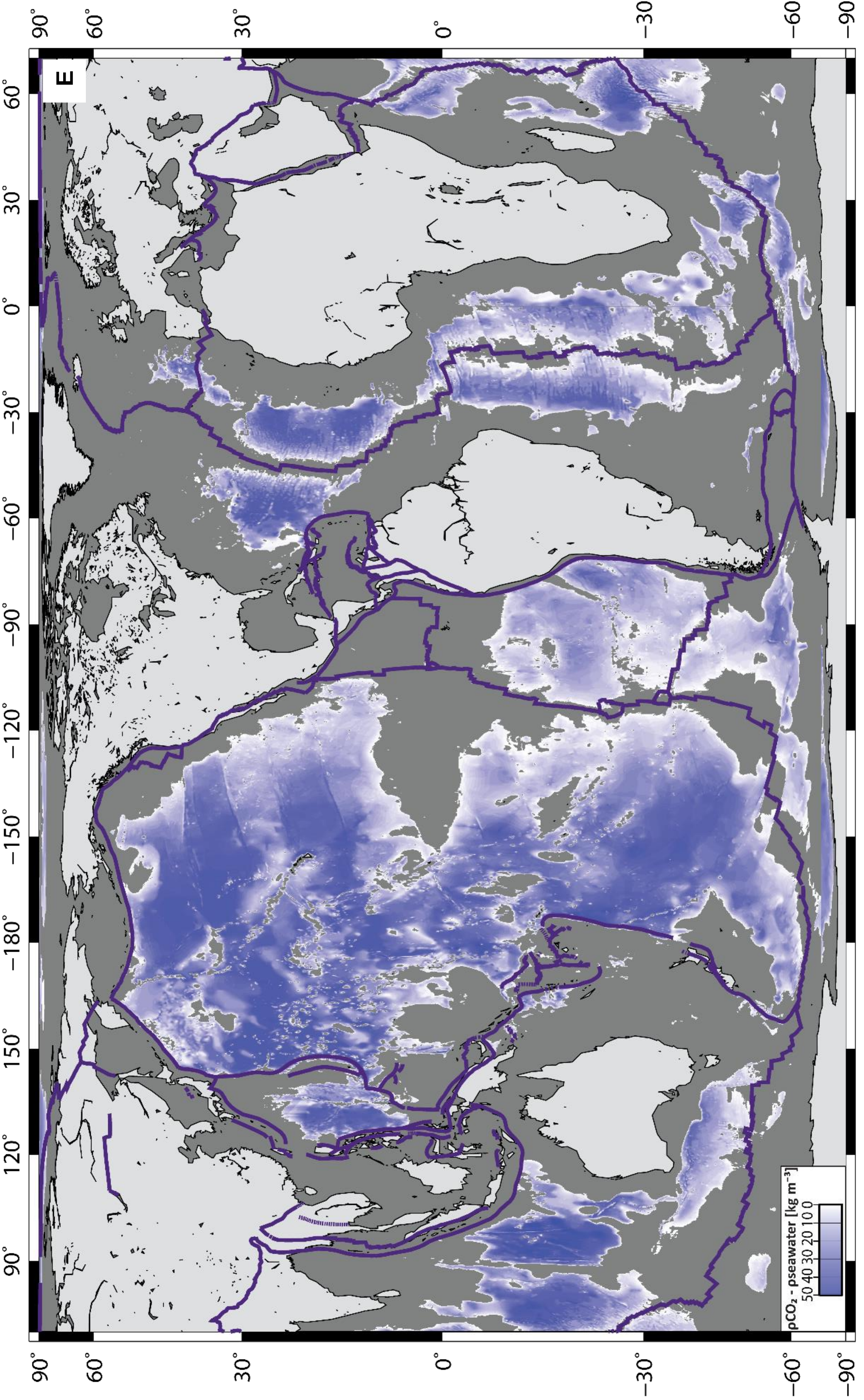
E
90° 60° 30° 0° −30° −60° −90°
60° 30° 0° −30° −60° −90° −120° −150° −180° 150° 120° 90°
ρCO₂ - ρseawater [kg m⁻³]
50 40 30 20 10 0

A-Chapter 4, Methods

CH4-1: Alkalinity titration for seawater, modified from *Haraldsson et al. (1997).*

MATERIAL**:**

Syringe (0.1-1 mL)
Becker 10mL
0.0005M HCl (in dark glass bottle) – solution prepared from HCl 0.1 mol/L (0.1M) ConvoL
Deionized (DI) water
pH electrode (FB68801, Fisherbrand™)
pH meter (Fisher Scientific™ accumet™ AB15/15+)
Magnetic stirrer (Metrohm 728), 1.5 cm magnetic follower (Fisherbrand™) and retriever
Titrator (Metrohm 775 Dosimat)

CALIBRATION:

Calibrate the pH probe using mercury free buffer solutions Reagecon at pH 4.00, 7.00 and 10.00. Rinse the pH probe with DI water.

TITRATION:

Inject 0.5 mL of sample in 4.5 mL of DI water (necessary to have enough "depth" for the pH measurement). Insert the magnetic follower and power the magnetic stirrer. Run the titration. Always collect the magnetic follower with the retriever before rinsing the equipment. Always rinse the equipment between titrations.

CALCULATIONS:

Calculate the Gran function (G):

$$G = (V + V_0) * 10^{-pH} \tag{19}$$

where V = the volume of acid added and V_0 = the initial volume of solution (0.5mL in this case).

Plot G as a function of the total volume of acid added; find the equivalence point by extrapolating the linear part of the graph to its intersect with the x-axis.

The total alkalinity of the sample (in units of mmol/L) is given by:

$$\frac{\text{Volume of acid at equivalence point (mL)} * \text{acid molarity (mol/L)}}{\text{V}_0 \text{ (mL)}} * 1000 \tag{20}$$

CH4-2: Methodology for measuring the cation concentrations in seawater with inductively coupled plasma optical emission spectrometry (ICP-OES, Perkin-Elmer Optima 4300 DV).

MATERIAL:
"A" x 20 mL acid clean (10% HNO_3) bottles (depending on "A" samples)
8 x 125 mL acid clean (10% HNO_3) bottles
3 x 20 mL acid clean (10% HNO_3) bottles – for intermediate bottles
3% HNO_3, 5ppb In, 5ppb Re, 20ppb Be (for diluting samples and standards)
10% HNO_3
Pipettes 100-1000 µL and 10-100 µL
Deionized (DI) water (for cleaning pipette)
6M HCl (for cleaning pipette)

INITIAL CONCENTRATIONS of elements (ppm):
K^+ = 9777.6
Ca^{2+} = 9631.4
S = 10000
Mg^{2+} = 9521.8
Na^+ = 9688.3
Sr^{2+} = 999
Si = 9552.6

CALCULATION FOR DILUTIONS:

$$C_1 = (C_0 * V_0)/V_1$$

C_0 Initial concentrations of a certain element [ppm = mg/kg]
C_1 Final concentrations of a certain element [ppm = mg/kg]
V_0 Initial volume of a certain element [mL]
V_1 Final volume of a certain element (diluted with 3% HNO_3, 5ppb In, 5ppb Re, 20ppb Be) [mL]

Sample dilution:
50 fold dilution (0.15 mL of sample in 7.35 mL of 3% HNO_3 (5ppb In, 5ppb Re, 20ppb Be).

Standards dilutions:
V_1 = 100 mL

We are making 6 X standards (multiple elements) each of 100 mL with the following concentrations C_1 (in ppm):

	Std 1	**Std 2**	**Std 3**	**Std 4**	**Std 5**	**Std 6**
K^+	1	5	7	8	10	15
Ca^{2+}	1	5	7	8	10	15
S	5	10	15	18	20	25
Mg^{2+}	18	22	25	27	30	32
Na^+	190	200	210	215	220	225
Sr^{2+}	0.05	0.15	0.20	0.50	1.00	2.00
Si	0.05	0.10	0.50	1.00	1.50	2.00

CALIBRATIONS:

- Using “blank samples”, with only 3% HNO3 (5ppb In, 5ppb Re, 20ppb Be) or 3% HNO3
- Using 6 standards
- Using one of the standard as a drift monitor
- Using IAPSO
- Using seawater from tank CaribSea Inc (not acidified with CO_2)

IAPSO Reference *[Summerhayes and Thorpe, 1996]*:

	Ca^{2+}	**K^+**	**Mg^{2+}**	**Na^+**	**S (total)**	**Si**	**Sr^{2+}**
ppm	412	399	1290	10770	904	2.8	7.9

SEAWATER Reference [*Millero et al., 2008*]:

	Ca^{2+}	**K^+**	**Mg^{2+}**	**Na^+**	**SO_4^{2-}**		**Sr^{2+}**
ppm	412	399	1284	10781	2712		8

NB

- Preserve major elements in samples with a drop of 3% HNO_3 in 0.5 mL of sample.
- Preserve the samples in vial closed with parafilm and refrigerated to avoid evaporation effects.
- For the analysis we used 4-5 mL of each 50 fold diluted samples

ACCURACY and precision on IAPSO:

		Ca^{2+}	**K^+**	**Mg^{2+}**	**Na^+**	**S (total)**	**Si**	**Sr^{2+}**
Average N=9	ppm	420	393	1280	10800	900	3.02	7.91
Accuracy	%	1.84	1.58	0.87	0.04	0.45	7.91	0.08
Precision	%RSD	1.85	2.61	1.77	1.26	0.38	55.5	1.09
Error 1σ	ppm	7.75	10.3	22.6	136	3.43	1.68	0.09
	mmol/L	0.19	0.26	0.93	5.92	0.11	0.06	0.001
Error 1σ in logarithmic unit σ_{log}= 0.434 *(σ/average)		0.01	0.01	0.01	0.01	0.002	0.24	0.005

ACCURACY on standards (ppm):

		K^+	Ca^{2+}	S	Mg^{2+}	Na^+	Sr^{2+}	Si
Std 1	known value	0.95	0.94	4.86	18.2	189	0.05	0.03
	average N=9	0.99	1.01	4.84	18.4	190	0.05	0.03
Std 2	known value	5.09	5.06	9.58	22.7	203	0.11	0.09
	average N=9	5.18	5.28	9.66	22.9	202	0.12	0.09
Std 3	known value	7.25	7.21	15.2	24.7	217	0.18	0.47
	average N=9	7.45	7.55	15.2	24.8	217	0.19	0.48
Std 4	known value	8.21	8.16	18.2	26.4	219	0.49	0.94
	average N=9	8.46	8.46	18.3	26.7	219	0.50	0.95
Std 5	known value	9.93	9.88	20.2	30.4	224	0.98	1.40
	average N=9	9.98	10.0	20.1	30.1	223	0.98	1.39
Std 6	known value	15.4	15.3	24.8	32.1	227	1.94	1.89
	average N=9	15.1	14.8	24.8	31.7	228	1.94	1.89
Average accuracy	%	1.34	3.52	1.15	1.00	0.26	6.35	1.37

PRECISION on standards used as drift monitors:

	DM-run 2 Std 3	**DM-run 3 Std 2**	**DM-run 4 Std 5**	**Average**
	%RSD	%RSD	%RSD	%RSD
K^+	1.09	0.93	0.91	0.98
Ca^{2+}	1.64	1.10	0.94	1.23
S	0.18	0.20	0.21	0.20
Mg^{2+}	0.73	0.46	0.37	0.52
Na^+	0.82	0.62	0.87	0.77
Sr^{2+}	0.43	0.55	0.86	0.61
Si	0.71	1.30	0.60	0.87

CH4-3: Methodology for measuring the anion concentrations in seawater with ion chromatography (Dionex ICS2500).

MATERIAL:
"A" x 20 mL bottles (depending on "A" samples)
8 x 125 mL bottles
Pipettes 100-1000 µL
Deionized (DI) water (for diluting samples and standards)
Deionized (DI) water (for cleaning pipette)
6M HCl (for cleaning pipette)

INITIAL CONCENTRATIONS of elements (ppm):
Cl^- = 5028.4
SO_4^{2-} = 1000
Br^- = 1000
F^- = 1000

CALCULATION FOR DILUTIONS:

$$C_1 = (C_0 * V_0)/V_1$$

C_0	Initial concentrations of a certain element [ppm = mg/kg]
C_1	Final concentrations of a certain element [ppm = mg/kg]
V_0	Initial volume of a certain element [ml]
V_1	Final volume of a certain element (diluted with DI water) [mL]

Sample dilution:
100 fold dilution (0.10 mL of sample in 9.90 mL of DI water).

Standards dilutions:
V_1 = 50 mL for Std 1, and 2
V_1 = 100 mL for Std 3, 4, 5, and 6

We are making 6 X standards (multiple elements) with the following concentrations C_1 (in ppm):

	Std 1	**Std 2**	**Std 3**	**Std 4**	**Std 5**	**Std 6**
Cl^-	3.24	32.4	108	180	300	500
SO_4^{2-}	0.97	9.72	32.4	54.0	90.0	150
Br^-	0.03	0.32	1.08	1.80	3.00	5.00
F^-	0.01	0.13	0.43	0.72	1.20	2.00

CALIBRATIONS:
- Using "blank samples", with only DI water
- Using 6 standards
- Using one of the standard as a drift monitor
- Using IAPSO
- Using seawater from tank CaribSea Inc (not acidified with CO_2)

IAPSO Reference *[Summerhayes and Thorpe, 1996]*:

	Cl^-	SO_4^{2-}	Br^-	F^-
ppm	19354	2712	67	1.3

SEAWATER Reference [*Millero et al., 2008*]:

	Cl^-	SO_4^{2-}	Br^-	F^-
ppm	19353	2712	67	1

NB

- Preserve the samples in vial closed with parafilm and refrigerated to avoid evaporation effects.
- For the analysis we used 5 mL of each 100 fold diluted samples

ACCURACY and precision on IAPSO:

		Cl^-	SO_4^{2-}	Br^-	F^-
Average N=5	ppm	19700	2200	66.4	1.02
Accuracy	%	1.58	2.65	17.67	21.84
Precision	%RSD	0.70	1.16	25.73	59.13

ACCURACY on standards (ppm):

		Cl^-	SO_4^{2-}	Br^-	F^-
Std 1	known value	3.26	0.95	0.03	0.01
	average N=6	4.82	0.80	0.04	0.01
Std 2	known value	33.2	9.63	0.319	0.13
	average N=6	31.8	8.35	0.321	0.13
Std 3	known value	111	32.2	1.06	0.42
	average N=6	110	30.7	1.06	0.40
Std 4	known value	185	53.6	1.77	0.69
	average N=6	185	53.2	1.71	0.67
Std 5	known value	307	89.0	2.95	1.15
	average N=6	308	90.5	3.01	1.18
Std 6	known value	514	149	4.93	1.93
	average N=6	514	149	4.92	1.92
Average accuracy	%	8.83	5.97	4.35	2.63
Average accuracy without Std 1	%	1.04	4.12	1.39	1.85

PRECISION on standards used as drift monitors:

	DM-run 2 Std 4	**DM-run 3 Std 3**	**DM-run 4 Std 5**	**Average**
	%RSD	%RSD	%RSD	%RSD
Cl^-	0.32	0.37	1.37	0.69
SO_4^{2-}	0.57	0.18	1.40	0.72
Br^-	7.92	6.16	6.18	6.75
F^-	2.92	3.80	4.04	3.59

CH4-4: Terminology for textural description of mafic rocks in thin section.

Grain size:

CRYPTOCRYSTALLINE <0.1 mm
MICROCRYSTALLINE = 0.1 – 0.2 mm
FINE GRAINED = 0.2 – 1 mm
MEDIUM GRAINED = 1 – 5 mm
COARSE GRAINED = 5 – 30 mm
PEGMATITIC = >30 mm

Texture:

GLOMEROPORPHYRITIC = large crystals that are surrounded by finer-grained matrix (phenocrysts) cluster and grow together.

GRANOBLASTIC = approximately equidimensional grains have sutured boundaries, and meet at ~120° triple junctions; characteristic of recrystallization.

INTERGRANULAR = angular interstices between feldspars occupied by pyroxene granules (very small grains).

INTERSERTAL = interstices filled with a mixture of glass and some pyroxene.

SUBOPHITIC = larger plagioclase are partially enclosed by pyroxene or olivine; the plagioclase laths typically impinge on one another to form sharp angles.

VARIOLITIC = divergent plagioclase laths with interstitial glass or intergrown with pyroxene granules

VESICULAR = cavities from expanded gases (vesicles) cover less than half of the specimen volume.

CH4-5: Inductively coupled plasma mass spectrometry (ICP-MS) methodology to analyse major, tracer, and rare earth elements. The method includes the preparation of silicate whole rocks via dissolution.

Dissolution of silicate whole rocks- "*mother solution*"

1) Accurately weigh the appropriate amount of powdered samples into an acid cleaned Savillex pot (usually 50 - 100 mg).
2) Add 10 drops of 15M HNO_3 (sb) per 10 mg of powdered sample to make a slurry.
3) In a scrubbed fume cupboard add ~1 drop of Artisar HF per mg of powdered sample.
4) Firmly screw on the lid and place on a hotplate set at 120 to 130 ˚C for at least 12 hours.
5) Remove samples from hotplate to cool.
6) Once cold, carefully remove lids (in a scrubbed fume cupboard) and check no sample remains undissolved and place back on the hotplate (lids off) and wait for samples to dry to incipient dryness (do not overdry).
7) If undissolved sample was present, repeat the HF - step 3.
8) Once dry and no sample is left undissolved, carefully remove from hotplate and add sufficient 6M HCl (sb) to dissolve the sample (at least 2 mL).
9) Replace the lid and leave on hotplate to reflux until all sample has dissolved.
10) If undissolved sample remains, add additional HCl and leave to reflux. If undissolved material still remains, dry down and carry out repeat attacks of concentrated HNO_3 (sb) and concentrated HCl (sb).
11) Once the sample is fully dissolved in 6M HCl (sb), remove lids and allow to dry to incipient dryness, be careful not to overdry.
12) Once dry add sufficient 6M HCl (sb) and leave to dissolve for at least 2 hours.
13) Transfer sample to a labelled and weighed acid cleaned HDPE bottle and rinse out the Savillex pot thoroughly with 6M HCl (sb) and Milli-Q water to make the solution ("*mother solution*") up to an appropriate volume then reweigh.

Dilution factors of the *mother solutions* were calculated (usually on the order of 400). At least one laboratory blank accompanied each batch of samples and this underwent the same digestion procedure as the samples, but without the addition of any sample powder.

Dilution for tracer and rare earth elements analysis – "*daughter solution-4'000*"

Daughter solutions-4'000 for ICP-MS analysis were produced by subsampling the *mother solutions* (~1 mL) of dissolved rock, drying down on a hot plate and redissolving in 3 % (0.68 M) HNO_3 (sb) spiked with Indium and Rhenium (5 ppb) and Beryllium (20 ppb) internal standards, to give ~4000 times dilution for rocks.

Dilution for major elements analysis – "*daughter solution-80'000*"

Daughter solutions-80'000 for ICP-MS analysis were produced by subsampling the *daughter solutions-4'000* (~250 µL), and redissolving in 3 % (0.68 M) HNO_3 (sb) spiked with Indium and Rhenium (5 ppb) and Beryllium (20 ppb) internal standards, to give ~80000 times dilution for rocks.

ICP-MS analysis procedure

Major, trace and rare earth elements (REE) were analysed on the Thermo X-Series 2 ICP-MS at the University of Southampton in solution mode. Before each analysis the instrument was tuned using a multi-element solution (Co, Y, In, La, Re, Bi and U) in order to obtain optimum sensitivity and stability. After tuning, the instrument was left to stabilise for at least a further 30 minutes. Samples were run in random order with six calibration standards and a blank acid at the start and end of each run. At the very end of the run, several blank acids were analysed to constrain detection limits.

International standard JA2 was used to test for accuracy, and this standard as well as internal standards BAS206 and BRR1 were used to assess precision. Accuracy and precision of measurements are shown in Tables A.1 and A.2, respectively. Certified values for JA2 are from the online GeoREM database (http://georoc.mpchmainz.gwdg.de). Internal precision was monitored by measuring each sample four times and calculating the percentage relative standard deviation (%RSD) which is expressed as the standard deviation of the mean as a percentage of the mean. Data with RSD of >10 % were rejected. Results were measured as counts per second (CPS), these were processed using the Plasmalab software which calibrated counts to concentration using the calibration standards BHV2, BIR1, JB1a, JB3, and JGb1, . Further processing that was applied using this software package included blank, drift and matrix corrections. Internal drift was monitored using the spikes added to each solution (In, Re and Be). In runs where REEs were measured further data processing involved correction for REE oxide formation using results from Ba and REE single tuning solutions that allow oxide formation during each run to be measured and corrected for.

Table A.1 - Accuracy JA2

Element		cert. values	average N = 30-70	average N = 20-30	average accuracy %
Li	µg/g = ppm	29.1	29.0		4.31
Na	µg/g	23100		23900	7.26
Mg	µg/g	45800		44600	7.18
Al	µg/g	81600		84400	7.04
K	µg/g	15000		16900	9.20
Ca	µg/g	45000	45600		8.62
Sc	µg/g	18.4	18.2		9.83
Ti	µg/g	4169	4000		5.92
V	µg/g	122	113		6.47
Cr	µg/g	450	389		6.22
Mn	µg/g	852	800		23.7
Fe	µg/g	43400		43000	10.9
Co	µg/g	27.0	27.7		3.96
Ni	µg/g	134	125		3.82
Cu	µg/g	27.9	30.4		5.51
Zn	µg/g	65.0	72.4		12.1
Rb	µg/g	71.0	76.4		5.45
Sr	µg/g	250	246		5.26
Y	µg/g	18.1	17.5		5.38
Zr	µg/g	112	120		7.63
Nb	µg/g	9.00	9.00		4.50
Cs	µg/g	4.90	5.18		6.01
Ba	µg/g	315	323		6.44
La	µg/g	16.1	16.1		5.07
Ce	µg/g	33.7	33.9		5.34
Pr	µg/g	3.70	3.84		3.76
Nd	µg/g	14.2	14.6		3.54
Sm	µg/g	3.10	3.12		3.71
Eu	µg/g	0.91	0.91		3.36
Gd	µg/g	3.00	3.06		3.74
Tb	µg/g	0.48	0.48		4.21
Dy	µg/g	2.90	2.93		4.44
Ho	µg/g	0.61	0.60		4.49
Er	µg/g	1.70	1.72		5.22
Tm	µg/g	0.26	0.26		4.83
Yb	µg/g	1.68	1.70		5.33
Lu	µg/g	0.25	0.26		4.59
Hf	µg/g	2.93	2.96		8.41
Ta	µg/g	0.70	0.76		19.2
Pb	µg/g	19.3	22.0		10.4
Th	µg/g	5.00	4.90		5.55
U	µg/g	2.20	2.26		4.66

Table A.2 - Precision

Element	JA2 %RSD	BAS206 %RSD	BRR-1 %RSD	Average %RSD
Li	2.16	5.14	4.95	4.08
Na	3.10	2.43	2.02	2.52
Mg	3.79	2.63	2.11	2.84
Al	3.49	2.46	2.78	2.91
K	3.92	5.02	16.4	8.44
Ca	4.28	2.13	2.68	3.03
Sc	5.10	2.63	2.18	3.30
Ti	3.11	1.75	2.66	2.50
V	3.52	2.88	3.23	3.21
Cr	3.63	6.07	3.43	4.38
Mn	13.1	2.22	2.33	5.89
Fe	5.62	2.77	2.76	3.72
Co	1.97	1.49	1.85	1.77
Ni	2.09	2.60	2.21	2.30
Cu	2.56	2.14	6.37	3.69
Zn	78.1	8.91	8.19	31.7
Rb	2.61	11.0	20.9	11.5
Sr	2.73	7.50	9.25	6.49
Y	2.85	2.66	2.34	2.62
Zr	3.51	2.89	6.40	4.27
Nb	2.30	614	4.02	207
Cs	2.93	4.84	15.0	7.60
Ba	3.25	11.6	7.70	7.53
La	2.62	5.94	1.74	3.43
Ce	2.75	5.79	1.90	3.48
Pr	1.87	5.73	1.27	2.96
Nd	1.77	5.68	1.12	2.86
Sm	1.88	5.54	1.32	2.91
Eu	1.71	5.77	1.19	2.89
Gd	1.83	6.66	1.29	3.26
Tb	2.26	5.93	1.61	3.26
Dy	2.26	5.67	1.28	3.07
Ho	2.30	5.59	1.36	3.08
Er	2.61	5.77	1.67	3.35
Tm	2.92	5.80	1.80	3.51
Yb	2.68	5.80	1.78	3.42
Lu	2.71	5.90	1.77	3.46
Hf	3.53	19.5	18.0	13.7
Ta	8.99	11.0	219	79.8
Pb	4.75	14.7	56.3	25.3
Th	2.94	10.2	85.8	33.0
U	2.34	6.30	3.88	4.17

A-Chapter 4, Analyses

CH4-6: Summary of SEM analyses on whole rocks.
SEM images are shown divided for each rock in BSE-back scatter electron, elemental line, and mineral phase mode.
SEM-EDS analyses and correspondent analytical error (standard deviation, σ) are shown for both whole rock and single phases. To note: the total for SEM-EDS analyses is forced to be 100 % from the software.
Accuracy and precision for SEM-EDS analyses have been calibrated with the standard glass sample BIR1G.

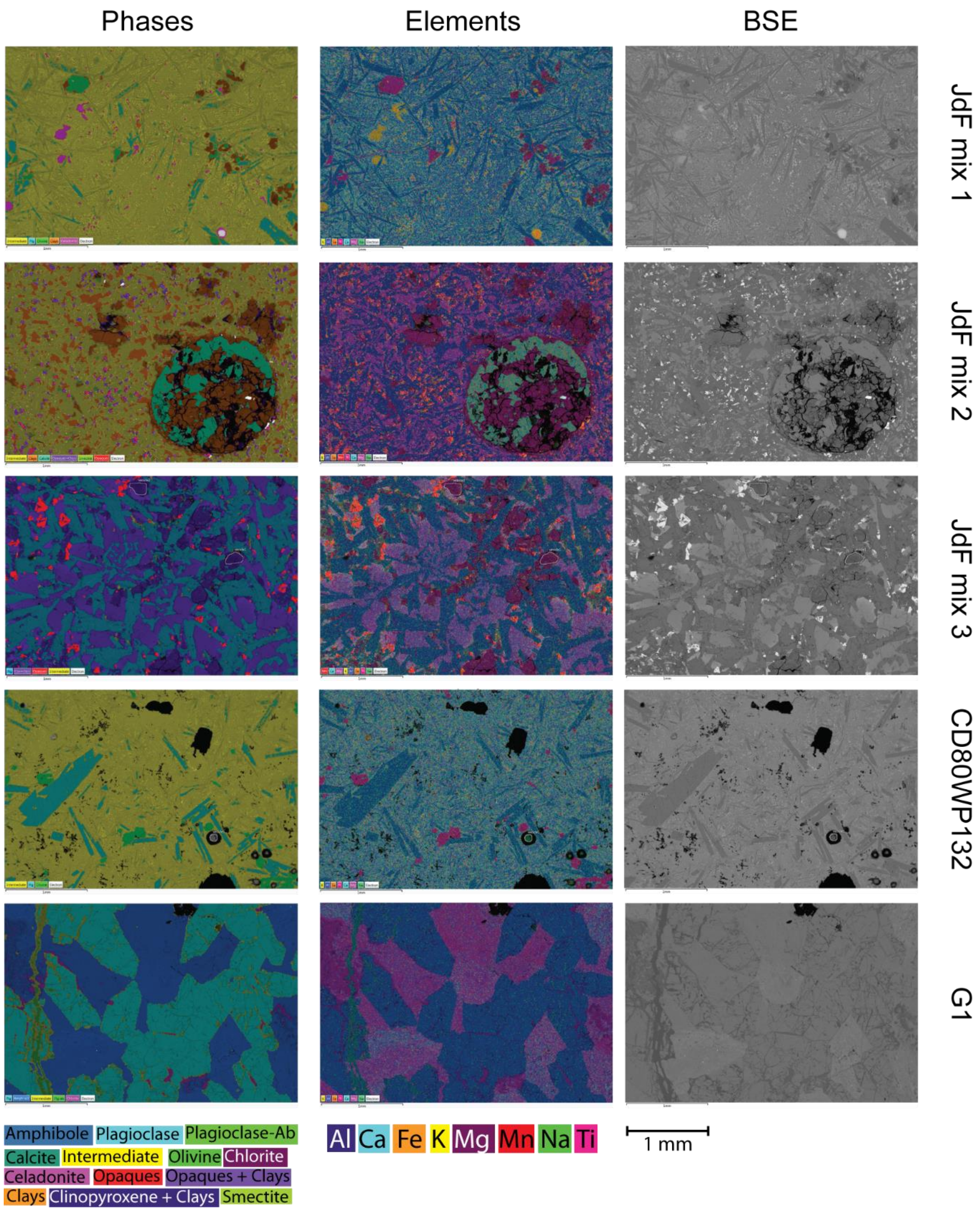

DATA FOR OXIDES ANALYSES SEM-EDS (%)

	SiO_2	TiO_2	Al_2O_3	Fe_2O_3	MnO	MgO	CaO	Na_2O	K_2O	P_2O_5	SO_3	CO_2
JdF mix 1												
Bulk rock	49.88	1.45	16.07	11.20	0.14	6.88	10.70	3.18	0.49			
Intermediate	50.23	1.52	15.94	11.05		6.44	11.11	3.26	0.45			
Plagioclase-labradorite	50.16		31.44	1.11		0.41	12.98	3.90				
Olivine	40.37			16.66		42.53	0.45					
Clays	53.12		2.85	17.54		22.63	1.66	1.19	1.01			
Celadonite	44.95	2.90	4.03	37.23		4.02	1.50	1.56	3.82			
JdF mix 2												
Bulk rock	48.94	1.39	14.86	9.98	0.36	8.55	12.08	3.26	0.20		0.38	
Intermediate	52.91	0.78	20.97	6.06		4.81	9.63	4.54	0.17		0.13	
Clays	52.79	0.86	3.90	14.33	0.16	18.79	8.40	0.55	0.22			
Smectite	79.75		5.26	5.83		4.80	1.62	2.31	0.43			
Opaques	8.62	20.38	3.30	64.39		2.05		1.25				
Oxides + clays	33.24	10.18	6.83	35.14	0.39	6.84	3.34	2.75	0.37	0.32	0.60	
Calcite	0.61			0.86	2.74	0.83	36.78				0.59	57.54
JdF mix 3												
Bulk rock	50.58	1.16	17.21	8.74	0.11	7.70	10.57	3.57	0.23	0.13		
Intermediate	44.69		15.69	15.79		6.30	13.95	3.58				
Plagioclase-labradorite1	53.18		27.17	2.25		1.42	10.53	5.31	0.15			
Plagioclase-labradorite2	52.06		31.05				12.29	4.60				
Clinopyroxene	51.12	0.86	2.78	12.08		15.80	17.36					
Clinopyroxene + clays	52.28		5.34	13.52		15.58	11.82	1.47				
Vesicle 1 - saponite	55.42		4.95	15.45		21.10	0.85	1.72	0.50			
Vesicle 2 - saponite	54.48		5.94	16.72		21.45	1.41					
Opaques	6.25	24.42	2.84	63.72		1.76	0.80		0.20			
CD80WP132												
Bulk rock	49.43	1.13	16.78	11.45	0.15	6.76	11.27	2.71	0.07		0.24	
Intermediate	50.1	1.28	15.24	12.48		6.8	11.32	2.72	0.07			
Plagioclase-labradorite	49.24		31.96			0.44	14.31	3.18				
Vesicle 1	74.89			0.87		4.10	9.06	11.95				
Olivine	38.48		0.78	20.24		39.73	0.78					
G1												
Bulk rock	48.3	0.09	23.31	5.26		9.67	12.76	1.46	0.15			
Intermediate	49.83		26.85	2.78		8.27	5.21	6.53	0.53			
Plagioclase-anorthite	44.54		35.84	0.68		0.93	16.6	1.26	0.16			
Plagioclase-albite	57.00		26.34				0.60	15.81	0.25			
Amphibole-actinolite	54.29	0.22	4.53	8.72	0.17	20.89	10.57	0.52	0.09			
Chlorite	39.75		19.19	9.67		29.50	1.42	0.48				

ERROR (σ) FOR OXIDES ANALYSES SEM-EDS (%)

	SiO_2	TiO_2	Al_2O_3	Fe_2O_3	MnO	MgO	CaO	Na_2O	K_2O	P_2O_5	SO_3	CO_2
JdF mix 1												
Bulk rock	0.04	0.01	0.03	0.03	0.01	0.02	0.02	0.02	0.01			
Intermediate	0.04	0.02	0.03	0.03		0.02	0.02	0.02	0.01			
Plagioclase-labradorite	0.22		0.16	0.08		0.06	0.10	0.09				
Olivine	0.38			0.30	0.33		0.08					
Clays	0.33		0.14	0.24		0.22	0.08	0.11	0.06			
Celadonite	0.38	0.15	0.17	0.36		0.17	0.10	0.16	0.10			
JdF mix 2												
Bulk rock	0.05	0.02	0.03	0.03	0.01	0.02	0.02	0.02	0.01		0.01	
Intermediate	0.06	0.02	0.04	0.03		0.02	0.02	0.03	0.01		0.02	
Clays	0.09	0.03	0.04	0.06	0.02	0.06	0.03	0.03	0.01			
Smectite	0.60		0.24	0.29		0.22	0.13	0.20	0.09			
Opaques	0.44	0.55	0.37	0.85		0.34		0.38				
Oxides + clays	0.18	0.11	0.11	0.19	0.06	0.11	0.06	0.10	0.03	0.08	0.07	
Calcite	0.04			0.06	0.06	0.04	0.18				0.04	0.71
JdF mix 3												
Bulk rock	0.04	0.01	0.03	0.03	0.01	0.02	0.02	0.02	0.01	0.02		
Intermediate	0.89		0.59	0.74		0.44	0.44	0.40				
Plagioclase-labradorite1	0.06		0.04	0.03		0.02	0.03	0.03	0.01			
Plagioclase-labradorite2	1.00		0.73				0.44	0.41				
Clinopyroxene	0.50	0.16	0.21	0.35		0.31	0.26					
Clinopyroxene + clays	0.07		0.03	0.05		0.04	0.03	0.02				
Vesicle 1 - saponite	0.99		0.48	0.70		0.64	0.21	0.36	0.16			
Vesicle 2 - saponite	1.04		0.50	0.74		0.67	0.23					
Opaques	0.17	0.26	0.15	0.36		0.15	0.07		0.05			
CD80WP132												
Bulk rock	0.04	0.01	0.03	0.03	0.01	0.02	0.02	0.02	0.01		0.01	
Intermediate	0.05	0.02	0.03	0.03		0.02	0.02	0.02	0.01			
Plagioclase-labradorite	0.13		0.10	0.05		0.04	0.06	0.05				
Vesicle 1	1.86					0.72	0.70	1.01				
Olivine	0.28		0.11	0.24		0.25	0.06					
G1												
Bulk rock	0.04	0.01	0.03	0.02		0.02	0.02	0.01	0.01			
Intermediate	0.18		0.13	0.08		0.09	0.06	0.08	0.03			
Plagioclase-anorthite	0.06		0.05	0.02		0.02	0.03	0.02	0.01			
Plagioclase-albite	0.43		0.30				0.08	0.24	0.06			
Amphibole-actinolite	0.07	0.02	0.03	0.04	0.02	0.04	0.03	0.02	0.01			
Chlorite	0.35		0.27	0.23		0.27	0.08	0.11				

STANDARD BIR1G ANALYSES:

	Certified value (%)	**Average N=13 (%)**	**Accuracy (%)**	**Precision % RSD**
SiO_2	47.3	47.2	1.06	1.14
TiO_2	0.98	1.04	9.70	7.59
Al_2O_3	15.6	15.6	1.37	1.30
Fe_2O_3	10.5	11.6	2.10	1.36
MnO	0.18	0.23	7.86	4.04
MgO	9.37	9.75	1.72	1.37
CaO	13.4	13.3	1.86	1.32
Na_2O	1.89	1.90	4.34	2.91
K_2O	0.03	-	-	-

CH4-7: Inductively coupled plasma mass spectrometry (ICP-MS) analyses on major, tracer, and rare earth elements, for both grain size fractions (63-125 µm and <63 µm). The element composition is given in µg/g. Analytical errors are reported in a separated table for both grain size fractions, and are given in percentage relative standard deviation (%RSD), which is expressed as the standard deviation of the mean as a percentage of the mean.

DATA (ppm)

ID	JdF mix 1		JdF mix 2		JdF mix 3		CD80WP132		G1		
	63-125 µm	<63µm	63-125 µm	<63µm	63-125 µm	<63µm	63-125 µm	<63µm	63-125 µm	<63µm	<63µm CLEAN
Na	21200	24500	22200	24700	22600	23600	18000	17200	5430	3680	4910
Mg	44100	51000	52200	54500	50900	48000	56900	54800	75200	70500	80900
Al	80300	95200	90300	101000	89300	92600	83400	84200	114000	69000	102000
K	1820	2160	1240	1360	1880	1640	337	267	322	196	269
Ca	87800	104000	102000	113000	104000	103000	101000	98300	129000	83400	121000
Mn	1930	2180	1710	1820	1880	1880	1970	1770	916	836	960
Fe	78100	80000	77600	81900	83400	82900	114000	85300	37500	34400	40100
Sr	119	141	127	141	125	135	75.4	73.8	56.3	37.5	49.5
Li	6.02	5.59	5.37	5.27	5.43	5.37	5.04	4.67	5.39	7.17	5.24
Sc	50.1	47.8	51.3	50.3	52.9	49.7	53.1	52.2	36.2	40.3	39.6
Rb	3.56	3.61	2.21	2.23	4.43	3.19	0.80	0.73	1.00	1.18	1.04
Sr	120	118	114	118	113	117	67.1	68.4	49.8	45.0	45.2
Y	48.0	43.9	32.8	30.8	32.8	29.4	34.4	31.6	2.79	3.01	3.13
Zr	127	114	78.9	72.4	77.0	68.4	61.9	56.0	1.26	1.39	1.47
Nb	3.12	2.91	2.05	1.88	2.16	2.12	1.50	1.37	0.14	0.14	0.15
Sn	1.28	1.19	1.01	0.92	1.05	0.98	0.81	0.85	0.23	0.23	0.25
Cs	0.14	0.14	0.08	0.08	0.13	0.10	0.01	0.01	0.03	0.03	0.03
Ba	17.0	14.3	8.63	8.35	8.98	7.97	9.36	8.62	2.91	3.01	3.24
La	4.36	3.91	2.53	2.25	2.36	2.00	1.78	1.61	0.06	0.06	0.07
Ce	13.7	12.3	8.15	7.29	7.65	6.51	5.90	5.33	0.15	0.17	0.18
Pr	2.43	2.19	1.48	1.35	1.40	1.21	1.12	1.02	0.03	0.03	0.03
Nd	13.3	12.0	8.29	7.66	7.99	6.94	6.70	6.07	0.20	0.20	0.22
Sm	4.70	4.29	3.11	2.88	3.05	2.70	2.71	2.49	0.12	0.13	0.14
Eu	1.64	1.52	1.19	1.16	1.21	1.13	1.04	0.96	0.08	0.08	0.09
Gd	6.57	6.03	4.46	4.17	4.41	3.95	4.15	3.83	0.26	0.27	0.30
Tb	1.20	1.10	0.82	0.78	0.83	0.74	0.80	0.74	0.06	0.06	0.06
Dy	7.96	7.28	5.49	5.17	5.56	4.98	5.57	5.11	0.45	0.47	0.50
Ho	1.71	1.57	1.20	1.13	1.20	1.09	1.24	1.14	0.10	0.11	0.12
Er	5.00	4.61	3.50	3.29	3.52	3.17	3.74	3.44	0.33	0.35	0.37
Tm	0.76	0.70	0.53	0.50	0.53	0.48	0.58	0.53	0.05	0.06	0.06
Yb	4.91	4.50	3.44	3.25	3.48	3.15	3.81	3.50	0.35	0.39	0.39
Lu	0.74	0.68	0.53	0.50	0.53	0.48	0.58	0.54	0.05	0.06	0.06
Hf	3.49	3.17	2.32	2.16	2.26	2.04	1.86	1.72	0.06	0.07	0.07
Ta	0.21	0.20	0.14	0.13	0.14	0.14	0.10	0.09	0.01	0.01	0.01
Pb	0.65	0.66	0.42	0.38	0.44	0.39	0.30	0.37	0.15	0.17	0.17
Th	0.21	0.19	0.12	0.11	0.11	0.09	0.10	0.09	0.01	0.01	0.01
U	0.09	0.08	0.07	0.06	0.08	0.07	0.05	0.06	0.01	0.01	0.01

ERROR (% RSD)

ID	JdF mix 1 - %RSD		JdF mix 2 - %RSD		JdF mix 3 - %RSD		CD80WP132 - %RSD		G1 - %RSD		
	63-125 µm	<63µm	63-125 µm	<63µm	63-125 µm	<63µm	63-125 µm	<63µm	63-125 µm	<63µm	<63µm CLEAN
Na	0.54	0.74	1.02	0.45	0.59	0.39	0.27	0.55	0.95	0.37	1.31
Mg	0.54	0.56	0.30	0.32	0.39	0.39	0.29	0.60	0.34	0.27	0.51
Al	0.37	0.20	0.46	0.44	0.78	0.48	0.72	0.39	0.44	0.66	0.47
K	1.51	1.04	2.61	3.57	1.64	1.41	3.06	17.65	6.32	10.06	11.13
Ca	1.17	1.02	1.00	0.81	0.37	0.67	1.01	1.47	0.68	0.73	0.20
Mn	0.53	0.43	0.44	0.60	0.73	0.42	0.72	0.71	0.32	0.71	0.73
Fe	0.86	3.15	0.45	1.20	1.54	3.51	0.43	22.25	0.56	0.57	0.24
Sr	1.19	1.23	1.14	1.55	1.80	0.76	1.13	2.87	2.09	3.01	2.30
Li	1.98	1.38	1.25	2.08	1.95	1.69	1.28	1.23	1.24	0.64	1.69
Sc	0.30	0.85	0.76	0.71	0.85	0.42	0.27	0.36	0.60	0.22	0.38
Rb	0.79	0.74	1.22	1.16	0.92	1.09	1.16	1.60	1.96	1.80	1.16
Sr	0.42	0.46	0.38	0.40	0.70	0.64	0.24	0.28	0.78	0.71	0.45
Y	0.45	0.22	0.28	0.17	0.10	0.31	0.24	0.25	1.61	0.62	0.71
Zr	0.34	0.68	0.32	0.36	0.22	0.28	0.36	0.29	1.34	1.40	1.50
Nb	0.49	0.74	1.54	0.76	0.71	0.56	0.88	1.21	2.37	2.50	1.75
Sn	2.11	1.11	0.54	1.25	1.28	0.70	2.39	1.92	1.51	1.26	1.55
Cs	1.85	1.96	3.29	3.49	2.06	3.63	9.19	10.34	4.82	3.56	6.70
Ba	0.79	0.66	1.20	0.68	0.84	1.42	0.70	1.45	1.53	1.89	0.79
La	0.51	0.67	0.58	0.70	0.45	0.58	0.82	0.32	5.10	1.61	1.75
Ce	0.41	0.12	0.16	0.56	0.48	0.38	0.32	0.12	3.11	1.44	1.49
Pr	0.91	0.28	0.41	0.38	1.02	0.60	0.16	0.55	3.92	1.60	6.70
Nd	0.41	0.66	0.72	0.70	0.66	0.52	0.37	0.33	2.83	5.61	2.99
Sm	1.43	1.04	1.43	0.75	1.15	0.63	0.99	0.94	2.98	7.36	4.20
Eu	0.71	0.65	0.88	0.41	0.96	0.95	0.59	1.33	1.95	0.96	3.04
Gd	0.66	0.43	0.74	0.56	0.43	1.06	0.73	0.71	2.94	1.96	2.59
Tb	0.48	0.46	0.26	0.75	0.34	0.40	0.86	1.32	2.91	2.59	2.28
Dy	0.40	0.23	0.36	0.74	0.39	0.98	0.35	0.77	2.06	0.48	0.71
Ho	0.25	0.39	0.44	0.63	0.30	0.43	0.49	0.88	0.89	2.64	2.59
Er	0.26	0.44	0.27	0.73	0.37	0.95	1.02	0.49	2.18	1.87	1.18
Tm	0.49	0.75	0.63	1.15	0.19	0.84	0.97	0.82	3.66	3.06	0.79
Yb	0.22	0.36	0.38	0.16	0.90	0.80	0.28	0.39	1.83	1.05	1.34
Lu	0.20	0.31	0.62	0.66	0.38	0.95	0.29	0.31	4.90	2.92	1.59
Hf	0.38	0.27	0.59	0.46	0.59	0.80	0.40	0.80	2.88	2.66	1.44
Ta	1.19	1.40	0.82	1.72	2.51	0.97	1.67	1.34	5.80	1.92	10.07
Pb	0.99	1.16	1.21	1.47	1.12	2.12	0.87	1.91	0.62	2.90	1.87
Th	1.20	1.04	0.83	1.09	1.32	1.50	1.34	1.11	2.97	8.62	4.28
U	2.76	2.00	2.58	2.39	4.12	2.10	3.10	1.52	1.82	5.41	4.81

CH4-8: X-ray diffraction (XRD) analyses on mineralogical composition of rocks, for both grain size fractions (63-125 µm and <63 µm).

MINERALOGICAL COMPOSITIONS (%)

ID		Plagioclase - anorthite	Plagioclase - labradorite	Plagioclase - andesine	Clinopyroxene - augite	Clinopyroxene - diopside	Amphibole	Chlorite	Talc	TOTAL
JdF mix 1	63-125 µm	19.4	15.7	20.0	42.2					97.3
	<63 µm	20.8	15.2	21.4	43.7					101.1
JdF mix 2	63-125 µm	21.9	20.3	19.7	41.4					103.3
	<63 µm	21.1	19.4	22.4	41.5					104.4
JdF mix 3	63-125 µm	19.0	27.5	11.1	43.0					100.6
	<63 µm	24.9	32.3	11.2	41.2					109.6
CD80WP132 (normalized)	63-125 µm	55.5				44.5				100
	<63 µm	57.8				42.2				100
G1	63-125 µm	76.0				12.8	23.0	1.0	4.3	117.1
	<63 µm	58.8				10.9	27.7	1.4	7.7	106.5
	<63 µm CLEAN	69.4				12.3	27.8	0.9	6.1	116.5

CH4-9: X-ray fluorescence (XRF) analyses on chemical composition of rocks (divided in major and trace elements), for both grain size fractions (63-125 µm and <63 µm). International standard OU-6 was used to test for accuracy, precision and limits of detection (LOD). Precision is given in percentage relative standard deviation (%RSD), which is expressed as the standard deviation of the mean as a percentage of the mean.

MAJOR ELEMENTS: DATA (%)

ID	**JdF mix 1**		**JdF mix 2**		**JdF mix 3**		**CD80WP132**		**G1**		
	63-125 µm	<63 µm	63-125 µm	<63 µm	63-125 µm	<63 µm	63-125 µm	<63 µm	63-125 µm	<63 µm	<63 µm CLEAN
SiO_2	49.56	48.32	48.60	49.64	50.06	49.55	49.00	50.86	44.89	47.36	46.92
TiO_2	1.93	2.03	1.66	1.60	1.70	1.95	1.24	1.05	0.09	0.10	0.10
Al_2O_3	13.56	13.33	13.66	14.27	13.74	14.18	12.54	13.65	17.20	14.38	15.67
Fe_2O_3	11.72	12.41	11.19	10.63	11.63	12.23	14.45	12.55	5.54	6.44	6.08
MnO	0.23	0.24	0.20	0.19	0.20	0.21	0.22	0.19	0.11	0.13	0.12
MgO	6.47	6.82	7.40	7.18	6.79	6.35	7.65	7.57	11.08	13.17	11.77
CaO	12.39	12.88	13.88	13.41	12.86	12.84	12.88	12.29	17.09	14.07	15.38
Na_2O	2.35	2.20	2.15	2.09	2.12	2.05	1.70	1.51	0.95	1.08	0.89
K_2O	0.20	0.21	0.12	0.11	0.18	0.13	0.02	0.02	0.04	0.05	0.05
P_2O_5	0.15	0.12	0.07	0.05	0.06	0.06	0.05	0.06	<0.01	<0.01	<0.01
SO_3	0.10	0.10	0.13	0.14	0.08	0.11	0.24	0.21	<0.03	<0.03	<0.03
LOI	1.33	1.33	0.93	0.69	0.58	0.35	-0.18	-0.38	2.70	2.90	2.70
TOTAL	99.99	99.99	99.99	100.00	100.00	100.01	99.82	99.58	99.66	99.64	99.66

TRACE ELEMENTS: DATA (ppm)

ID	**JdF mix 1**		**JdF mix 2**		**JdF mix 3**		**CD80WP132**		**G1**		
	63-125 µm	<63 µm	63-125 µm	<63 µm	63-125 µm	<63 µm	63-125 µm	<63 µm	63-125 µm	<63 µm	<63 µm CLEAN
V	380	372	371	354	375	379	347	383	140	158	169
Cr	250	247	306	264	276	201	210	246	488	584	525
Co	51	44	47	47	58	47	53	59	24	36	31
Ni	62	70	62	58	48	50	78	76	96	120	108
Cu	53	54	54	47	39	40	113	114	27	46	20
Zn	108	108	100	98	105	101	102	101	27	33	29
Ga	17	17	19	18	18	19	17	15	9	9	8
Ge	< 3	< 3	< 3	< 3	< 3	< 3	< 3	< 3	< 1	< 1	< 1
As	< 3	< 3	< 3	< 3	< 3	< 3	< 3	< 3	< 1	< 1	< 1
Se	< 3	< 3	< 3	< 3	< 3	< 3	< 3	< 3	< 1	< 1	< 1
Br	< 3	< 3	< 3	< 3	< 3	< 3	< 3	< 3	< 1	< 1	< 1
Rb	4	4	2	3	5	4	2	1	1	2	2
Sr	120	123	127	131	126	125	68	72	50	45	45
Y	42	41	32	31	32	28	30	26	3	3	3
Zr	127	121	89	83	86	76	62	58	7	7	7
Nb	5	5	< 1	1	5	4	3	< 2	2	1	1
Mo	< 3	< 3	< 3	< 3	< 3	< 3	< 3	< 3	< 2	< 2	< 2
Ag	< 3	< 3	< 3	< 3	< 3	< 3	< 3	< 3	< 2	< 2	< 2
Cd	< 3	< 3	< 3	< 3	< 3	< 3	< 3	< 3	< 2	< 2	< 2
In	< 3	< 3	< 3	< 3	< 3	< 3	< 3	< 3	< 3	< 3	< 3
Sn	< 3	< 3	< 3	< 3	< 3	< 3	< 3	2	< 3	< 3	< 3
Sb	< 3	< 3	< 3	< 3	< 3	< 3	< 3	< 3	< 3	< 3	< 3
Ba	68	73	64	71	50	100	98	56	5	9	7
La	8	< 5	< 5	6	5	< 5	5	< 5	< 3	< 3	< 3
Ce	19	10	12	13	12	9	11	10	5	4	5
Pb	< 3	< 3	< 3	< 3	< 3	< 3	6	2	1	1	1
Th	< 3	< 3	< 3	< 3	3	< 3	< 3	1	< 2	< 2	< 2
U	< 3	< 3	< 3	< 3	< 3	< 3	< 3	< 3	< 2	< 2	< 2

STANDARD OU-6 ANALYSES:

MAJOR ELEMENTS	Certified value (%)	Average N=36 (%)	Accuracy (%)	% RSD	LOD
SiO_2	57.35	57.33	0.41	0.20	0.35
TiO_2	0.99	0.99	1.65	0.82	0.02
Al_2O_3	20.45	20.34	0.58	0.29	0.10
Fe_2O_3	8.99	8.99	0.99	0.50	0.13
MnO	0.28	0.30	2.27	1.06	0.01
MgO	2.41	2.37	2.73	1.38	0.10
CaO	0.74	0.76	1.96	0.96	0.02
Na_2O	1.78	1.78	4.72	2.36	0.13
K_2O	3.04	3.01	1.43	0.72	0.07
P_2O_5	0.12	0.12	10.82	5.39	0.02

TRACE ELEMENTS	Certified value (ppm)	Average N=10 (ppm)	Accuracy (%)	% RSD	LOD
V	129	130	3.27	1.62	6.32
Cr	71	70.8	4.08	2.04	4.34
Co	29	29.4	12.55	6.19	5.46
Ni	40	40.0	6.38	3.19	3.83
Cu	40	39.5	5.24	2.65	3.14
Zn	111	113	6.16	3.03	10.2
Ga	24	23.9	4.92	2.48	1.77
Ge	#	#	#	#	#
As	13	13.0	11.18	5.60	2.18
Se	#	#	#	#	#
Br	#	#	#	#	#
Rb	120	121	1.34	0.66	2.41
Sr	132	129	3.10	1.58	6.13
Y	28	28.0	10.33	5.16	4.34
Zr	174	176	3.02	1.50	7.89
Nb	14	12.4	7.35	4.16	1.54
Mo	1	1.30	10.11	3.90	0.15
Ag	#	#	#	#	#
Cd	#	#	#	#	#
In	#	#	#	#	#
Sn	3	2.71	20.00	11.08	0.90
Sb	1	1.16	35.68	7.69	0.27
Ba	480	475	4.89	2.47	35.2
La	33	32.3	21.87	11.18	10.8
Ce	77	77.7	8.33	4.12	9.62
Pb	28	29.9	14.89	6.97	6.26
Th	12	13.0	3.41	1.58	0.61
U	2	2.18	50.19	23.03	1.51

CH4-10: Summary of SEM-EDS analyses on grains in ground samples (63-125 µm), before each experiments.

The red crosses on SEM-EDS images indicates the analysed spot. Images, data, and correspondent analytical error (standard deviation, σ) are shown for each sample used in the dissolution experiments.

Accuracy and precision for SEM-EDS analyses have been calibrated with the standard glass sample BIR1G (See Appendix CH4-6).

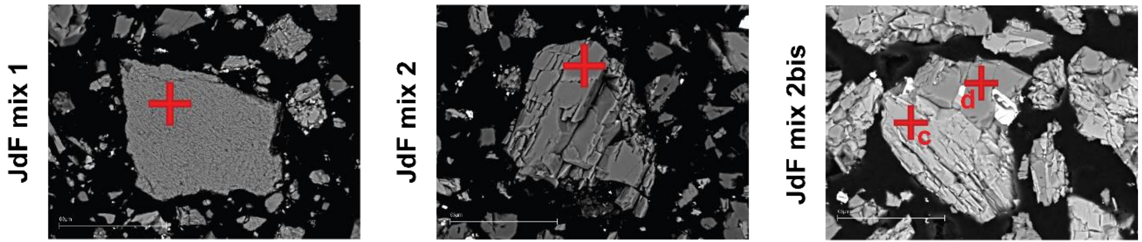

a) Intermediate 2000X

b) Clinopyroxene 2000X

c) Clinopyroxene 2000X
d) Plagioclase 2000X

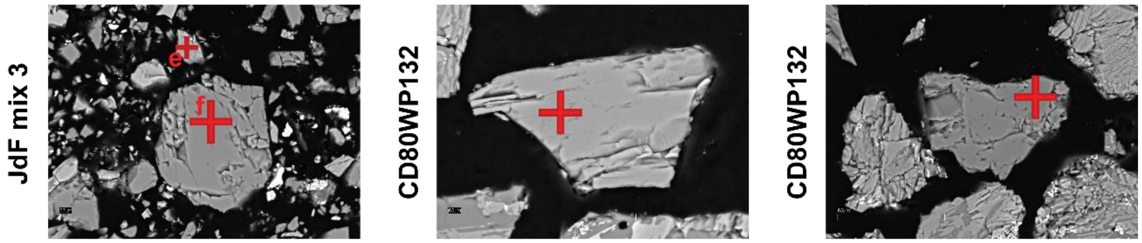

e) Clinopyroxene 2000X
f) Plagioclase 2000X

g) Clinopyroxene 3500X

h) Plagioclase 2000X

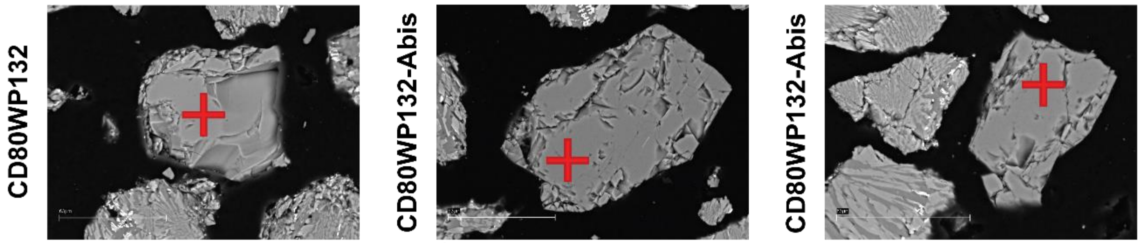

i) Olivine 2000X

l) Plagioclase 2000X

m) Plagioclase 2500X

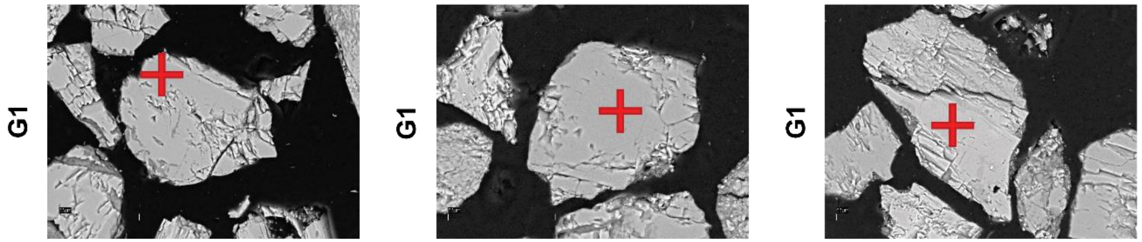

n) Plagioclase 1500X

o) Plagioclase 2000X

p) Amphibole 1500X

DATA FOR OXIDES ANALYSES (%)

	Sample	Mineral	SiO_2	TiO_2	Al_2O_3	Fe_2O_3	MnO	MgO	CaO	Na_2O	Cr_2O_3	TOT
a	JdF mix 1	Int	48.95	2.90	12.76	12.65		8.81	12.58	2.20		100.84
b	JdF mix 2	Cpx	50.99	0.75	2.70	8.32		17.09	18.51	0.29		98.65
c	JdF mix 2bis	Cpx	50.62	1.67	4.37	12.62	0.35	16.79	16.44			102.85
d	JdF mix 2bis	Plg	54.32		28.08	1.23			10.74	5.13		99.50
e	JdF mix 3	Cpx	51.85	0.96	3.69	8.48		18.35	17.86			101.17
f	JdF mix 3	Plg	53.31		28.91	1.01			11.89	4.89		100.01
g	CD80WP132	Cpx	51.27	0.31	2.45	6.95		17.65	19.39	0.30	0.35	98.66
h	CD80WP132	Plg	45.46		32.49	0.80		0.25	16.17	2.11		97.27
i	CD80WP132	Ol	37.29			21.93	0.29	40.04	0.38			99.93
l	CD80WP132-Abis	Plg	48.82		31.66	0.85		0.31	14.91	2.91		99.47
m	CD80WP132-Abis	Plg	48.62		32.45	0.71		0.29	15.65	2.83		100.55
n	G1	Plg-An	42.82		35.57	0.55			19.02	0.56		98.51
o	G1	Plg-An	42.65		35.44	0.65			19.29	0.64		98.68
p	G1	Amph	52.77	0.30	1.13	6.21		17.14	21.63			99.18

ERROR (σ) FOR OXIDES ANALYSES (%)

	Sample	Mineral	SiO_2	TiO_2	Al_2O_3	Fe_2O_3	MnO	MgO	CaO	Na_2O	Cr_2O_3
a	JdF mix 1	Int	0.29	0.11	0.16	0.20		0.14	0.13	0.10	
b	JdF mix 2	Cpx	0.29	0.08	0.10	0.17		0.17	0.15	0.07	
c	JdF mix 2bis	Cpx	0.31	0.10	0.12	0.20	0.08	0.18	0.14		
d	JdF mix 2bis	Plg	0.31		0.21	0.10			0.12	0.12	
e	JdF mix 3	Cpx	0.31	0.09	0.11	0.18		0.18	0.15		
f	JdF mix 3	Plg	0.31		0.21	0.10			0.13	0.11	
g	CD80WP132	Cpx	0.29	0.08	0.10	0.16		0.17	0.15	0.07	0.08
h	CD80WP132	Plg	0.29		0.22	0.10		0.06	0.14	0.09	
i	CD80WP132	Ol	0.28			0.25	0.07	0.25	0.05		
l	CD80WP132-Abis	Plg	0.30		0.22	0.10		0.07	0.14	0.10	
m	CD80WP132-Abis	Plg	0.30		0.22	0.09		0.07	0.14	0.10	
n	G1	Plg-An	0.29		0.23	0.09			0.15	0.07	
o	G1	Plg-An	0.29		0.23	0.09			0.15	0.07	
p	G1	Amph	0.31	0.08	0.09	0.16		0.17	0.16		

CH4-11: Summary of SEM analyses on ground samples (63-125 µm), before and after each experiments.

SEM images are shown divided for each rock in BSE-back scatter electron, elemental line, and mineral phase mode. SEM-EDS analyses and correspondent analytical error (standard deviation, σ) are shown for both bulk rock and single phases. To note: the total for SEM-EDS analyses is forced to be 100 % from the software.

Accuracy and precision for SEM-EDS analyses have been calibrated with the standard glass sample BIR1G (See Appendix CH4-6).

INITIAL SAMPLES (before experiments):

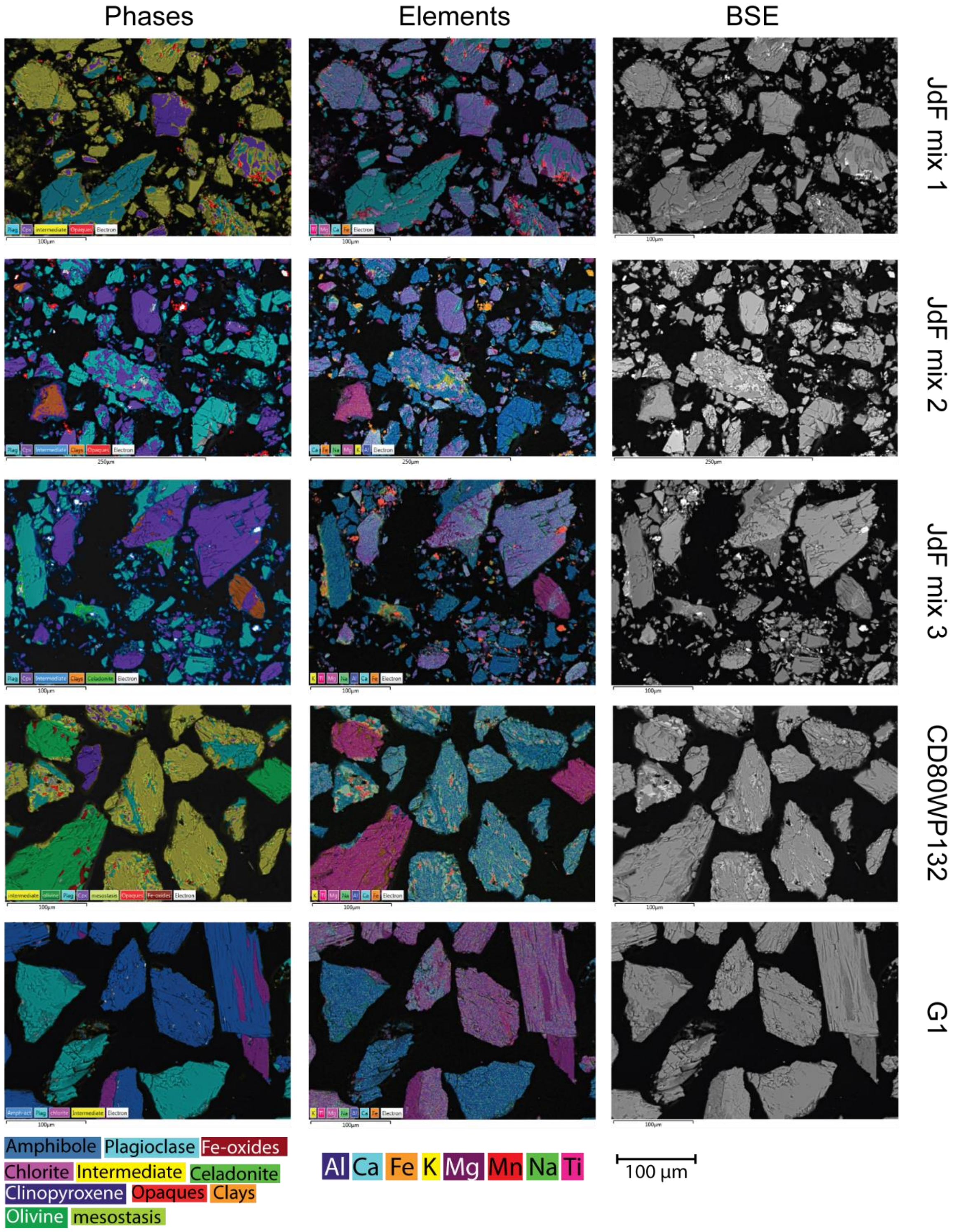

DATA FOR OXIDES ANALYSES (%)

	SiO_2	TiO_2	Al_2O_3	Fe_2O_3	FeO	MnO	MgO	CaO	Na_2O	K_2O	P_2O_5	SO_3
JdF mix 1												
Bulk rock	50.80	1.85	16.91		8.59	0.15	6.70	11.26	3.32	0.25		0.17
Plagioclase-labradorite	53.02		28.30		1.53		0.73	11.20	5.09	0.13		
Clinopyroxene	50.66	1.43	4.21		10.61	0.25	16.88	15.46	0.51			
Intermediate	51.15	1.82	14.83		9.67	0.17	7.51	11.15	3.09	0.31	0.12	0.18
Opaques	15.46	21.00	5.02	50.36		1.32	2.47	2.35	1.63	0.38		
JdF mix 2												
Bulk rock	50.75	1.41	16.73		8.45	0.15	7.45	11.66	3.00	0.26		0.14
Plagioclase-labradorite	53.13		26.37	2.77			1.56	11.30	4.87			
Clinopyroxene	51.59	1.15	4.80		11.47		15.76	14.50	0.73			
Intermediate	52.98	1.58	15.00		9.25		7.12	11.12	2.57	0.37		
Clays-saponite	55.6		3.14		17.07		20.27	2.02	0.78	1.11		
Opaques	17.44	17.83	4.83	52.23			3.8	2.68	0.85	0.34		
JdF mix 3												
Bulk rock	51.16	1.46	14.86		10.12	0.14	7.63	10.95	3.29	0.29		0.10
Plagioclase-labradorite	55.07	0.17	27.07		1.38		0.49	9.50	6.17	0.15		
Clinopyroxene	50.76	1.34	3.34		13.26	0.26	15.36	14.97	0.60	0.10		
Intermediate	50.13	2.47	16.30		12.39		5.13	9.55	3.34	0.51		0.17
Clays - saponite	54.98	0.34	4.71		16.26		20.15	1.83	1.09	0.62		
Celadonite	59.20	1.05	8.97		16.20		4.23	3.42	4.06	1.88	0.99	
CD80WP132												
Bulk rock	47.09	0.93	11.77		12.93	0.17	16.40	8.32	2.06	0.06		0.27
Plagioclase-labradorite	52.66	0.34	26.97		2.67		0.95	11.45	4.70	0.07		0.20
Intermediate	51.23	0.98	14.23		10.71	0.17	7.81	11.96	2.56	0.07		0.28
Olivine	39.10				17.57	0.22	42.53	0.39	0.18			
Clinopyroxene	51.51	0.62	3.77		9.30	0.24	17.52	16.56	0.47			
Mesostasis	45.56	4.90	8.63		27.59	0.25	3.00	6.38	2.37	0.20	0.24	0.88
Opaques	26.07	11.94	6.56	50.35				1.76	2.28			1.05
Iddingsite	15.15			69.26			14.00	1.59				
G1												
Bulk rock	49.69	0.09	17.15		5.73	0.10	13.80	12.64	0.71	0.08		
Plagioclase-anorthite	44.31		35.92		0.58		0.30	17.91	0.97			
Amphibole-actinolite	54.83		4.23		8.14	0.17	20.11	11.78	0.54	0.08		
Chlorite	36.32		20.74	11.51			30.13	1.10	0.20			
Intermediate	54.15		17.34		5.06		11.07	11.26	1.12			

ERROR (σ) FOR OXIDES ANALYSES (%)

	SiO_2	TiO_2	Al_2O_3	Fe_2O_3	FeO	MnO	MgO	CaO	Na_2O	K_2O	P_2O_5	SO_3
JdF mix 1												
Bulk rock	0.02	0.02	0.03		0.03	0.01	0.02	0.02	0.02	0.01		0.02
Plagioclase-labradorite	0.10		0.07		0.04		0.03	0.04	0.04	0.01		
Clinopyroxene	0.15	0.05	0.07		0.09	0.04	0.09	0.07	0.05			
Intermediate	0.07	0.02	0.04		0.04	0.02	0.03	0.03	0.03	0.01	0.02	0.02
Opaques	0.29	0.30	0.21	0.43		0.15	0.20	0.11	0.21	0.07		
JdF mix 2												
Bulk rock	0.06	0.02	0.03		0.03	0.02	0.03	0.02	0.02	0.01		0.02
Plagioclase-labradorite	0.08		0.06	0.04			0.02	0.03	0.03			
Clinopyroxene	0.10	0.03	0.04		0.06		0.06	0.05	0.03			
Intermediate	0.14	0.06	0.09		0.08		0.07	0.06	0.06	0.03		
Clays-saponite	0.36		0.14		0.24		0.22	0.09	0.11	0.07		
Opaques	0.29	0.27	0.20	0.41			0.20	0.11	0.20	0.07		
JdF mix 3												
Bulk rock	0.06	0.02	0.03		0.03	0.02	0.03	0.02	0.02	0.01		0.02
Plagioclase-labradorite	0.10	0.03	0.07		0.03		0.03	0.04	0.04	0.01		
Clinopyroxene	0.09	0.03	0.04		0.06	0.02	0.05	0.04	0.03	0.01		
Intermediate	0.11	0.04	0.07		0.07		0.05	0.04	0.05	0.02		0.04
Clays - saponite	0.33	0.09	0.15		0.21		0.21	0.08	0.12	0.05		
Celadonite	0.37	0.11	0.18		0.23		0.15	0.10	0.16	0.07	0.15	
CD80WP132												
Bulk rock	0.04	0.01	0.03		0.03	0.01	0.03	0.02	0.02	0.01		0.02
Plagioclase-labradorite	0.04	0.04	0.10		0.05		0.04	0.06	0.06	0.02		0.04
Intermediate	0.06	0.02	0.04		0.04	0.02	0.03	0.03	0.02	0.01		0.02
Olivine	0.08				0.06	0.02	0.07	0.02	0.03			
Clinopyroxene	0.22	0.07	0.10		0.13	0.06	0.14	0.11	0.07			
Mesostasis	0.20	0.09	0.11		0.16	0.06	0.08	0.07	0.09	0.03	0.07	0.07
Opaques	0.41	0.29	0.26	0.51				0.12	0.25			0.18
Iddingsite	0.61			1.04			0.63	0.26				
G1												
Bulk rock	0.05	0.02	0.03		0.03	0.01	0.03	0.02	0.02	0.01		
Plagioclase-anorthite	0.08		0.07		0.03		0.02	0.04	0.03			
Amphibole-actinolite	0.07		0.03		0.04	0.01	0.04	0.03	0.02	0.01		
Chlorite	0.18		0.15	0.13			0.14	0.04	0.06			
Intermediate	0.57		0.38		0.31		0.32	0.26	0.28			

SAMPLES AFTER FIRST SET OF EXPERIMENTS:

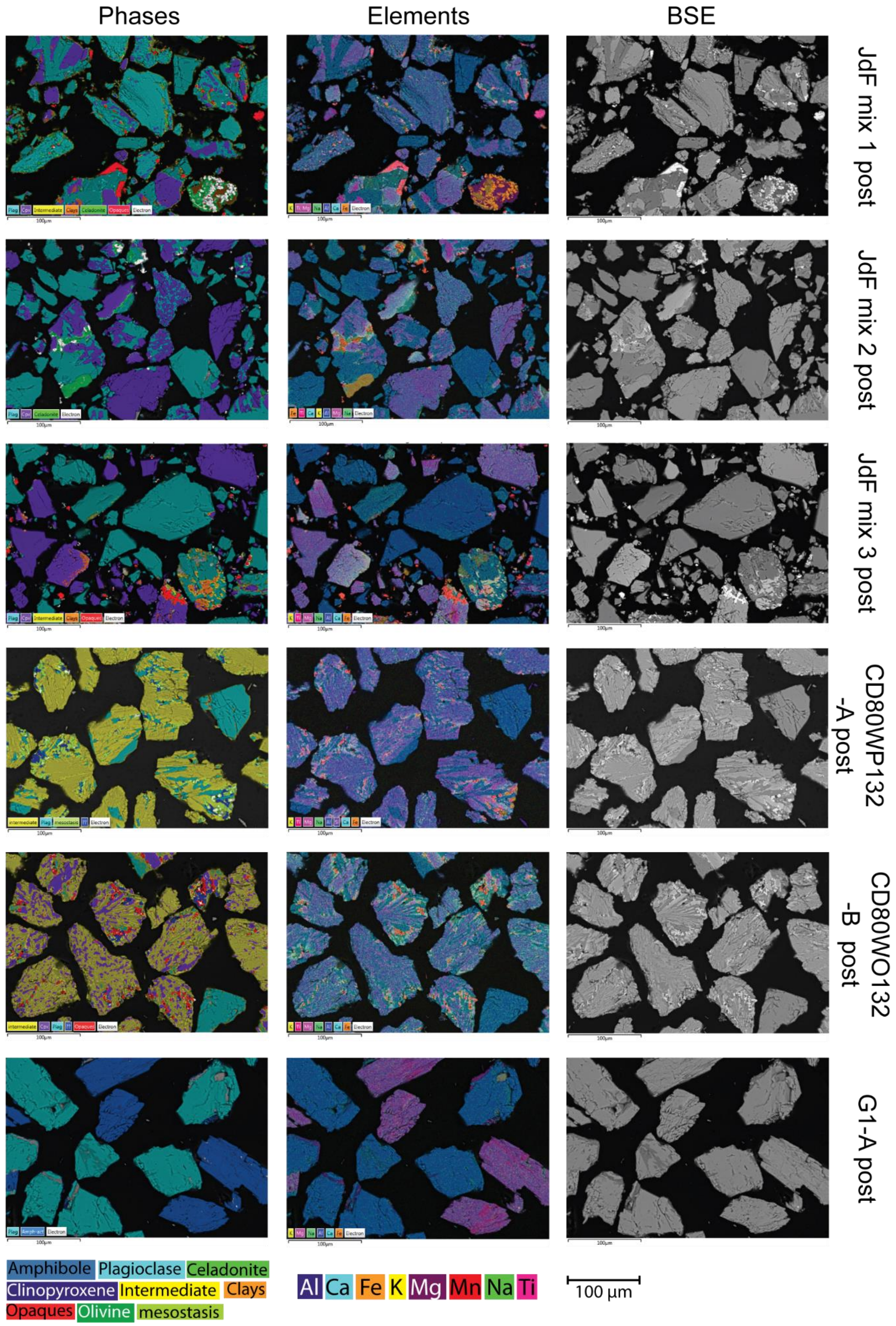

DATA FOR OXIDES ANALYSES (%)

	SiO_2	TiO_2	Al_2O_3	Fe_2O_3	FeO	MnO	MgO	CaO	Na_2O	K_2O	P_2O_5	SO_3	Cr_2O_3
JdF mix 1 post													
Bulk rock	50.52	2.14	15.33		1.01	0.18	6.89	10.09	3.45	0.26		0.13	
Plagioclase-labradorite	53.43	1.04	19.84		6.00		4.53	10.28	4.56	0.20	0.13		
Clinopyroxene	50.20	1.74	4.62		12.66	0.31	15.02	14.75	0.72				
Intermediate	51.73	2.41	15.06		11.19		6.07	10.27	2.84	0.42			
Clays-saponite	53.92	0.40	3.29		16.64		22.53	2.90		0.32			
Celadonite	47.00	3.13	7.26		23.75	0.32	9.11	6.68	1.61	1.12			
Iddingsite	26.54	0.31	1.89	64.15			5.45	0.72		0.93			
Opaques	13.67	22.73	5.07	50.77		1.37	1.95	2.09	1.49	0.21	0.64		
JdF mix 2 post													
Bulk rock	50.80	1.12	17.60		7.13	0.14	7.48	12.37	3.05	0.24		0.06	
Plagioclase-labradorite	52.85	0.32	27.07		2.19		1.36	11.23	4.85	0.13			
Clinopyroxene	50.85	1.25	6.26		9.72	0.21	15.42	15.07	0.94	0.10			0.17
Celadonite	52.34	1.54	8.29		21.73	0.32	4.89	5.47	1.95	2.98	0.49		
JdF mix 3 post													
Bulk rock	51.32	1.17	18.1		7.74	0.15	5.98	11.69	3.63	0.23			
Plagioclase-labradorite	53.95	0.16	27.91		1.33		0.51	10.49	5.50	0.15			
Clinopyroxene	51.20	1.14	2.90		12.40	0.29	15.82	15.69	0.48	0.08			
Intermediate	52.58	1.03	12.17		14.73	0.32	5.72	7.27	3.79	1.27	1.14		
Clays	47.08	1.36	1.98		28.75	0.68	6.93	11.84	0.72	0.18	0.48		
Opaques	6.20	23.21	2.77	63.86		1.21	1.66	0.83		0.28			
CD80WP132-A post													
Bulk rock	50.89	1.22	15.74		10.99	0.15	6.56	11.41	2.67	0.08		0.29	
Plagioclase-labradorite	51.52	0.20	28.97		2.01		0.67	12.57	3.99	0.07			
Intermediate	51.14	0.99	13.44		10.96	0.19	8.64	12.12	2.32			0.21	
Mesostasis	45.86	4.64	8.79		27.59	0.29	2.68	6.43	2.61	0.28		0.83	
CD80WP132-B post													
Bulk rock	50.64	1.27	15.74		10.90	0.16	6.67	11.54	2.72	0.07		0.28	
Plagioclase-labradorite	49.48		32.16		0.78		0.31	13.99	3.29				
Clinopyroxene	50.24	1.02	7.88		13.50	0.28	12.91	12.99	1.17				
Intermediate	51.69	0.98	16.57		9.39	0.15	6.14	11.70	3.06	0.07		0.26	
Opaques	36.76	7.93	7.95	38.20		0.30	1.34	3.66	2.59	0.17		1.09	
G1-A post													
Bulk rock	48.26	3.23	25.12		3.23		8.05	14.49	0.77	0.08			
Plagioclase-anorthite	44.11		36.15		0.54		0.28	18.06	0.86				
Amphibole-actinolite	56.00	0.14	4.11		7.59	0.14	21.17	10.20	0.45	0.06			0.13

ERROR (σ) FOR OXIDES ANALYSES (%)

	SiO_2	TiO_2	Al_2O_3	Fe_2O_3	FeO	MnO	MgO	CaO	Na_2O	K_2O	P_2O_5	SO_3	Cr_2O_3
JdF mix 1 post													
Bulk rock	0.05	0.02	0.03		0.03	0.01	0.02	0.02	0.02	0.01		0.02	
Plagioclase-labradorite	0.06	0.02	0.04		0.03		0.02	0.03	0.03	0.01	0.02		
Clinopyroxene	0.12	0.04	0.05		0.08	0.03	0.07	0.06	0.04				
Intermediate	0.16	0.07	0.10		0.10		0.07	0.07	0.07	0.03			
Clays-saponite	0.42	0.11	0.17		0.28			0.11		0.07			
Celadonite	0.24	0.09	0.12		0.18	0.07	0.12	0.08	0.09	0.05			
Iddingsite	0.25	0.09	0.12	0.31			0.16	0.06		0.06			
Opaques	0.19	0.21	0.14	0.30		0.10	0.12	0.07	0.14	0.05	0.11		
JdF mix 2 post													
Bulk rock	0.04	0.01	0.03		0.02	0.01	0.02	0.02	0.02	0.01		0.01	
Plagioclase-labradorite	0.06	0.02	0.04		0.02		0.02	0.03	0.03	0.01			
Clinopyroxene	0.06	0.02	0.03		0.04	0.02	0.04	0.03	0.02	0.01			0.02
Celadonite	0.26	0.08	0.13		0.18	0.07	0.11	0.08	0.10	0.06	0.10		
JdF mix 3 post													
Bulk rock	0.05	0.02	0.03		0.03	0.01	0.02	0.02	0.02	0.01			
Plagioclase-labradorite	0.06	0.02	0.05		0.02		0.02	0.03	0.03	0.01			
Clinopyroxene	0.08	0.03	0.03		0.05	0.02	0.05	0.04	0.03	0.01			
Intermediate	0.27	0.08	0.15		0.17	0.07	0.12	0.10	0.12	0.05	0.11		
Clays	0.32	0.11	0.12		0.26	0.10	0.16	0.14	0.12	0.05	0.12		
Opaques	0.24	0.35	0.21	0.51		0.17	0.21	0.10		0.08			
CD80WP132-A post													
Bulk rock	0.04	0.02	0.03		0.03	0.01	0.02	0.02	0.02	0.01		0.02	
Plagioclase-labradorite	0.11	0.03	0.08		0.04		0.03	0.05	0.04	0.02			
Intermediate	0.05	0.02	0.03		0.03	0.01	0.03	0.02	0.02			0.02	
Mesostasis	0.17	0.08	0.09		0.14	0.05	0.07	0.06	0.08	0.03		0.06	
CD80WP132-B post													
Bulk rock	0.04	0.01	0.03		0.03	0.01	0.02	0.02	0.02	0.01		0.02	
Plagioclase-labradorite	0.16		0.12		0.05		0.04	0.07	0.06				
Clinopyroxene	0.09	0.03	0.05		0.06	0.03	0.05	0.04	0.03				
Intermediate	0.05	0.02	0.03		0.03	0.01	0.02	0.02	0.02	0.01		0.02	
Opaques	0.20	0.11	0.12	0.21		0.06	0.08	0.06	0.10	0.03		0.08	
G1-A post													
Bulk rock	0.05		0.04		0.02		0.02	0.02	0.02	0.01			
Plagioclase-anorthite	0.06		0.05		0.02		0.02	0.03	0.02				
Amphibole-actinolite	0.09	0.02	0.04		0.04	0.02	0.05	0.03	0.03	0.01			0.02

SAMPLES AFTER SECOND SET OF EXPERIMENTS:

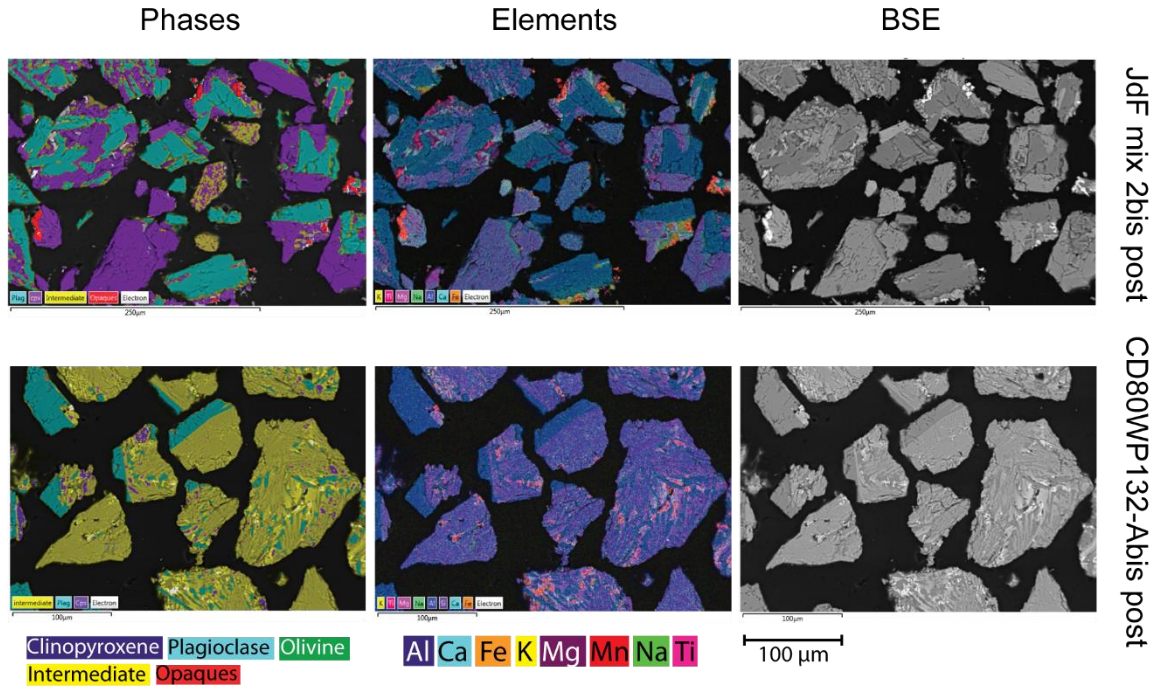

DATA FOR OXIDES ANALYSES (%)

	SiO_2	TiO_2	Al_2O_3	Fe_2O_3	FeO	MnO	MgO	CaO	Na_2O	K_2O	P_2O_5	SO_3	Cr_2O_3
JdF mix 2bis post													
Bulk rock	50.52	1.59	15.73		8.13	0.12	8.10	12.46	2.96	0.19		0.10	0.11
Plagioclase-labradorite	53.57	0.18	27.79		1.34		0.68	10.96	5.37	0.10			
Clinopyroxene	50.49	1.39	5.21		10.76	0.19	15.44	15.39	0.71	0.15		0.09	0.18
Intermediate	52.75	1.04	19.34		6.90		4.89	10.82	3.99	0.27			
Opaques	7.02	22.13	2.80	64.02		1.04	1.89	0.83		0.28			
CD80WP132-Abis post													
Bulk rock	50.69	1.23	16.25		10.65	0.14	6.44	11.50	2.72	0.08		0.28	
Plagioclase-labradorite	51.12	0.14	29.46		1.82		0.67	12.88	3.91				
Clinopyroxene	50.32	0.96	5.03		12.78		16.70	13.72	0.50				
Intermediate	51.25	1.27	13.93		11.66	0.17	7.42	11.37	2.56	0.09		0.26	

ERROR (σ) FOR OXIDES ANALYSES (%)

	SiO_2	TiO_2	Al_2O_3	Fe_2O_3	FeO	MnO	MgO	CaO	Na_2O	K_2O	P_2O_5	SO_3	Cr_2O_3
JdF mix 2bis post													
Bulk rock	0.05	0.02	0.03		0.03	0.01	0.02	0.02	0.02	0.01		0.02	0.01
Plagioclase-labradorite	0.08	0.02	0.05		0.03		0.02	0.03	0.03	0.01			
Clinopyroxene	0.07	0.02	0.03		0.04	0.02	0.04	0.03	0.02	0.01		0.02	0.02
Intermediate	0.13	0.04	0.08		0.07		0.05	0.05	0.05	0.02			
Opaques	0.24	0.34	0.20	0.50		0.15	0.20	0.10		0.07			
CD80WP132-Abis post													
Bulk rock	0.04	0.02	0.03		0.03	0.01	0.02	0.02	0.02	0.01		0.02	
Plagioclase-labradorite	0.11	0.03	0.08		0.04		0.03	0.05	0.04				
Clinopyroxene	0.26	0.08	0.12		0.16		0.16	0.12	0.09				
Intermediate	0.05	0.02	0.03		0.03	0.01	0.02	0.02	0.02	0.01		0.02	

CH4-12: inductively coupled plasma optical emission spectrometry (ICP–OES) and ion chromatography (IC) analyses on major cations and anions in solutions, respectively. The element compositions are listed in two separated tables reporting their original values and the correspondent corrected values for the linear evaporation effect, respectively. The data are given in mmol/L. ICP-OES analytical errors are reported in a third table, and are given in percentage relative standard deviation (%RSD), which is expressed as the standard deviation of the mean as a percentage of the mean.

DATA – ORIGINAL VALUES (mmol/L)

		ICP-OES							IC			
Sample	**ID**	**Na**	**Mg**	**Si**	**K**	**Ca**	**Sr**	**S**	**F^-**	**Cl^-**	**Br^-**	**SO_4^{2-}**
Blank 2	E5-1	484	53.5	0.02	10.4	10.9	0.09	29.3	0.01	646	0.78	33.1
	E5-2	486	55.1	0.02	10.7	10.9	0.09	29.6	0.03	572	0.79	28.8
	E5-3	489	55.1	0.02	10.6	11.0	0.09	29.7	0.05	591	0.79	29.6
	E5-4	493	55.6	0.02	10.9	10.9	0.09	29.9	0.04	639	1.01	32.4
	E5-5	496	56.8	0.02	10.8	10.9	0.09	29.9	0.04	617	0.76	30.8
	E5-6	506	57.6	0.02	11.1	11.3	0.09	30.2	0.04	612	0.72	30.8
	E5-7	514	58.0	0.03	11.5	11.4	0.10	30.9	0.01	616	1.05	30.7
JdF mix 1	E6-1	482	53.9	0.03	10.3	10.7	0.09	29.0	0.02	622	0.95	31.2
	E6-2	474	54.2	0.30	10.5	12.5	0.09	29.4	<0.01	568	0.92	28.8
	E6-3	483	53.7	0.40	10.4	13.1	0.09	29.8	<0.01	582	0.96	29.6
	E6-4	486	54.5	0.50	10.4	13.4	0.09	29.8	0.02	584	0.85	29.4
	E6-5	479	54.2	0.57	10.3	13.5	0.09	29.6	<0.01	569	0.8	28.8
	E6-6	485	55.2	0.67	10.4	13.4	0.09	29.9	<0.01	569	0.93	29.0
	E6-7	480	54.5	0.77	10.4	13.6	0.09	29.7	0.01	574	0.91	29.0
JdF mix 2	E7-1	478	53.6	0.04	10.4	10.9	0.09	29.2	0.03	576	0.78	29.2
	E7-2	482	54.2	0.30	10.3	12.3	0.09	29.5	0.04	574	0.7	28.9
	E7-3	473	54.1	0.43	10.3	12.6	0.09	29.2	<0.01	568	0.67	28.6
	E7-4	479	54.8	0.49	9.9	12.8	0.09	29.3	0.02	678	0.9	34.3
	E7-5	480	55.5	0.57	10.4	12.9	0.09	29.4	<0.01	575	0.69	28.8
	E7-6	483	54.3	0.66	10.3	13.1	0.09	29.5	<0.01	567	0.96	28.5
	E7-7	490	55.8	0.77	10.5	13.4	0.10	30.0	0.01	585	0.92	29.5
JdF mix 3	E8-1	482	54.6	0.02	10.4	10.9	0.09	29.5	0.04	581	0.93	29.5
	E8-2	483	54.1	0.23	10.6	12.0	0.09	29.5	<0.01	581	0.73	29.4
	E8-3	485	55.5	0.38	10.7	12.2	0.09	29.5	0.04	579	0.81	29.2
	E8-4	485	55.1	0.48	10.7	12.4	0.09	29.7	0.02	576	0.89	29.1
	E8-5	482	55.2	0.56	10.6	12.4	0.09	29.4	0.02	687	1.13	34.5
	E8-6	486	55.6	0.67	10.7	12.7	0.10	30.0	0.02	577	0.94	29.2
	E8-7	486	55.1	0.80	10.7	12.5	0.09	29.7	0.03	586	0.8	29.5
Blank 3	E9-1	490	54.8	0.02	10.2	11.0	0.09	29.6	<0.01	579	0.65	29.4
	E9-2	493	55.7	0.01	10.5	11.2	0.10	29.9	0.04	580	0.93	29.5
	E9-3	494	55.9	0.02	10.3	11.0	0.10	30.1	0.02	587	0.72	29.6
	E9-4	555	62.1	0.02	11.8	12.2	0.11	33.4	0.03	593	0.98	29.8
	E9-5	500	56.4	0.02	10.5	11.3	0.09	29.9	0.05	593	0.8	30.1
	E9-6	518	57.4	0.07	11.0	11.6	0.10	30.5	0.08	600	1.01	30.5
	E9-7	527	58.9	0.02	10.9	12.0	0.10	31.5	0.02	605	0.82	30.5
	E9-8	519	57.9	0.02	10.9	11.5	0.10	31.1	0.09	614	0.79	30.7
	E9-9	477	53.4	0.02	10.3	10.6	0.09	28.8	0.02	621	0.87	31.3
	E9-10	541	59.9	0.02	11.3	12.0	0.10	32.4	<0.01	633	0.82	31.9
	E9-11	546	61.6	0.03	11.9	12.4	0.11	33.3	0.01	646	0.93	32.6
	E9-12	546	61.4	0.02	11.6	12.2	0.10	32.8	0.02	650	0.89	32.8
	E9-13	613	68.5	0.02	13.1	13.8	0.12	36.6	0.08	666	1.05	34.0
	E9-14	563	63.5	0.02	12.1	12.7	0.11	33.9	0.05	664	0.74	33.5
CD80WP132-A	E11-1	499	55.8	0.02	10.3	10.8	0.09	29.7	0.06	580	0.55	29.1
	E11-2	494	56.1	0.14	10.5	11.1	0.09	29.8	0.02	582	0.66	29.5
	E11-3	500	56.6	0.17	10.4	11.4	0.10	30.1	<0.01	584	0.73	29.2
	E11-4	507	57.1	0.21	10.7	11.6	0.10	30.1	0.08	591	0.88	29.6
	E11-5	509	57.4	0.25	10.7	11.8	0.10	30.5	0.06	586	0.64	29.5
	E11-6	500	56.8	0.27	10.7	11.4	0.09	30.0	0.02	588	0.79	29.1
	E11-7	504	57.0	0.29	10.8	11.7	0.10	30.3	0.01	598	0.69	29.9
	E11-8	513	56.8	0.31	10.8	11.6	0.10	30.2	0.15	599	0.92	29.9
	E11-9	511	57.4	0.34	11.0	11.7	0.10	30.2	0.02	607	0.79	30.2
	E11-10	513	57.3	0.37	11.0	11.6	0.10	30.6	0.01	608	0.74	30.3
	E11-11	518	58.4	0.40	11.2	11.8	0.10	30.8	0.02	615	0.83	30.7
	E11-12	520	59.2	0.43	11.2	12.1	0.10	31.2	0.04	626	0.79	31.5
	E11-13	530	59.7	0.45	11.3	12.1	0.10	31.5	0.03	623	0.91	31.0
	E11-14	522	59.3	0.45	11.3	12.2	0.10	31.3	0.03	633	0.93	31.6

DATA – ORIGINAL VALUES (mmol/L), continued

		ICP-OES							IC			
Sample	**ID**	**Na**	**Mg**	**Si**	**K**	**Ca**	**Sr**	**S**	**F^-**	**Cl^-**	**Br^-**	**SO_4^{2-}**
G1-A	E12-1	495	55.4	0.03	10.3	10.9	0.09	29.8	0.05	577	0.57	29.0
	E12-2	493	56.0	0.16	10.3	11.8	0.10	29.8	0.05	590	0.82	29.4
	E12-3	505	56.8	0.20	10.4	12.0	0.10	30.4	0.02	579	0.67	28.8
	E12-4	500	57.3	0.24	10.4	12.4	0.10	30.1	0.02	587	0.80	29.5
	E12-5	498	57.0	0.27	10.3	12.4	0.10	30.2	0.04	591	0.79	29.8
	E12-6	493	56.3	0.30	10.3	12.2	0.09	29.3	0.02	584	0.73	29.4
	E12-7	490	55.8	0.32	10.3	12.2	0.09	29.6	0.02	590	0.92	29.7
	E12-8	501	56.2	0.35	10.3	12.2	0.09	29.9	0.01	595	0.87	29.6
	E12-9	495	56.3	0.39	10.5	12.5	0.09	29.8	<0.01	594	0.76	30.1
	E12-10	507	56.5	0.41	10.4	12.4	0.09	30.1	0.06	594	0.77	30.1
	E12-11	492	56.4	0.45	10.3	12.4	0.09	29.8	<0.01	596	0.83	29.8
	E12-12	498	56.6	0.47	10.4	12.7	0.10	30.0	0.01	599	0.88	30.1
	E12-13	596	68.1	0.58	12.5	15.1	0.11	35.8	<0.01	594	0.74	29.8
	E12-14	499	57.2	0.50	10.6	12.7	0.10	30.3	0.01	600	0.84	30.1
Blank 4	E13-1	479	47.8	0.10	10.6	10.6	0.09	29.7	0.13	539	1.22	30.6
	E13-2	482	47.9	0.05	10.6	10.7	0.09	29.8	0.11	541	0.93	30.1
	E13-3	476	47.6	0.06	10.5	10.6	0.09	29.8	0.10	542	1.22	30.2
	E13-4	482	47.7	0.02	10.7	10.7	0.09	29.8	0.14	543	1.11	29.7
	E13-5	487	54.0	0.07	10.4	11.0	0.09	29.7	0.15	543	0.74	30.5
	E13-6	491	53.9	0.06	10.5	11.1	0.09	29.8	0.19	545	0.85	30.2
	E13-7	490	54.1	0.06	10.4	11.1	0.09	30.0	0.20	546	1.45	31.0
	E13-8	493	54.2	0.02	10.5	11.1	0.09	30.0	0.30	545	1.31	30.6
JdF mix 2bis	E14-1	481	47.7	0.02	10.7	10.7	0.09	29.9	0.41	540	0.93	30.4
	E14-2	483	48.5	0.16	10.5	11.0	0.09	30.0	0.55	545	1.14	30.1
	E14-3	481	48.4	0.24	10.5	11.1	0.10	30.1	<0.01	545	1.21	29.7
	E14-4	480	48.7	0.29	10.6	11.0	0.10	30.2	0.13	543	1.11	30.3
	E14-5	478	48.9	0.34	10.5	11.2	0.10	30.2	0.21	549	1.19	30.1
	E14-6	493	54.9	0.42	10.4	11.4	0.09	30.0	0.61	545	1.10	30.2
	E14-7	492	55.1	0.48	10.4	11.5	0.10	30.3	0.21	549	1.35	30.6
	E14-8	489	55.4	0.52	10.3	11.5	0.09	30.2	0.27	552	1.27	31.4
CD80WP132-Abis	E15-1	475	47.7	0.02	10.4	10.5	0.09	29.6	0.10	535	1.42	29.6
	E15-2	478	47.5	0.06	10.4	10.6	0.09	29.6	0.21	537	2.05	30.7
	E15-3	474	47.4	0.09	10.4	10.5	0.09	29.5	0.18	532	0.77	29.9
	E15-4	478	47.6	0.10	10.5	10.6	0.09	29.6	0.08	537	1.40	30.2
	E15-5	479	50.8	0.13	10.4	10.7	0.09	29.7	0.13	538	1.08	30.0
	E15-6	485	53.4	0.16	10.3	10.9	0.09	29.5	0.25	537	1.10	30.1
	E15-7	483	53.5	0.20	10.3	10.8	0.09	29.7	0.08	539	1.05	30.3
	E15-8	488	54.0	0.23	10.3	10.9	0.09	29.6	0.13	537	0.82	28.5
CD80WP132-B	E16-1	479	48.1	0.01	10.5	10.8	0.09	30.1	0.19	542	1.15	30.6
	E16-2	484	48.4	0.09	10.6	10.9	0.09	30.1	0.08	542	1.21	30.8
	E16-3	485	48.2	0.12	10.6	10.8	0.09	30.0	0.35	546	1.80	31.0
	E16-4	490	48.6	0.14	10.8	10.9	0.09	30.2	0.14	548	1.05	30.5
	E16-5	494	54.9	0.17	10.5	11.1	0.09	30.1	0.08	548	1.19	31.0
	E16-6	497	55.0	0.20	10.6	11.3	0.09	30.2	0.29	553	1.23	30.2
	E16-7	502	55.1	0.22	10.7	11.3	0.09	30.5	0.19	554	0.85	30.4
	E16-8	503	55.3	0.24	10.6	11.3	0.09	30.3	0.16	558	0.98	31.6

DATA – CORRECTED VALUES (mmol/L)

					ICP-OES					IC		
Sample	**ID**	**Na**	**Mg**	**Si**	**K**	**Ca**	**Sr**	**S**	**F^-**	**Cl^-**	**Br^-**	**SO_4^{2-}**
Blank 2	E5-1	477	52.8	0.02	10.2	10.7	0.09	28.9	0.01	637	0.77	32.6
	E5-2	476	54.0	0.01	10.5	10.7	0.09	29.0	0.03	560	0.77	28.2
	E5-3	475	53.6	0.02	10.3	10.7	0.09	28.9	0.05	574	0.77	28.7
	E5-4	475	53.6	0.02	10.5	10.5	0.09	28.8	0.04	616	0.98	31.2
	E5-5	475	54.4	0.02	10.3	10.4	0.09	28.6	0.04	590	0.73	29.4
	E5-6	476	54.2	0.02	10.4	10.6	0.09	28.4	0.04	576	0.68	29.0
	E5-7	469	52.9	0.03	10.4	10.4	0.09	28.1	0.01	561	0.96	28.0
JdF mix 1	E6-1	481	53.8	0.03	10.3	10.7	0.09	29.0	0.02	620	0.95	31.2
	E6-2	473	54.1	0.30	10.5	12.5	0.09	29.3	0.01	566	0.92	28.7
	E6-3	481	53.5	0.40	10.3	13.0	0.09	29.7	0.01	580	0.96	29.5
	E6-4	484	54.3	0.50	10.4	13.4	0.09	29.7	0.02	581	0.85	29.3
	E6-5	477	53.9	0.57	10.3	13.5	0.09	29.5	0.01	566	0.79	28.6
	E6-6	481	54.8	0.66	10.3	13.3	0.09	29.6	<0.01	565	0.92	28.8
	E6-7	474	53.8	0.76	10.2	13.4	0.09	29.4	0.01	567	0.90	28.7
JdF mix 2	E7-1	476	53.4	0.04	10.4	10.8	0.09	29.1	0.03	574	0.78	29.1
	E7-2	479	53.8	0.30	10.3	12.2	0.09	29.3	0.04	570	0.69	28.7
	E7-3	469	53.7	0.43	10.2	12.5	0.09	29.0	0.01	563	0.66	28.4
	E7-4	474	54.2	0.49	9.8	12.6	0.09	29.0	0.02	670	0.89	33.9
	E7-5	474	54.7	0.56	10.3	12.8	0.09	29.0	0.01	567	0.68	28.4
	E7-6	474	53.3	0.66	10.2	12.9	0.09	28.9	<0.01	556	0.94	28.0
	E7-7	476	54.2	0.77	10.2	13.1	0.09	29.2	0.01	568	0.90	28.7
JdF mix 3	E8-1	481	54.4	0.02	10.4	10.9	0.09	29.4	0.04	578	0.92	29.4
	E8-2	480	53.9	0.23	10.5	12.0	0.09	29.4	0.01	578	0.73	29.3
	E8-3	481	55.1	0.38	10.6	12.1	0.09	29.3	0.04	575	0.81	29.0
	E8-4	480	54.6	0.47	10.6	12.3	0.09	29.4	0.02	570	0.88	28.8
	E8-5	476	54.5	0.56	10.5	12.2	0.09	29.1	0.02	678	1.12	34.1
	E8-6	478	54.7	0.67	10.5	12.5	0.09	29.5	0.02	567	0.93	28.8
	E8-7	474	53.7	0.80	10.4	12.2	0.09	28.9	0.03	571	0.78	28.8
Blank 3	E9-1	473	52.9	0.02	9.9	10.6	0.09	28.6	0.01	559	0.63	28.4
	E9-2	473	53.4	0.01	10.0	10.8	0.09	28.7	0.03	556	0.89	28.3
	E9-3	470	53.2	0.02	9.8	10.4	0.09	28.6	0.02	558	0.69	28.1
	E9-4	524	58.6	0.02	11.1	11.5	0.10	31.5	0.02	560	0.92	28.1
	E9-5	468	52.8	0.02	9.8	10.6	0.09	28.1	0.05	556	0.75	28.2
	E9-6	481	53.4	0.07	10.2	10.8	0.09	28.4	0.07	558	0.94	28.4
	E9-7	486	54.4	0.02	10.1	11.0	0.09	29.0	0.02	559	0.76	28.1
	E9-8	476	53.1	0.02	10.0	10.6	0.09	28.5	0.09	563	0.73	28.1
	E9-9	430	48.2	0.02	9.3	9.5	0.08	26.0	0.02	560	0.78	28.2
	E9-10	481	53.3	0.02	10.1	10.7	0.09	28.9	0.01	564	0.73	28.4
	E9-11	476	53.7	0.02	10.3	10.8	0.09	29.0	0.01	563	0.81	28.4
	E9-12	466	52.5	0.02	9.9	10.4	0.09	28.0	0.02	555	0.76	28.0
	E9-13	517	57.7	0.02	11.0	11.6	0.10	30.8	0.07	561	0.88	28.6
	E9-14	471	53.1	0.02	10.1	10.6	0.09	28.3	0.04	556	0.62	28.0
CD80WP132-A	E11-1	490	54.8	0.02	10.1	10.6	0.09	29.1	0.06	570	0.54	28.6
	E11-2	483	54.9	0.14	10.2	10.9	0.09	29.2	0.02	569	0.65	28.9
	E11-3	487	55.1	0.17	10.1	11.1	0.09	29.4	<0.01	568	0.71	28.5
	E11-4	492	55.4	0.21	10.4	11.2	0.09	29.2	0.08	574	0.85	28.7
	E11-5	492	55.5	0.24	10.4	11.4	0.09	29.4	0.05	566	0.62	28.5
	E11-6	481	54.7	0.27	10.3	11.0	0.09	28.8	0.02	566	0.76	28.0
	E11-7	483	54.6	0.28	10.4	11.2	0.09	29.0	0.01	574	0.66	28.7
	E11-8	490	54.3	0.30	10.3	11.1	0.09	28.9	0.14	572	0.87	28.6
	E11-9	483	54.4	0.33	10.4	11.0	0.09	28.5	0.02	574	0.75	28.6
	E11-10	482	53.9	0.36	10.3	10.9	0.09	28.7	0.01	571	0.69	28.5
	E11-11	481	54.2	0.38	10.4	11.0	0.09	28.6	0.02	571	0.77	28.5
	E11-12	477	54.3	0.41	10.3	11.1	0.09	28.6	0.04	575	0.72	28.9
	E11-13	483	54.4	0.41	10.3	11.1	0.09	28.7	0.03	568	0.83	28.2
	E11-14	474	53.9	0.41	10.3	11.1	0.09	28.4	0.03	574	0.84	28.7
G1-A	E12-1	491	55.0	0.03	10.3	10.8	0.09	29.6	0.05	573	0.57	28.8
	E12-2	489	55.5	0.16	10.2	11.7	0.09	29.6	0.05	585	0.81	29.1
	E12-3	500	56.2	0.20	10.3	11.9	0.10	30.1	0.02	573	0.66	28.5
	E12-4	494	56.7	0.23	10.3	12.2	0.09	29.7	0.02	580	0.79	29.2
	E12-5	491	56.3	0.27	10.2	12.2	0.09	29.8	0.04	583	0.78	29.4
	E12-6	486	55.4	0.30	10.2	12.0	0.09	28.9	0.02	575	0.72	29.0
	E12-7	482	54.9	0.32	10.1	12.0	0.09	29.1	0.02	580	0.91	29.2
	E12-8	492	55.2	0.34	10.1	12.0	0.09	29.4	0.01	584	0.85	29.1
	E12-9	485	55.1	0.38	10.3	12.2	0.09	29.2	<0.01	581	0.75	29.4
	E12-10	495	55.2	0.41	10.2	12.1	0.09	29.3	0.06	579	0.75	29.4
	E12-11	478	54.7	0.44	10.0	12.0	0.09	29.0	<0.01	579	0.81	28.9
	E12-12	481	54.8	0.46	10.1	12.2	0.09	29.0	0.01	580	0.85	29.1
	E12-13	575	65.6	0.56	12.1	14.5	0.11	34.5	<0.01	573	0.71	28.7
	E12-14	481	55.1	0.48	10.2	12.2	0.09	29.2	0.01	577	0.81	29.0

DATA – CORRECTED VALUES (mmol/L), continued

		ICP-OES							IC			
Sample	**ID**	**Na**	**Mg**	**Si**	**K**	**Ca**	**Sr**	**S**	**F^-**	**Cl^-**	**Br^-**	**SO_4^{2-}**
Blank 4	E13-1	476	47.5	0.10	10.6	10.5	0.09	29.5	0.13	535	1.21	30.4
	E13-2	478	47.5	0.05	10.5	10.6	0.09	29.6	0.11	537	0.93	29.9
	E13-3	471	47.1	0.06	10.4	10.5	0.09	29.5	0.10	536	1.21	29.9
	E13-4	476	47.1	0.02	10.6	10.6	0.09	29.5	0.13	536	1.10	29.3
	E13-5	480	53.2	0.07	10.2	10.8	0.09	29.3	0.15	535	0.73	30.1
	E13-6	482	52.9	0.06	10.3	10.9	0.09	29.2	0.18	535	0.84	29.7
	E13-7	479	52.9	0.06	10.2	10.8	0.09	29.3	0.20	534	1.42	30.3
	E13-8	480	52.9	0.02	10.2	10.8	0.09	29.3	0.29	531	1.27	29.8
JdF mix 2bis	E14-1	477	47.3	0.02	10.6	10.6	0.09	29.6	0.41	535	0.92	30.1
	E14-2	478	48.0	0.16	10.4	10.9	0.09	29.6	0.54	539	1.13	29.7
	E14-3	474	47.7	0.24	10.4	10.9	0.09	29.7	<0.01	538	1.19	29.3
	E14-4	472	47.9	0.29	10.4	10.9	0.09	29.7	0.13	534	1.09	29.8
	E14-5	469	48.0	0.34	10.3	10.9	0.09	29.7	0.21	539	1.17	29.5
	E14-6	481	53.5	0.42	10.2	11.2	0.09	29.3	0.60	531	1.07	29.4
	E14-7	477	53.5	0.47	10.1	11.2	0.09	29.4	0.20	533	1.31	29.7
	E14-8	472	53.5	0.50	10.0	11.1	0.09	29.1	0.26	533	1.22	30.3
CD80WP132-Abis	E15-1	473	47.5	0.02	10.4	10.5	0.09	29.5	0.10	533	1.41	29.4
	E15-2	476	47.3	0.06	10.4	10.5	0.09	29.4	0.21	535	2.04	30.5
	E15-3	471	47.1	0.09	10.3	10.4	0.09	29.4	0.18	529	0.76	29.7
	E15-4	474	47.2	0.10	10.4	10.5	0.09	29.4	0.08	533	1.39	30.0
	E15-5	475	50.3	0.13	10.3	10.6	0.09	29.5	0.13	534	1.07	29.7
	E15-6	480	52.8	0.16	10.2	10.8	0.09	29.2	0.24	531	1.09	29.8
	E15-7	477	52.8	0.20	10.2	10.7	0.09	29.3	0.08	532	1.03	29.9
	E15-8	480	53.2	0.22	10.1	10.8	0.09	29.2	0.13	529	0.81	28.1
CD80WP132-B	E16-1	474	47.6	0.01	10.4	10.6	0.09	29.8	0.18	537	1.14	30.3
	E16-2	478	47.8	0.09	10.5	10.8	0.09	29.7	0.08	536	1.20	30.4
	E16-3	477	47.4	0.12	10.5	10.7	0.09	29.6	0.35	537	1.77	30.6
	E16-4	482	47.7	0.14	10.6	10.7	0.09	29.7	0.13	538	1.04	29.9
	E16-5	483	53.7	0.16	10.3	10.9	0.09	29.5	0.08	537	1.17	30.4
	E16-6	484	53.5	0.20	10.3	11.0	0.09	29.4	0.28	538	1.19	29.4
	E16-7	486	53.4	0.22	10.4	10.9	0.09	29.5	0.18	537	0.83	29.4
	E16-8	484	53.2	0.23	10.2	10.9	0.09	29.2	0.15	537	0.94	30.4

RSD (%) – ICP-OES

Sample	ID	Na	Mg	Si	K	Ca	Sr	S
Blank 2	E5-1	0.84	0.51	12.61	0.40	0.91	0.31	0.22
	E5-2	1.17	0.27	7.40	1.59	0.53	0.44	0.27
	E5-3	1.07	0.18	13.60	0.66	0.61	0.25	0.32
	E5-4	0.78	0.79	9.91	0.83	0.70	0.21	0.25
	E5-5	0.41	1.13	2.97	1.72	1.42	0.26	0.38
	E5-6	0.74	0.75	10.14	1.14	0.71	0.62	0.18
	E5-7	0.72	0.73	5.07	0.94	1.69	0.31	0.23
JdF mix 1	E6-1	0.48	0.62	9.03	1.65	0.94	0.30	0.08
	E6-2	0.37	0.83	1.71	0.84	1.16	0.19	0.30
	E6-3	0.47	0.53	0.80	0.36	0.43	0.36	0.43
	E6-4	1.01	0.18	0.33	0.43	0.95	0.04	0.32
	E6-5	0.20	1.00	0.74	0.75	1.57	0.17	0.20
	E6-6	0.58	0.93	0.56	1.30	0.71	0.23	0.29
	E6-7	0.54	0.64	1.54	1.12	2.03	0.89	0.19
JdF mix 2	E7-1	0.65	0.36	4.91	0.63	0.74	0.27	0.38
	E7-2	1.33	1.32	1.74	1.55	0.88	0.04	0.14
	E7-3	0.97	0.62	1.23	0.35	0.58	0.45	0.07
	E7-4	0.95	1.05	0.25	8.77	1.72	0.35	0.13
	E7-5	1.23	0.47	0.47	1.34	0.70	0.49	0.08
	E7-6	1.35	1.00	0.75	0.99	1.02	0.35	0.04
	E7-7	1.54	0.87	0.88	1.26	1.06	0.40	0.34
JdF mix 3	E8-1	0.98	0.67	14.54	0.85	1.29	0.06	0.18
	E8-2	0.81	0.88	0.99	0.87	1.08	0.35	0.08
	E8-3	1.04	0.96	0.37	0.61	0.46	0.43	0.15
	E8-4	0.99	0.96	0.82	1.34	0.72	0.39	0.09
	E8-5	1.11	1.11	0.89	1.87	1.02	0.42	0.29
	E8-6	0.60	0.63	0.51	0.78	0.91	0.43	0.15
	E8-7	1.20	0.76	0.23	0.62	0.96	0.41	0.20
Blank 3	E9-1	0.27	0.27	13.85	0.26	0.77	0.08	0.07
	E9-2	0.28	0.31	28.68	0.83	0.10	0.13	0.32
	E9-3	0.74	0.46	12.41	3.00	4.98	0.37	0.35
	E9-4	0.51	0.80	7.03	0.81	2.46	0.64	0.21
	E9-5	0.71	0.14	19.23	1.32	1.25	0.66	0.36
	E9-6	1.52	1.02	1.71	1.56	0.39	0.22	0.15
	E9-7	0.64	0.82	6.83	1.37	0.34	0.96	0.07
	E9-8	0.95	0.18	4.74	1.30	1.31	0.30	0.17
	E9-9	1.66	0.09	4.70	0.24	1.12	0.09	0.18
	E9-10	0.12	0.91	3.68	0.22	0.58	0.33	0.02
	E9-11	1.21	0.75	8.68	0.76	1.25	0.35	0.27
	E9-12	1.72	0.50	24.88	0.76	1.12	0.25	0.18
	E9-13	0.69	0.31	15.80	0.33	1.48	0.21	0.28
	E9-14	0.76	0.60	6.77	0.21	1.04	0.09	0.59
CD80WP132-A	E11-1	0.56	0.18	6.00	0.72	1.61	0.46	0.01
	E11-2	0.57	0.53	3.03	0.96	0.86	0.17	0.31
	E11-3	1.04	0.28	1.15	0.43	1.42	0.81	0.39
	E11-4	0.46	0.15	0.35	0.45	0.68	0.45	0.32
	E11-5	1.33	0.32	0.31	0.54	0.89	0.39	0.22
	E11-6	0.03	0.49	0.63	0.68	0.68	0.29	0.28
	E11-7	0.90	0.50	0.39	0.94	1.97	0.13	0.14
	E11-8	0.76	0.45	1.42	2.02	0.47	0.60	0.32
	E11-9	0.26	0.47	0.35	0.79	0.39	0.21	0.77
	E11-10	0.81	0.47	1.37	0.67	0.36	0.57	0.28
	E11-11	0.67	0.36	0.99	0.90	0.65	0.42	0.08
	E11-12	1.11	0.34	0.86	0.62	0.68	0.25	0.19
	E11-13	0.18	0.23	0.64	0.47	0.26	0.16	0.61
	E11-14	1.08	0.71	0.57	1.29	0.87	0.38	0.01
G1-A	E12-1	0.99	0.19	6.34	0.38	1.15	1.02	0.24
	E12-2	0.29	0.23	1.81	1.57	0.43	0.53	0.95
	E12-3	0.22	0.44	0.29	0.30	0.63	0.53	0.02
	E12-4	0.90	0.58	0.27	0.54	0.51	0.28	0.52
	E12-5	0.40	0.24	0.76	0.54	0.85	0.47	0.12
	E12-6	0.56	0.52	0.31	0.91	0.95	0.35	1.07
	E12-7	0.51	0.90	0.73	0.62	0.63	0.34	0.16
	E12-8	0.95	0.70	0.83	0.64	1.39	0.22	0.35
	E12-9	0.81	0.14	0.61	1.07	0.79	0.18	0.52
	E12-10	0.90	0.16	0.29	1.53	1.45	0.72	0.32
	E12-11	0.86	0.57	0.73	0.94	0.97	0.51	0.27
	E12-12	0.57	0.50	0.42	0.93	1.58	0.43	0.32
	E12-13	1.31	0.25	0.70	0.96	1.32	0.35	0.26
	E12-14	0.57	0.27	0.88	1.28	1.05	0.17	0.24

RSD (%) – ICP-OES, continued

Sample	ID	Na	Mg	Si	K	Ca	Sr	S
Blank 4	E13-1	0.94	0.53	2.50	0.71	1.08	0.62	0.21
	E13-2	0.66	0.60	4.66	1.02	0.84	0.40	0.31
	E13-3	0.56	0.42	2.99	1.09	0.82	0.44	0.31
	E13-4	0.81	0.51	5.02	0.75	0.87	0.38	0.19
	E13-5	0.69	0.47	5.58	0.74	1.00	0.25	0.25
	E13-6	1.05	0.60	3.87	1.26	1.02	0.20	0.23
	E13-7	1.09	0.32	3.99	0.76	0.83	0.59	0.31
	E13-8	1.00	0.36	8.56	1.21	0.87	0.43	0.25
JdF mix 2bis	E14-1	0.87	0.51	10.56	0.94	0.72	0.36	0.31
	E14-2	0.40	0.56	1.28	1.06	0.79	0.44	0.33
	E14-3	1.01	0.27	0.54	0.72	0.71	0.36	0.25
	E14-4	0.62	0.26	0.73	0.88	0.88	0.46	0.29
	E14-5	0.73	0.24	0.86	1.09	1.03	0.45	0.17
	E14-6	0.70	0.50	0.50	1.04	0.80	0.46	0.16
	E14-7	0.58	0.29	0.60	0.56	0.77	0.40	0.19
	E14-8	1.17	0.51	0.76	0.93	0.85	0.33	0.27
CD80WP132-Abis	E15-1	0.60	0.25	9.73	1.13	0.63	0.45	0.28
	E15-2	0.70	0.41	2.71	1.00	0.73	0.30	0.25
	E15-3	0.85	0.59	2.72	1.13	0.74	0.32	0.13
	E15-4	0.78	0.29	1.20	0.54	0.68	0.32	0.21
	E15-5	0.78	0.51	1.48	1.62	0.99	0.28	0.32
	E15-6	0.73	0.44	0.73	0.78	1.03	0.38	0.22
	E15-7	1.01	0.29	0.84	1.51	1.87	0.59	0.26
	E15-8	0.58	0.63	0.94	0.62	0.90	0.31	0.18
CD80WP132-B	E16-1	0.68	0.42	14.70	0.92	0.69	0.54	0.24
	E16-2	0.50	0.66	1.82	0.72	0.98	0.35	0.18
	E16-3	0.78	0.54	2.06	0.83	1.32	0.49	0.26
	E16-4	0.44	0.71	0.99	1.09	0.96	0.42	0.16
	E16-5	0.69	0.31	1.25	0.91	0.99	0.39	0.16
	E16-6	1.28	0.43	0.84	1.00	0.98	0.49	0.39
	E16-7	0.50	0.31	1.07	0.80	1.01	0.34	0.28
	E16-8	0.95	0.46	1.25	0.99	0.67	0.34	0.24

A-Chapter 4, Samples

CH4-13: Complete list of samples, divided by textural group, from the scientific cruise IODP 327, at Site U1362, Hole A.

JdF mix 1, cryptocrystalline basalts
15 samples

JdF mix 2, microcrystalline basalts

14 samples

JdF mix 3, altered fine grained basalts
11 samples

CH4-14: Pillow basalt from Mid-Atlantic Ridge (MAR) dredged during the *RRS Charles Darwin Cruise 80*, specifically at the *Way Point 132*.

CD80WP132, cryptocrystalline vesicular basalt

CH4-15: Gabbro from Troodos ophiolite (Cyprus), sampled during a fieldwork close to the locality of Kato Amiandos.

G1, recrystallized medium grained gabbro

Bibliography

(1972), Penrose field conference on ophiolites, in *Geotimes*, edited, pp. 24-25.

Al Eidan, A. A., S. Bachu, L. S. Melzer, E. I. Lars, and M. Ackiewicz (2015), Technical Challenges in the Conversion of CO_2-EOR Projects to CO_2 Storage Projects, edited, Society of Petroleum Engineers.

Alfredsson, H. A., B. S. Hardarson, H. Franzson, and S. R. Gislason (2008), CO_2 sequestration in basaltic rock at the Hellisheidi site in SW Iceland: stratigraphy and chemical composition of the rocks at the injection site, *Mineralogical Magazine*, *72*(1), 1-5.

Allen, M. R., D. J. Frame, C. Huntingford, C. D. Jones, J. A. Lowe, M. Meinshausen, and N. Meinshausen (2009), Warming caused by cumulative carbon emissions towards the trillionth tonne, *Nature*, *458*(7242), 1163-1166.

Alt, J. C. (1995), Subseafloor processes in mid-ocean ridge hydrothermal systems, in *Seafloor Hydrothermal Systems: Physical, Chemical, Biological, and Geological Interactions*, edited by Susan E. Humphris, Robert A. Zierenberg, L. S. Mullineaux and R. E. Thomson, pp. 85-114, AGU, Washington, DC.

Alt, J. C., and D. A. H. Teagle (1999), The uptake of carbon during alteration of ocean crust, *Geochimica et Cosmochimica Acta*, *63*(10), 1527-1535.

Alt, J. C., C. Laverne, R. M. Coggon, D. A. H. Teagle, N. R. Banerjee, S. Morgan, C. E. Smith-Duque, M. Harris, and L. Galli (2010), Subsurface structure of a submarine hydrothermal system in ocean crust formed at the East Pacific Rise, ODP/IODP Site 1256, *Geochemistry, Geophysics, Geosystems*, *11*(10), Q10010.

Alt, J. C., et al. (1993), *Proc. ODP, Init. Repts., 148, Ocean Drilling Program, College Station, TX*.

Alt, J. C., et al. (1996), *Proc. ODP, Sci. Results, 148, Ocean Drilling Program, College Station, TX*.

Anbeek, C. (1992), Surface roughness of minerals and implications for dissolution studies, *Geochimica et Cosmochimica Acta*, *56*(4), 1461-1469.

Anderson, R. N., M. D. Zoback, S. H. Hickman, and R. L. Newmark (1985), Permeability versus depth in the upper oceanic crust: In situ measurements in DSDP hole 504B, eastern equatorial Pacific, *Journal of Geophysical Research: Solid Earth*, *90*(B5), 3659-3669.

Andreani, M., L. Luquot, P. Gouze, M. Godard, E. Hoisé, and B. Gibert (2009), Experimental study of carbon sequestration reactions controlled by the percolation of CO_2-rich brine through peridotites, *Environmental Science & Technology*, *43*(4), 1226-1231.

Aspelund, A. (2010), Gas purification, compression and liquefaction processes and technology for carbon dioxide (CO_2) transport, in *Developments and Innovation in Carbon Dioxide (CO_2) Capture and Storage Technology*, edited by M. M. Maroto-Valer, pp. 383-407, Woodhead Publishing.

Auzende, J. M., D. Bideau, E. Bonatti, M. Cannat, J. Honnorez, Y. Lagabrielle, J. Malavieille, V. Mamaloukas-Frangoulis, and C. Mevel (1989), Direct observation of a section through slow-spreading oceanic crust, *Nature*, *337*(6209), 726-729.

Bach, W., and G. L. Früh-Green (2010), Alteration of the Oceanic Lithosphere and Implications for Seafloor Processes, *Elements*, *6*(3), 173-178.

Bachu, S. (2000), Sequestration of CO_2 in geological media: criteria and approach for site selection in response to climate change, *Energy Conversion and Management*, *41*(9), 953-970.

Bachu, S., and W. D. Gunter (2004), Acid-gas injection in the Alberta basin, Canada: a CO2-storage experience, *Geological Society, London, Special Publications*, *233*(1), 225-234.

Bachu, S., D. Bonijoly, J. Bradshaw, R. Burruss, S. Holloway, N. P. Christensen, and O. M. Mathiassen (2007), CO_2 storage capacity estimation: Methodology and gaps, *International Journal of Greenhouse Gas Control*, *1*(4), 430-443.

Banfield, J. F., B. F. Jones, and D. R. Veblen (1991), An AEM-TEM study of weathering and diagenesis, Abert Lake, Oregon: I. Weathering reactions in the volcanics, *Geochimica et Cosmochimica Acta*, *55*(10), 2781-2793.

Barnola, J. M., D. Raynaud, Y. S. Korotkevich, and C. Lorius (1987), *Vostok ice core provides 160,000-year record of atmospheric CO_2*.

Béarat, H., M. J. McKelvy, A. V. G. Chizmeshya, D. Gormley, R. Nunez, R. W. Carpenter, K. Squires, and G. H. Wolf (2006), Carbon Sequestration via Aqueous Olivine Mineral Carbonation: Role of Passivating Layer Formation, *Environmental Science & Technology*, *40*(15), 4802-4808.

Becker, K. (1996), Permeability measurements in Hole 896A and implications for the lateral variability of upper crustal permeability at Sites 504 and 896. In *Alt, J.C., Kinoshita, H., Stokking, L.B., and Michael, P.J. (Eds.), Proc. ODP, Sci. Results,* 148: College Station, TX (Ocean Drilling Program).

Becker, K., and A. T. Fisher (2000), Permeability of upper oceanic basement on the eastern flank of the Juan de Fuca Ridge determined with drill-string packer experiments, *Journal of Geophysical Research: Solid Earth*, *105*(B1), 897-912.

Becker, K., H. Sakai, and et al. (1988), P*roc. ODP, Init. Repts.,* 111: College Station, TX (Ocean Drilling Program), edited.

Becker, K., A. T. Fisher, and T. Tsuji (2013), New packer experiments and borehole logs in upper oceanic crust: evidence for ridge-parallel consistency in crustal hydrogeological properties, *Geochemistry, Geophysics, Geosystems*.

Becker, K., E. E. Davis, F. N. Spiess, and C. P. deMoustier (2004), Temperature and video logs from the upper oceanic crust, Holes 504B and 896A, Costa Rica Rift flank: implications for the permeability of upper oceanic crust, *Earth and Planetary Science Letters*, *222*(3–4), 881-896.

Becker, K., et al. (1989), Drilling deep into young oceanic crust, Hole 504B, Costa Rica Rift, *Reviews of Geophysics*, *27*(1), 79-102.

Benson, S. M., and D. R. Cole (2008), CO_2 sequestration in deep sedimentary formations, *Elements*, *4*(5), 325-331.

Berg, A., and S. A. Banwart (2000), Carbon dioxide mediated dissolution of Ca-feldspar: implications for silicate weathering, *Chemical Geology*, *163*(1–4), 25-42.

Blum, A. E. (1994), Feldspars in weathering, in *Feldspars and their reactions*, edited, pp. 595-630, Springer.

Blum, A. E., and A. Lasaga (1988), Role of surface speciation in the low-temperature dissolution of minerals, *Nature*, *331*(6155), 431-433.

Bonatti, E., J. Honnorez, P. Kirst, and F. Radicati (1975), Metagabbros from the Mid-Atlantic Ridge at 06°N: Contact-Hydrothermal-Dynamic Metamorphism beneath the Axial Valley, *The Journal of Geology*, *83*(1), 61-78.

Brady, P. V. (1991), The effect of silicate weathering on global temperature and atmospheric CO_2, *Journal of Geophysical Research: Solid Earth*, *96*(B11), 18101-18106.

Brady, P. V., and S. R. Gíslason (1997), Seafloor weathering controls on atmospheric CO_2 and global climate, *Geochimica et Cosmochimica Acta*, *61*(5), 965-973.

Brantley, S. L., and N. P. Mellott (2000), Surface area and porosity of primary silicate minerals, *American Mineralogist*, *85*(11-12), 1767-1783.

Brereton, N. R. (1992), Physical property relationships from Sites 765 and 766. *In Gradstein, F.M., Ludden, J.N., et al., Proc. ODP, Scientific Results*, *123: College Station, TX (Ocean Drilling Program)*, 453-468.

Brewer, P. G., G. Friederich, E. T. Peltzer, and F. M. Orr Jr. (1999), Direct experiments on the ocean disposal of fossil fuel CO_2, *Science*, *284*(5416), 943-945.

Brown, E., A. Colling, D. Park, J. Phillips, D. Rothery, and J. Wright (1995), *Seawater: Its composition, properties, and behaviour (Second Edition)*, 166 pp., Elsevier Ltd., Oxford.

Bryant, E. (1997), *Climate process and change*, 209 pp., Cambridge University Press, Cambridge, UK.

Bryant, W. R., and F. R. Rack (1990), Consolidation characteristics of Weddell Sea sediments. In *P. F. Barker and J. P. Kennet (Eds.), Proc. ODP, Sci. Results, 113: College Station, TX (Ocean Drilling Program)*, 211-223.

Bullard, E. C. (1947), The time necessary for a bore hole to attain temperature equilibrium, *Geophysical Journal International*, *5*, 127-130.

Canadell, J. G., C. Le Quéré, M. R. Raupach, C. B. Field, E. T. Buitenhuis, P. Ciais, T. J. Conway, N. P. Gillett, R. A. Houghton, and G. Marland (2007), Contributions to accelerating atmospheric CO_2 growth from economic activity, carbon intensity, and efficiency of natural sinks, *Proceedings of the National Academy of Sciences*, *104*(47), 18866-18870.

Cann, J. R., and B. M. Funnell (1967), Palmer Ridge: a Section through the Upper Part of the Ocean Crust?, *Nature*, *213*(5077), 661-664.

Cann, J. R., S. M. White, R. N. Anderson, J. R. Lawrence, J. H. Natland, V. L. Nekhoroshkov, N. N. Pertsev, V. N. Ponomarev, and M. D. Zoback (1983a), Initial Reports DSDP, 69*Rep.*, U.S. Govt. Print Office, Washington, DC.

Cann, J. R., et al. (1983b), Sites 501 and 504: Sediments and Ocean Crust in an Area of High Heat Flow on the Southern Flank of the Costa Rica Rift. *In* DSDP *Initial Reports*, edited, pp. 31-173.

Cannat, M. (1993), Emplacement of mantle rocks in the seafloor at mid-ocean ridges, *Journal of Geophysical Research: Solid Earth*, *98*(B3), 4163-4172.

Cannat, M. (1996), How thick is the magmatic crust at slow spreading oceanic ridges?, *Journal of Geophysical Research: Solid Earth*, *101*(B2), 2847-2857.

Carlson, R. L. (2010), How crack porosity and shape control seismic velocities in the upper oceanic crust: Modeling downhole logs from Holes 504B and 1256D, *Geochemistry, Geophysics, Geosystems*, *11*(4), n/a-n/a.

Carlson, R. L., and C. N. Herrick (1990), Densities and porosities in the oceanic crust and their variations with depth and age, *Journal of Geophysical Research: Solid Earth*, *95*(B6), 9153-9170.

Carroll, S. A., and K. G. Knauss (2005), Dependence of labradorite dissolution kinetics on $CO_{2(aq)}$, $Al_{(aq)}$, and temperature, *Chemical Geology*, *217*(3–4), 213-225.

Casey, J. F., J. F. Dewey, P. J. Fox, J. A. Karson, and E. Rosencrantz (1981), Heterogeneous nature of the oceanic crust and upper mantle: A perspective from the Bay of Islands Ophiolite, in *The Sea*, edited by C. E. Emiliani, pp. 305–338, Wiley-Interscience, New York.

Casey, W. H., H. R. Westrich, and G. R. Holdren (1991), Dissolution rates of plagioclase at pH= 2 and 3, *American Mineralogist;(United States)*, *76*.

Castillo, D. A. (1992), Thermal and hydrologic properties of old oceanic crust in Hole 765D, Argo Abyssal Plain, Indian Ocean. *In Gradstein, F.M., Ludden, J.N., et al., Proc. ODP, Sci. Results, 123: College Station, TX (Ocean Drilling Program)*, 515–522.

Chadwick, A., R. Arts, C. Bernstone, F. May, S. Thibeau, and P. Zweigel (2008), *Best Practice for the Storage of CO_2 in Saline Aquifers-Observations and Guidelines from the SACS and CO2STORE projects*, British Geological Survey.

Choptiany, J. M. H., R. Pelot, and K. Sherren (2014), An Interdisciplinary Perspective on Carbon Capture and Storage Assessment Methods, *Journal of Industrial Ecology*, *18*(3), 445-458.

Chou, L., and R. Wollast (1985), Steady-state kinetics and dissolution mechanisms of albite, *American Journal of Science*, *285*(10), 963-993.

Clauser, C. (2006), Geothermal energy, in *K. Heinloth (ed), Landolt-Börnstein, Group VIII: Advanced materials and technologies, Vol. 3: Energy Technologies, Subvol. C: Renewable Energies*, edited, pp. 493-604, Springer Verlag, Heidelberg-Berlin.

Clow, D., and J. Drever (1996), Weathering rates as a function of flow through an alpine soil, *Chemical Geology*, *132*(1), 131-141.

Coady, D., I. Parry, L. Sears, and B. Shang (2015), How Large Are Global Energy Subsidies? (May 2015), *IMF Working Paper No. 15/105. Available at SSRN: http://ssrn.com/abstract=2613304*.

Coggon, R. M., D. A. H. Teagle, M. J. Cooper, and D. A. Vanko (2004), Linking basement carbonate vein compositions to porewater geochemistry across the eastern flank of the Juan de Fuca Ridge, ODP Leg 168, *Earth and Planetary Science Letters*, *219*(1–2), 111-128.

Coggon, R. M., D. A. H. Teagle, C. E. Smith-Duque, J. C. Alt, and M. J. Cooper (2010), Reconstructing past seawater Mg/Ca and Sr/Ca from mid-ocean ridge flank calcium carbonate veins, *Science*, *327*(5969), 1114-1117.

Coleman, R. G. (1977), *Ophiolites: ancient oceanic lithosphere?*, 229 pp., Springer-Verlag., Berlin.

Conference of the Parties Twenty-first Session (2015), U.N.Framework Convention on Climate Change, Adoption of the Paris Agreement, U.N. Doc. FCCC/CP/2015/L.9, pmbl. (Dec. 12, 2015), edited.

Coogan, L. A., and K. M. Gillis (2013), Evidence that low-temperature oceanic hydrothermal systems play an important role in the silicate-carbonate weathering cycle and long-term climate regulation, *Geochemistry, Geophysics, Geosystems*, *14*.

Coogan, L. A., R. R. Parrish, and N. M. W. Roberts (2016), Early hydrothermal carbon uptake by the upper oceanic crust: Insight from in situ U-Pb dating, *Geology*, *44*(2), 147-150.

Critelli, T., L. Marini, J. Schott, V. Mavromatis, C. Apollaro, T. Rinder, R. De Rosa, and E. H. Oelkers (2014), Dissolution rates of actinolite and chlorite from a whole-rock experimental study of metabasalt dissolution from 2 ≤ pH ≤ 12 at 25 °C, *Chemical Geology*, *390*, 100-108.

Crovisier, J. L., J. Honnorez, and J. P. Eberhart (1987), Dissolution of basaltic glass in seawater: Mechanism and rate, *Geochimica et Cosmochimica Acta*, *51*(11), 2977-2990.

Cubillas, P., S. Köhler, M. Prieto, C. Chaïrat, and E. H. Oelkers (2005), Experimental determination of the dissolution rates of calcite, aragonite, and bivalves, *Chemical Geology*, *216*(1–2), 59-77.

Danyushevsky, L. V. (2001), The effect of small amounts of H_2O on crystallisation of mid-ocean ridge and backarc basin magmas, *Journal of Volcanology and Geothermal Research*, *110*(3–4), 265-280.

Daval, D., et al. (2011), Influence of amorphous silica layer formation on the dissolution rate of olivine at 90°C and elevated pCO_2, *Chemical Geology*, *284*(1-2), 193-209.

Davis, E. E., and K. Becker (1998), Borehole observatories record driving forces for hydrotheraial circulation in young oceanic crust, *Eos, Transactions American Geophysical Union*, *79*(31), 369-370.

Davis, E. E., K. Becker, and J. He (2004), Costa Rica Rift revisited: constraints on shallow and deep hydrothermal circulation in young oceanic crust, *Earth and Planetary Science Letters*, *222*(3–4), 863-879.

Davis, E. E., M. J. Mottl, A. T. Fisher, and J. V. Firth (1997), *Proc. ODP, Init. Repts., 168, 470 pp., Ocean Drilling Program, College Station, TX*.

Davis, E. E., et al. (1992), FlankFlux: an experiment to study the nature of hydrothermal circulation in young oceanic crust, *Canadian Journal of Earth Sciences*, *29*(5), 925-952.

Decarre, S., J. Berthiaud, N. Butin, and J.-L. Guillaume-Combecave (2010), CO_2 maritime transportation, *International Journal of Greenhouse Gas Control*, *4*(5), 857-864.

Deer, W. A., R. A. Howie, and J. Zussman (1963), *Rock-forming minerals. Vol. 4B, Framework silicates: silica minerals, feldspathoides and the zeolites*, Geological Society.

Deer, W. A., R. A. Howie, and J. Zussman (1978), *Rock-forming minerlas. Vol.2 , Single-chain silicates*, Longman London.

Deer, W. A., R. A. Howie, and J. Zussman (1997), Rock-Forming Mineral. Vol. 3, Double-chain silicates, paper presented at The Geological Society, London.

Dessert, C., B. Dupré, J. Gaillardet, L. M. François, and C. J. Allègre (2003), Basalt weathering laws and the impact of basalt weathering on the global carbon cycle, *Chemical Geology*, *202*(3–4), 257-273.

Divins, D. L. (2003), Total sediment thickness of the world's oceans and marginal seas, edited by N. N. G. D. Center, Boulder, CO.

Divins, D. L., and P. D. Rabinowitz (1990), Thickness of Sedimentary Cover for the South Atlantic, in International Geological-Geophysical Atlas of the Atlantic Ocean, in *Intergovernmental Oceanographic Commission*, edited by G. B. Udintsev, pp. 126-127, Moscow.

Dri, M., A. Sanna, and M. M. Maroto-Valer (2014), Mineral carbonation from metal wastes: Effect of solid to liquid ratio on the efficiency and characterization of carbonated products, *Applied Energy*, *113*, 515-523.

Duan, Z., R. Sun, C. Zhu, and I. M. Chou (2006), An improved model for the calculation of CO_2 solubility in aqueous solutions containing Na^+, K^+, Ca^{2+}, Mg^{2+}, Cl^-, and SO_4^{2-}, *Marine Chemistry*, *98*(2–4), 131-139.

Eakins, B. W., and G. F. Sharman (2010), Volumes of the World's Oceans from ETOPO1, edited, NOAA National Geophysical Data Center, Boulder, CO.

Eccles, J. K., and L. Pratson (2012), Global CO_2 storage potential of self-sealing marine sedimentary strata, *Geophys. Res. Lett.*, *39*, L19604.

Eggleton, R. A., C. Foudoulis, and D. Varkevisser (1987), Weathering of basalt: changes in rock chemistry and mineralogy, *Clays and Clay Minerals*, *35*(3), 161-169.

Elderfield, H., and A. Schultz (1996), Mid-ocean ridge hydrothermal fluxes and the chemical composition of the ocean, *Annual Review of Earth and Planetary Sciences*, *24*, 191-224.

Elderfield, H., C. G. Wheat, M. J. Mottl, C. Monnin, and B. Spiro (1999), Fluid and geochemical transport through oceanic crust: a transect across the eastern flank of the Juan de Fuca Ridge, *Earth and Planetary Science Letters*, *172*(1–2), 151-165.

EPA (2015), Inventory of U.S. Greenhouse gas emissions and sinks: 1990-2014. Annex 2 (Methodology and data for estimating CO_2 emissions from fossil fuel combustion), *U.S. Environmental Protection Agency, Washington, DC. U.S. EPA*.

Exon, N. F., and J. B. Willcox (1978), Geology and petroleum potential of Exmouth Plateau area off Western Australia, *AAPG Bulletin*, *62*(1), 40-72.

Fehn, U., K. E. Green, R. P. Von Herzen, and L. M. Cathles (1983), Numerical models for the hydrothermal field at the Galapagos Spreading Center, *Journal of Geophysical Research: Solid Earth*, *88*(B2), 1033-1048.

Fisher, A. T. (1998), Permeability within basaltic oceanic crust, *Rev. Geophys.*, *36*(2), 143-182.

Fisher, A. T., and E. E. Davis (2000), An introduction to the scientific results of Leg 168, in *Proc. ODP, Sci. Results, 168*, edited by A. T. Fisher, E. E. Davis and C. Escutia, pp. 3-5, Ocean Drilling Program, College Station, TX.

Fisher, A. T., T. Tsuji, K. Petronotis, and the Expedition 327 Scientists (2011), *Proc.* IODP, 327: Tokyo (Integrated Ocean Drilling Program Management International, Inc.).

Fisher, A. T., K. Becker, I. T. N. Narasimhan, M. G. Langseth, and M. J. Mottl (1990), Passive, off-axis convection through the southern flank of the Costa Rica Rift, *Journal of Geophysical Research: Solid Earth*, *95*(B6), 9343-9370.

Fisher, A. T., et al. (2003), Hydrothermal recharge and discharge across 50 km guided by seamounts on a young ridge flank, *Nature*, *421*(6923), 618-621.

Fofonoff, N. P., R. C. J. Millard, and United Nations Educational, Scientific, and Cultural Organization, Paris (France). Div. of Marine Sciences (1983), *Algorithms for computation of fundamental properties of seawater. Endorsed by Unesco: SCOR/ICES/IAPSO joint panel on oceanographic tables and standards and SCOR Working Group 51. Unesco Technical Papers in Marine Science, No. 44/N. P. Fofonoff and R. C. Millard, Jr*, Distributed by ERIC Clearinghouse, [Washington, D.C.].

Fox, P. J., and J. B. Stroup (1981), The plutonic foundation of the oceanic crust, in *The sea*, edited by C. E. Emiliani, pp. 119-218, Wiley and Sons, New York.

Francheteau, J., R. Armijo, J. L. Cheminée, R. Hekinian, P. Lonsdale, and N. Blum (1990), 1 Ma East Pacific Rise oceanic crust and uppermost mantle exposed by rifting in Hess Deep (equatorial Pacific Ocean), *Earth and Planetary Science Letters*, *101*(2), 281-295.

Franks, P. J., D. L. Royer, D. J. Beerling, P. K. Van de Water, D. J. Cantrill, M. M. Barbour, and J. A. Berry (2014), New constraints on atmospheric CO_2 concentration for the Phanerozoic, *Geophysical Research Letters*, *41*(13), 2014GL060457.

Fridriksson, T., P. S. Neuhoff, S. Arnórsson, and D. K. Bird (2001), Geological constraints on the thermodynamic properties of the stilbite—stellerite solid solution in low-grade metabasalts, *Geochimica et Cosmochimica Acta*, *65*(21), 3993-4008.

Frölicher, T. L., and F. Joos (2010), Reversible and irreversible impacts of greenhouse gas emissions in multi-century projections with the NCAR global coupled carbon cycle-climate model, *Climate Dynamics*, *35*(7), 1439-1459.

Gadikota, G., J. M. Matter, P. Kelemen, and A.-h. A. Park (2014a), Chemical and morphological changes during olivine carbonation for CO_2 storage in the presence of NaCl and $NaHCO_3$, *Physical Chemistry Chemical Physics*, *16*(10), 4679-4693.

Gadikota, G., E. J. Swanson, H. Zhao, and A.-H. A. Park (2014b), Experimental design and data analysis for accurate estimation of reaction kinetics and conversion for carbon mineralization, *Industrial & Engineering Chemistry Research*, *53*(16), 6664-6676.

Galeczka, I., D. Wolff-Boenisch, E. H. Oelkers, and S. R. Gislason (2014), An experimental study of basaltic glass–H_2O–CO_2 interaction at 22 and 50°C: Implications for subsurface storage of CO_2, *Geochimica et Cosmochimica Acta*, *126*(0), 123-145.

Gautier, J.-M., E. H. Oelkers, and J. Schott (2001), Are quartz dissolution rates proportional to B.E.T. surface areas?, *Geochimica et Cosmochimica Acta*, *65*(7), 1059-1070.

Gerdemann, S. J., W. K. O'Connor, D. C. Dahlin, L. R. Penner, and H. Rush (2007), Ex situ aqueous mineral carbonation, *Environmental Science & Technology*, *41*(7), 2587-2593.

GERM (2000), The Geochemical Earth Reference Model, http://EarthRef.org/agenda.htm.

Gillis, K. M., and L. A. Coogan (2011), Secular variation in carbon uptake into the ocean crust, *Earth and Planetary Science Letters*, *302*(3–4), 385-392.

Gillis, K. M., J. N. Ludden, T. Plank, and L. D. Hoy (1992), Low-temperature alteration and subsequent reheating of shallow oceanic crust at Hole 765D, Argo Abyssal Plain. In Gradstein, F.M., Ludden, J.N., et al., Proc. ODP, Sci. Results, 123: College Station, TX (Ocean Drilling Program), 191–199.

Gislason, S. R., and E. H. Oelkers (2003), Mechanism, rates, and consequences of basaltic glass dissolution: II. An experimental study of the dissolution rates of basaltic glass as a function of pH and temperature, *Geochimica et Cosmochimica Acta*, *67*(20), 3817-3832.

Gislason, S. R., and E. H. Oelkers (2014), Carbon storage in basalt, *Science*, *344*(6182), 373-374.

Gislason, S. R., et al. (2010), Mineral sequestration of carbon dioxide in basalt: a pre-injection overview of the CarbFix project, *International Journal of Greenhouse Gas Control*, *4*(3), 537-545.

Gislason, S. R., et al. (2014), Rapid solubility and mineral storage of CO_2 in basalt, *Energy Procedia*, *63*, 4561-4574.

Global CCS Institute (2015), The Global Status of CCS: 2015 Summary *Rep.*, Melbourne, Australia.

Godard, M., P. B. Kelemen, S. Nasir, and D. A. H. Teagle (2011), Geological carbon capture & storage in mafic and ultramafic rocks *Rep.*

Goldberg, D. S. (1999), CO_2 Sequestration Beneath The Seafloor: Evaluating The In Situ Properties of Natural Hydrate-Bearing Sediments and Oceanic Basalt Crust, *International Journal of the Society of Materials Engineering for Resources*, *7*(1), 11-16.

Goldberg, D. S., and A. L. Slagle (2009), A global assessment of deep-sea basalt sites for carbon sequestration, *Energy Procedia*, *1*(1), 3675-3682.

Goldberg, D. S., T. Takahashi, and A. L. Slagle (2008), Carbon dioxide sequestration in deep-sea basalt, *Proceedings of the National Academy of Sciences*, *105(29)*, 9920-9925.

Goldberg, D. S., D. V. Kent, and P. E. Olsen (2010), Potential on-shore and off-shore reservoirs for CO_2 sequestration in Central Atlantic magmatic province basalts, *Proceedings of the National Academy of Sciences*, *107 (4)*, 1327-1332.

Goldberg, D. S., K. S. Lackner, P. Han, A. L. Slagle, and T. Wang (2013), Co-location of air capture, subseafloor CO_2 sequestration, and energy production on the Kerguelen Plateau, *Environmental Science & Technology*, *47*(13), 7521-7529.

Golubev, S. V., O. S. Pokrovsky, and J. Schott (2005), Experimental determination of the effect of dissolved CO_2 on the dissolution kinetics of Mg and Ca silicates at 25 C, *Chemical Geology*, *217*(3), 227-238.

Govers, R., and P. T. Meijer (2001), On the dynamics of the Juan de Fuca plate, *Earth and Planetary Science Letters*, *189*(3–4), 115-131.

Gradstein, F. M., and J. N. Ludden (1992), Radiometric age determinations for basement from Sites 765 and 766, Argo Abyssal Plain and northwestern Australian margin, paper presented at Proceedings of the ocean drilling program, Scientific Results.

Gradstein, F. M., J. N. Ludden, and and Shipboard Scientific Party (1990), Background and introduction. In *Ludden, J.N., Gradstein, F.M., et al., Proc. ODP, Init. Repts., 123: College Station, TX (Ocean Drilling Program)*, 3-12.

Gradstein, F. M., J. N. Ludden, and et al. (1992), Proc. ODP, Sci. Results, 123: College Station, TX (Ocean Drilling Program).

Grandstaff, D. E. (1978), Changes in surface area and morphology and the mechanism of forsterite dissolution, *Geochimica et Cosmochimica Acta*, *42*(12), 1899-1901.

Gudbrandsson, S., D. Wolff-Boenisch, S. R. Gislason, and E. H. Oelkers (2011), An experimental study of crystalline basalt dissolution from 2 ≤ pH ≤ 11 and temperatures from 5 to 75 ˚C, *Geochimica et Cosmochimica Acta*, *75*(19), 5496-5509.

Gudbrandsson, S., D. Wolff-Boenisch, S. R. Gislason, and E. H. Oelkers (2014), Experimental determination of plagioclase dissolution rates as a function of its composition and pH at 22 °C, *Geochimica et Cosmochimica Acta*, *139*, 154-172.

Guerin, G., K. Becker, R. Gable, and P. A. Pezard (1996), Temperature measurements and heat-flow analysis in Hole 504B, in *In Alt, J.C., Kinoshita, H., Stokking, L.B., and Michael, P.J. (Eds.), Proc. ODP, Sci. Results, 148: College Station, TX (Ocean Drilling Program)*, edited, pp. 291–296.

Gunter, W. D., E. H. Perkins, and T. J. McCann (1993), Aquifer disposal of CO_2-rich gases: reaction design for added capacity, *Energy Conversion and management*, *34*(9-11), 941-948.

Gunter, W. D., B. Wiwehar, and E. H. Perkins (1997), Aquifer disposal of CO_2-rich greenhouse gases: Extension of the time scale of experiment for CO_2-sequestering reactions by geochemical modelling, *Mineralogy and Petrology*, *59*(1-2), 121-140.

Guy, C., and J. Schott (1988), Multi-site surface reaction versus transport control during the hydrolisis of a complex oxide, *Chemical Geology*, *70*(1–2), 78.

Gysi, A. P., and A. Stefánsson (2008), Numerical modelling of CO_2-water-basalt interaction, *Mineralogical Magazine*, *72*(1), 55-59.

Gysi, A. P., and A. Stefánsson (2012a), Experiments and geochemical modeling of CO_2 sequestration during hydrothermal basalt alteration, *Chemical Geology*, *306–307*, 10-28.

Gysi, A. P., and A. Stefánsson (2012b), Mineralogical aspects of CO_2 sequestration during hydrothermal basalt alteration - An experimental study at 75 to 250 °C and elevated pCO_2, *Chemical Geology*, *306–307*, 146-159.

Gysi, A. P., and A. Stefánsson (2012c), CO_2-water–basalt interaction. Low temperature experiments and implications for CO_2 sequestration into basalts, *Geochimica et Cosmochimica Acta*, *81*, 129-152.

Hamilton, E. L., and R. T. Bachman (1982), Sound velocity and related properties of marine sediments, *The Journal of the Acoustical Society of America*, *72*(6), 1891-1904.

Haraldsson, C., L. G. Anderson, M. Hassellöv, S. Hulth, and K. Olsson (1997), Rapid, high-precision potentiometric titration of alkalinity in ocean and sediment pore waters, *Deep Sea Research Part I: Oceanographic Research Papers*, *44*(12), 2031-2044.

Harper, G. D. (1984), The Josephine ophiolite, northwestern California, *Geological Society of America Bulletin*, *95*(9), 1009-1026.

Harris, M., R. Coggon, D. Teagle, N. Roberts, and R. Parrish (2014), Laser ablation MC-ICP-MS U/Pb geochronology of ocean basement calcium carbonate veins, paper presented at AGU Fall Meeting Abstracts.

Harris, R. N., and D. S. Chapman (2004), Deep-seated oceanic heat flux, heat deficits, and hydrothermal circulation, in *Hydrology of the Oceanic Lithosphere*, edited by E. E. Davis and H. Elderfield, pp. 311-336, Cambridge University Press, Cambridge.

Harrison, A. L., I. M. Power, and G. M. Dipple (2012), Accelerated carbonation of brucite in mine tailings for carbon sequestration, *Environmental Science & Technology*, *47*(1), 126-134.

Haugen, H. A., N. Eldrup, C. Bernstone, S. Liljemark, H. Pettersson, M. Noer, J. Holland, P. A. Nilsson, G. Hegerland, and J. O. Pande (2009), Options for transporting CO_2 from coal fired power plants Case Denmark, *Energy Procedia*, *1*(1), 1665-1672.

Hawkins, D. G. (2004), No exit: thinking about leakage from geologic carbon storage sites, *Energy*, *29*(9-10), 1571-1578.

Hay, W. W., J. L. Sloan, and C. N. Wold (1988), Mass/age distribution and composition of sediments on the ocean floor and the global rate of sediment subduction, *Journal of Geophysical Research: Solid Earth*, *93*(B12), 14933-14940.

Hayes, D. E., and J. L. LaBrecque (1991), Sediment Isopachs: Circum-Antarctic to 30S, in Marine Geological and Geophysical Atlas of the Circum-Antarctic to 30S, in *American Geophys. Union*, edited by D. E. Hayes, pp. 29-33, Washington, D.C.

Hayes, D. E., L. A. Frakes, and et al. (1975), *Initial Reports of the Deep Sea Drilling Project*, 19-48 pp., Washington (U.S. Government Printing Office).

Heberling, C., R. P. Lowell, L. Liu, and M. R. Fisk (2010), Extent of the microbial biosphere in the oceanic crust, *Geochem. Geophys. Geosyst.*, *11*, Q08003.

Helgeson, H. C., W. M. Murphy, and P. Aagaard (1984), Thermodynamic and kinetic constraints on reaction rates among minerals and aqueous solutions. II. Rate constants, effective surface area, and the hydrolysis of feldspar, *Geochimica et Cosmochimica Acta*, *48*(12), 2405-2432.

Hirai, S., K. Okazaki, Y. Tabe, K. Hijikata, and Y. Mori (1997), Dissolution rate of liquid CO_2 in pressurized water flows and the effect of clathrate films, *Energy-International Symposium on CO_2 Fixation and Efficient Utilization of Energy*, *22*(2), 285-293.

Hoffert, M. I., et al. (2002), Advanced technology paths to global climate stability: Energy for a greenhouse planet, *Science*, *298*(5595), 981-987.

Hofmann, D. J., J. H. Butler, and P. P. Tans (2009), A new look at atmospheric carbon dioxide, *Atmospheric Environment*, *43*(12), 2084-2086.

Holdren, G. R., and P. M. Speyer (1987), Reaction rate-surface area relationships during the early stages of weathering. II. Data on eight additional feldspars, *Geochimica et Cosmochimica Acta*, *51*(9), 2311-2318.

House, K. Z., D. P. Schrag, C. F. Harvey, and K. S. Lackner (2006), Permanent carbon dioxide storage in deep-sea sediments, *Proceedings of the National Academy of Sciences*, *103*(33), 12291-12295.

Hubbert, M. K., and D. G. Willis (1972), Mechanics of hydraulic fracturing.

Hutnak, M., A. T. Fisher, L. Zühlsdorff, V. Spiess, P. H. Stauffer, and C. W. Gable (2006), Hydrothermal recharge and discharge guided by basement outcrops on 0.7–3.6 Ma seafloor east of the Juan de Fuca Ridge: observations and numerical models, *Geochemistry, Geophysics, Geosystems*, *7*, Q07O02.

IEA (2010), *Energy Technology Perspectives 2010 - Scenarios & strategies to 2050*, OECD.

IEA (2012), *Energy Technology Perspectives 2012 - Pathways to a clean energy system*, OECD.

IEA (2015), *Energy technology perspectives 2015*, OECD/IEA, Paris.

IEAGHG (2010), Injection Strategies for CO_2 Storage Sites, 2010/04, June.

International Energy Agency Greenhouse Gas R&D Programme (2002), Building the cost curves for CO_2 storage, Part 1: Sources of CO_2 *Rep.*, Cheltenham, U. K.

International Ocean Discovery Program (2015), Archive of geosample information from scientific ocean drilling., edited, NOAA National Centers for Environmental Information.

IOC, IHO, and BODC (2003), Centenary Edition of the GEBCO Digital Atlas, published on CD-ROM on behalf of the Intergovernmental Oceanography Commission and the International Hydrographic Organization as part of the General Bathymetric Chart of the Oceans, edited by BODC, Liverpool, U.K.

IPCC (2005a), IPCC Special Report on Carbon Dioxide Capture and Storage, edited by B. Metz, O. Davidson, H. de Coninck, M. Loos and L. Meyer, pp. 197-265, Cambridge Univ. Press.

IPCC (2005b), *IPCC Special Report on Carbon Dioxide Capture and Storage*, 442 pp., Cambridge Univ. Press, Cambridge, United Kingdom and New York, NY, USA.

IPCC (2007), Climate Change 2007: Synthesis Report. Contribution of Working Groups I, II and III to the Fourth Assessment Report of the Intergovernmental Panel on Climate Change, in *IPCC*, edited by P. Core Writing Team, R.K. and Reisinger, A., p. 104, Geneva, Switzerland.

IPCC (2013), *Climate Change 2013: The Physical Science Basis. Contribution of Working Group I to the Fifth Assessment Report of the Intergovernmental Panel on Climate Change*, 1535 pp., Cambridge University Press, Cambridge, United Kingdom and New York, NY, USA.

IPCC (2014a), *Climate Change 2014: Mitigation of Climate Change. Contribution of Working Group III to the Fifth Assessment Report of the Intergovernmental Panel on Climate Change [Edenhofer, O., R. Pichs-Madruga, Y. Sokona, E. Farahani, S. Kadner, K. Seyboth, A. Adler, I. Baum, S. Brunner, P. Eickemeier, B. Kriemann, J. Savolainen, S. Schlömer, C. von Stechow, T. Zwickel and J.C. (eds.)]*, 1132 pp., Cambridge University Press, Cambridge, United Kingdom and New York, NY, USA.

IPCC (2014b), *Climate Change 2014: Impacts, Adaptation, and Vulnerability. Part A: Global and Sectoral Aspects. Contribution of Working Group II to the Fifth Assessment Report of the Intergovernmental Panel on Climate Change [Field, C.B., V.R. Barros, D.J. Dokken, K.J. Mach, M.D. Mastrandrea, T.E. Bilir, M. Chatterjee, K.L. Ebi, Y.O. Estrada, R.C. Genova, B. Girma, E.S. Kissel, A.N. Levy, S. MacCracken, P.R. Mastrandrea, and L.L. White (eds.)]*, 1132 pp., Cambridge University Press, Cambridge, United Kingdom and New York, NY, USA.

Ishiwatari, A. (1992), Petrology, geochemistry, and mineralogy of the Early Cretaceous evolved N-MORB from Sites 765 and 766, eastern Indian Ocean. In *Gradstein, F.M., Ludden, J.N., et al., Proc. ODP, Sci. Results, 123: College Station, TX (Ocean Drilling Program)*, 201-213.

Jarrard, R. D., L. J. Abrams, R. Pockalny, R. L. Larson, and T. Hirono (2003), Physical properties of upper oceanic crust: Ocean Drilling Program Hole 801C and the waning of hydrothermal circulation, *Journal of Geophysical Research: Solid Earth*, *108*(B4), 2188.

Jessen, K., A. R. Kovscek, and F. M. Orr Jr. (2005), Increasing CO_2 storage in oil recovery *Energ Convers Manage*, *46*, 293-311.

Johnson, H. P., and M. J. Pruis (2003), Fluxes of fluid and heat from the oceanic crustal reservoir, *Earth and Planetary Science Letters*, *216*(4), 565-574.

Judkins, R. R., W. Fulkerson, and M. K. Sanghvi (1993), The dilemma of fossil fuel use and global climate change, *Energy & Fuels*, *7*(1), 14-22.

Kaszuba, J. P., D. R. Janecky, and M. G. Snow (2005), Experimental evaluation of mixed fluid reactions between supercritical carbon dioxide and NaCl brine: Relevance to the integrity of a geologic carbon repository, *Chemical Geology*, *217*(3–4), 277-293.

Kelemen, P. B., and J. M. Matter (2008), In situ carbonation of peridotite for CO_2 storage, *Proceedings of the National Academy of Sciences*, *105*(45), 17295-17300.

Kelemen, P. B., and C. E. Manning (2015), Reevaluating carbon fluxes in subduction zones, what goes down, mostly comes up, *Proceedings of the National Academy of Sciences*, *112*(30), E3997-E4006.

Kelemen, P. B., J. M. Matter, E. E. Streit, J. F. Rudge, W. B. Curry, and J. Blusztajn (2011), Rates and mechanisms of mineral carbonation in peridotite: natural processes and recipes for enhanced, in situ CO_2 capture and storage, *Annual Review of Earth and Planetary Sciences*, *39*(1), 545-576.

Kido, M., and T. Seno (1994), Dynamic topography compared with residual depth anomalies in oceans and implications for age-depth curves, *Geophysical Research Letters*, *21*(8), 717-720.

Knauss, K. G., S. N. Nguyen, and H. C. Weed (1993), Diopside dissolution kinetics as a function of pH, CO_2, temperature, and time, *Geochimica et Cosmochimica Acta*, *57*(2), 285-294.

Lackner, K. S. (2003), A guide to CO_2 sequestration, *Science*, *300*(5626), 1677-1678.

Lackner, K. S., C. H. Wendt, D. P. Butt, E. L. Joyce Jr, and D. H. Sharp (1995), Carbon dioxide disposal in carbonate minerals, *Energy*, *20*(11), 1153-1170.

Langseth, M. G., X. Le Pichon, and M. Ewing (1966), Crustal structure of the mid-ocean ridges: 5. Heat flow through the Atlantic Ocean floor and convection currents, *Journal of Geophysical Research*, *71*(22), 5321-5355.

Langseth, M. G., M. J. Mottl, M. A. Hobart, and A. T. Fisher (1988), The distribution of geothermal and geochemical gradients near Site 501/504: implications for hydrothermal circulation in the oceanic crust, in *In Becker, K., Sakai, H., et al., Proc. ODP, Init. Repts., 111: College Station, TX (Ocean Drilling Program)*, edited, pp. 23–32.

Le Quere, C., M. R. Raupach, J. G. Canadell, G. Marland, and et al. (2009), Trends in the sources and sinks of carbon dioxide, *Nature Geoscience*, *2*(12), 831-836.

Le Quéré, C., et al. (2014), Global carbon budget 2014, *Earth Syst. Sci. Data Discuss.*, *7*(2), 521-610.

Le Quéré, C., et al. (2015), Global Carbon Budget 2015, *Earth Syst. Sci. Data*, *7*(2), 349-396.

Leung, D. Y. C., G. Caramanna, and M. M. Maroto-Valer (2014), An overview of current status of carbon dioxide capture and storage technologies, *Renewable and Sustainable Energy Reviews*, *39*, 426-443.

Levine, J. S., J. M. Matter, D. S. Goldberg, A. Cook, and K. S. Lackner (2007), Gravitational trapping of carbon dioxide in deep sea sediments: permeability, buoyancy, and geomechanical analysis, *Geophys. Res. Lett.*, *34*, L24703.

Linstrom, P. J., and W. G. Mallard (Eds.) (2012), *NIST Chemistry WebBook, NIST Standard Reference Database Number 69*, National Institute of Standards and Technology, Gaithersburg MD, 20899, http://webbook.nist.gov, retrieved November 12, 2012.

Lister, C. R. B. (1974), On the penetration of water into hot rock, *Geophysical Journal of the Royal Astronomical Society*, *39*(3), 465-509.

Lowell, R. P., and P. A. Rona (1985), Hydrothermal models for the generation of massive sulfide ore deposits, *Journal of Geophysical Research: Solid Earth*, *90*(B10), 8769-8783.

Lowell, S., and J. E. Shields (2013), *Powder surface area and porosity*, Springer Science & Business Media.

Ludwig, W. J., and R. E. Houtz (1979), Isopach Map of the Sediments in the Pacific Ocean Basin, color map with text, in *Am. Assoc. Pet. Geol.*, edited, Tulsa, OK.

Luthi, D., et al. (2008), High-resolution carbon dioxide concentration record 650,000-800,000 years before present, *Nature*, *453*(7193), 379-382.

Lüttge, A., and R. S. Arvidson (2008), The mineral-water interface, in *Kinetics of Water-Rock Interaction*, edited by S. L. Brantley, J. D. Kubicki and A. F. White, pp. 73-107, Springer New York.

Luyendyk, B. P., and T. A. Davies (1974), Introduction and principal results; Leg 26 Deep Sea Drilling Project. College Station, TX, *Initial Reports of the Deep Sea Drilling Project*, *26*, 5-9.

Mann, D. M., and A. S. Mackenzie (1990), Prediction of pore fluid pressures in sedimentary basins, *Marine and Petroleum Geology*, *7*(1), 55-65.

Marieni, C., T. J. Henstock, and D. A. H. Teagle (2013), Geological storage of CO_2 within the oceanic crust by gravitational trapping, *Geophysical Research Letters*, *40*(23), 2013GL058220.

Maroto-Valer, M. M. (2010), *Developments and Innovation in Carbon Dioxide (CO_2) Capture and Storage Technology: Carbon Dioxide (CO_2) Storage and Utilisation*, Elsevier.

Mathias, S. A., P. E. Hardisty, M. R. Trudell, and R. W. Zimmerman (2009), Approximate solutions for pressure buildup during CO_2 injection in brine aquifers, *Transport in Porous Media*, *79*(2), 265-284.

Matter, J. M., and P. B. Kelemen (2009), Permanent storage of carbon dioxide in geological reservoirs by mineral carbonation, *Nature Geosci*, *2*(12), 837-841.

Matter, J. M., T. Takahashi, and D. S. Goldberg (2007), Experimental evaluation of in situ CO_2-water-rock reactions during CO_2 injection in basaltic rocks: implications for geological CO_2 sequestration, *Geochem. Geophys. Geosyst.*, *8*, Q02001.

Matter, J. M., M. Stute, P. Schlosser, and W. Broecker (2015), Radiocarbon as a reactive tracer for tracking permanent CO_2 storage in basaltic rocks*Rep.*, The Trustees Of Columbia University In The City Of New York Inc., NY (United States).

Matter, J. M., W. S. Broecker, M. Stute, S. R. Gislason, E. H. Oelkers, A. Stefánsson, D. Wolff-Boenisch, E. Gunnlaugsson, G. Axelsson, and G. Björnsson (2009), Permanent carbon dioxide storage into basalt: the CarbFix Pilot Project, Iceland, *Energy Procedia*, *1*(1), 3641-3646.

Matter, J. M., et al. (2013), American Geophysical Union Fall Meeting, abstract V41A-2753.

Matter, J. M., et al. (2011), The CarbFix Pilot Project–Storing carbon dioxide in basalt, *Energy Procedia*, *4*(0), 5579-5585.

Matter, J. M., et al. (2016), Rapid carbon mineralization for permanent disposal of anthropogenic carbon dioxide emissions, *Science*, *352*(6291), 1312-1314.

Matthias, P. K., P. D. Rabinowitz, and N. Dipiazza (1988), Sediment Thickness map of the Indian Ocean, Map 505, in *Am. Assoc. Pet. Geol.*, edited, Tulsa, OK.

McGrail, B. P., F. A. Spane, J. E. Amonette, C. R. Thompson, and C. F. Brown (2014), Injection and monitoring at the Wallula Basalt Pilot Project, *Energy Procedia*, *63*(0), 2939-2948.

McGrail, B. P., H. T. Schaef, A. M. Ho, Y.-J. Chien, J. J. Dooley, and C. L. Davidson (2006), Potential for carbon dioxide sequestration in flood basalts, *Journal of Geophysical Research: Solid Earth*, *111*, B12201.

McKenzie, D. P. (1967), Some remarks on heat flow and gravity anomalies, *Journal of Geophysical Research*, *72*(24), 6261-6273.

McKinsey & Company (2008), Carbon Capture and Storage: Assessing the Economics.

Meschede, M., and U. Barckhausen (2000), Plate tectonic evolution of the Cocos-Nazca spreading center. In *Silver, E.A., Kimura, G., and Shipley, T.H. (Eds.), Proceedings of the Ocean Drilling Program, Scientific Results*, *College Station, TX (Ocean Drilling Program)*, *170*.

Millero, F. J., R. Feistel, D. G. Wright, and T. J. McDougall (2008), The composition of standard seawater and the definition of the reference-composition salinity scale, *Deep Sea Research Part I: Oceanographic Research Papers*, *55*(1), 50-72.

Millero, F. J., T. B. Graham, F. Huang, H. Bustos-Serrano, and D. Pierrot (2006), Dissociation constants of carbonic acid in seawater as a function of salinity and temperature, *Marine Chemistry*, *100*(1–2), 80-94.

Moores, E. M., and F. J. Vine (1971), The Troodos Massif, Cyprus and other ophiolites as oceanic crust: evaluation and implications, *Philosophical Transactions of the Royal Society of London A: Mathematical, Physical and Engineering Sciences*, *268*(1192), 443-467.

Mottl, M. J. (1983), Metabasalts, axial hot springs, and the structure of hydrothermal systems at mid-ocean ridges, *Geological Society of America Bulletin*, *94*(2), 161-180.

Mottl, M. J., and C. G. Wheat (1994), Hydrothermal circulation through mid-ocean ridge flanks: fluxes of heat and magnesium, *Geochimica et Cosmochimica Acta*, *58*(10), 2225-2237.

Müller, R. D., M. Sdrolias, C. Gaina, and W. R. Roest (2008), Age, spreading rates and spreading symmetry of the world's ocean crust, *Geochem. Geophys. Geosyst.*, *9*, Q04006.

Müller, R. D., W. R. Roest, J. Y. Royer, L. M. Gahagan, and J. G. Sclater (1997), Digital isochrons of the world's ocean floor, *Journal of Geophysical Research: Solid Earth*, *102*(B2), 3211-3214.

Munschy, M., and R. Schlich (1989), The Rodriguez Triple Junction (Indian Ocean): Structure and evolution for the past one million years, *Marine Geophysical Researches*, *11*(1), 1-14.

Nafe, J. E., and C. L. Drake (1961), Physical properties of marine sediments*Rep.*, DTIC Document.

Nesbitt, H. W., and R. E. Wilson (1992), Recent chemical weathering of basalts, *American Journal of Science*, *292*(10), 740-777.

Nicolas, A. (1989), Structure of ophiolites and dynamics of oceanic lithosphere Kluwer Academic Publishing, *Dordrecht, The Netherlands*.

O'Connor, W. K., D. C. Dahlin, D. N. Nilsen, G. Rush, R. P. Walters, and P. C. Turner (2000), CO_2 storage in solid form: a study of direct mineral carbonation*Rep.*, Albany Research Center (ARC), Albany, OR.

Oelkers, E. H. (2001a), An experimental study of forsterite dissolution rates as a function of temperature and aqueous Mg and Si concentrations, *Chemical Geology*, *175*(3–4), 485-494.

Oelkers, E. H. (2001b), General kinetic description of multioxide silicate mineral and glass dissolution, *Geochimica et Cosmochimica Acta*, *65*(21), 3703-3719.

Oelkers, E. H., and J. Schott (1995), Experimental study of anorthite dissolution and the relative mechanism of feldspar hydrolysis, *Geochimica et Cosmochimica Acta*, *59*(24), 5039-5053.

Oelkers, E. H., and S. R. Gislason (2001), The mechanism, rates and consequences of basaltic glass dissolution: I. An experimental study of the dissolution rates of basaltic glass as a function of aqueous Al, Si and oxalic acid concentration at 25°C and pH = 3 and 11, *Geochimica et Cosmochimica Acta*, *65*(21), 3671-3681.

Oelkers, E. H., and D. R. Cole (2008), Carbon dioxide sequestration a solution to a global problem, *Elements*, *4*(5), 305-310.

Oelkers, E. H., J. Schott, and J. L. Devidal (1994), The effect of aluminum, pH, and chemical affinity on the rates of aluminosilicate dissolution reactions, *Geochimica et Cosmochimica Acta*, *58*(9), 2011-2024.

Oelkers, E. H., S. R. Gislason, and J. M. Matter (2008), Mineral carbonation of CO_2, *Elements*, *4*(5), 333-337.

Olsson, J., S. L. S. Stipp, and S. R. Gislason (2014), Element scavenging by recently formed travertine deposits in the alkaline springs from the Oman Semail Ophiolite, *Mineralogical Magazine*, *78*(6), 1479-1490.

Oxburgh, R., J. I. Drever, and Y.-T. Sun (1994), Mechanism of plagioclase dissolution in acid solution at 25 °C, *Geochimica et Cosmochimica Acta*, *58*(2), 661-669.

Pacala, S., and R. Socolow (2004), Stabilization wedges: Solving the climate problem for the next 50 years with current technologies, *Science*, *305*(5686), 968-972.

Parker, R. L., and D. W. Oldenburg (1973), Thermal model of ocean ridges, *Nature*, *242*(122), 137-139.

Parsons, B., and J. G. Sclater (1977), An analysis of the variation of ocean floor bathymetry and heat flow with age, *J. Geophys. Res.*, *82*(5), 803-827.

Paukert, A. N., J. M. Matter, P. B. Kelemen, E. L. Shock, and J. R. Havig (2012), Reaction path modeling of enhanced in situ CO_2 mineralization for carbon sequestration in the peridotite of the Samail Ophiolite, Sultanate of Oman, *Chemical Geology*, *330–331*, 86-100.

Pokrovsky, O. S., and J. Schott (2000), Kinetics and mechanism of forsterite dissolution at 25 °C and pH from 1 to 12, *Geochimica et Cosmochimica Acta*, *64*(19), 3313-3325.

Pollack, H. N., S. J. Hurter, and J. R. Johnson (1993), Heat flow from the Earth's interior: analysis of the global data set, *Rev. Geophys.*, *31*(3), 267-280.

Portier, S., and C. Rochelle (2005), Modelling CO_2 solubility in pure water and NaCl-type waters from 0 to 300 °C and from 1 to 300 bar: Application to the Utsira Formation at Sleipner, *Chemical Geology*, *217*(3), 187-199.

Power, I. M., A. L. Harrison, G. M. Dipple, S. A. Wilson, P. B. Kelemen, M. Hitch, and G. Southam (2013), Carbon mineralization: from natural analogues to engineered systems, *Reviews in Mineralogy and Geochemistry*, *77*(1), 305-360.

Prentice, I. C., G. Farquhar, M. Fasham, M. Goulden, M. Heimann, V. Jaramillo, H. Kheshgi, C. LeQuéré, R. Scholes, and D. W. Wallace (2001), The carbon cycle and atmospheric carbon dioxide, in *Climate Change 2001: The Scientific Basis*, edited by J. T. Houghton et al., pp. 183–237, Cambridge University Press.

Pribnow, D. F. C., E. E. Davis, and A. T. Fisher (2000), Borehole heat flow along the eastern flank of the Juan de Fuca Ridge, including effects of anisotropy and temperature dependence of sediment thermal conductivity, *Journal of Geophysical Research: Solid Earth*, *105*(B6), 13449-13456.

Raitt, R. W. (1963), The crustal rocks, in *The Sea, Ideas and Observations on Progress in the Study of the Seas, The Earth Beneath The Seas*, edited by M. N. Hill, pp. 85-102, John Wiley and Sons, New York.

Rausch, S. (2012), Carbonate veins as recorders of seawater evolution, CO_2 uptake by the ocean crust, and seawater-crust interaction during low-temperature alteration, Doctoral dissertation thesis, Universität Bremen: Geowissenschaften, Bremen.

Rochelle, C. A., I. Czernichowski-Lauriol, and A. E. Milodowski (2004), The impact of chemical reactions on CO_2 storage in geological formations: a brief review, *Geological Society, London, Special Publications*, *233*(1), 87-106.

Rosenbauer, R. J., B. Thomas, J. L. Bischoff, and J. Palandri (2012), Carbon sequestration via reaction with basaltic rocks: geochemical modeling and experimental results, *Geochimica et Cosmochimica Acta*, *89*, 116-133.

Rosenberg, N. D., F. J. Spera, and R. M. Haymon (1993), The relationship between flow and permeability field in seafloor hydrothermal systems, *Earth and Planetary Science Letters*, *116*(1), 135-153.

Rubin, E. S. (2008), CO_2 capture and transport, *Elements*, *4*(5), 311-317.

Rubin, E. S., J. E. Davison, and H. J. Herzog (2015), The cost of CO_2 capture and storage, *International Journal of Greenhouse Gas Control*, *40*, 378-400.

Sabine, C. L., et al. (2004), The oceanic sink for anthropogenic CO_2, *Science*, *305*(5682), 367-371.

Schaef, H. T., and B. P. McGrail (2009), Dissolution of Columbia River Basalt under mildly acidic conditions as a function of temperature: Experimental results relevant to the geological sequestration of carbon dioxide, *Applied Geochemistry*, *24*(5), 980-987.

Schaef, H. T., B. P. McGrail, and A. T. Owen (2010), Carbonate mineralization of volcanic province basalts, *International Journal of Greenhouse Gas Control*, *4*(2), 249-261.

Schaef, H. T., B. P. McGrail, and A. T. Owen (2011), Basalt reactivity variability with reservoir depth in supercritical CO_2 and aqueous phases, *Energy Procedia*, *4*(0), 4977-4984.

Schettino, A., and C. R. Scotese (2005), Apparent polar wander paths for the major continents (200 Ma to the present day): a palaeomagnetic reference frame for global plate tectonic reconstructions, *Geophysical Journal International*, *163*(2), 727-759.

Schrag, D. P. (2009), Storage of carbon dioxide in offshore sediments, *Science*, *325*(5948), 1658-1659.

Sclater, J. G., and J. Francheteau (1970), The Implications of Terrestrial Heat Flow Observations on Current Tectonic and Geochemical Models of the Crust and Upper Mantle of the Earth, *Geophysical Journal of the Royal Astronomical Society*, *20*(5), 509-542.

Sclater, J. G., C. Jaupart, and D. Galson (1980), The heat flow through oceanic and continental crust and the heat loss of the Earth, *Reviews of Geophysics*, *18*(1), 269-311.

Scott, V. (2013), What can we expect from Europe's carbon capture and storage demonstrations?, *Energy Policy*, *54*, 66-71.

Second IMO GHG Study 2009 *International Maritime Organization (IMO)*, Buhaug, Ø., Corbett, J.J., Endresen, Ø., Eyring, V., Faber, J., Hanayama, S., Lee, D.S., Lee, D., Lindstad, H., Markowska, A.Z., Mjelde, A., Nelissen, D., Nilsen, J., Pålsson, C., Winebrake, J.J., Wu, W., Yoshida, K., London, UK, April 2009.

Seifritz, W. (1990), CO_2 disposal by means of silicates, *Nature*, *345*.

Seyfried, W. E. J., and M. J. Mottl (1982), Hydrothermal alteration of basalt by seawater under seawater-dominated conditions, *Geochimica et Cosmochimica Acta*, *46*(6), 985-1002.

Shackley, S., D. Reiner, P. Upham, H. de Coninck, G. Sigurthorsson, and J. Anderson (2009), The acceptability of CO_2 capture and storage (CCS) in Europe: An assessment of the key determining factors: Part 2. The social acceptability of CCS and the wider impacts and repercussions of its implementation, *International Journal of Greenhouse Gas Control*, *3*(3), 344-356.

Sharqawy, M. H., J. H. Lienhard, and S. M. Zubair (2010), Thermophysical properties of seawater: a review of existing correlations and data, *Desalination and Water Treatment*, *16*(1-3), 354-380.

Shibuya, T., M. Yoshizaki, Y. Masaki, K. Suzuki, K. Takai, and M. J. Russell (2013), Reactions between basalt and CO_2-rich seawater at 250 and 350°C, 500 bars:

Implications for the CO_2 sequestration into the modern oceanic crust and the composition of hydrothermal vent fluid in the CO_2-rich early ocean, *Chemical Geology*, *359*, 1-9.

Sigfusson, B., et al. (2015), Solving the carbon-dioxide buoyancy challenge: The design and field testing of a dissolved CO_2 injection system, *International Journal of Greenhouse Gas Control*, *37*, 213-219.

Sinton, J. M., and R. S. Detrick (1992), Mid-ocean ridge magma chambers, *Journal of Geophysical Research: Solid Earth*, *97*(B1), 197-216.

Sipilä, J., S. Teir, and R. Zevenhoven (2008), Carbon dioxide sequestration by mineral carbonation Literature review update 2005–2007, *Report VT*, *1*, 2008.

Slagle, A. L., and D. S. Goldberg (2011), Evaluation of ocean crustal Sites 1256 and 504 for long-term CO_2 sequestration, *Geophys. Res. Lett.*, *38*, L16307.

Snæbjörnsdóttir, S. Ó., F. Wiese, T. Fridriksson, H. Ármansson, G. M. Einarsson, and S. R. Gislason (2014), CO_2 storage potential of basaltic rocks in Iceland and the oceanic ridges, *Energy Procedia*, *63*(0), 4585-4600.

Solomon, S., G.-K. Plattner, R. Knutti, and P. Friedlingstein (2009), Irreversible climate change due to carbon dioxide emissions, *Proceedings of the National Academy of Sciences of the United States of America*, *106*(6), 1704-1709.

Solomon, S. C., and D. R. Toomey (1992), The structure of mid-ocean ridges, *Annual Review of Earth and Planetary Sciences*, *20*, 329-364.

Span, R., and W. Wagner (1996), A new equation of state for carbon dioxide covering the fluid region from the triple-point temperature to 1100 K at pressures up to 800 MPa, *J. Phys. Chem. Ref. Data*, *25*(6), 1509-1596.

Spinelli, G. A., and A. T. Fisher (2004), Hydrothermal circulation within topographically rough basaltic basement on the Juan de Fuca Ridge flank, *Geochemistry, Geophysics, Geosystems*, *5*(2), n/a-n/a.

Spinelli, G. A., E. R. Giambalvo, and A. T. Fisher (2004), Sediment permeability, distribution, and influence on fluxes in oceanic basement, *Hydrogeology of the oceanic lithosphere*, 151-188.

Staudigel, H., S. R. Hart, H.-U. Schmincke, and B. M. Smith (1989), Cretaceous ocean crust at DSDP Sites 417 and 418: Carbon uptake from weathering versus loss by magmatic outgassing, *Geochimica et Cosmochimica Acta*, *53*(11), 3091-3094.

Stein, C. A., and S. Stein (1992), A model for the global variation in oceanic depth and heat flow with lithospheric age, *Nature*, *359*(6391), 123-129.

Stein, C. A., and S. Stein (1994), Constraints on hydrothermal heat flux through the oceanic lithosphere from global heat flow, *Journal of Geophysical Research: Solid Earth*, *99*(B2), 3081-3095.

Stein, C. A., S. Stein, and A. M. Pelayo (1995), Heat flow and hydrothermal circulation, in *Seafloor Hydrothermal Systems: Physical, Chemical, Biological, and Geological Interactions*, edited, pp. 425-445, AGU, Washington, DC.

Stillings, L. L., J. I. Drever, S. L. Brantley, Y. Sun, and R. Oxburgh (1996), rates of feldspar dissolution at pH 3–7 with 0–8 m M oxalic acid, *Chemical Geology*, *132*(1–4), 79-89.

Strens, M. R., and J. R. Cann (1982), A model of hydrothermal circulation in fault zones at mid-ocean ridge crests, *Geophysical Journal of the Royal Astronomical Society*, *71*(1), 225-240.

Summerhayes, C. P., and S. A. Thorpe (1996), *Oceanography: an Illustrated Guide*, Manson Publishing, London.

Svensson, R., M. Odenberger, F. Johnsson, and L. Strömberg (2005), Transportation infrastructure for CCS - Experiences and expected development, in *Greenhouse Gas Control Technologies 7*, edited, pp. 2531-2534, Elsevier Science Ltd, Oxford.

Takahashi, T., D. S. Goldberg, and J. C. Mutter (2000), Secure, long-term sequestration of CO_2 in deep saline aquifers associated with oceanic and continental basaltic rock, paper presented at SRI International Symposium "Deep Sea & CO_2 2000".

Talwani, M., C. C. Windisch, and M. G. Langseth (1971), Reykjanes ridge crest: A detailed geophysical study, *Journal of Geophysical Research*, *76*(2), 473-517.

Teagle, D. A. H., B. Ildefonse, P. Blum, and a. t. E. Scientists/ (2012), Proc. IODP, 335: Tokyo (Integrated Ocean Drilling Program Management International, Inc.).

Teagle, D. A. H., J. C. Alt, S. Umino, S. Miyashita, N. R. Banerjee, D. S. Wilson, and the Expedition 309/312 Scientists (2006), *Proc. IODP, 309/312, Integrated Ocean Drilling Program Management International, Inc.*, Washington, DC.

Teir, S., H. Revitzer, S. Eloneva, C.-J. Fogelholm, and R. Zevenhoven (2007), Dissolution of natural serpentinite in mineral and organic acids, *International Journal of Mineral Processing*, *83*(1–2), 36-46.

Tenzer, R., and V. Gladkikh (2014), Assessment of Density Variations of Marine Sediments with Ocean and Sediment Depths, *The Scientific World Journal*, *2014*, 9.

Terzaghi, K., R. B. Peck, and G. Mesri (1996), *Soil mechanics in engineering practice*, John Wiley & Sons.

Tollefson, J. (2013), Pilot projects bury carbon dioxide in basalt, *Nature*, *500*(7460), 18.

Tominaga, M., D. A. H. Teagle, J. C. Alt, and S. Umino (2009), Determination of the volcanostratigraphy of oceanic crust formed at superfast spreading ridge: electrofacies analyses of ODP/IODP Hole 1256D, *Geochem. Geophys. Geosyst.*, *10*(1), Q01003.

Torp, T. A., and K. R. Brown (2004), CO_2 underground storage costs as experienced at Sleipner and Weyburn, paper presented at Proceedings of the 7th International Conference on Greenhouse Gas Control Technologies (GHGT-7).

Turcotte, D. L., and E. R. Oxburgh (1967), Finite amplitude convective cells and continental drift, *Journal of Fluid Mechanics*, *28*(01), 29-42.

Turcotte, D. L., and G. Schubert (1982), *Geodynamics: Applications of continuum physics to geological problems, 450 pp*, John Wiley, New York.

Turcotte, D. L., and G. Schubert (2002), *Geodynamics*, Second ed., 456 pp., Cambridge University Press, Cambridge.

van Grinsven, J. J. M., and W. H. van Riemsdijk (1992), Evaluation of batch and column techniques to measure weathering rates in soils, *Geoderma*, *52*(1), 41-57.

Van Pham, T. H., P. Aagaard, and H. Hellevang (2012), On the potential for CO_2 mineral storage in continental flood basalts – PHREEQC batch- and 1D diffusion–reaction simulations, *Geochemical Transactions*, *13*, 5-5.

Veevers, J. J., J. R. Heirtzler, and et al. (1974), *Initial Reports of the Deep Sea Drilling Project*, Washington (U.S. Government Printing Office).

Von Herzen, R. P., and S. Uyeda (1963), Heat flow through the eastern Pacific ocean floor, *Journal of Geophysical Research*, *68*(14), 4219-4250.

von Rad, U., B. U. Haq, and et al. (1992), *Proc. ODP, Sci. Results*, 122: College Station, TX (Ocean Drilling Program).

Wall, M., H. Pugh, A. Reay, and J. Krol (2002), *Failure Modes, Reliability and Integrity of Floating Storage Unit (FPSO, FSU) Turret and Swivel Systems*, Great Britain, Health and Safety Executive.

Walther, C. H. (2003), The crustal structure of the Cocos ridge off Costa Rica, *Journal of Geophysical Research: Solid Earth (1978–2012)*, *108*(B3).

Weiss, R. F. (1974), Carbon dioxide in water and seawater: the solubility of a non-ideal gas, *Marine Chemistry*, *2*(3), 203-215.

Wheat, C. G., and M. J. Mottl (2000), Composition of pore and spring waters from Baby Bare: global implications of geochemical fluxes from a ridge flank hydrothermal system, *Geochimica et Cosmochimica Acta*, *64*(4), 629-642.

Wheat, C. G., H. W. Jannasch, M. Kastner, J. N. Plant, and E. H. DeCarlo (2003), Seawater transport and reaction in upper oceanic basaltic basement: chemical data from continuous monitoring of sealed boreholes in a ridge flank environment, *Earth and Planetary Science Letters*, *216*(4), 549-564.

Wheat, C. G., M. J. Mottl, A. T. Fisher, D. Kadko, E. E. Davis, and E. Baker (2004), Heat flow through a basaltic outcrop on a sedimented young ridge flank, *Geochem. Geophys. Geosyst.*, *5*, Q12006.

White, R. S., D. McKenzie, and R. K. O'Nions (1992), Oceanic crustal thickness from seismic measurements and rare earth element inversions, *Journal of Geophysical Research: Solid Earth*, *97*(B13), 19683-19715.

Williams, D. L., R. P. Von Herzen, J. G. Sclater, and R. N. Anderson (1974), The Galapagos Spreading Centre: Lithospheric Cooling and Hydrothermal Circulation, *Geophysical Journal International*, *38*(3), 587-608.

Wilson, D. S. (1996), Fastest known spreading on the Miocene Cocos-Pacific Plate Boundary, *Geophysical Research Letters*, *23*(21), 3003-3006.

Wilson, D. S., D. A. H. Teagle, G. D. Acton, and et al. (2003), Proc. ODP, Init. Repts., 206: College Station, TX (Ocean Drilling Program).

Wilson, D. S., et al. (2006a), Drilling to gabbro in intact ocean crust, *Science*, *312*(5776), 1016-1020.

Wilson, S. A. (1997), Data compilation for USGS reference material BHVO-2, Hawaiian Basalt: U.S. Geological Survey Open-File Report.

Wilson, S. A., M. Raudsepp, and G. M. Dipple (2006b), Verifying and quantifying carbon fixation in minerals from serpentine-rich mine tailings using the Rietveld method with X-ray powder diffraction data, *American Mineralogist*, *91*(8-9), 1331-1341.

Wolff-Boenisch, D. (2011), On the buffer capacity of CO_2-charged seawater used for carbonation and subsequent mineral sequestration, *Energy Procedia*, *4*, 3738-3745.

Wolff-Boenisch, D., and S. R. Gíslason (2002), Dissolution rate of volcanic glass as a function of glass composition (abstract), *Geochimica et Cosmochimica Acta*, *66*, A843.

Wolff-Boenisch, D., S. R. Gislason, E. H. Oelkers, and C. V. Putnis (2004), The dissolution rates of natural glasses as a function of their composition at pH 4 and 10.6, and temperatures from 25 to 74°C, *Geochimica et Cosmochimica Acta*, *68*(23), 4843-4858.

Wolff-Boenisch, D., S. Wenau, S. R. Gislason, and E. H. Oelkers (2011), Dissolution of basalts and peridotite in seawater, in the presence of ligands, and CO_2: implications for mineral sequestration of carbon dioxide, *Geochimica et Cosmochimica Acta*, *75*(19), 5510-5525.

Wright, M. J., D. A. H. Teagle, and P. M. Feetham (2014), A quantitative evaluation of the public response to climate engineering, *Nature Clim. Change*, *4*(2), 106-110.

Xu, T., J. A. Apps, and K. Pruess (2005), Mineral sequestration of carbon dioxide in a sandstone–shale system, *Chemical Geology*, *217*(3–4), 295-318.

Zeebe, R. E., and D. Wolf-Gladrow (Eds.) (1993), *CO_2 in seawater: equilibrium, kinetics, isotopes*.

ZEP (2011a), The costs of CO_2 transport: post-demonstration. CCS in the EU, *European Technology Platform for Zero Emission Fossil Fuel Power Plants*.

ZEP (2011b), The costs of CO_2 storage: post-demonstration. CCS in the EU, *European Technology Platform for Zero Emission Fossil Fuel Power Plants*.